Scattering Studies of Proton Transfer Reactions between Rare Gas Atoms

A thesis submitted by

Debasish Koner

to

Indian Institute of Technology Guwahati

in fulfillment of the requirements for the degree of

Doctor of Philosophy

Department of Chemistry

INDIAN INSTITUTE OF TECHNOLOGY GUWAHATI

Guwahati 781039

INDIA

December 2016


भारतीय प्रौद्योगिकी संस्थान गुवाहाटी
Indian Institute of Technology Guwahati

Scattering Studies of Proton Transfer Reactions between Rare Gas Atoms

Doctoral Thesis

Author:

Debasish Koner

Roll No. 11612220

Supervisor:

Dr. Aditya N. Panda

Department of Chemistry

Indian Institute of Technology Guwahati

Guwahati 781039

INDIA

December 2016

Declaration

I, Debasish Koner, declare that this thesis titled, *'Scattering Studies of Proton Transfer Reactions between Rare Gas Atoms'* and the work presented in it are my own. I confirm that this work was done by me during the period from July 2011 to June 2016 in candidature for the degree of Doctor of Philosophy at Indian Institute of Technology Guwahati under the guidance and supervision of Dr. Aditya N. Panda, associate professor, Department of Chemistry. Any part of this thesis has not previously been submitted for a degree or any other qualification at this Institution or any other university/institution. Where I have consulted the published work of others, this is always clearly attributed. I have acknowledged all main sources of help.

Signed:

Debasish Koner

Date:

Certificate

This is to certify that the thesis titled *'Scattering Studies of Proton Transfer Reactions between Rare Gas Atoms'* submitted for the award of degree of Doctor of Philosophy by **Debasish Koner** is the record of research work carried out by him during the period July 2011 to June 2016 under my guidance and supervision. This work has not formed the basis for the award of any degree, diploma, associateship, fellowship or other titles in this Institution or in any other university/institution.

Signed:
Dr. Aditya N. Panda
Associate Professor
Date:

Acknowledgements

First and foremost, I would like to express my sincere gratitude to my thesis advisor Dr. Aditya Narayan Panda for giving me the opportunity to work with him. I warmly appreciate his guidance, ideas, patience and contribution of time to my research work. I am thankful to him for his continuous support, motivation and encouragements throughout my PhD career. The lessons that I have learned in the last five years through his valuable advices will help me immensely in my future academic and personal life. I express my heartiest gratitude with profound respect to him for the excellent example he has shown as a good teacher and friendly supervisor.

I heartily thank Dr. Tomás Gonález and Lizandra Barrios for the scientific collaboration. I am thankful to Prof. Miguel Gonález, Prof. Octavio Roncero, Prof. Rex T. Skodje, Prof. Dario De Fazio, Prof. Ke-Li Han, Prof. Hua Guo and Dr. Pablo Gamallo for their kind and prompt replies to my research related queries and for sending me reference data files, surface routines and scientific documents in many occasions.

I would like to thank my doctoral committee members, Prof. Ashish Kumar Gupta, Dr. Sandip Paul and Dr. Padma Kumar Padmanabhan for their insightful comments, valuable suggestions and encouragements. I thank Dr. Manabendra Sarma, as it was an interesting experience to work with him as a teaching assistant.

I would like to acknowledge the financial support from Indian Institute of Technology, Guwahati. I am very thankful to the Department of Chemistry for giving me the opportunity to work as a research scholar in this department. I acknowledge the computational facility from CDAC-Pune and ORANG-HPCC, IIT Guwahati.

I gratefully recall the knowledge that I have gained from my university and school teachers. I am indebted to all of them.

I thank my labmates Sayakda, Hari, Anurag, Manish, Juri, Sayantani, Darnesh, Shashwat and Rishabh for their company and cooperation in lab. Special thanks to Hari for helping me many times in my research works. I thank Renjithda for motivating and encouraging me in my PhD days.

I am thankful to all of my school, university and IIT friends. I feel myself very lucky as I enjoyed my PhD journey with Kandida, Boss, Sahu, Sourav, Pakhida, Hochi, Hari, Kobirul, Utpal, Kartick, Tapas, Barunda, Suman, Samir, Barman, Samit, Dinabandhu, Subhashishda, Bishu, Sujoyda, Arindamda, Palashda, Rambabu, Bishuda, Anabilda, Baretoda, Satyada, Shilaj, Srikrishna, Gourab, Uday, Keshab, Koushik, Kallol, Sudinda, Ramiz, Ashish, Sourav, Shubhankar, Ganesh, Ujjwal, Shubhra, Surajit, Tarai, Shubhadip, Buddha, Sabyasachi, Prakash, Ashraful, Kundu, Ronson.

I wish to convey my heartiest thank to all my villagers who love me so much whenever I am in my village.

Finally and most importantly, I thank all the members of my big family, especially my parents, sister and grandmother for their unconditional support and encouragement.

I dedicate this thesis to my respected teacher Dr. Aditya N. Panda and my well wishers.

Synopsis

The question "how a chemical reaction takes place?" at microscopic level lies at the heart of chemistry. Most of the chemical transformations occur via several elementary steps of basic chemical events known as *elementary chemical reactions*, which occupy the central place in unraveling the mechanisms of a chemical transformation (e.g., formation of water from hydrogen and oxygen involves several elementary reactions). Bimolecular reactions are the most common types among elementary reactions. Studying the dynamics of A + BC or AB + CD type of bimolecular reactions in gas phase is one the important areas of research, both in experimental and theoretical chemistry. Tremendous advances in molecular beam and laser experiments give the experimentalists opportunity to precisely determine state-to-state transition attributes. On the theoretical front, the basic requirement for studying the dynamics is the potential energy surface (PES) which describes the forces acting on different species. The Born-Oppenheimer approximation decouples the electronic and nuclear motions to produce adiabatic PESs. Study of reactive/non-reactive scattering involves solving the dynamical equations using either classical or quantum methods on the PESs. This provides knowledge about the influence of internal quantum state, relative kinetic energy and geometric orientation of reactants on the reaction, as well as rotational, vibrational energy and angular distributions of products.

Hydrogen and light rare gases are amongst the most abundant elements of the universe. Reactive collisions are thus possible in the interstellar clouds, planetary ionospheres among the light rare gases and proton (H^+), and investigation on these processes may be relevant for understanding the evolution of our solar system. This importance explains why simple rare gas complexes like RgH_2^+, Rg_2H^+ and $[RgHRg']^+$ (Rg/Rg' = rare gas) have been the center of attraction to many researchers for last few decades. However, global analytic PESs for $[HeHNe]^+$ and $[NeHNe]^+$ and theoretical scattering dynamics studies on possible processes for these systems are not reported in the literature till date. Keeping in mind that both the systems might be important and relevant in proton-rare gas as well as in fundamental chemistry, these two systems and possible reactive processes are explored in this thesis. The objective of the present thesis is to compute analytical global PESs for these systems, compute the eigenvalue spectra and study the dynamics of various proton transfer processes.

Chapter 1: Introduction

This chapter introduces the area of gas phase reaction dynamics, in addition to presenting a survey of the relevant literature.

Chapter 2: Methodology

This chapter presents the methodologies used to investigate the $[HeHNe]^+$ and $[NeHNe]^+$ systems. The generation of analytical PESs from *ab initio* energies, computation of ro-vibrational states of triatomic complexes and details of reactive scattering methodologies are presented. Following the methodologies, Fortran codes were written to compute the eigen states of the stable complexes and to investigate the quantum dynamics by following time dependent wave packet propagation method. Quantum dynamics codes are designed to calculate total reaction probabilities, within both centrifugal sudden (CS) approximation and Coriolis coupled (CC) frameworks. Shared memory parallelization procedure was implemented in the CS code, while both shared memory and message passing interface parallelization algorithm was implemented in the CC code. Fortran programs were also written to calculate quasi-classical trajectories for a triatomic bimolecular reaction and to analyze those trajectories by following histogram binning (HB) and Gaussian binning (GB) approaches.

Chapter 3: Global Potential Energy Surfaces for $[HeHNe]^+$ and $[NeHNe]^+$ Systems and Bound States

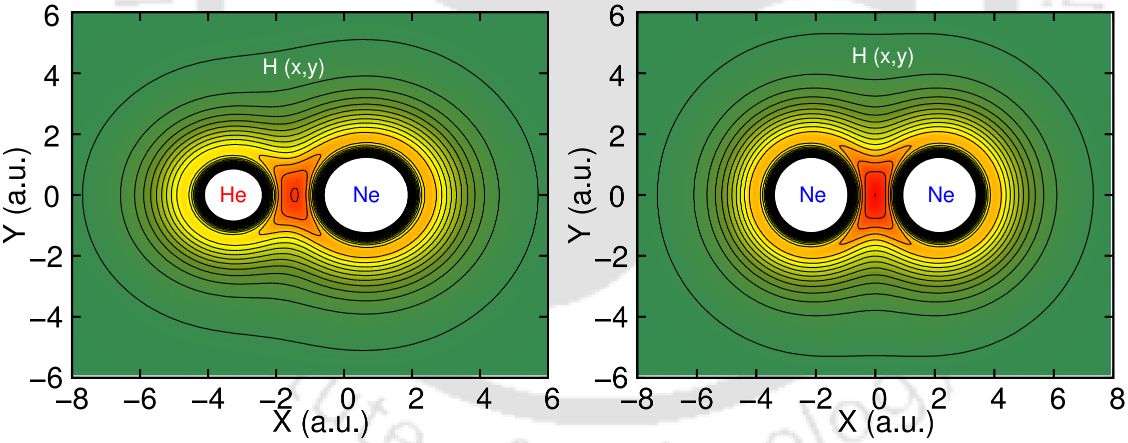

In this chapter, electronic structural details of two proton-rare gas dimer molecular complex systems, $[HeHNe]^+$ and $[NeHNe]^+$, are explored, and full dimensional analytical potential energy surfaces with very small root mean square error values are generated for both the systems from *ab initio* energies calculated at CCSD(T)/aug-cc-pVQZ level. For both the surfaces, the global minima correspond to linear configurations with the hydrogen atom located in between the two rare gas atoms. Excellent agreements between the analytic and *ab initio* energies are achieved at short- and long-range interaction regions for both the PESs. In addition to this, the bound vibrational states for $J = 0$ for the most stable structures of both the systems are calculated. The number of bound states are found to be 6 and 37 for $[\mathrm{HeHNe}]^+$ and $[\mathrm{NeHNe}]^+$, respectively.

Chapter 4: The He + NeH$^+$ → HeH$^+$ + Ne Reaction

In this chapter, a real wave packet based TDQM, TIQM and QCT methods are employed to study the dynamics of the He + NeH$^+$ → HeH$^+$ + Ne reaction on the analytical PES generated in Chapter 3. Different initial state selected total reaction probabilities and total integral cross sections (ICS) have been calculated for the title reaction by using TDQM and TIQM methods.

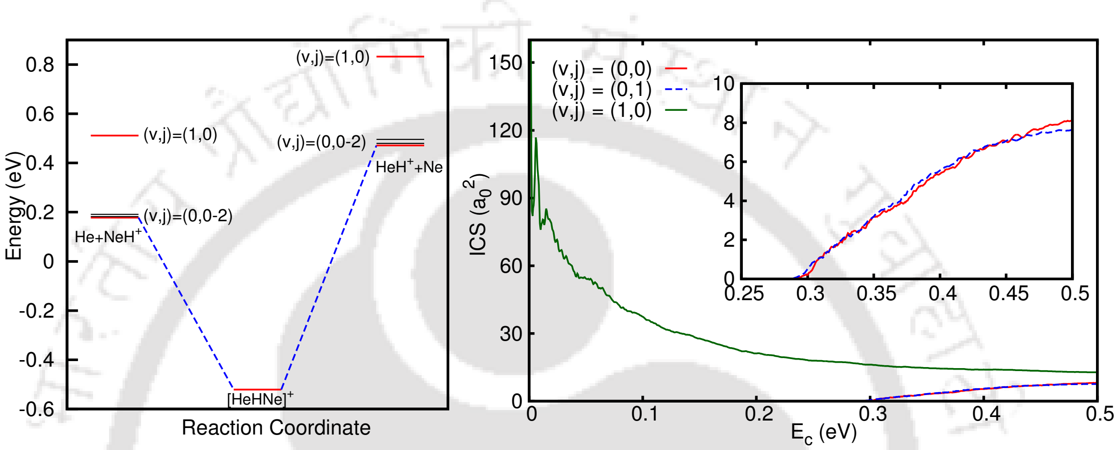

Sharp oscillatory structures of the probability curves are observed for low values of J in the low energy region, which are mostly washed out in the ICSs curves. Differences observed between the CC and CS probabilities indicate the importance of inclusion of Coriolis coupling in the quantum mechanical studies for this process. Vibrational excitation of the reactants strongly enhances the reaction, while rotational excitation has small effect on the reaction. QCT-GB method is found to describe the process fairly well for ground ro-vibrational reactant state. State-to-state dynamics for the reaction have been investigated at different collision energies by means of TIQM and QCT calculations starting from ground ro-vibrational reactant state. Angular distributions for the reaction show a prominent peak in the forward directions. QCT simulations were run to find out different mechanisms associated with the process at different collision energies. The reaction is mainly direct, but indirect paths influence the reaction at low energies. Both nearside and farside scatterings have been observed for the reactive trajectories with direct mechanisms.

Chapter 5: The Ne + HeH$^+$ → NeH$^+$ + He Reaction

The dynamics of Ne + HeH$^+$ → NeH$^+$ + He reaction is investigated by carrying out TIQM, real wave packet based TDQM and QCT calculations in this chapter. Total reaction probabilities and ICSs have been computed for the title reaction for different initial states by using TDQM, TIQM and QCT methods. As with the reverse reaction, numerous resonances are seen in the QM probability curves indicating the presence of metastable states of the collision complex. TDQM ICSs differ remarkably compared to the TIQM ICSs in the low-energy region, while the QCT ICSs are overall in a good accord with the TIQM results. This highlights QCT as an efficient method to study this reaction. Initial state selected rate constants for the title reaction are calculated for a wide range of temperatures, which agree well with the available experimental result at 300 K. Simple Langevin capture model is used to obtained ICSs and rate constant for this reaction and was found to describe the reaction well. A few collision energies are chosen to investigate the state-to-state dynamics for the title reaction for ground ro-vibrational reactant state by using TIQM and QCT methods. Reactive scattering for this process shows marked preference for the forward direction. An analysis carried out by using quasi-classical simulations shows that the reaction is dominated by direct mechanisms producing both nearside and farside scattered products. At low collision energies, a small fraction of trajectories form collision complexes.

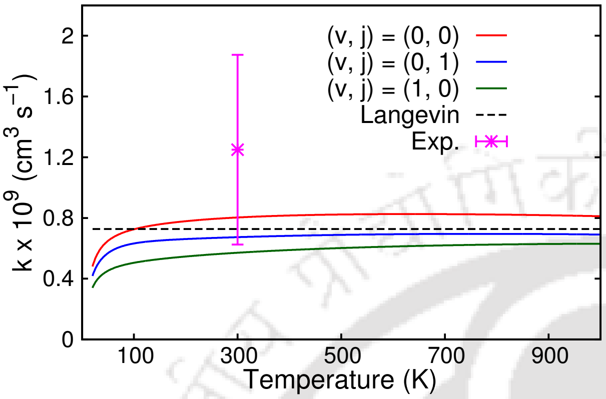

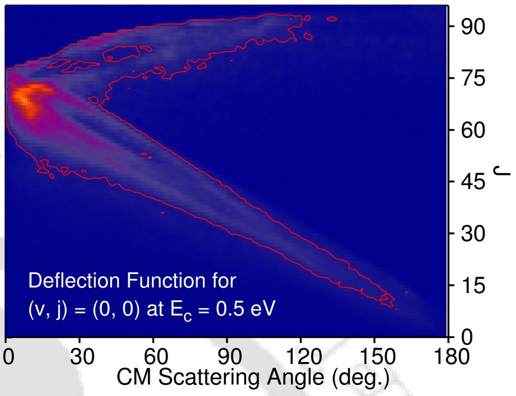

Chapter 6: The Ne + NeH$^+$ → NeH$^+$ + Ne Reaction

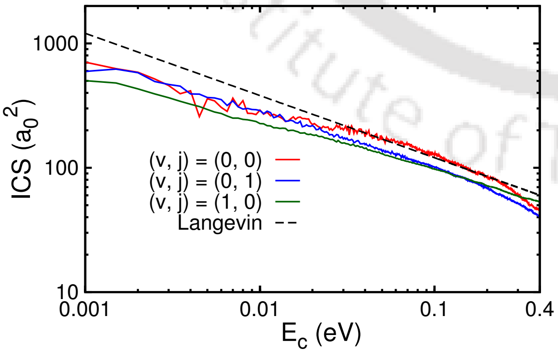

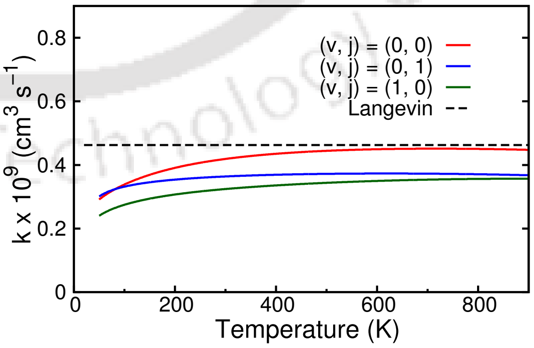

In this chapter, initial state selected dynamics of the Ne + NeH$^+$ → NeH$^+$ + Ne reaction are reported by carrying out quantum mechanical studies on the ground electronic state. Total reaction probabilities, total integral cross sections and thermally averaged rate constants have been calculated for ground ro-vibrational, first excited rotational and first excited vibrational states of the reactants. TDQM method is found to describe the reaction poorly in the low-energy region. However, an overall excellent agreement is found between TDQM-CC and TIQM results in moderate and high energy regions. Rotational excitation of the reactant diatom inhibits the reaction at moderate and high values of collision energies, while vibrational excitation of the reactants is found to inhibit the reaction at low and moderate energies and promote the reaction at high energies. ICSs and rate constants are also calculated by following the Langevin capture model, which are in a good agreement with QM results. In order to investigate the sharp resonances found in the QM ICSs in the low energy region for ground ro-vibrational reactant state, QCT calculations were performed at few selected resonance peaks. Presence of numerous trapped long lived trajectories for this reaction suggests that a major portion of the reaction occurs via indirect mechanisms at low energies.

Chapter 7: Summary and Conclusions

A brief summary of the thesis and concluding remarks are presented in this chapter. Global analytical PESs are generated on the ground electronic states using high level *ab initio* energies for two triatomic proton bound rare gas systems, $[\mathrm{HeHNe}]^+$ and $[\mathrm{NeHNe}]^+$. Bound states and eigen spectra are calculated for zero total angular momentum for the most stable structures for both the systems. Reactive scattering dynamics are performed for the proton transfer reactions, $\mathrm{He} + \mathrm{NeH}^+ \rightarrow \mathrm{HeH}^+ + \mathrm{Ne}$, $\mathrm{Ne} + \mathrm{HeH}^+ \rightarrow \mathrm{NeH}^+ + \mathrm{He}$ and $\mathrm{Ne} + \mathrm{NeH}^+ \rightarrow \mathrm{NeH}^+ + \mathrm{Ne}$ by using TDQM, TIQM and QCT methods on the newly generated analytical surfaces for first time.

Contents

List of Figures

List of Tables

Abbreviations

3D	**T**hree **D**imension
BF	**B**ody **F**ixed
BO	**B**orn **O**ppenheimer
CC	**C**oriolis **C**oupled
CS	**C**entrifugal **S**udden
CRWP	**C**hebyshev **R**eal **W**ave **P**acket
DCS	**D**iffrential **C**ross **S**ection
DVR	**D**iscrete **V**ariable **R**epresentation
FBR	**F**inite **B**asis **R**epresentation
FT	**F**ourier **T**ransformation
FFT	**F**ast **F**ourier **T**ransformation
FWHM	**F**ull **W**idth **H**alf **M**aximum
ICS	**I**ntegral **C**ross **S**ection
ISM	**I**nter **S**tellar **M**edium
MEP	**M**inimum **E**nergy **P**athway
MPI	**M**essage **P**assing **I**nterface
PES	**P**otential **E**nergy **S**urface
QCT	**Q**uasi **C**lassical **T**rajectory
QM	**Q**uantum **M**echanics
RWP	**R**eal **W**ave **P**acket
Rg	**R**are **g**as
SF	**S**pace **F**ixed
SO	**S**plit **O**perator
TD	**T**ime **D**ependent
TDQM	**T**ime **D**ependent **Q**uantum **M**echanics
TDWP	**T**ime **D**ependent **W**ave **P**acket
TDSE	**T**ime **D**ependent **S**chrödinger **E**quation
TI	**T**ime **I**ndependent

TIQM	**T**ime **I**ndependent **Q**uantum **M**echanics
TISE	**T**ime **I**ndependent **S**chrödinger **E**quation
WF	**W**ave **F**unction
WP	**W**ave **P**acket

Physical Parameters & Unit Conversions

Mass of hydrogen = 1.0078 amu

Mass of helium = 4.0026 amu

Mass of neon = 19.9924 amu

1 amu = 1822.888486192 a.u.

1 Hartree = 627.509 kcal/mol

1 Hartree = 27.2116 eV

1 bohr = 0.5291772 Å

1 a.u. = 0.02418884326505 fs

Chapter 1

Introduction

Chemical reaction dynamics, related to description of the atomic motions during chemical transformations, lies at the very heart of chemistry. The central goal of reaction dynamics is gaining an understanding of any chemical reaction at microscopic level i.e., getting the answer of the question, *"how a chemical reaction takes place?"*. Thus, studying chemical reaction dynamics is the key for interpreting the chemical kinetics for a system at macroscopic level. The field has immense importance in exploring different chemical phenomena occurring in planetary atmosphere and interstellar media, as well as in understanding the chemistry of different combustion reactions. Most of the chemical transformations occur via several elementary steps of basic chemical events called as *elementary chemical reactions*, which occupy the central place in unraveling the mechanisms of a chemical transformation e.g., formation of water from hydrogen and oxygen involves several elementary reactions. Every single elementary reaction bears its own unique fingerprint, and studying the reaction dynamics of an elementary reaction provides knowledge about the influence of reactants internal quantum state, relative kinetic energy and geometric orientation on the reaction, as well as rotational, vibrational energy and angular distributions of products. Bimolecular reactions are one of the most common type among elementary reactions. Studying reaction dynamics of simple bimolecular processes in gas phase is one of the important areas of research, both in experimental and theoretical chemistry. The main focus of this thesis is to study a few selected bimolecular triatomic elementary processes in the gas phase.

In the last few decades, many experimental techniques have been developed, e.g., crossed molecular beam experiments, pump-probe femtosecond spectroscopy, laser induced fluorescence spectroscopy, time-of-flight spectroscopy, velocity map imaging methods etc. Nowadays, tremendous advances in molecular beam and laser experiments give the experimentalists opportunity to precisely determine state-to-state transitions. The emerging field of the femtosecond chemistry brings a new era in researches by tracking chemical events in real time.

On the theoretical side, the main goal is to predict the dynamical outcomes of a chemical reaction based on basic physical principles. The description of atomic motion for a chemical transformation is related to forces or, equivalently a potential. So, it begins with the concept of *potential energy surface* describing the forces of chemical reactions, which govern the motion of the nuclei during a chemical event. Determination of potential energies for a system is greatly simplified by the Born-Oppenheimer approximation, which decouples the electronic and nuclear motions. Thus potential energies of a system for a particular electronic state can be computed as a function of nuclear coordinates. For most of the reactions, a single state PES is sufficient to describe the nuclear dynamics. However, for non-adiabatic reactions, conical interactions between PESs exist, and multiple PESs as well as non-adiabatic coupling elements are needed in describing the nuclear dynamics. In this thesis, investigation on the reactive processes are limited to the ground electronic states. Enormous advances in the field of computation and development of *ab initio* quantum chemistry methods for calculating highly accurate electronic structures of molecular systems from first principles help researchers to obtain accurate potential energies. To study the dynamics of a reaction, global PES is needed covering all the possible configurations of that reactive system. In principle, highly accurate potential energies are calculated by solving the electronic Schrödinger equation via *ab initio* methods for different nuclear configurations. Global analytical PES for the system is then constructed by fitting those *ab initio* energies to suitable analytic functions or following interpolation schemes. Reliability of the dynamical calculations depends on the accuracy of the PES.

Once the PES of a system is available, reactive scattering dynamics can be studied by solving the equations related to the motions of nuclei on the PES by following quantum, classical or statistical mechanical methods. In quantum mechanical methodologies, the nuclear dynamics of the reactive systems are studied by solving either time-independent Schrödinger equation or time-dependent Schrödinger equation. In time-independent approach, the asymptotic basis functions are used to expand the time-independent scattering wave functions. Hyperspherical coordinates, which are independent of arrangement channels, are the most convenient to describe the reactive scattering for triatomic systems in TIQM approach. However, for larger systems it is not straightforward to use the hyperspherical coordinates. In the TIQM method, in each calculation the S-matrix is extracted for only a single energy but for different energetically available initial internal state of the reactants. An alternative approach is the TDQM approach, is based on wave packet propagation. In this approach, the time-dependent Schrödinger equation is solved in grid or basis representation. An initial wave packet that describes a range of energies is chosen for a particular internal state of interest for the reactants. The wave packet is then propagated for sufficiently long time by following an efficient and stable propagation scheme. The scattering information can be calculated by computing either the outgoing flux or the S-matrix. Generally, reactant or product Jacobi coordinates are used during propagation of the wave packet, which is efficient for studying tri-, tetra-atomic or even larger systems. As time is incorporated in this method, a mechanistic view of the reaction can be obtained by analyzing the wave packet with respect to time. However, to calculate the reaction probabilities at very low energies the propagation has to be done for comparatively longer time and this method may become inefficient.

In the classical or quasi-classical trajectory calculation method the Hamilton's equations of motion are solved via numerical integration and trajectories are calculated for a single collision event. Different reaction attributes are calculated via sampling large number of trajectories with different initial conditions in the entire phase space of the reactants using Monte-Carlo algorithm. In this method, products are obtained with a continuous energy distribution, and binning methods are used to assign the product states. The QCT method interprets reactions as classical collisions between particles, thus giving a vivid mechanistic details of the reaction. However, the true quantum phenomena like tunneling, resonance, interference can not be explained in this method. In a semi-classical approach these quantum phenomena are incorporated.

The statistical approach, which can be applied on intermediate complex forming reactions, is based on the energy randomization of the complex intermediate. If the intermediate complex has sufficiently long lifetime, complete energy randomization can be achieved, and decaying of the complex to all the open channels are calculated statistically by their availability. State-to-state probabilities are then calculated from the capture probabilities in all the open channels.

Theoretical studies yield various state averaged and state-to-state reaction attributes, which includes reaction probabilities, integral cross sections, differential cross sections, rate constants. In order to calculate the reaction cross sections, reaction probabilities are summed over different partial waves (J), which requires computation of probabilities for a series of Js. By taking the advantage of the total angular momentum conservation, the dynamical simulations are therefore divided into separate calculations for a particular value of partial wave or total angular momentum. The bound states of molecular systems can also be computed theoretically. The theoretically predicted results are then compared quantitatively with the available experimental results to check the accuracy of different theoretical methods as well as the PES. Nowadays, with enormous progress in the field of chemical reaction dynamics, new experimental and theoretical methods are developed, and results obtained from both type of studies agree closely revealing interesting dynamical features of different chemical reactions (see Ref. 1 and references therein).

1.1 STUDIES ON BIMOLECULAR REACTIONS

Studying the scattering dynamics of bimolecular reactions have been a very popular subject for a long time. $H + H_2 \rightarrow H_2 + H$ is the simplest bimolecular reaction. Investigation on the collinear $H+H_2$ process has been started in late 1930s[2,3] and early forties.[4] Benchmark 3D QCT calculations were done on the $H+H_2$ system in 1965.[5] Full dimensional quantum calculation on this simplest reaction was difficult up to 1970s, until the development of efficient algorithms and advance computing systems. Since

1976, when the first full dimensional quantum reactive scattering study of H+H_2 system was carried out,[6] a number of methods[7–10] have been developed to study the quantum scattering for the H+H_2 and other triatomic bimolecular processes. In the experimental side, the H+H_2 reactive system and its isotopic analogs are explored via molecular beam studies.[11–15] It is worth mentioning here that even after considerable progress in theory and experiment, the simplest H+H(D)$_2$ reactive system remains as attractive to be explored as it was in earlier. Recently, advanced experiments carried out on this system yield surprise results and more sophisticated theories are prescribed to deal with it.[16–19] Thus the 'simplest' reaction has become less simple[17] over time and it is expected that more exciting results would be revealed showing the importance of the reaction dynamics field.

Like H+H_2, F+H_2 system is also very popular in the reactive scattering field. The reaction is best known for the effect of Feshbach resonances on the reaction dynamics, and is studied in many instances both experimentally and theoretically.[20–24] Scattering dynamics for other hydrogen abstraction reactions like Cl+H_2,[25,26] Br+H_2,[27] O+H_2,[28] C+H_2,[29,30] S+H_2[31,32] are also investigated extensively. There have been a number of studies on various ion-molecule type reactive processes like H^++H_2,[33–36] He+H_2^+,[37,38], Ne+H_2^+,[39–41] Ar+H_2^+,[42], O^++H_2,[43,44] Li+H_2^+[45,46], and neutral C+OH,[47,48] S+OH,[49] Li+HF[50,51] systems. Among the tetra-atomic bimolecular reactive systems plentiful researches have been done on processes like H_2+OH[52–54], H_2+CN[55–57], OH+CO[58,59]. Reactive scattering studies have been performed on dozens of other bimolecular reactive processes in the last few decades.[60–64] However, full dimensional quantum mechanical investigation of elementary reactions comprising more then four atoms is quite challenging, even with the advent of larger and faster computers due to increase complexity with increase in degrees of freedom. Multi-configurational time-dependent Hartree and QCT methods are applied to study comparatively larger polyatomic systems like H+CH_4,[65] O+CH_4,[66], Cl+NH_3[67].

For some of the reactions, potential energy landscapes usually show a barrier which separates the reactants from the products, e.g., H+H_2, Br+H_2. These reactions are generally very fast and follow direct mechanisms, i.e., a simultaneous bond breaking and a bond making process. Dynamical calculations for these reactions, whether quantum or classical are quite easy and straightforward because of very simple forms of the potential energy surfaces. The excitation functions for these reactions show a clear threshold due to the activation barrier. Beyond the threshold the cross section increases to a maximum with increase in energy before decreasing again. The rate constants for these reactions follow Arrhenius behavior. For systems like F+H_2, Feshbach resonances can be seen in the probability curves, as the typical shape of the vibrationally adiabatic PES close to the transition state region temporarily traps the reactant flux.

For the reaction with no barrier occurring mostly in the ISM,[68] excitations functions exhibit large value at very low energies due to the long-range attractive interactions. The cross section decreases with increase in energy and remain almost invariant at high energies. The rate constants for most of these reactions do not follow Arrhenius equation, and have values typically in the range of 10^{-11} - 10^{-9} cm^3 s^{-1}. Capture theory can readily be applied for these type of exothermic reactions. According to capture theory, a collision with energy that surmounts the effective potential barrier, must be a reactive one. In Langevin capture model,[69,70] analytical formula are derived for various types of exothermic reactions, which yields a temperature independent rate constant for ion-molecule type reactions.

There is another type of bimolecular reactions, having potential well(s) in the reaction path, which proceed via indirect paths because of formation of intermediate collision-complex in the potential well regions of the the PESs. Numerous sharp oscillations stemming from the quasibound states of the intermediate complex are manifested in the reaction probability curves, which are the signatures of indirect mechanisms associated to those reactions. Most of the ion-molecular systems like H^++H_2, He+H_2^+, Ne+H_2^+, O^++H_2 are examples of this kind of reaction. For the reactions with deep potential wells, e.g., H^++H_2, C+H_2 symmetric angular distributions of the products are observed. Reactive scattering study of this type of reactions is quite challenging, as large spatial grid is needed to describe the deep potential well and long-range electrostatic interaction in the asymptotic regions. These reactions generally possess no barrier in the entrance channel and a large number of partial waves is required to converge the cross sections. Inclusion of Coriolis coupling in the quantum dynamical simulations is of paramount importance for these type of bimolecular complex-forming scattering systems.[71–73]

1.2 PROTON-RARE GAS SYSTEMS

Hydrogen and light rare gases are amongst the most abundant elements of the universe. Hydrogen and helium, the two most abundant elements of our galaxy, are the results of primordial nucleosynthesis, which played an important role in the early universe evolution scenario.[74–77] In a series of chemical reactions, these elements formed the first molecular ionic system of the universe, HeH^+,[75,78] which was then followed by formation of H_2^+.[78] Other two light rare gases neon and argon are also present in a considerable amount in the ISM.[79–82] In fact, neon is the fifth most abundant element in our solar system.[83] Neutral Mass Spectrometer of NASA's Lunar Atmosphere and Dust Environment Explorer (LADEE) spacecraft confirms the existence of neon in lunar exosphere, which mainly comes from solar wind.[84] Recently ArH^+ molecular ion has been detected in Crab nebula from spectra recorded by the Herschel Space Observatory.[80] Reactive collisions are thus possible among the light rare gases, proton (H^+), HeH^+ and H_2^+ in ISM environment, i.e., interstellar clouds, planetary ionospheres. Investigation on this process are relevant for understanding the evolution of our solar system and thermonuclear experiments in plasma physics. Therefore, electronic structure, spectroscopic and gas phase reactive scattering studies of various atom-molecular ionic systems have been the center of attraction to many researchers for last few decades.

1.2.1 RgH^+ systems

Rare gases are inert in nature and their bonding with other elements is of weak van der Waals type. A charged cationic species (e.g., H^+) can cause significant charge delocalization in the electron rich rare gases resulting stronger covalent and charge induced electrostatic interactions. Thus, proton can form stable complexes by interacting with rare gases or rare gas clusters. The simplest rare gas complexes RgH^+ (Rg = He, Ne, Ar, Kr, Xe) have been the subject of numerous experimental and theoretical studies for a long time. Formation of HeH^+ ion, for example, was noticed as early as in 1925.[85] In sixties, in several experimental studies, RgH^+ (Rg = He, Ne, Ar) ion were produced from ion-molecule reactions in the mixture of hydrogen and rare gases using electron impact ionization, photoionization techniques.[86–88] Formation of ArH^+, KrH^+ and XeH^+ in the reactions of Rg^+ with H_2 are reported by Aquilanti *et al.* in high-pressure mass spectrometer ion source experiment.[89] Fundamental band of the infrared spectrum have been detected for HeH^+[90] and NeH^+[91] by Amano *et al.* Emission spectrum of ArH^+[92] and KrH^+[93] have been observed in hollow-cathode discharge experiments in rare gases and hydrogen mixtures. A number of studies have been performed on the stability of RgH^+ molecules using different theoretical methods.[94–101] The binding energies for RgH^+ increase with the increase of atomic number of the rare gases. These diatomic molecules dissociate into Rg + H^+, with only exception for XeH^+. As the ionization energy of hydrogen is higher than xenon, XeH^+ dissociates into Xe^+ + H.

1.2.2 RgH_2^+ systems

RgH_2^+ are formed as intermediate complex in reaction of Rg with H_2^+. Among the RgH_2^+ systems HeH_2^+, NeH_2^+ and ArH_2^+ have been studied widely. The proton transfer reactions, Rg (Rg= He, Ne, Ar) + $H_2^+ \rightarrow RgH^+ + H$ are the sources of RgH^+ ions. These reactions have been the subject of investigation for a long time because of the fundamental importance of ion-molecular reactive system.

Being the simplest system among these a large number of theoretical and experimental studies have been performed on the HeH_2^+. Studies on HeH_2^+ system started long time back, in fact, evidence of its existence was found in 1925 by Hogness and Lunn in an electron impact ionization experiment with hydrogen and helium mixture.[85] Reactive scattering of the He+H_2^+ was studied experimentally by Yuan *et al.* in 1984 and the initial vibrational state selected cross sections were reported.[102] In theory, *ab intio* based 3D PES for the HeH_2^+ system was constructed by Joseph and Sathyamurthy[103] using the *ab initio* energies calculated by McLaughlin and Thompson.[104] The HeH_2^+ reactive system was studied by Sathyamurthy group in many instances to explore the scattering dynamics and resonances.[37,103,105–110] A number of highly accurate PESs have been constructed for the HeH_2^+ after 2000.[38,111–113] In 2005, initial state selected integral cross sections have been calculated for He + $H_2^+(v = 0 - 15, j = 1) \rightarrow HeH^+ +$ H using pulsed-field ionization-photoelectron-secondary ion coincidence (PFI-PESICO) experimental technique.[114] Results obtained from Coriolis coupled TDQM and TIQM calculations agree well with those experimental results.[38,115] He+H_2^+ proton transfer reaction is endothermic for ground ro-vibrational reactant state. A potential well of depth ~ 0.35 eV is found in the reaction path because of the most stable collinear He-H-H geometry for this system. Numerous resonances originated from the quasibound states of the intermediate He-H_2^+ complex are seen in the probability curves, and are investigated in several theoretical studies.[106,107] The reverse reaction, i.e., $HeH^+ + H \rightarrow He +$ H_2^+ has also been studied recently using QM method covering a wide range of collision energies.[116,117]

Many theoretical as well as experimental investigations have been done on the NeH_2^+ system including electronic structure calculations, PES constructions and scattering studies on the endothermic Ne+H_2^+ process. In 1981, crossed molecular beam study was performed on this reaction covering a relative translational energy range of 0.87 - 4.05 eV.[118] Initial vibrational state selected cross sections are determined for the reaction for $H_2^+(v = 0-8)$ using a photoelectron product ion delayed coincidence method by Niehaus *et al.*[119] Early in this century, Dressler *et al.* studied the reaction for different initial states of H_2^+ using PFI-PESICO experiment and reported integral cross sections for 0.7, 1.7 and 4.5 eV translational energies.[120,121] Availability of rich experimental results make this reaction attractive for theoretical research. Urban and coworkers computed 3D PES for NeH_2^+ on the ground electronic states based on *ab initio* energies obtained from coupled electron pair approach (CEPA) and did QCT simulations to study the scattering process.[122,123] Pendargast and coworkers fitted the *ab initio* energies calculated using CEPA method to three different functionals to construct three PESs named as PHHJ3 for this system and studied the reactive scattering using bending-corrected rotating linear model and investigated the role of resonances on the Ne+H_2^+ reaction.[124,125] This reaction is further studied using PHHJ3 PESs by following QCT, TIQM and TDQM methods by several groups.[126–130] Two new PESs named as LZHH[39] and XYTWM[131] are developed on this system recently using high level MRCI *ab initio* energies. Coriolis coupled QM and QCT studies including state-to-state dynamics have been carried out for this proton transfer process on the LZHH surface in many instances.[40,41,132–134] NeH_2^+ is an analogous with HeH_2^+ and the most stable structure for the NeH_2^+ system is a collinear Ne-H-H geometry. A potential well with a depth of ~ 0.54 eV corresponding to the equilibrium structure presents in the minimum energy path for the $Ne+H_2^+$ process. Sharp resonances seen in the reaction probabilities survive also in the integral cross sections, are studied by González *et al.*,[40] who suggest the reaction to be a Feshbach-resonance mediated.

For the $Ar+H_2^+$ system, the ground state PES is energetically well separated from other electronic states except when the reactants are far apart from each other, where $Ar+H_2^+$ and Ar^++H_2 curve crossing occurs.[135] Thus nonadiabatic transitions (charge transfer) can occur at large intermolecular distances. However, the only reactive process, $Ar + H_2^+ \rightarrow ArH^+ + H$, occurs in the ground adiabatic state. Crossed beam experiments have been carried out to investigate this proton transfer reaction by Bilotta *et al.*[136,137] Experimental state selected cross sections have been measured for this reaction by Ng. and coworkers.[138] In 2006, Dressler *et al.* determined the initial state selected experimental cross sections for this reaction for $H_2^+(v = 0-17, j = 1)$ using PFI-PESICO technique.[121] In the theoretical front, Kuntz and Roach developed a diatomic-in-molecules (DIM) PES for ArH_2^+ system based on semiempirical SCFMO energies.[139] First 3D QM calculations on this process have been carried out in 1994 using the DIM PES. Recently Liu *et al.* constructed two global PESs for the ground state of ArH_2^+ system, one using UCCSD(T)/aug-cc-pV5Z energies named as LLZ PES[140] and another using MRCI+Q/aug-cc-pVQZ energies named as HXLTL PES.[42] The LLZ PES is not smooth enough in the asymptotic regions because of convergence failure of the UCCSD(T) method at large internuclear distances. TDQM studies have been performed for this proton transfer process using the HXLTL PES for the ground rovibrational reactant state.[42] Unlike $He+H_2^+$ and $Ne+H_2^+$ processes, $Ar + H_2^+ \rightarrow ArH^+ + H$ is exothermic in nature. However, like the other two RgH_2^+ systems, a collinear Ar-H-H geometry is the most stable structure which is energetically ~ 1.78 eV lower than the $Ar+H_2^+$ asymptote.

1.2.3 [RgHRg/Rg′]$^+$ systems

Presence of H$^+$ ion in the weakly bound rare gas dimers plays an important role in making stable proton-bound rare gas dimer complex. These complexes are the fundamental species in the rare gas matrix produced during solvation of proton. There have been a number of experimental and theoretical studies reported in literature about the formation and stability of [RgHRg]$^+$ or [RgHRg′]$^+$ complexes. In 1970, formation of Rg_2H^+ (Rg = He, Ne, Ar) are reported by Adams *et al.* in reactions of Rg_2^+ with H_2.[141] Possible existence of Ar_2H^+ and Kr_2H^+ have been indicated in the rare gas-hydrogen matrix on glow discharge by Bondybey and Pimentel.[142] Formation of Ar_2H^+ has been reported by Hvistendahl *et al.* using high pressure mass spectrometry technique in the reaction mixture of Ar and H_2.[143] Kunttu *et al.* recorded the infrared spectra of Rg_2H^+ (Rg = Ar, Kr, Xe) by irradiating the solid rare gas matrices doped with hydrogen halide prepared by cooling the mixture of hydrogen halide and rare gases, and indicated a linear centrosymmetric Rg-H-Rg type structure for these complexes.[144,145] Fundamental bands of Kr_2H^+, Xe_2H^+, [ArHKr]$^+$, [ArHXe]$^+$ and [KrHXe]$^+$ are detected and assigned by Fridgen and Parnis using FT infrared spectroscopy in an electron bombardment matrix isolation experiment on rare gases and methanol mixtures.[146] In a recent experimental study, [KrHKr]$^+$, [XeHXe]$^+$ and [KrHXe]$^+$ complexes produced by electron bombardment of a gaseous H_2, D_2 and Rg mixture are characterized via FT infrared absorption spectroscopy.[147] Equilibrium structures of He_2H^+ and Ne_2H^+ are calculated using different *ab initio* methods and linear centrosymmetric Rg-H-Rg geometries are found as the most stable structures for these systems.[148–153] Various *ab initio* methods as well as density functional theory (DFT) are employed to study the stability and structural details of Ar_2H^+, Kr_2H^+ and Xe_2H^+ by several groups and collinear Rg-H-Rg structures are reported as equilibrium geometries.[98,147,150,154–157] For Ne_2H^+[151] and Ar_2H^+,[151] local potential minima have been observed for collinear Rg-Rg-H geometries. The proton bound mixed rare gas dimers, [ArHKr]$^+$, [ArHXe]$^+$ and [KrHXe]$^+$, are also investigated theoretically using *ab initio* and DFT level of theory.[98,147,155,156] Like [RgHRg]$^+$ systems, the most stable structures for [RgHRg′]$^+$ systems correspond to linear Rg-H-Rg′ geometries.

In the reaction dynamics field, He_2H^+ is studied extensively which includes generation of PES, calculation of eigenstates and carrying out reactive scattering simulations. In 1983, an *ab initio* PES for the He_2H^+ system was constructed by Dykstra using double substituted coupled cluster energies.[148] This PES was reconstructed by refitting a few more energy points to higher order polynomials by Lee and Secrest.[149] Ro-vibrational states of the $[HeHHe]^+$ complex were also computed by them. The equilibrium geometry of this system was further investigated by Baccarelli *et al.* and Kim and Lee computing *ab initio* PESs using MRD-CI/cc-pVTZ and MP4/6-311++G(3df,3pd) level calculations, respectively.[151,158] In 2003, a global analytical PES for He_2H^+ system has been developed by Panda and Sathyamurthy using CCSD(T)/d-aug-cc-pVTZ energies.[152] Bound vibrational states were also calculated for the $[HeHHe]^+$ complex using a TDWP approach. The PES was later used to study the $He + HeH^+ \rightarrow HeH^+ + He$ proton transfer reaction using TDQM method within centrifugal sudden approximation.[159] In 2012, an analytical PES has been generated for this system using high level *ab initio* energies obtained from MRCI+Q method and d-aug-cc-pV5Z basis set by Zhang *et al.*[153] Reactive scattering for the proton transfer $He+HeH^+$ process has been studied on the recent PES using Coriolis coupled TDQM and QCT methods by several groups.[153,160–162] A potential energy well with a depth of ∼ 0.58 eV presents in the PES for collinear and near-collinear configuration of He-H-He. Dense resonances originated from the potential well have been seen in the QM probability curves for the proton transfer reaction in the low energy region. A DIM PES for the collinear $Ne + NeH^+$ proton transfer process was developed by Matcha *et al.*[163] Bound vibrational states of Ar_2H^+ system has been computed by Li *et al.*[164] An analytical global PES was constructed for the Ar_2H^+ system for the ground electronic state based on QCISD/6-311++G(3df,3pd) level *ab initio* energies.[157] Among the mixed rare gas-proton systems, for the collinear $[HeHNe]^+$ system, a DIM PES is reported in literature by Matcha *et al.*[165] The $Ne + HeH^+ \rightarrow NeH^+ + He$ reaction was studied via selected ion flow experiment and the rate constant at 300 K was calculated by Glosík *et al.*[166] Here it is worth mentioning that apart from the proton-rare gas systems numerous cationic rare gas species formed in the gas phase are investigated and reported in literature (see Ref. 167 and references therein).

1.3 PROBLEM FORMULATION FOR THIS THESIS

From the above discussions it is well understood that studying the reaction dynamics of ion-molecule type proton rare gas systems have drawn intense attention of many researchers because of their fundamental importance as well as relevance in astrochemistry. Although a large number of studies have been performed on various reactive systems, in literature, there is no 3D PES reported for $[HeHNe]^+$ and $[NeHNe]^+$ systems. Theoretical studies on reactive scatterings for the possible processes for these two systems are therefore not reported in literature. However, these systems might be interesting in the chemical reaction dynamics field as well as in rare gas and astrochemistry. Both the systems being light-heavy-light type are relevant in fundamental chemistry and can be used as model system in future. In this thesis work, two rare gas-proton systems, $[HeHNe]^+$ and $[NeHNe]^+$, are studied which includes generation of global analytical PESs, studying reactive scattering for the possible proton transfer process i.e., He+NeH^+, Ne+HeH^+ and Ne+NeH^+. A large number of high level *ab initio* energies are computed and fitted to analytical forms. The ro-vibrational states of the most stable structures are calculated, will act as reference data in future experimental works on these systems. As it is seen Coriolis couplings play significant role in the dynamics of ion-molecule and complex forming reactions, inclusion of CC in QM simulations are thus necessary for these reactions. These reactions are studied using TDQM methodology within both CC and CS framework. CS results can quantify the effect of CC for these reaction. TIQM is applied here to study the reactions and TIQM results can act as reference in converging the TDQM calculations, similarly the reverse case can also happen. A QCT approach is very helpful in investigating the mechanistic pathways for a reaction, and picturesque details of a chemical reaction can be depicted from the quasiclassical trajectories. Therefore, QCT simulations are also run for those proton transfer reaction in this thesis. Simple models like Langevin capture model which describe ion-molecule type barrierless reactions well are also applied. It is expected that all these studies presented here will stimulate more experimental as well as theoretical work on $[HeHNe]^+$ and $[NeHNe]^+$ systems.

1.4 THESIS OVERVIEW

Chapter 2: Methodology

This chapter deals with the methodologies used to investigate the $[\mathrm{HeHNe}]^+$ and $[\mathrm{NeHNe}]^+$ systems, which includes generation of analytical PESs from *ab initio* energies, computation of ro-vibrational states of triatomic complexes and studying the reactive scatterings. Fortran Programs are written to compute the eigen states of ABC type systems and to investigate the quantum dynamics of A+BC processes by following time dependent wave packet propagation method. Quantum dynamics codes are designed to take the advantages of shared memory as well as MPI parallelization techniques. Fortran Programs are also written to calculate quasi-classical trajectories for triatomic bimolecular reactions and to analyze those trajectories by following histogram binning (HB) and Gaussian binning (GB) approaches.

Chapter 3: Global Potential Energy Surfaces for $[\mathrm{HeHNe}]^+$ and $[\mathrm{NeHNe}]^+$ Systems and Bound States

In this chapter, electronic structural details of two proton-rare gas dimer molecular complex systems, $[\mathrm{HeHNe}]^+$ and $[\mathrm{NeHNe}]^+$, are explored, and global analytical potential energy surfaces with very small root mean square error values are generated for both the systems from *ab initio* energies. In addition to this, the bound vibrational states for $J = 0$ for the most stable structures of both the systems are calculated.

Chapter 4: The He + $\mathrm{NeH}^+ \rightarrow \mathrm{HeH}^+$ + Ne Reaction

In this chapter, a real wave packet based time-dependent quantum mechanical (TDQM), time-independent quantum mechanical (TIQM) and quasiclassical trajectory methods are employed to study the dynamics of the $\mathrm{He} + \mathrm{NeH}^+ \rightarrow \mathrm{HeH}^+ + \mathrm{Ne}$ reaction on the analytical PES generated in Chapter 3. Different initial state selected total reaction probabilities and ICSs have been calculated for the title reaction by using TDQM, TIQM and QCT methods. State-to-state dynamics of the title reaction starting from ground ro-vibrational reactant state has been investigated at few selected collision energies in the moderate to high energy regions by means of TIQM and QCT calculations. Different mechanisms associated with the process are also investigated as a function of the collision energy.

Chapter 5: The Ne + $HeH^+ \rightarrow NeH^+$ + He Reaction

In this chapter, the dynamics of Ne + $HeH^+ \rightarrow NeH^+$ + He reaction is investigated by carrying out TIQM, real wave packet based TDQM and QCT calculations. Total reaction probabilities and ICSs have been computed for the title reaction for different initial states by using TDQM, TIQM and QCT methods. Initial state selected rate constants for the title reaction are calculated for a wide range of temperatures and compared with the available experimental result. Langevin capture model is also used to obtain ICSs and rate constant for this reaction. A few collision energies are chosen to investigate the state-to-state dynamics for the title reaction for ground ro-vibrational reactant state by following TIQM and QCT methods. Different mechanisms associated to this reaction are explored as a function of the collision energy.

Chapter 6: The Ne + $NeH^+ \rightarrow NeH^+$ + Ne Reaction

In this chapter, initial state selected dynamics of the Ne + $NeH^+ \rightarrow NeH^+$ + Ne reaction are reported by carrying out quantum mechanical studies on the ground electronic state. Total reaction probabilities, total integral cross sections and thermally averaged rate constants have been calculated for ground ro-vibrational, first excited rotational and first excited vibrational states of the reactants. ICSs and rate constants are also calculated by following the Langevin capture model and compared with the QM results. In order to investigate the resonances found in the QM ICSs in the low energy region, quasiclassical simulations have been carried out for the reaction at few collision energies for ground ro-vibrational reactant state.

Chapter 7: Summary and Conclusions

In this chapter, a short summary of the thesis is presented along with concluding remarks.

References

[1] Crim, F. F. *PNAS* **2008**, *105*, 12647.

[2] Eyring, H.; Polanyi, M. *Z. Physik. Chem. B* **1931**, *12*, 279.

[3] Hirschfelder, J. O.; Eyring, H. M.; Topley, B. *J. Chem. Phys.* **1936**, *4*, 170.

[4] Hulbert, H. M.; Hirschfelder, J. O. *J. Chem. Phys.* **1943**, *11*, 276.

[5] Karplus, M.; Porter, R. N.; Sharma, R. D. *J. Chem. Phys.* **1965**, *43*, 3259.

[6] Schatz, G. C.; Kuppermann, A. *J. Chem. Phys.* **1976**, *65*, 4668.

[7] Zhang, J. Z. H.; Miller, W. H. *J. Chem. Phys.* **1989**, *91*, 1528.

[8] Jäckle, A.; Meyer, H. *J. Chem. Phys.* **1995**, *102*, 5605.

[9] Althorpe, S. C.; Kouri, D. J.; Hoffman, D. K. *Chem. Phys. Lett.* **1997**, *275*, 173.

[10] Gray, S. K.; Balint-Kurti, G. G. *J. Chem. Phys.* **1998**, *108*, 950.

[11] Götting, R.; Mayne, H. R.; Toennies, J. P. *J. Chem. Phys.* **1984**, *80*, 2230.

[12] Götting, R.; Mayne, H. R.; Toennies, J. P. *J. Chem. Phys.* **1986**, *85*, 6396.

[13] Götting, R.; Herrero, V.; Toennies, J.; Vodegel, M. *Chem. Phys. Lett.* **1987**, *137*, 524.

[14] Continetti, R. E.; Balko, B. A.; Lee, Y. T. *J. Chem. Phys.* **1990**, *93*, 5719.

[15] Schnieder, L.; Seekamp-Rahn, K.; Wrede, E.; Welge, K. H. *J. Chem. Phys.* **1997**, *107*, 6175.

[16] Greaves, S. J.; Murdock, D.; Wrede, E.; Althorpe, S. C. *J. Chem. Phys.* **2008**, *128*, 164306.

[17] Jankunas, J.; Sneha, M.; Zare, R. N.; Bouakline, F.; Althorpe, S. C.; Herráez-Aguilar, D.; Aoiz, F. J. *PNAS* **2014**, *111*, 15.

[18] Jambrina, P. G.; Herráez-Aguilar, D.; Aoiz, F. J.; Sneha, M.; Jankunas, J.; Zare, R. N. *Nat. Chem.* **2015**, *7*, 661.

[19] Jambrina, P. G.; Aldegunde, J.; Aoiz, F. J.; Sneha, M.; Zare, R. N. *Chem. Sci.* **2016**, *7*, 642.

[20] Neumark, D. M.; Wodtke, A. M.; Robinson, G. N.; Hayden, C. C.; Lee, Y. T. *J. Chem. Phys.* **1985**, *82*, 3045.

[21] Neumark, D. M.; Wodtke, A. M.; Robinson, G. N.; Hayden, C. C.; Lee, Y. T. *Phys. Rev. Lett.* **1984**, *53*, 226.

[22] Qiu, M.; Ren, Z.; Che, L.; Dai, D.; Harich, S. A.; Wang, X.; Yang, X.; Xu, C.; Xie, D.; Gustafsson, M.; Skodje, R. T.; Sun, Z.; Zhang, D. H. *Science* **2006**, *311*, 1440.

[23] Ren, Z.; Che, L.; Qiu, M.; Wang, X.; Dai, D.; Harich, S. A.; Wang, X.; Yang, X.; Xu, C.; Xie, D.; Sun, Z.; Zhang, D. H. *J. Chem. Phys.* **2006**, *125*, 151102.

[24] Chen, J.; Sun, Z.; Zhang, D. H. *J. Chem. Phys.* **2015**, *142*, 024303.

[25] Yang, B.-H.; Tang, B.-Y.; Yin, H.-M.; Han, K.-L.; Zhang, J. Z. H. *J. Chem. Phys.* **2000**, *113*, 7182.

[26] Aoiz, F. J.; Bañares, L.; Castillo, J. F.; Menéndez, M.; Skouteris, D.; Werner, H.-J. *J. Chem. Phys.* **2001**, *115*, 2074.

[27] Panda, A. N.; Herráez-Aguilar, D.; Jambrina, P. G.; Aldegunde, J.; Althorpe, S. C.; Aoiz, F. J. *Phys. Chem. Chem. Phys.* **2012**, *14*, 13067.

[28] Lin, S. Y.; Guo, H. *J. Phys. Chem. A* **2009**, *113*, 4285.

[29] Lin, S. Y.; Guo, H. *J. Chem. Phys.* **2003**, *119*, 11602.

[30] Sun, Z.; Zhang, C.; Lin, S.; Zheng, Y.; Meng, Q.; Bian, W. *J. Chem. Phys.* **2013**, *139*, 014306.

[31] Yang, H.; Han, K.-L.; Schatz, G. C.; Smith, S. C.; Hankel, M. *Phys. Chem. Chem. Phys.* **2010**, *12*, 12711.

[32] Yang, H.; Han, K.-L.; Schatz, G. C.; Lee, S. H.; Liu, K.; Smith, S. C.; Hankel, M. *Phys. Chem. Chem. Phys.* **2009**, *11*, 11587.

[33] González-Lezana, T.; Roncero, O.; Honvault, P.; Launay, J.-M.; Bulut, N.; Aoiz, F. J.; Bañares, L. *J. Chem. Phys.* **2006**, *125*, 094314.

[34] Aoiz, F. J.; González-Lezana, T.; Sáez Rábanos, V. *J. Chem. Phys.* **2007**, *127*, 174109.

[35] González-Lezana, T.; Honvault, P. *Int. Rev. Phys. Chem.* **2014**, *33*, 371.

[36] González-Lezana, T.; Scribano, Y.; Honvault, P. *J. Phys. Chem. A* **2014**, *118*, 6416.

[37] Panda, A. N.; Sathyamurthy, N. *J. Chem. Phys.* **2005**, *122*, 054304.

[38] de Fazio, D.; de Castro-Vitores, M.; Aguado, A.; Aquilanti, V.; Cavalli, S. *J. Chem. Phys.* **2012**, *137*, 244306.

[39] Lv, S.-J.; Zhang, P.-Y.; Han, K.-L.; He, G.-Z. *J. Chem. Phys.* **2010**, *132*, 014303.

[40] Gamallo, P.; Huarte-Larrañaga, F.; González, M. *J. Phys. Chem. A* **2013**, *117*, 5393.

[41] Gamallo, P.; Martínez, R.; Sierra, J. D.; González, M. *Phys. Chem. Chem. Phys.* **2014**, *16*, 6641.

[42] Hu, M.; Xu, W.; Liu, X.; Tan, R.; Li, H. *J. Chem. Phys.* **2013**, *138*, 174305.

[43] Xu, W.; Li, W.; Lv, S.; Zhai, H.; Duan, Z.; Zhang, P. *J. Phys. Chem. A* **2012**, *116*, 10882.

[44] Bulut, N.; Castillo, J.; Jambrina, P. G.; Kłos, J.; Roncero, O.; Aoiz, F. J.; Bañares, L. *J. Phys. Chem. A* **2015**, *119*, 11951.

[45] Bulut, N.; Castillo, J. F.; Aoiz, F. J.; Bañares, L. *Phys. Chem. Chem. Phys.* **2008**, *10*, 821.

[46] Aslan, E.; Bulut, N.; Castillo, J. F.; nares, L. B.; Roncero, O.; Aoiz, F. J. *J. Phys. Chem. A* **2012**, *116*, 132.

[47] Roy, T.; Mahapatra, S. *J. Chem. Phys.* **2012**, *136*, 174313.

[48] Jorfi, M.; González-Lezana, T.; Zanchet, A.; Honvault, P.; Bussery-Honvault, B. *J. Phys. Chem. A* **2013**, *117*, 1872.

[49] Goswami, S.; Rao, T. R.; Mahapatra, S.; Bussery-Honvault, B.; Honvault, P. *J. Phys. Chem. A* **2014**, *118*, 5915.

[50] Aguado, A.; Paniagua, M.; Lara, M.; Roncero, O. *J. Chem. Phys.* **1997**, *107*, 10085.

[51] Zanchet, A.; Roncero, O.; González-Lezana, T.; Rodríguez-López, A.; Aguado, A.; Sanz-Sanz, C.; Gómez-Carrasco, S. *J. Phys. Chem. A* **2009**, *113*, 14488.

[52] Bhattacharya, S.; Panda, A. N.; Meyer, H.-D. *J. Chem. Phys.* **2010**, *132*, 214304.

[53] Xiao, C.; Xu, X.; Liu, S.; Wang, T.; Dong, W.; Yang, T.; Sun, Z.; Dai, D.; Xu, X.; Zhang, D. H.; Yang, X. *Science* **2011**, *333*, 440.

[54] Bhattacharya, S.; Panda, A. N.; Meyer, H.-D. *J. Chem. Phys.* **2011**, *135*, 194302.

[55] Takayanagi, T.; Schatz, G. C. *J. Chem. Phys.* **1997**, *106*, 3227.

[56] Bethardy, G. A.; Wagner, A. F.; Schatz, G. C.; ter Horst, M. A. *J. Chem. Phys.* **1997**, *106*, 6001.

[57] Zhu, W.; Zhang, J. Z. H.; Zhang, Y. C.; Zhang, Y. B.; Zhan, L. X.; Zhang, S. L.; Zhang, D. H. *J. Chem. Phys.* **1998**, *108*, 3509.

[58] Valero, R.; Kroes, G.-J. *Phys. Rev. A* **2004**, *70*, 040701.

[59] Liu, S.; Xu, X.; Zhang, D. H. *Theor. Chem. Acc.* **2012**, *131*, 1.

[60] Althorpe, S. C.; Clary, D. C. *Annu. Rev. Phys. Chem.* **2003**, pages 493.

[61] Hu, W.; Schatz, G. C. *J. Chem. Phys.* **2006**, *125*, 132301.

[62] Yang, X. *Annu. Rev. Phys. Chem.* **2007**, pages 433.

[63] Clary, D. C. *PNAS* **2008**, *105*, 12649.

[64] Guo, H. *Int. Rev. Phys. Chem.* **2012**, *31*, 1.

[65] Welsch, R.; Manthe, U. *J. Chem. Phys.* **2012**, *137*, 244106.

[66] Troya, D.; Schatz, G. C.; Garton, D. J.; Brunsvold, A. L.; Minton, T. K. *J. Chem. Phys.* **2004**, *120*, 731.

[67] Monge-Palacios, M.; Corchado, J. C.; Espinosa-Garcia, J. *Phys. Chem. Chem. Phys.* **2012**, *14*, 7497.

[68] Smith, I. W. M. *Angew. Chem. Int. Ed.* **2006**, *45*, 2842.

[69] Gioumousis, G.; Stevenson, D. P. *J. Chem. Phys.* **1958**, *29*, 294.

[70] Drake, G. W. F. *Handbook of Atomic, Molecular, and Optical Physics;* Springer, 2006.

[71] Chu, T.-S.; Han, K.-L. *Phys. Chem. Chem. Phys.* **2008**, *10*, 2431.

[72] Chu, T.-S.; Han, K.-L. *Ann. Rep. Prog. Chem., Sect. C: Phys. Chem.* **2012**, *108*, 10.

[73] Chu, T.; Liang, D.; Xu, J.; Dong, S. *Int. J. Quant. Chem.* **2015**, *115*, 803.

[74] Croswell, K. *The Alchemy of the Heavens: Searching for Meaning in the Milky Way;* New York: Anchor Books/Doubleday, 1995.

[75] Zygelman, B.; Stancil, P. C.; Dalgarno, A. *Astrophys. J.* **1998**, *508*, 151.

[76] Ferrière, K. M. *Rev. Mod. Phys.* **2001**, *73*, 1031.

[77] Lepp, S.; Stancil, P. C.; Dalgarno, A. *J. Phys. B: At. Mol. Opt. Phys.* **2002**, *35*, R57.

[78] Dalgarno, A. *Faraday Discuss.* **2006**, *133*, 9.

[79] Yao, Y.; Wang, Q. D. *Astrophys. J.* **2006**, *641*, 930.

[80] Barlow, M. J.; Swinyard, B. M.; Owen, P. J.; Cernicharo, J.; Gomez, H. L.; Ivison, R. J.; Krause, O.; Lim, T. L.; Matsuura, M.; Miller, S.; Olofsson, G.; Polehampton, E. T. *Science* **2013**, *342*, 1343.

[81] Bochsler, P.; Petersen, L.; Möbius, E.; Schwadron, N. A.; Wurz, P.; Scheer, J. A.; Fuselier, S. A.; McComas, D. J.; Bzowski, M.; Frisch, P. C. *Astrophys. J. Suppl. Ser.* **2012**, *198*, 13.

[82] Park, J.; Kucharek, H.; Möbius, E.; Leonard, T.; Bzowski, M.; Sokół, J. M.; Kubiak, M. A.; Fuselier, S. A.; McComas, D. J. *Astrophys. J.* **2014**, *795*, 97.

[83] Asplund, M.; Grevesse, N.; Sauval, A. J.; Scott, P. *Annu. Rev. Astron. Astrophys.* **2009**, *47*, 481.

[84] http://sservi.nasa.gov/articles/nasas-ladee-spacecraft-finds-neon-in-lunar-atmosphere/.

[85] Hogness, T. R.; Lunn, E. G. *Phys. Rev.* **1925**, *26*, 44.

[86] von Koch, H.; Friedman, L. *J. Chem. Phys.* **1963**, *38*, 1115.

[87] Moran, T. F.; Friedman, L. *J. Chem. Phys.* **1963**, *39*, 2491.

[88] Chupka, W. A.; Russel, M. E. *J. Chem. Phys.* **1968**, *49*, 5426.

[89] Aquilanti, V.; Galli, A.; Giardini-Guidoni, A.; Volpi, G. G. *J. Chem. Phys.* **1965**, *43*, 1969.

[90] Bernath, P.; Amano, T. *Phys. Rev. Lett.* **1982**, *48*, 20.

[91] Wong, M.; Bernath, P.; Amano, T. *J. Chem. Phys.* **1982**, *77*, 693.

[92] Brault, J. W.; Davis, S. P. *Phys. Scr.* **1982**, *25*, 268.

[93] Johns, J. W. C. *J. Mol. Spec.* **1984**, *106*, 124.

[94] Banyard, K. E.; Sutton, A. *J. Chem. Phys.* **1967**, *46*, 2143.

[95] Vasudevan, K. *Mol. Phys.* **1975**, *30*, 437.

[96] Bishop, D. M.; Cheung, L. M. *J. Mol. Spec.* **1979**, *75*, 462.

[97] Pyykkö, P.; Diercksen, G. H. F.; Müller-Plathe, F.; Laaksonen, L. *Chem. Phys. Lett.* **1987**, *141*, 535.

[98] Lundell, J. *J. Mol. Struct.* **1995**, *355*, 291.

[99] Rosenkrantz, M. E. *Chem. Phys. Lett.* **1990**, *173*, 378.

[100] Last, I.; George, T. F. *J. Chem. Phys.* **1990**, *93*, 8925.

[101] Schutte, C. J. H. *Chem. Phys. Lett.* **2002**, *353*, 389.

[102] Turner, T.; Dutuit, O.; Lee, Y. T. *J. Chem. Phys.* **1984**, *81*, 3475.

[103] Joseph, T.; Sathyamurthy, N. *J. Chem. Phys.* **1987**, *86*, 704.

[104] McLaughlin, D. R.; Thompson, D. L. *J. Chem. Phys.* **1979**, *70*, 2748.

[105] Joseph, T.; Sathyamurthy, N. *J. Chem. Phys.* **1984**, *80*, 5332.

[106] Mahapatra, S.; Sathyamurthy, N. *J. Chem. Phys.* **1995**, *102*, 6057.

[107] Mahapatra, S.; Sathyamurthy, N. *J. Chem. Phys.* **1997**, *107*, 6621.

[108] Kumar, S.; Kapoor, H.; Sathyamurthy, N. *Chem. Phys. Lett.* **1998**, *289*, 361.

[109] Maiti, B.; Kalyanaraman, C.; Panda, A. N.; Sathyamurthy, N. *J. Chem. Phys.* **2002**, *117*, 9719.

[110] Kolakkandy, S.; Giri, K.; Sathyamurthy, N. *J. Chem. Phys.* **2012**, *136*, 244312.

[111] Palmieri, P.; Puzzarini, C.; Aquilanti, V.; Capecchi, G.; Cavalli, S.; de Fazio, D.; Aguilar, A.; Giménez, X.; Lucas, J. M. *Mol. Phys.* **2000**, *98*, 1835.

[112] Ramachandran, C.; Fazio, D. D.; Cavalli, S.; Tarantelli, F.; Aquilanti, V. *Chem. Phys. Lett.* **2009**, *469*, 26 .

[113] Xu, W.; Liu, X.; Luan, S.; Zhang, Q.; Zhang, P. *Chem. Phys. Lett.* **2008**, *464*, 92 .

[114] Tang, X. N.; Xu, H.; Zhang, T.; Hou, Y.; Chang, C.; Ng, C. Y.; Chiu, Y.; Dressler, R. A.; Levandier, D. J. *J. Chem. Phys.* **2005**, *122*, 164301.

[115] Zhao, J.; Luo, Y. *J. Phys. Chem. A* **2012**, *116*, 2388.

[116] de Fazio, D. *Phys. Chem. Chem. Phys.* **2014**, *16*, 11662.

[117] Gamallo, P.; Akpinar, S.; Defazio, P.; Petrongolo, C. *J. Phys. Chem. A* **2014**, *118*, 6451.

[118] Bilotta, R. M.; Farrar, J. M. *J. Chem. Phys.* **1981**, *75*, 1776.

[119] Pijkeren, D. V.; Boltjes, E.; Eck, J. V.; Niehaus, A. *Chem. Phys.* **1984**, *91*, 293 .

[120] Zhang, T.; Qian, X.-M.; Tang, X. N.; Ng, C. Y.; Chiu, Y.; Levandier, D. J.; Miller, J. S.; Dressler, R. A. *J. Chem. Phys.* **2003**, *119*, 10175.

[121] Dressler, R. A.; Chiu, Y.; Levandier, D. J.; Tang, X. N.; Hou, Y.; Chang, C.; Houchins, C.; Xu, H.; Ng, C.-Y. *J. Chem. Phys.* **2006**, *125*, 132306.

[122] Urban, J.; Jaquet, R.; Staemmler, V. *Int. J. Quant. Chem.* **1990**, *38*, 339.

[123] Urban, J.; Klimo, V.; Staemmler, V.; Jaquet, R. *Z Phys. D: At., Mol. Clusters* **1991**, *21*, 329.

[124] Pendergast, P.; Heck, J. M.; Hayes, E. F.; Jaquet, R. *J. Chem. Phys.* **1993**, *98*, 4543.

[125] Kress, J. D.; Walker, R. B.; Hayes, E. F.; Pendergast, P. *J. Chem. Phys.* **1994**, *100*, 2728.

[126] González, M.; Blasco, R. M.; Giménez, X.; Aguilar, A. *Chem. Phys.* **1996**, *209*, 355.

[127] Huarte-Larrañaga, F.; Giménez, X.; M. Lucas, J.; Aguilar, A.; Launay, J.-M. *Phys. Chem. Chem. Phys.* **1999**, *1*, 1125.

[128] Huarte-Larrañaga, F.; Giménez, X.; Lucas, J. M.; .; Aguilar, A.; Launay, J.-M. *J. Phys. Chem. A* **2000**, *104*, 10227.

[129] Mayneris, J.; Sierra, J. D.; González, M. *J. Chem. Phys.* **2008**, *128*, 194307.

[130] Mayneris-Perxachs, J.; González, M. *J. Phys. Chem. A* **2009**, *113*, 4105.

[131] Xiao, J.; Yang, C.-L.; Tong, X.-F.; Wang, M.-S.; Ma, X.-G. *J. Phys. Chem. A* **2011**, *115*, 1486.

[132] Gamallo, P.; Defazio, P.; González, M. *J. Phys. Chem. A* **2011**, *115*, 11525.

[133] Yao, C.-X.; Zhang, P.-Y. *J. Phys. Chem. A* **2014**, *118*, 5076.

[134] Wu, H.; Yao, C.-X.; He, X.-H.; Zhang, P.-Y. *J. Chem. Phys.* **2016**, *144*, 184301.

[135] Aguillon, F.; Sizun, M. *J. Chem. Phys.* **1997**, *106*, 9551.

[136] Bilotta, R. M.; Preuninger, F. N.; Farrar, J. M. *J. Chem. Phys.* **1980**, *73*, 1637.

[137] Bilotta, R. M.; Farrar, J. M. *J. Chem. Phys.* **1981**, *74*, 1699.

[138] Liao, C. L.; Xu, R.; Flesch, G. D.; Baer, M.; Ng, C. Y. *J. Chem. Phys.* **1990**, *93*, 4818.

[139] Kuntz, P. J.; Roach, A. C. *J. Chem. Soc., Faraday Trans. 2* **1972**, *68*, 259.

[140] Liu, X.; Liu, H.; Zhang, Q. *Chem. Phys. Lett.* **2011**, *507*, 24 .

[141] Adams, N. G.; Bohme, D. K.; Ferguson, E. E. *J. Chem. Phys.* **1970**, *52*, 5101.

[142] Bondybey, V. E.; Pimentel, G. C. *J. Chem. Phys.* **1972**, *56*, 3832.

[143] Hvistendahl, G.; Saastad, O. W.; Uggerud, E. *Int. J. Mass Spectrom. Ion Processes* **1990**, *98*, 167 .

[144] Kunttu, H.; Seetula, J.; Räsänen, M.; Apkarian, V. A. *J. Chem. Phys.* **1992**, *96*, 5630.

[145] Kunttu, H. M.; Seetula, J. A. *Chem. Phys.* **1994**, *189*, 273.

[146] Fridgen, T. D.; Parnis, J. M. *J. Chem. Phys.* **1998**, *109*, 2155.

[147] Tsuge, M.; Kalinowski, J.; Gerber, R. B.; Lee, Y.-P. *J. Phys. Chem. A* **2015**, *119*, 2651.

[148] Dykstra, C. E. *J. Mol. Struct. THEOCHEM* **1983**, *103*, 131.

[149] Lee, J. S.; Secrest, D. *J. Chem. Phys.* **1986**, *85*, 6565.

[150] Kim, S. T.; Lee, J. S. *Bull. Korean Chem. Soc.* **1995**, *16*, 1232.

[151] Kim, S. T.; Lee, J. S. *J. Chem. Phys.* **1999**, *110*, 4413.

[152] Panda, A. N.; Sathyamurthy, N. *J. Phys. Chem. A* **2003**, *107*, 7125.

[153] Liang, J.-J.; Yang, C.-L.; Wang, L.-Z.; Zhang, Q.-G. *J. Chem. Phys.* **2012**, *136*, 094307.

[154] Filippone, F.; Gianturco, F. A. *Europhys. Lett.* **1998**, *44*, 585.

[155] Fridgen, T. D.; Parnis, J. M. *J. Chem. Phys.* **1998**, *109*, 2162.

[156] Lundell, J.; Pettersson, M.; Räsänen, M. *Phys. Chem. Chem. Phys.* **1999**, *1*, 4151.

[157] Qu, J. Y.; Li, W.; Guo, R.; Zhao, X. S. *J. Chem. Phys.* **2002**, *117*, 2592.

[158] Baccarelli, I.; Gianturco, F. A.; Schneider, F. *J. Phys. Chem. A* **1997**, *101*, 6054.

[159] Bhattacharya, S.; Panda, A. N. *J. Phys. B: At. Mol. Opt. Phys.* **2009**, *42*, 085201.

[160] Xu, W.; Zhang, P. *J. Phys. Chem. A* **2013**, *117*, 1406.

[161] Wu, D.; Guo, M.; Wang, Y.; Yin, S.; Sun, Z.; Hoffmann, M. R. *Theor. Chem. Acc.* **2014**, *133*, 1552.

[162] Yao, C. *Theor. Chem. Acc.* **2014**, *133*, 1554.

[163] Matcha, R. L.; Milleur, M. B.; Meier, P. F. *J. Chem. Phys.* **1978**, *68*, 4748.

[164] Li, W.; Qu, J. Y.; Zhao, X. S. *Chin. J. Chem. Phys.* **2002**, *15*, 188.

[165] Matcha, R. L.; Pettitt, B. M.; Meier, P. F.; Pendergast, P. *J. Chem. Phys.* **1978**, *69*, 2264.

[166] Glosík, J.; Twiddy, N. D.; Javahery, G.; Ferguson, E. E. *Int. J. Mass Spectrom. Ion Processes* **1991**, *109*, 75.

[167] Grandinetti, F. *Eur. J. Mass Spectrom.* **2011**, *17*, 423.

Chapter 2

Methodology

This chapter deals with the formalisms used for studying the scattering dynamics of a triatomic (atom+diatom) system. This includes generation of analytical PES from *ab initio* energies, computation of ro-vibrational states and details of reactive scattering methodologies. In the present thesis, the scattering studies are carried out on the ground electronic states of the systems. Hence, all the electronic structure calculations are performed to compute the ground electronic states within the BO approximation. Procedures to generate a global analytical PES from the *ab initio* PES and to perform reactive scattering studies using either quantum mechanical or quasiclassical trajectory calculation methods are discussed in this chapter. The practicalities of applying these methods in computer simulations and predict the outcome of elementary triatomic bimolecular chemical reactions as well as a brief sketch for the calculations of ro-vibrational eigenstates for triatomic systems are also outlined here.

2.1 POTENTIAL ENERGY SURFACE

A potential energy surface describes the potential energies of a system for different configurations. Carrying out dynamical simulations requires potential energies or gradients at numerous configurations of the system. In 'on-the-fly' techniques, the energies or gradients required to study the dynamics are computed directly by using *ab initio* electronic structure calculation programs during the dynamical calculations. However, for most of the polyatomic systems with many electrons, the computational cost of *ab initio* calculations is very high, and in the dynamical calculations, significantly large number of data are needed. Therefore, in practice (for tri and tetra atomic systems), highly accurate *ab initio* energies are calculated at comparatively fewer geometries, which covers the entire phase space including the important interaction regions. Analytical PES is then constructed for the system using the *ab initio* energies either via interpolation scheme or by fitting the *ab initio* data points with suitable functional forms. During the dynamical calculations, energies or gradients are calculated from the analytical PES. However, construction of global PESs is not very straightforward for larger systems (systems with five atoms or more) as the number of degrees of freedom also becomes larger.

2.1.1 Molecular energy calculations

A point on the potential energy surface is determined by calculating the molecular energy of the system at the configuration of interest. The molecular energy levels of a system are calculated by solving the time-independent Schrödinger equation.

$$\hat{H}\Psi(\mathbf{r},\mathbf{R}) = E\Psi(\mathbf{r},\mathbf{R}). \tag{2.1}$$

In Eq. 2.1, $\mathbf{r}$ represents the electronic coordinates and $\mathbf{R}$ represents the nuclear coordinates. $\hat{H}$, the Hamiltonian operator for the system, is a summation of nuclear kinetic energy operator energy ($\hat{T}_N$), electronic kinetic energy operator ($\hat{T}_e$) and electron-nucleus, nucleus-nucleus and electron-electron interaction energy operators ($\hat{V}$). It is a formidable task to solve Eq. 2.1 analytically. At this point, Born-Oppenheimer adiabatic approximation is invoked, which simplifies the theoretical implementations.

2.1.1.1 The Born-Oppenheimer approximation

The Born-Oppenheimer approximation decouples the electronic and nuclear motions. As the ratio of nuclear and electronic masses is very large (of the order of 10^3-10^5), the electrons move much faster than the nuclei, and Eq. 2.1 can readily be approximated as the so called adiabatic approximation. Within this approximation, $\hat{T}_N$ can be considered as an external perturbation and $\Psi(\mathbf{r},\mathbf{R})$ is written as

$$\Psi(\mathbf{r},\mathbf{R}) = \sum_{i=0}^{\infty} \chi_i(\mathbf{R})\psi_i(\mathbf{r};\mathbf{R}) \tag{2.2}$$

with

$$\hat{H}_e\psi_i(\mathbf{r};\mathbf{R}) = E_i\psi_i(\mathbf{r};\mathbf{R}). \tag{2.3}$$

Here, $\hat{H}_e = \hat{T}_e + \hat{V}$ and $\psi_i(\mathbf{r};\mathbf{R})$ is the electronic wave function of i-th electronic state, which is a function of the position of electrons and depends parametrically on the positions of nuclei (assuming that the electrons move around stationary nuclei). Eq. 2.3 is called the time-independent electronic Schrödinger equation. By solving Eq. 2.3 the adiabatic energy (E_i) for the i-th electronic state of a system is obtained. The coefficients $\chi_i(\mathbf{R})$ in Eq. 2.2 are functions of the nuclear coordinates only. Now, Eq. 2.1 can be rewritten as

$$(\hat{T}_N + \hat{H}_e)\sum_{i=0}^{\infty}\chi_i(\mathbf{R})\psi_i(\mathbf{r};\mathbf{R}) = E\sum_{i=0}^{\infty}\chi_i(\mathbf{R})\psi_i(\mathbf{r};\mathbf{R}), \tag{2.4}$$

where E is the total energy of the system. By omitting the notations of the variables,

$$\sum_{i=0}^{\infty}\left[\sum_{\alpha=1}^{N}-\frac{1}{2M_\alpha}\nabla_\alpha^2 + \hat{H}_e\right]\chi_i\psi_i = E\sum_{i=0}^{\infty}\chi_i\psi_i, \tag{2.5}$$

$$\sum_{i=0}^{\infty}\left[\sum_{\alpha=1}^{N}-\frac{1}{2M_\alpha}\nabla_\alpha(\psi_i\nabla_\alpha\chi_i + \chi_i\nabla_\alpha\psi_i) + \chi_i\hat{H}_e\psi_i\right] = E\sum_{i=0}^{\infty}\chi_i\psi_i, \tag{2.6}$$

$$\sum_{i=0}^{\infty}\left[\sum_{\alpha=1}^{N}-\frac{1}{2M_\alpha}(\psi_i\nabla_\alpha^2\chi_i + 2\nabla_\alpha\chi_i\nabla_\alpha\psi_i) + \chi_i\nabla_\alpha^2\psi_i) + \chi_iE_i\psi_i\right] = E\sum_{i=0}^{\infty}\chi_i\psi_i. \tag{2.7}$$

Multiplying both sides by ψ_j^* and integrating over the electronic coordinates, one can get

$$\sum_{\alpha=1}^{N}-\frac{1}{2M_\alpha}\nabla_\alpha^2\chi_j + E_j\chi_j - \sum_{i=0}^{\infty}\sum_{\alpha=1}^{N}\frac{1}{2M_\alpha}(2\langle\psi_j|\nabla_\alpha|\psi_i\rangle\nabla_\alpha\chi_i + \langle\psi_j|\nabla_\alpha^2|\psi_i\rangle\chi_i) = E\chi_j. \tag{2.8}$$

Within the Born-Oppenheimer approximation, the terms inside parentheses in Eq. 2.8 (these are the nonadiabatic couplings between the nuclear WF for j-th electronic state and the nuclear WF for all other electronic states) are neglected and the TI nuclear Schrödinger equation is expressed as

$$[\hat{T}_N + E_j(\mathbf{R})]\chi_j(\mathbf{R}) = \left[\sum_{\alpha=1}^{N}-\frac{1}{2M_\alpha}\nabla_\alpha^2 + E_j(\mathbf{R})\right]\chi_j(\mathbf{R}) = E\chi_j(\mathbf{R}), \tag{2.9}$$

and the TD nuclear Schrödinger equation is expressed as

$$i\hbar\frac{\partial\chi_j(\mathbf{R},t)}{\partial t} = [\hat{T}_N + E_j(\mathbf{R})]\chi_j(\mathbf{R},t). \tag{2.10}$$

Exclusion of the nonadiabatic coupling terms from Eq. 2.8 is certainly an approximation, which is valid when the electronic states are far apart. However, when the electronic states are very close, the terms like $\langle\psi_j|\nabla_\alpha|\psi_i\rangle$ are large and cannot be neglected.

2.1.1.2 Solving the TISE

The TISE is not exactly solvable except for simple systems like harmonic oscillator or hydrogen atom. For all other cases, approximate methods are employed. As per example, applying the variational method one can converge the ground state wave function to the exact one starting from a trial basis function. The electronic TISE for the ground state of a system is expressed as

$$\hat{H}_e\psi_0 = E_0\psi_0. \tag{2.11}$$

Eq. 2.11 can be written as

$$E_0 = \frac{\int \psi_0\hat{H}_e\psi_0 d\tau}{\int \psi_0\psi_0 d\tau}. \tag{2.12}$$

Here, $d\tau$ is the volume element. According to the variational principle, if one starts out with a trial WF ψ_{trial}, which represents a guess of the exact ground state WF, and calculate

$$E_{\text{trial}} = \frac{\int \psi_{\text{trial}}\hat{H}_e\psi_{\text{trial}} d\tau}{\int \psi_{\text{trial}}\psi_{\text{trial}} d\tau}, \tag{2.13}$$

then,

$$E_{\text{trial}} \geq E_0. \tag{2.14}$$

By optimizing the parameters of ψ_{trial} to minimize E_{trial}, the ground state WF (ψ_0) can be obtained.

Methods for solving Eq. 2.3 from the first principles are called *ab initio* methods, e.g., Hartree-Fock, Møller-Plesset perturbation theory, coupled cluster and various multi-reference methods. In an *ab initio* calculation a model is chosen for the electronic WF and the electronic TISE is solved. The spin orbitals or the wave functions, are represented by a complete set of basis functions, e.g., Slater type orbitals (STO), Gaussian type Pople basis sets, Dunning's Correlation-consistent zeta basis sets. Today, there are many commercial/free softwares available to carry out *ab initio* calculations to obtain highly accurate structures and potentials for a system.

2.1.2 Construction of analytical PES

2.1.2.1 Interpolation

In this approach, the energy of any configuration is estimated from a set of known values of *ab initio* energies already computed at known configurations by interpolation. In an interpolation scheme, the interpolated values precisely agree to the known value at data points. For diatomic and triatomic molecules, interpolation can easily be done by cubic spline interpolation. However, for multidimensional systems spline interpolation can not be applied readily. Other methods such as reproducing kernel Hilbert space[1] and modified Shepard interpolation[2,3] are notable among many other interpolation schemes.

2.1.2.2 Fitting

As the name says, in fitting, functional form(s) are fitted to the *ab initio* data points. These functions consist of a set of adjustable parameters which are determined numerically.

The complete adiabatic surface of a triatomic system ABC can be expressed analytically by the many-body expansion form[4]

$$\begin{aligned} V_{\mathrm{ABC}}(R_{\mathrm{AB}}, R_{\mathrm{AC}}, R_{\mathrm{BC}}) = {} & V_{\mathrm{A}}^{(1)} + V_{\mathrm{B}}^{(1)} + V_{\mathrm{C}}^{(1)} + V_{\mathrm{AB}}^{(2)}(R_{\mathrm{AB}}) + V_{\mathrm{AC}}^{(2)}(R_{\mathrm{AC}}) \\ & + V_{\mathrm{BC}}^{(2)}(R_{\mathrm{BC}}) + V_{\mathrm{ABC}}^{(3)}(R_{\mathrm{AB}}, R_{\mathrm{AC}}, R_{\mathrm{BC}}), \end{aligned} \tag{2.15}$$

where R_{ij} are the distances between the atoms i and j, V_{ABC} $(R_{\mathrm{AB}}, R_{\mathrm{AC}}, R_{\mathrm{BC}})$ is the potential energy of the triatom at the corresponding geometry. $V_i^{(1)}$, $V_i^{(2)}(R_i)$ and

$V^{(3)}_{\mathrm{ABC}}(R_{\mathrm{AB}}, R_{\mathrm{AC}}, R_{\mathrm{BC}})$ are the one, two and three-body (3B) interaction energies respectively, at corresponding geometries. All the $V_i^{(1)}$s are taken as zero as the isolated atoms are in their ground states regardless of their charge.

For a diatomic molecule, the simplest expression that can be used is the Morse potential, which is written as

$$V_M(R) = D_e\left[e^{-\alpha(R-R_e)} - 1\right]^2, \tag{2.16}$$

where R_e is the equilibrium bond length and D_e is the dissociation energy. The Aguado-Paniagua[5] type potential for a diatomic molecule AB has the following polynomial form,

$$V_{AP}(R_{\mathrm{AB}}) = \frac{c_0 e^{\alpha_{\mathrm{AB}} R_{\mathrm{AB}}}}{R_{\mathrm{AB}}} + \sum_{i=1}^{M} c_i \rho^i_{\mathrm{AB}}, \tag{2.17}$$

with the restriction $c_0 > 0$ to ensure $V_{AP}(R_{\mathrm{AB}}) \to \infty$ at $R_{\mathrm{AB}} \to 0$ and $\rho_{\mathrm{AB}} = R_{\mathrm{AB}} e^{-\beta^{(2)}_{\mathrm{AB}} R_{\mathrm{AB}}}$. The linear parameters c_i and the nonlinear parameters α_{AB} and $\beta^{(2)}_{\mathrm{AB}}$ are to be determined by fitting.

The two-body interaction energies $V_i^{(2)}$, used in Eq 2.15, can be calculated at different geometries by interpolation or by fitting the functional forms of Eq. 2.16/2.17 to the *ab initio* energies. 3B interaction energies are then calculated by subtracting one and two body interaction energies from the triatomic potential energies. Therefore, the root-mean-square (rms) errors for the diatomic fittings have to be at least one half of that rms error be obtained in the fitting of 3B terms. The 3B interaction energy is expressed by the Aguado and Paniagua function[5] having the following form,

$$V^{(3)}_{\mathrm{ABC}}(R_{\mathrm{AB}}, R_{\mathrm{AC}}, R_{\mathrm{BC}}) = \sum_{i,j,k=0}^{M} d_{ijk} \rho^i_{\mathrm{AB}} \rho^j_{\mathrm{AC}} \rho^k_{\mathrm{BC}}. \tag{2.18}$$

Here, d_{ijk}s are the linear parameters and $\rho_{\mathrm{AB}} = R_{\mathrm{AB}} \exp(-\beta^{(3)}_{\mathrm{AB}} R_{\mathrm{AB}})$. The constraints, $i + j + k \neq i \neq j \neq k$ and $i + j + k \leq M$, are applied as the 3B potential becomes zero at all the dissociation limits and when at least one of the internuclear distances is zero. The Levenberg-Marquardt method, one of the best nonlinear multidimensional fitting method, can be applied to determine the linear and nonlinear parameters of the functional forms for two and three body interaction energies. Details of the numerical methodology for the Levenberg-Marquardt approach is discussed in Ref. 6.

2.2 TIME DEPENDENT QUANTUM DYNAMICS

In reactive scattering study, the dynamical simulation carried out within TDQM methodology is often called as time dependent wave packet dynamics, because in this method an initial wave packet is constructed to describe the range of energy to be investigated and the initial conditions, which is then propagated for a sufficient time on spatial grids to solve the TDSE. Invented in late sixties, TDWP becomes a popular tool for studying reactive scattering in late eighties with the availability of improved algorithm and advanced computational techniques. Nowadays TDWP is a realistic approach to study atom-diatom, diatom-diatom, atom-triatom bimolecular reactions. Numerous direct and complex forming bimolecular reactions, for example H+H_2,[7] F+H_2,[8] Br+H_2,[9] C+H_2,[10,11] H+O_2,[12] C+OH,[13] S+OH,[14] H+H_2^+,[15] O^++H_2,[16] He+H_2^+,[17,18] Ne+H_2^+,[19–21] Ar+H_2^+,[22] H+HeH^+,[23] He+HeH^+,[24,25] have been investigated successfully via TDQM method. Since the reactive scattering studies discussed in this thesis are taken place on a single adiabatic PES, corresponding dynamical calculations were restricted in solving nuclear TDSE (Eq. 2.10) within the Born-Oppenheimer approximation. In this thesis work, a parallel (MPI+OPENMP) code is written in order to solve the TDSE for studying the reactive scattering of A+BC type reaction and computing initial state selected total reaction probabilities. The procedure is discussed below in detail.

2.2.1 The Hamiltonian operator

The Hamiltonian operator ($\hat{H}$) of a system is the sum of all forms of the kinetic energy operators and the potential energy operators. For A + BC system, $\hat{H}$ is written in BF Jacobi coordinates as[26]

$$\hat{H} = -\frac{\hbar^2}{2\mu_R}\frac{\partial^2}{\partial R^2} - \frac{\hbar^2}{2\mu_r}\frac{\partial^2}{\partial r^2} + \frac{\mathbf{l}^2}{2\mu_R R^2} + \frac{\mathbf{j}^2}{2\mu_r r^2} + \mathbf{V}(R, r, \theta), \tag{2.19}$$

where r is the BC bond length, R is the distance between the center of mass of BC diatom and A atom, θ is the angle between $\mathbf{R}$ and $\mathbf{r}$. μ_R is the reduced mass of the triatom and μ_r is the reduced mass of BC. Here, $\mathbf{l}$ is the orbital angular momentum operator expressed as $(\mathbf{J} - \mathbf{j})$, where $\mathbf{J}$ and $\mathbf{j}$ are the total angular momentum and rotational angular momentum operators, respectively. $\mathbf{V}(R, r, \theta)$ is the interaction potential of the system. The BF z-axis is parallel to $\mathbf{R}$ and the BC diatom is in the xz plane.

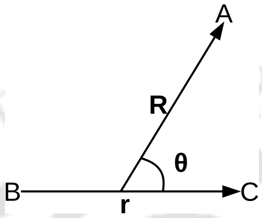

FIGURE 2.1: Schematic representation of reactant Jacobi coordinates for A+BC.

In BF representation $(\hat{J} - \hat{j})^2$ can be expressed as

$$(\hat{J} - \hat{j})^2 = (\hat{J}^2 + \hat{j}^2 - 2\hat{J}_z\hat{j}_z) - (\hat{J}_+\hat{j}_- + \hat{j}_-\hat{J}_+). \tag{2.20}$$

Here, $\hat{J}_z$ is the projection of J on the BF z-axis and $\hat{J}_\pm = \hat{J}_x \pm i\hat{J}_y$ are raising and lowering operators. Similarly, $\hat{j}_z$ and $\hat{j}_\pm$ are the projection of j along BF z-axis and the raising and the lowering operators, respectively. The choice of BF frame makes the projection of J along z-azis the same as that of j. The application of these rotational operators on the eigenfunction $|J, K, M\rangle$ is carried out as follows:

$$\hat{J}^2|J, K, M\rangle = \hbar^2 J(J+1)|J, K, M\rangle, \tag{2.21}$$

$$\hat{J}_z|J, K, M\rangle = \hbar K|J, K, M\rangle, \tag{2.22}$$

$$\hat{J}_\pm|J, K, M\rangle = \hbar\lambda^\pm_{JK}|J, K \pm 1, M\rangle. \tag{2.23}$$

Here, K is the projection of J on BF z-axis, M is is the projection of J on SF z-axis and $\lambda^\pm_{JK} = \sqrt{J(J+1) - K(K \pm 1)}$.

In order to solve the TDSE, the time-dependent wave function is expanded in terms of translational, vibrational and BF total angular momentum basis and is written in a mixed grid representation. A direct product DVR for radial coordinates and a FBR for the angular coordinates are used. For the radial degrees of freedom, evenly spaced grids are defined, whereas Gauss-Legendre quadrature points described the angular degrees of freedom. In this discrete grid representation, the resulting Hamiltonian takes the shape of a tridiagonal matrix in the BF frame and is expressed as[26,27]

$$\begin{aligned}\hat{H} &= \Big[-\frac{\hbar^2}{2\mu_R}\frac{\partial^2}{\partial R^2} - \frac{\hbar^2}{2\mu_r}\frac{\partial^2}{\partial r^2} + \frac{j(j+1)}{2\mu_r r^2} + \frac{J(J+1)+j(j+1)-2K^2}{2\mu_R R^2} + V(R,r,\theta)\Big]\delta_{KK'} \\ &- \frac{\hbar^2}{2\mu_R R^2}\lambda^{+}_{JK}\lambda^{+}_{jK}\sqrt{1+\delta_{K0}}\,\delta_{K+1,K'} - \frac{\hbar^2}{2\mu_R R^2}\lambda^{-}_{JK}\lambda^{-}_{jK}\sqrt{1+\delta_{K1}}\,\delta_{K-1,K'}. \qquad (2.24)\end{aligned}$$

The coupling between different K states (Coriolis coupling) make the centrifugal potential tridiagonal, whereas the interaction potential is diagonal in BF frame. In CC calculations, the full Hamiltonian in Eq. 2.24 is used. Although for most of the cases the maximum value of K ($K_{\max}$) converges to a comparatively smaller number (truncated CC calculation), the computational cost (computation time, memory and storage required) is very high for truncated CC calculation. Exclusion of the off-diagonal terms in the Eq. 2.24 results in the CS approximation,[28,29] where K becomes a good quantum number and is taken as a constant. This approximation freezes the rotation of triatomic molecular plane and the whole dynamics is carried out in a fixed plane. Thus CS approximation significantly reduces the computational cost by reducing the dimensionality and often used as an efficient tool to study direct reactions. However, for complex-forming or resonance mediated reactions, CS approximation evokes significant errors in the reaction probabilities for larger values of J.

2.2.2 Chebyshev real wave packet propagation

For a time-independent Hamiltonian, the solution of TDSE can be written as

$$\psi(q, t+\Delta t) = e^{-i\hat{H}\Delta t/\hbar}\psi(q,t) \qquad (2.25)$$

An exponential function can be expanded as $e^{ikx} = \cos(kx) + i\,\sin(kx)$. Now, Eq. 2.25 is time reversible, and thus one can write[30]

$$\psi(q, t+\Delta t) = -\psi(q, t-\Delta t) + 2\text{cos}\left(\frac{\hat{H}\Delta t}{\hbar}\right)\psi(q, t). \tag{2.26}$$

Since, i ($\sqrt{1}$) is not involved in Eq. 2.26 the real and imaginary part of $\psi(q, t)$ can be propagated separately and independently.

Chebyshev polynomials are orthogonal polynomials defined as

$$T_k(\omega) = \cos(k\,\cos^{-1}\omega), \qquad \omega \in [-1, , 1] \tag{2.27}$$

where ω is a scalar quantity. These polynomials are evaluated with high accuracy by following the recurrence relation

$$T_k(\omega) = 2\omega T_{k-1}(\omega) - T_{k-2}(\omega), \tag{2.28}$$

with $T_0(\omega) = 1$ and $T_1(\omega) = \omega$.

In operator form, the Chebyshev polynomials for any operator ($\hat{H}$) defined in [-1,1] written as

$$T_k(\hat{H}) = \cos(k\,\cos^{-1}\hat{H}) = \cos(k\hat{\Theta}), \tag{2.29}$$

where $\hat{\Theta} = \cos^{-1}\hat{H}$ is the Chebyshev angle operator. The Chebyshev operator $T_k(\hat{H})$ is simply a cosine propagator and can be imagined as the real part of the exponential time evolution operator.[30–33] In this particular case, the Hamiltonian is normalized to [-1,1] by introducing a scaled Hamiltonian ($\hat{H}_s$) which is represented as[31,32]

$$\hat{H}_s = (\hat{H} - H^+)/H^-, \tag{2.30}$$

where $H^+ = (H_{\text{max}} + H_{\text{min}})/2$ and $H^- = (H_{\text{max}} - H_{\text{min}})/2$. $H_{\text{max}} = T_{\text{max}} + V_{\text{max}}$ and $H_{\text{min}} = V_{\text{min}}$ are the upper and the lower bounds of the eigenvalues of the Hamiltonian, respectively. With this choice and including absorption(D) at grid edges, Eq. 2.28 can be written as a modified Chebyshev recursion relation[34]

$$\Phi_{k+1} = D(2\hat{H}_s\Phi_k - D\Phi_{k-1}), \tag{2.31}$$

where $\Phi_0 = \psi(R, r, \theta, t = 0)$, the initial real WP and $\Phi_1 = D\hat{H}_s\Phi_0$. The CRWP method can easily be parallelized by using MPI algorithm.

2.2.3 Action of Hamiltonian operator on the wave function

In order to compute the action of operators on the wave function, both grid as well as basis set representations are chosen. The action of potential operator ($\hat{V}$) in grid based method is just a multiplication ($\hat{V}\psi$) at every grid point. However, the radial kinetic energy operators involve second derivatives and Fourier transformation technique is applied to evaluate these operations. After FT to the momentum space, the application of kinetic energy operator becomes simply a multiplication. The resultant wave function is then transformed back to the position space by a reverse FT. The method is illustrated below for a one dimensional wave packet $\psi(x)$

$$\psi(k) = \frac{1}{\sqrt{2\pi}}\int_{-\infty}^{\infty}\psi(x)e^{-ikx}dx, \tag{2.32}$$

$$\psi(x) = \frac{1}{\sqrt{2\pi}}\int_{-\infty}^{\infty}\psi(k)e^{ikx}dk, \tag{2.33}$$

$$\frac{\partial\psi(x)}{\partial x} = \frac{1}{\sqrt{2\pi}}i\int_{-\infty}^{\infty}k\psi(k)e^{ikx}dk, \tag{2.34}$$

$$\frac{\partial^2\psi(x)}{\partial x^2} = \frac{1}{\sqrt{2\pi}}\int_{-\infty}^{\infty}-k^2\psi(k)e^{ikx}dk, \tag{2.35}$$

where, $\psi(x)$ and $\psi(k)$ are the wave function represented in space and momentum coordinates respectively and k is the wavenumber. Efficient discrete FT subroutines (often called as FFT) are available in AMD Core Math Library (ACML) package[35] and used in the code. In CRWP method, the action of radial kinetic energy operator on ψ is computed by following FT in R (or r) coordinate as

$$-\frac{\hbar^2}{2\mu_R}\frac{\partial^2}{\partial R^2}\psi = -\frac{\hbar^2}{2\mu_R}\mathrm{FFT}^{-1}[-k_R^2(\mathrm{FFT}\ \psi)], \tag{2.36}$$

where, FFT^{-1} represents reverse FT.

Although FT method can compute the exact derivatives for periodic functions, it can be applied for the nonperiodic wave functions having zero values at the grid edges. While at small R or r values the potential energies remain large enough to fulfill this condition, absorbing potential or damping function is used at grid edges where the potential is not large. Use of absorbing potential or damping function makes the procedure free from unnecessary reflection of the wave function at the grid edges.

To perform the numerical integration of TDSE in θ coordinate, quadrature DVR method developed by Light and coworkers[36] is followed. The wave function $\psi(x)$ can be expanded in terms of a complete set of orthonormal basis set $(\phi_j(x))$, yielding the finite basis representation

$$\psi(x) = \sum_{j=1}^{N} a_j \phi_j(x), \tag{2.37}$$

with

$$a_j = \int \phi_j^*(x)\psi(x)dx. \tag{2.38}$$

The N-point Gaussian quadrature formula to evaluate this integral is written as

$$a_j = \sum_{n=1}^{N} \omega_n \phi_j(x_n)\psi(x_n), \tag{2.39}$$

where x_n are DVR points and ω_n are weights. DVR points are obtained by diagonalizing the coordinate operator in FBR basis.

In this work, a Legendre DVR is used as the associated Legendre polynomials $(P_l^m(\cos\theta))$, which are the eigenfunctions of the angular momentum operator

$$\hat{l}^2 = -\frac{1}{\sin\theta}\frac{\partial}{\partial\theta}\sin\theta\frac{\partial}{\partial\theta} + \frac{m^2}{\sin^2\theta}. \tag{2.40}$$

The orthonormal basis functions are thus

$$\widetilde{P}_l^m(\cos\theta) = (-1)^m \sqrt{\frac{2l+1}{2}\frac{(l-m)!}{(l+m)!}}\, P_l^m(\cos\theta), \tag{2.41}$$

with $m \geq 0$ and $m \leq l \leq m+N-1$. The recursion relation of the associated Legendre polynomials is

$$c_{l+1}\widetilde{P}^{m}_{l+1}(x) - x\widetilde{P}^{m}_{l}(x) + c_l\widetilde{P}^{m}_{l-1}(x) = 0, \tag{2.42}$$

where $x = \cos\theta$ and

$$c_l = \sqrt{\frac{l^2 - m^2}{4l^2 - 1}}. \tag{2.43}$$

The DVR grid points in terms of $\cos\theta$ are obtained by diagonalizing the matrix form of $\hat{x}$

$$\mathbf{U}_{ij} = \langle \widetilde{P}^{m}_{i} | \hat{x} | \widetilde{P}^{m}_{j} \rangle. \tag{2.44}$$

The DVR weights (ω_n) are then calculated as

$$\omega_n^{1/2} = \sqrt{\frac{2^{m+1} m!}{(2m+1)!!}} \sin^{-m}(\theta_n) \mathbf{U}_{1n}. \tag{2.45}$$

To evaluate the action of the rotational kinetic energy operators on the wave function, a transformation matrix $\mathbf{F}_{n,j} = \sqrt{w_n}\widetilde{P}^{m}_{j}(\cos\theta_n)$ is introduced. The wave function on the DVR grid is first transformed to the FBR by multiplying with $\mathbf{F}_{nj}$ and then the angular momentum operator in Eq. 2.24 is operated on this transformed wave function in local representation and the final expression is obtained by transforming back to the DVR basis.

As R approaches to zero, matrix elements of the local angular momentum operators become very large and the CC calculations become unmanageable. To get rid of this problem, the recipe proposed by Zanchet *et al.*[37] is followed. In this formulation, a particular value of R, R_{cut}, is chosen for a particular J. At $R = R_{\text{cut}}$, the average value of the matrix elements of $\mathbf{l}^2$ operator in Eq. 2.24 is equal to a given E_{cut} (E_{cut} is a sufficiently high constant energy value[11,38]). In the CC calculations, $R < R_{\text{cut}}$ are replaced by R_{cut}.

2.2.4 Damping function

As mentioned earlier, use of damping function or absorbing potential at the grid ends is necessary to avoid unphysical reflections of the WP, which arise due to FT on a finite grid. In the CRWP approach, the damping function D is included in the recursion formula and it is a real function. A Gaussian type function of the following form can be used in Chebyshev propagation.[30]

$$D(x) = \begin{cases} 1, & \text{for } x \leq x_d \\ e^{-A_x(x-x_d)^2}, & \text{for } x > x_d \end{cases} \tag{2.46}$$

Here, x_d is the starting point of the damping function and A_x is the strength of the damping function.

For reactions with potential well(s) in the reaction path, damping functions of the following forms are generally used to increase the efficiency.[39] Along a grid x, it is expressed as

$$D(x) = \exp\left[-\Delta_c A_x \left(\frac{x - x_d}{x_{\max} - x_d}\right)^2\right], \quad \text{for } x_d \leq x \leq x_{\max}. \tag{2.47}$$

Here, Δ_c is defined as

$$\Delta_c = \frac{a_s \hbar}{\sqrt{1 - \bar{E}_s^2}}, \tag{2.48}$$

where $a_s = 1/H^-$ and $\bar{E}_s$ is the scaled central energy of the initial wave packet. For the reactions with complicated kinetic energy structures, $D(r)$ along r grid is sometimes divided into two parts:[39]

$$D(r) = \begin{cases} \exp\left[-\Delta_c A_{r1}\left(\frac{r - r_{d1}}{r_{d2} - r_{d1}}\right)^2\right], & \text{for } r_{d1} \leq r \leq r_{d2} \\ \exp\left[-\Delta_c A_{r2}\left(\frac{r - r_{d2}}{r_{\max} - r_{d2}}\right)^2 - \Delta_c A_{r1}\right], & \text{for } r_{d2} \leq r \leq r_{\max} \end{cases} \tag{2.49}$$

Here, A_{r1} and A_{r2} describe the strength of the absorbing potential. r_{d1} and r_{d2} are the starting points of the first and second part of the absorbing potential, respectively.

2.2.5 Preparation of the initial wave packet

In the CS calculations, the initial WP is prepared for a particular vibrational (v), rotational (j), total angular momentum (J) state in BF representation, and is written as follows,

$$\Psi_{jJ}(R, r, \theta, t = 0) \;=\; G_{k_0}(R)\ \phi_{vj}(r)\ \widetilde{P}_{jK}(\cos\theta). \tag{2.50}$$

In CRWP approach, $G_{k_0}(R)$ is a real Gaussian WP representing the relative translational motion of the system and is expressed as[10,38]

$$G_{k_0}(R) = N\ e^{\frac{-(R-R_0)^2}{2\delta^2}}\ \cos(k_0 R), \tag{2.51}$$

where R_0 is the location of the center of the WP, δ is the width parameter, k_0 is the momentum wave vector and N is the normalization constant of the WP. $\widetilde{P}_{jK}(\cos\theta)$ are the normalized associated Legendre polynomials

$$\widetilde{P}_{jK}(\cos\theta) = \sqrt{\frac{(2j+1)}{2}\frac{(j-K)!}{(j+K)!}}P_{jK}(\cos\theta). \tag{2.52}$$

$\phi_{vj}(r)$ in Eq. 2.50 are the ro-vibrational eigenfunctions of BC diatom and are computed by following the Colbert-Miller[40] DVR approach. In this method the kinetic energy of a diatom is written in matrix form as

$$T_{mn} = \begin{cases} \frac{\hbar^2}{2\mu_r \Delta r^2}(-1)^{m-n}\left(\frac{\pi^2}{3} - \frac{1}{2m^2}\right), & \text{if } m = n \\ \frac{\hbar^2}{2\mu_r \Delta r^2}(-1)^{m-n}\left(\frac{2}{(m-n)^2} - \frac{2}{(m+n)^2}\right), & \text{if } m \neq n \end{cases} \tag{2.53}$$

where Δr is the grid spacing. The eigenstates of the diatoms are obtained by diagonalizing the diatomic Hamiltonian

$$H_{mn} = \begin{cases} T_{mn}, & \text{if } m \neq n \\ T_{mn} + V(r) + j(j+1)/2\mu_r r^2, & \text{if } m = n \end{cases} \tag{2.54}$$

where $V(r)$ is the diatomic interaction potential.

In case of CC calculation, preparation of initial WP is different than in case of CS. Here, the initial WP is prepared in the SF representation for a particular v, j and l state, and is written as

$$\Psi^{JMp}_{vjl}(R,r,\theta,t=0) \;=\; G_{k_0}(R)\;\phi_{vj}(r)\;|JMjlp\rangle \tag{2.55}$$

where $|JMjlp\rangle$ is the parity-adapted total angular momentum eigenfunction with p being the parity of the system. The initial orbital angular momentum quantum number l lies between $|J-j|$ to $J+j$, for a given J and j. But the propagation is carried out in BF representation and for this, the initial l-dependent WP is transformed into the corresponding K-dependent wave function in BF representation as[12,26,41]

$$|JMjlp\rangle = \sum_{K\geq 0} C^{jJp}_{lK}\;|JMjK\rangle. \tag{2.56}$$

Here C^{jJp}_{lK} is the transformation matrix between the two representations given by

$$C^{jJp}_{lK} = \sqrt{\frac{(2l+1)}{2J+1}}\;\sqrt{(2-\delta_{K,0})}\;\langle jKl0|JK\rangle, \tag{2.57}$$

where $\langle jKl0|JK\rangle$ is the Clebsch-Gordan coefficient.

2.2.6 Total reaction probability

The energy-dependent total reaction probability ($P^r(E)$) is evaluated by summing the total flux of the energy dependent WP going through a fixed analysis surface located at sufficiently large distance (r_s) in the product channel.[10,12,42] In CRWP method,

$$\begin{aligned} P^r(E) =& \frac{1}{2\pi\mu_r|a_i(E)|^2(H^-)^2\;sin^2\;\Theta} \times \mathrm{Im}\Big\langle \sum_k (2-\delta_{k0})\;\mathrm{Exp}(-ik\Theta)\;\Phi_k \\ & \Big|\sum_{k'}(2-\delta_{k'0})\;\mathrm{Exp}(-ik'\Theta)\times\Big[\delta(r-r_s)\frac{\delta}{\delta r}\Phi_{k'}\Big]\Big\rangle. \end{aligned} \tag{2.58}$$

Here, $\Theta = \cos^{-1}((E - H^{+})/H^{-})$ and $a_i(E)$ are the energy weights of the initial translational WP and is expressed as[11,38,43]

$$a_i(E) = \left\langle i\sqrt{\frac{\mu_R k_i}{2\pi}} R h_l^{(2)}(k_i R) | G_{k_0}(R) \right\rangle, \tag{2.59}$$

where $h_l^{(2)}$ are the spherical Hankel functions of the 2nd kind and $k_i = \sqrt{2\mu_R E_c}/\hbar$. Use of Hankel functions paves the way to place initial WP at small R where the interaction potential $V \to 0$. In the CS calculations for $j > 0$, l was approximated as the nearest integer root of l for the relation $l(l+1) = J(J+1) + j(j+1) - 2K^2$.[44] For the CC calculations, the J-dependent total reaction probabilities were calculated by averaging over all possible l-dependent total reaction probabilities.[11]

2.2.7 Probabilities via interpolation

CC calculations are computationally expensive and for some reactive systems a large number of Js are needed to compute the total integral cross sections (ICSs) in an energy range. For those cases, exact CC probabilities are calculated for some selected Js (in between $J = 0$ to $J_{\max}$) and a J-shifting technique is employed to compute the reaction probabilities for all the remaining Js. In this approach, probabilities for a particular J at a collision energy E_c is obtained from a linear interpolation of two known probabilities. The interpolation is carried out using the following formula:[45]

$$\begin{aligned} P_{vj}^{J}(E_c) &= P_{vj}^{J_1}(E_c)(E_c - (V_J^* - V_{J_1}^*))\frac{(J_2 - J)}{J_2 - J_1} \\ &\quad + P_{vj}^{J_2}(E_c)(E_c + (V_{J_2}^* - V_J^*))\frac{(J - J_1)}{J_2 - J_1}, \end{aligned} \tag{2.60}$$

where P^{J_i} are the probabilities for J_i and $J_1 < J < J_2$. Here, V_J^* is the threshold energy for the corresponding J, which is determined as[46] $V_J^* = AJ + BJ^2 + CJ^3$. Here the coefficients A, B and C are calculated by fitting the threshold energies of the probabilities for known J values.

2.2.8 Integral cross section and rate constant

The initial state selected total ICSs are calculated from the reaction probabilities as

$$\sigma_{v,j}(E_{\rm c}) = \frac{\pi}{\mathbf{k}_{v,j}^2} \sum_{J=0}^{J_{max}} \frac{(2J+1)}{(2j+1)} [2\ \min(J,j)+1] P_{v,j}^J(E_{\rm c}), \tag{2.61}$$

where $\mathbf{k}_{vj}$ is the magnitude of the wave vector corresponding to the initial state at a fixed E_c.

The initial state-specific thermal rate constants as a function of temperature ($k_{vj}(T)$) are calculated from the initial state selected total ICSs as

$$k_{vj}(T) = \sqrt{\frac{8k_BT}{\pi\mu_R}} \frac{1}{(k_BT)^2} \int_0^\infty E_{\rm c}\ \exp(-E_{\rm c}/k_BT)\ \sigma_{vj}(E_{\rm c})\ dE_{\rm c}, \tag{2.62}$$

where k_B is the Boltzmann constant.

2.3 TIME INDEPENDENT QUANTUM DYNAMICS

Reactive scattering can also be studied via TIQM approach. In this approach, the stationary Schrödinger equation is solved by propagating the scattering wave function. The S-matrix is then calculated at a particular energy by comparing them to the asymptotic wave functions. In contrast to TDQM approach, where initial state specific probabilities can be calculated for a set of energies in a single run, in the TIQM approach, all the state-to-state reaction probabilities can be computed in a single run, but for a particular energy. TI method is more advantageous in calculating the reaction attributes at low collision energies than TD method as the WP moves slowly at low collision energies and takes a long propagation time. However, the TIQM methodology involves a large number of coupled equations and manipulation of large matrices, which requires large storage capacity. Thus, TI method is difficult to scale for larger systems, whereas TD method can easily and efficiently be scaled for larger systems.

In this thesis work, ABC program[47] was used for studying the reactive scattering of A+BC type reactions via TIQM approach. This approach has been successfully employed for studying many direct as well as indirect reactive scattering including atom-molecular ion systems.[48–54] ABC solves the TI Schrödinger equation of motion within BO approximation for triatomic systems using coupled-channel approach in hyperspherical coordinates. The time-independent scattering wave functions consist of the basis functions of the ro-vibrational states of all arrangement channels. The coupled-channel hyperradial equations are solved by using a constant reference potential log derivative method between $\rho_{\max}$ to $\rho_{\min}$ in n_{sec} evenly spaced sectors. The S-matrix for all the channels is then computed from the final log derivative matrix by comparing to the asymptotic forms. In each run, S-matrix is computed for a particular J, diatomic parity (p) and triatomic parity (P). The parity-adapted scattering matrix elements obtained from these calculations are transformed to helicity representation, $S^J_{vjK;v'j'K'}$. A detail discussion on the TIQM methodology to study A+BC type reactive scattering can be found in Ref. 47 and references therein. State-to-state DCSs and ICSs are calculated as[55–57]

$$\frac{d\sigma_{vjK;v'j'K'}}{d\Omega}(\theta, E_c) = \frac{1}{(2j+1)}\left|\frac{1}{2ik_{vj}}\sum_J (2J+1) d^J_{KK'}(\pi-\theta) S^J_{vjK;v'j'K'}\right|^2 \tag{2.63}$$

where $d^J_{KK'}(\theta)$ are reduced Wigner rotational matrices and

$$\sigma_{vjK;v'j'K'}(E_c) = \frac{\pi}{(2j+1)k^2_{vj}} \sum_J (2J+1) \left|S^J_{vjK;v'j'K'}\right|^2. \tag{2.64}$$

In order to converge the reaction probabilities obtained via ABC calculations, three key convergence parameters $e_{\max}$, $j_{\max}$ and $K_{\max}$, which define the coupled-channel basis set for the calculations are determined first. The number of log derivative propagation sectors (n_{sec}) are then converged. Parameters $e_{\max}$, $j_{\max}$ and n_{sec} play the same role for all Js.

2.4 QUASICLASSICAL TRAJECTORY CALCULATION

A chemical reaction being the movement and collision of atoms and molecules can readily be studied via classical mechanics. Although some special quantum features like resonance, interference and tunneling cannot be described classically, aspects like quantization can be taken into account in part by simple techniques. In a quasiclassical trajectory calculation, initial conditions for a collision replicate quantized states, which is achieved via energy comparison to the quantum states. Hence, the trajectory calculation is called quasiclassical. Generally, averaged quantities like integral reaction cross sections are devoid of quantum structures and in these cases, a quasiclassical treatment becomes appropriate to provide a quick idea about the reactive attributes. Also when a full dimensional quantum calculation is very expensive and an approximation greatly reduces the accuracy, a quasiclassical approach may yield more reliable result for the highly averaged quantities. In addition, in a classical study it is relatively easy to understand most of the features of a collision dynamics and a mechanistic insight can be obtained by looking at the trajectories or movies of movement of atoms involved. The QCT methodology, which is described below, involves solving the set of Hamilton's differential equations of motion by numerical integration and it is well documented in literature.[58–60] Fortran codes are written in this thesis work to calculate quasiclassical trajectories for A+BC type reactive collisions and to analyze those trajectories. The methodologies are discussed below in detail.

2.4.1 The Hamiltonian

For a reaction A + BC → AB(C) + C(B), the Hamiltonian in reactant Jacobi coordinates can be written as

$$H = \frac{1}{2\mu_{BC}}\sum_{i=1}^{3} p_i^2 + \frac{1}{2\mu_{A,BC}}\sum_{i=1}^{3} P_i^2 + \frac{1}{2M}\sum_{i=1}^{3} P_{S_i}^2 + V(q_1, q_2, q_3, Q_1, Q_2, Q_3), \qquad (2.65)$$

where $\mu_{BC} = m_B m_C/(m_B + m_C)$, $\mu_{A,BC} = m_A(m_B + m_C)/M$ and $M = m_A + m_B + m_C$. m_A, m_B and m_C are the masses of A, B and C respectively. q_i and p_i $(i = 1, 2, 3)$ are the Cartesian coordinates of the BC distance and momentum vector, respectively. Q_i and P_i $(i = 1, 2, 3)$ represent the Cartesian coordinates of the distance vector from the center of mass of BC to A and corresponding momentum vector, respectively. S_i and P_{S_i} $(i = 1, 2, 3)$ represent the Cartesian coordinates of position and momentum, respectively, of the center of mass of ABC system. Here, V is the interaction potential of the system. In absence of any external field, V depends only on the relative coordinates, q_i and Q_i.

2.4.2 Hamilton's equations of motion

The set of Hamilton's differential equations of motion in reactant Jacobi coordinate is

$$\frac{\partial q_i}{\partial t} = \frac{p_i}{\mu_{BC}} \quad (i = 1, 2, 3) \tag{2.66}$$

$$\frac{\partial Q_i}{\partial t} = \frac{P_i}{\mu_{A,BC}} \quad (i = 1, 2, 3) \tag{2.67}$$

$$\frac{\partial S_i}{\partial t} = \frac{P_{S_i}}{M} \quad (i = 1, 2, 3) \tag{2.68}$$

$$\frac{\partial p_i}{\partial t} = -\frac{\partial V}{\partial q_i} \quad (i = 1, 2, 3) \tag{2.69}$$

$$\frac{\partial P_i}{\partial t} = -\frac{\partial V}{\partial Q_i} \quad (i = 1, 2, 3) \tag{2.70}$$

$$\frac{\partial P_{S_i}}{\partial t} = 0 \quad (i = 1, 2, 3) \tag{2.71}$$

Eqs. 2.68 and 2.71 correspond to the free motion of center of mass, i.e., $S_i(t) = S_i(t_0) + (P_{S_i}(t_0)/M)t$ and $P_{S_i}(t) = P_{S_i}(t_0)$.

2.4.3 Initial conditions

In absence of any external field, any initial condition for the center of mass motion can be chosen. Here, $P_{S_i}(t_0) = P^0_{S_i} = S_i(t_0) = S^0_i = 0$ are taken. From the equations of motion for the center of mass it can be written that at any time t, $P_{S_i}(t) = S_i(t) = 0$.

In order to simulate an average reactive attribute, a wide distribution of initial conditions must be taken into account, resulting in a large number of trajectory run. To start a trajectory calculation, initial conditions such as q^0_i, p^0_i, Q^0_i and P^0_i must be specified. Thus, an efficient choice of initial condition is essential.

In Figure 2.2 a schematic diagram of a bimolecular collision system is presented for simulating experimental situation. The origin of the coordinate system is at the center of mass of BC. The distance vector from the center of mass of BC to A atom is located on yz plane and the relative velocity vector (ν) of A relative to BC is parallel to positive z-axis. Let us assume that BC diatom is in a well defined vibrational (v) and rotational (j) state. The orientation of BC diatom is given by spherical angles θ and ϕ. η represents the angle of rotation of internal angular momentum vector ($\mathbf{J}_\mathrm{r}$) of BC diatom. Here, ρ is the distance from the center of mass of BC to A, and b is the impact parameter. For $j = 0$, b is related to the total angular momentum as $b = \frac{\sqrt{J(J+1)\hbar^2}}{\mu_{A,BC}\ \nu}$.

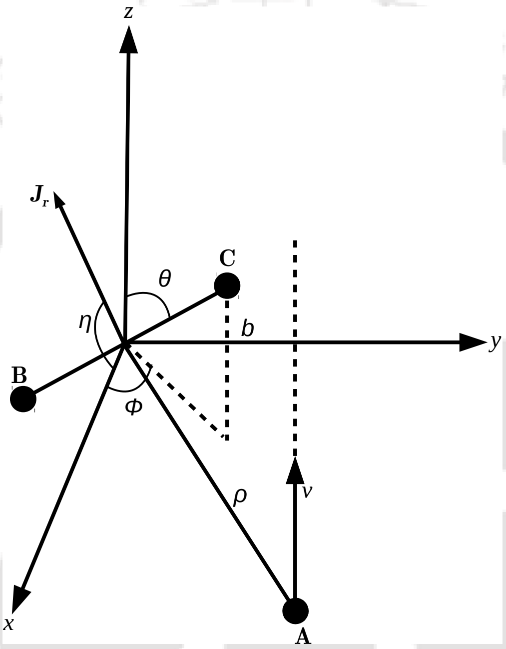

FIGURE 2.2: Initial arrangement of A+BC collision system in Cartesian coordinates.

The initial values of positions and momenta for the relative motion between A and BC are now written as

- $Q_1^0 = 0$,
- $Q_2^0 =$ b,
- $Q_3^0 = -\sqrt{\rho^2 - b^2}$,
- $P_1^0 = 0$,
- $P_2^0 = 0$,
- $P_3^0 = \mu_{A,BC}\ \nu = \sqrt{2\mu_{A,BC}E_c}$.

At the beginning of the trajectory run, A and BC are kept well separated to minimize the interaction between A and BC.

The ro-vibrational energies of the reactant diatom are obtained from quantum mechanical calculations by employing the Colbert-Miller DVR method.[40] The turning points of the diatom for a particular ro-vibrational state are calculated by equating the sum of potential ($V_{\mathrm{BC}}(q_\pm)$) and rotational energy ($\frac{\hbar^2 j(j+1)}{2\mu_{BC}q_\pm^2}$) to the ro-vibrational energy obtained from DVR calculation. Initial value for the diatomic distance can vary from q_+ to q_- and the initial diatomic momentum can vary depending on the initial value of diatomic separation and the phase of the vibration. To start from all the possible phases of the vibrating diatom random number ξ ($0 \leq \xi \leq 1$) are invoked for different trajectories. Before starting the integration of equations of motion for three body collision, the equations of motion for a rotating diatom (which is vibrating also) is solved for a time $\tau\xi$ or $\tau(\xi - 0.5)$ for $\xi < 0.5$ or $\xi \geq 0.5$ respectively. Here τ is the time period of vibrational motion, which is calculated by integrating the equations of motion for a rotating diatom starting from a turning point to another turning point. τ and $q_\pm$ are parameters which vary for different initial states and calculated once for a initial state specific calculation.

In order to randomize the initial condition for each trajectory, standard Monte Carlo sampling is considered. The initial values for θ, ϕ, η and ξ are determined from pseudo random numbers invoked by a computer program, which has a value in between 0 and 1. Hence, a new set of random variable θ', ϕ', η' and ξ' are to be declared, which are related to θ, ϕ, η and ξ as

$$\theta = \cos^{-1}(1 - 2\theta'), \tag{2.72}$$

$$\phi = 2\pi\phi', \tag{2.73}$$

$$\eta = 2\pi\eta', \tag{2.74}$$

$$\xi = \xi'. \tag{2.75}$$

As mentioned earlier, for a particular trajectory, at first the equations of motion for rotating oscillator are solved with a BC separation of q_- if $\xi < 0.5$ and from q_+

otherwise. In this case, the initial parameters are taken as

- $q_1(0) = q_{\pm}\sin\theta\ \cos\phi$,
- $q_2(0) = q_{\pm}\sin\theta\ \sin\phi$,
- $q_3(0) = q_{\pm}\cos\theta$,
- $p_1(0) = \frac{J_r}{q_{\pm}}(\sin\phi\ \cos\eta - \cos\theta\ \cos\phi\ \sin\eta)$,
- $p_2(0) = -\frac{J_r}{q_{\pm}}(\cos\phi\ \cos\eta + \cos\theta\ \sin\phi\ \sin\eta)$,
- $p_3(0) = \frac{J_r}{q_{\pm}}\sin\theta\ \sin\eta$,

with $J_r = \hbar\sqrt{j(j+1)}$. After integrating for due time span, the resulting values of q_i and p_i are taken as the initial value for solving the equations 2.66, 2.67, 2.69 and 2.70.

2.4.3.1 Sampling of initial conditions for $j > 0$

The formalism proposed by Aoiz *et al.*[61] is followed here to calculate trajectories for rotationally excited reactant states. For $j > 0$, l takes the value in between $(J + j)$ to $|J - j|$ for a particular set of J and j. The classical relationship between the moduli of **J**, **l** and **j** can be expressed by triangle rule

$$|\mathbf{J}|^2 = |\mathbf{l}|^2 + |\mathbf{j}|^2 + 2|\mathbf{l}||\mathbf{j}|\cos\theta_{lj}, \tag{2.76}$$

where θ_{lj} is the angle between the vectors **l** and **j**. The space fixed axes (X, Y, Z) are chosen as reference frame, where the initial relative velocity vector is parallel to Z-axis. **l** vector can be placed along X-axis without any loss of generality. Thus, $l_X = |\mathbf{l}|$ and $l_Y = l_Z = 0$. In this reference frame, the Cartesian components of **j** can be written as

$$j_X = \quad J_X - |\mathbf{l}| = |\mathbf{j}|\cos\theta_{lj}, \tag{2.77}$$

$$j_Y = \quad J_Y = |\mathbf{j}|\sin\theta_{lj}\ \sin\alpha, \tag{2.78}$$

$$j_Z = \quad J_Z = |\mathbf{j}|\sin\theta_{lj}\ \cos\alpha. \tag{2.79}$$

Here, α is the azimuthal angle of **j** in the YZ plane and is chosen randomly as $0 \leq \alpha \leq 2\pi$. The components of **j** can also be expressed in SF frame in terms of usual polar (θ_j) and azimuthal angle (ϕ_j) of **j** as

$$
\begin{aligned}
j_X &= |\mathbf{j}|\sin\theta_j\ \cos\phi_j, && (2.80)\\
j_Y &= |\mathbf{j}|\sin\theta_j\ \sin\phi_j, && (2.81)\\
j_Z &= |\mathbf{j}|\cos\theta_j. && (2.82)
\end{aligned}
$$

θ_j and ϕ_j are determined from these set of equations. For the special case, when $J = 0$ and **l** and **j** are anti-parallel to each other, and $\cos\theta_l j = -1$ then if **l** lies on X-axis, $\theta_j = \pi/2$ and $\phi_j = \pi$.

Now the initial value of position and momentum coordinates for the reactant diatom to start the integration of equation of motion for rotating oscillator can be expressed as

- $q_1(0) = q_\pm(\cos\theta_j\ \cos\phi_j\ \cos\eta_j - \sin\phi_j\ \sin\eta_j)$,
- $q_2(0) = q_\pm(\cos\theta_j\ \sin\phi_j\ \cos\eta_j - \cos\phi_j\ \sin\eta_j)$,
- $q_3(0) = -q_\pm\sin\theta_j\ \cos\eta_j$,
- $p_1(0) = \frac{j_r}{q_\pm}(-\cos\theta_j\ \cos\phi_j\ \sin\eta_j - \sin\phi_j\ \cos\eta_j)$,
- $p_2(0) = \frac{j_r}{q_\pm}(-\cos\theta_j\ \sin\phi_j\ \sin\eta_j + \cos\phi_j\ \cos\eta_j)$,
- $p_3(0) = \frac{j_r}{q_\pm}\sin\theta_j\ \sin\eta_j$.

2.4.4 Integration

There are many algorithms to integrate a set of coupled differential equations. Some of them are fixed time step integrators, while some of them are variable time step integrators. For most of the cases, variable step size integrators are more problematic and less efficient than fixed step size integrator. Runge-Kutta, Adams-Moulton predictor-corrector and symplectic integration methods are notable among different fixed step size efficient integrators. In this thesis, fourth order Runge-Kutta method with a fixed step size is used for numerical integrations.

2.4.5 Conservation check

Once the integrator has been chosen, the fixed step size must be found out carefully by checking the total energy and total angular momentum conservation during integration. It is always better choice to perform conservation check for each trajectory. The total energy of the system is calculated as

$$E_{\text{tot}} = \sum_{i=1}^{3} \frac{p_i^2}{2\mu_{BC}} + \sum_{i=1}^{3} \frac{P_i^2}{2\mu_{A,BC}} + V(q, Q). \tag{2.83}$$

Total angular momentum is the sum of internal angular momentum of BC and relative angular momentum of A+BC system:

$$\mathbf{J}_{\text{tot}} = \mathbf{J}_{\text{r}} + \mathbf{J}_{\text{rel}}. \tag{2.84}$$

The internal angular momentum can be expressed as

$$\mathbf{J}_{\text{r}} = \mathbf{q} \times \mathbf{p} = (q_2p_3 - q_3p_2)\hat{\mathbf{j}}_x + (q_3p_1 - q_1p_3)\hat{\mathbf{j}}_y + (q_1p_2 - q_2p_1)\hat{\mathbf{j}}_z, \tag{2.85}$$

and the relative angular momentum of A+BC system is expressed as

$$\mathbf{J}_{\text{rel}} = \mathbf{Q} \times \mathbf{P} = (Q_2P_3 - Q_3P_2)\hat{\mathbf{j}}_x + (Q_3P_1 - Q_1P_3)\hat{\mathbf{j}}_y + (Q_1P_2 - Q_2P_1)\hat{\mathbf{j}}_z. \tag{2.86}$$

2.4.6 Product analysis

After integrating to a sufficient time scale until the reactants or the products are well-separated with minimum interaction between them, the trajectory calculation is stopped and the products are identified and analyzed. There may be several outcomes for the reaction A + BC, but the analysis of the products AB + C and AC + B are discussed here. It is convenient to transform the position and momentum vectors from reactant to product coordinates. The transformation matrices for AB + C products are:

$$\begin{pmatrix} q_i' \\ Q_i' \end{pmatrix} = \begin{pmatrix} -\frac{m_c}{m_b+m_c} & -1 \\ \frac{m_b(m_a+m_b+m_c)}{(m_a+m_b)(m_b+m_c)} & -\frac{m_a}{m_a+m_b} \end{pmatrix} \begin{pmatrix} q_i \\ Q_i \end{pmatrix} \tag{2.87}$$

and

$$\begin{pmatrix} p'_i \\ P'_i \end{pmatrix} = \begin{pmatrix} -\frac{m_a}{m_a+m_b} & 1 \\ -\frac{m_b(m_a+m_b+m_c)}{(m_a+m_b)(m_b+m_c)} & -\frac{m_c}{m_b+m_c} \end{pmatrix} \begin{pmatrix} p_i \\ P_i \end{pmatrix}. \tag{2.88}$$

Similarly, the transformations matrices for AC + B are:

$$\begin{pmatrix} q'_i \\ Q'_i \end{pmatrix} = \begin{pmatrix} \frac{m_b}{m_b+m_c} & -1 \\ -\frac{m_c(m_a+m_b+m_c)}{(m_a+m_c)(m_b+m_c)} & -\frac{m_a}{m_a+m_c} \end{pmatrix} \begin{pmatrix} q_i \\ Q_i \end{pmatrix} \tag{2.89}$$

and

$$\begin{pmatrix} p'_i \\ P'_i \end{pmatrix} = \begin{pmatrix} \frac{m_a}{m_a+m_c} & -1 \\ -\frac{m_c(m_a+m_b+m_c)}{(m_a+m_c)(m_b+m_c)} & -\frac{m_b}{m_b+m_c} \end{pmatrix} \begin{pmatrix} p_i \\ P_i \end{pmatrix}. \tag{2.90}$$

The internal energy of the product diatom is calculated as

$$\varepsilon_{\text{int}} = \sum_{i=1}^{3} \frac{p'^2_i}{2\mu} + V(q'), \tag{2.91}$$

where μ is the reduced mass of the product diatom and $V(q')$ is the potential energy of the product diatom.

The internal angular momentum of the product diatom is evaluated as

$$\mathbf{J'}_{\text{r}} = \mathbf{q}' \times \mathbf{p}'. \tag{2.92}$$

The relative velocity vector of the products is calculated as

$$\nu' = \frac{1}{\mu}\sqrt{(\mathbf{P}'.\mathbf{P}')}, \tag{2.93}$$

where μ is the reduced mass of products.

The scattering angle (θ) is defined as the angle between the final relative velocity of the species which contains the initially free ‘A’ atom and the incident direction of initially free ‘A’ atom. The scattering angle is calculated as

$$\theta = \pi - \cos^{-1}\left(\frac{\nu.\nu'}{|\nu||\nu'|}\right). \tag{2.94}$$

The rotational quantum number of the product diatom can be calculated as a continuous number by equating $\sqrt{j'(j'+1)}\hbar$ to $\mathbf{J'}_{\rm r}$ and thus,

$$j' = -\frac{1}{2} + \frac{1}{2}\sqrt{1 + 4\mathbf{J'}_{\rm r}\mathbf{J'}_{\rm r}/\hbar^2}. \tag{2.95}$$

The vibrational quantum number (v') of the product diatom is assigned by following the procedure described in Refs. 62–64. v' is obtained as a continuous number by equating the internal energy $\varepsilon_{\rm int}$ of the product diatom to the Dunham expansion, which represents the ro-vibrational energies ($\varepsilon_{v',j'}$) of a diatomic molecule as

$$\varepsilon_{v',j'} = Y_{l,m}(v' + 1/2)^l (j'(j'+1))^m, \tag{2.96}$$

with l and m as 4 and 3, respectively. The coefficients of the Dunham expansion, $Y_{l,m}$, are calculated by fitting the QM ro-vibrational energies of the product diatom to the expansion form i.e., Eq. 2.96. Finally, the ro-vibrational states of the product diatom are assigned by rounding the continuous numbers to suitable integer numbers.

In the histogram binning (HB) method, final states for given trajectories are determined by simple rounding off the real v's and j's to the nearest integers. HB method sometimes leads to energetically closed product states, and thus evokes error in estimating reaction attributes. For the endothermic reactions, the HB method fails to describe the threshold region and introduces significant discrepancies when compared with the QM results.[65–68] This problem is mostly overcome by using weighted binning methods, as for example the Gaussian binning (GB) approach.[64,69,70] In GB method, each trajectory is weighted by a Gaussian shaped function

$$w(x_r) = \frac{1}{\sqrt{\pi\epsilon^2}}\exp(-(x_r - x_i)^2/\epsilon^2), \tag{2.97}$$

where x_r is the real valued number and x_i is the integer quantum number. Here, $\epsilon = \mathrm{FWHM}/2\sqrt{\log_e 2}$, where FWHM is full-width-half-maximum for the Gaussian function. The Gaussian function is centered at the correct quantum number in such a way that the closer the value of x_r to an integer, the larger is the weight for that trajectory. FWHM can be chosen arbitrarily between 0.05 to 0.12.

2.4.7 Reaction probability calculation

For a particular l, the impact parameter is constant and is expressed as

$$b = \sqrt{l(l+1)}\hbar/\sqrt{2\mu E_c}, \tag{2.98}$$

where μ is the reduced mass of reactants and E_c is the collision energy. For a particular collision energy the reaction probability is calculated as

$$P_r(l, E_c) = \frac{N_r(l, E_c)}{N_{\text{tot}}(l, E_c)}, \tag{2.99}$$

where $N_r(l, E_c)$ is the number of reactive trajectories and $N_{\text{tot}}(l, E_c)$ is the total number of trajectories. For $j = 0$, $J = l$ and thus $P_r(J, E_c) = P_r(l, E_c)$. But, for $j > 0$, $P_r(J, E_c)$ are calculated by averaging all possible $P_r(l, E_c)$.

2.4.8 Integral cross section

There are different approaches to calculate the ICS of a reaction by means of trajectory calculation. The most common approach is to sample the impact parameter (b). In this approach, a new parameter b' is sampled uniformly between 0 and 1 in a continuous way for each trajectory. b is then calculated as $b = b_{\text{max}}\sqrt{b'}$, where b_{max} is the maximum impact parameter for which a reactive collision occurs. b_{max} is determined for a particular collision energy by running small batches of trajectories for different bs. The ICS is then calculated as

$$\sigma(E_c) = \pi b_{\text{max}}^2 \frac{N_r(E_c)}{N_{\text{tot}}(E_c)}, \tag{2.100}$$

where $N_r(E_c)$ and $N_{\text{tot}(\text{E}_\text{c})}$ are the number of reactive trajectories and the total number of trajectories, respectively.

In a J-sampling technique,[61] J is sampled instead of b to calculate ICS at a particular collision energy. For each trajectory, at first, the value of J is sampled randomly and uniformly as an integer between 0 to J_{max}. J_{max} is determined for a given collision energy by running a small batches of trajectories for different Js. The value of l is then chosen following a procedure similar to J between $|J - j|$ to $(J + j)$. Thus, the probability for a given J can be calculated as[61]

$$P_r(J) = \frac{1}{2\ \min(J, j) + 1} \sum_{l=|J-j|}^{J+j} P_r(J, l). \tag{2.101}$$

Here $P_r(J, l) = N_r(J, l)/N_{\text{tot}}(J, l)$, where $N_r(J, l)$ and $N_{\text{tot}}(J, l)$ are the number of reactive and the total number of trajectories, respectively, for a given combination of J and l. The ICS is then computed as[61]

$$\sigma = \frac{\pi}{k^2} \frac{1}{2j + 1} \sum_{J=0}^{J_{\max}} (2J + 1)[2\ \min(J, j) + 1] P_r(J), \tag{2.102}$$

where $k = \sqrt{2\mu_R E_c/\hbar^2}$ is the wave number vector.

2.4.9 Differential cross section

For $j = 0$ initial reactant state the DCS $(d\sigma_r/d\Omega)$ is computed as

$$\frac{d\sigma_r}{d\Omega} = \frac{1}{2k^2 \sin\,\theta} \sum_{J=0}^{J_{\max}} (2J + 1) \frac{N_r(J, \theta)}{N_{\text{tot}}(J)} \frac{1}{\Delta\theta}, \tag{2.103}$$

where $N_r(J, \theta)$ and $N_{\text{tot}}(J)$ are the number of reactive trajectories scattered at an angle θ and the total number of trajectories, respectively, for a given J. $N_r(J, \theta)$ is determined by using histograms along the θ grid. The DCS can also be calculated by the method of moments expansion in Legendre polynomials as[63,71]

$$\frac{d\sigma_r}{d\Omega} = \frac{1}{2k^2} \sum_{J=0}^{J_{\max}} (2J + 1) P_r(J) \left(\frac{1}{2} + \sum_{m=1} a_m^J\ P_m(\cos\theta) \right). \tag{2.104}$$

The J-dependent coefficients a_m^J are given by

$$a_m^J = \frac{2m + 1}{2} \frac{1}{N_r(J)} \sum_{i=1}^{N_r(J)} P_m(\cos\theta_i). \tag{2.105}$$

2.5 BOUND STATE CALCULATION FOR ABC

Bound ro-vibrational eigenstates of a complex is essential to obtain spectroscopic information in relation to the structural and binding features. Advances in computation techniques have enabled us to treat weakly bound triatomic and polyatomic systems quantum mechanically with great accuracy. In experimental side laser spectroscopy and supersonic molecular beam studies produce highly resolved spectroscopic data and a direct comparison between theory and experiment can be made. The most common approach to solve a bound state problem is to diagonalize the Hamiltonian matrix, where the Hamiltonian matrix is constructed in a grid basis. The eigenenergies and eigenfunction of system can directly be obtained via the diagonalization procedure. DVR3D is a popular package by Tennyson *et al.*[72] to compute the ro-vibrational energies and corresponding state for triatomic systems. The program follows a DVR approach based on Gauss-Jacobi and Gauss-Laguerre quadrature for all the internal coordinates. A DVR based on associated Legendre polynomials is used for the angular coordinate and for the radial coordinates, DVRs based on either Morse oscillator or spherical oscillator functions are used. The methodological details of DVR3D program can be found in Ref. 72 and references therein.

An alternative approach for solving eigenvalue problems is to use TDWP approach. In this approach, an autocorrelation function is computed from an arbitrarily chosen initial wave packet followed by Fourier transformation of the autocorrelation function to obtain the energy spectra. In this thesis work, Fortran programs are written to calculate the eigenstates of triatomic (ABC) systems following the TDWP approach for zero total angular momentum. Below the methodology is discussed elaborately.

2.5.1 Hamiltonian

The Hamiltonian in Eq. 2.24 is used for the bound state problem, except that calculations are carried out only for $J = 0$.

2.5.2 Initial wave packet

The initial wave packet for time propagation is chosen arbitrarily with proper overlap with the eigenstate of the systems as[73]

$$\Psi_{j_0 J}(0) = G_R(R)\ G_r(r)\ \widetilde{P}_{j_0 K}(\cos\theta), \tag{2.106}$$

where $G_x(x)$ is a standard Gaussian function defined as

$$G_x(x) = \left(\frac{1}{\pi\delta_x^2}\right)^{\frac{1}{4}} \exp(-(x-x_0)^2/2\delta_x^2). \tag{2.107}$$

δ_x is the width parameter of the Gaussian wave packet. Here, $\widetilde{P}_{j_0 K}(\cos\theta)$ is the normalized associated Legendre polynomials.

2.5.3 Propagator

The split operator method, proposed first by Fleck *et al.*[74] is used to propagate the initial wave function. In this method, the exponential time evolution operator is split into several parts to minimize the numerical error and the time dependent wave packet $\psi(R, r, \theta, t + \Delta t)$ is calculated as

$$\begin{aligned}\psi(R, r, \theta, t+\Delta t) =& e^{-i\hat{V}(R,r,\theta)\Delta t/2\hbar} e^{-i\hat{T}(\theta)\Delta t/2\hbar} e^{-i\hat{T}(R,r)\Delta t/\hbar} e^{-i\hat{T}(\theta)\Delta t/2\hbar} \\ & \times e^{-i\hat{V}(R,r,\theta)\Delta t/2\hbar} \psi(R, r, \theta, t) + O(\Delta t)^3,\end{aligned} \tag{2.108}$$

where $O(\Delta t)^3$ is the error of third order, $\hat{V}(R, r, \theta)$ is the potential energy of the triatomic system, $\hat{T}(\theta)$ and $\hat{T}(R, r)$ are the angular and radial kinetic energy operators respectively.

2.5.4 Damping function

A sine function of the following form is used as damping function

$$f_{\text{damp}}(x) = \sin\left[\frac{\pi(x_d + \Delta x_d - x)}{2\Delta x_d}\right], \qquad x \geq x_d. \tag{2.109}$$

Here, x_d is the starting point of the damping function and Δx_d is the width of the damping function. $f_{\text{damp}}(\text{x})$ is multiplied with the WP at each time step during propagation.

2.5.5 Autocorrelation function

If Φ_n be the bound states of a system with corresponding eiegenenergies E_n, the initial wave packet can be expanded in this eigen basis functions as

$$\Psi(0) = \sum_n C_n \Phi_n, \tag{2.110}$$

where the coefficient C_n is given by

$$C_n = \langle \Phi_n | \Psi(0) \rangle. \tag{2.111}$$

The TDSE is written as

$$i\hbar \frac{\partial \Psi(t)}{\partial t} = \hat{H} \Psi(t), \tag{2.112}$$

thus

$$\Psi(t) = e^{-i\hat{H}t/\hbar} \Psi(0) = \sum_n C_n \ e^{-iE_n t/\hbar} \ \Phi_n. \tag{2.113}$$

Now an autocorrelation function ($A(t)$) is defined as

$$A(t) = \langle \Psi(0) | \Psi(t) \rangle. \tag{2.114}$$

$A(t)$ relates $\Psi(t)$ to the initial wave packet ($\Psi(0)$). Using Eq. 2.111 and 2.113 one can get

$$A(t) = \sum_n C_n \ e^{-iE_n t/\hbar} \ \langle \Psi(0) | \Phi_n \rangle = \sum_n \ e^{-iE_n t/\hbar} |C_n|^2 \tag{2.115}$$

2.5.6 Energy Spectrum

The generalized energy spectrum is obtained by performing a Fourier transformation of $A(t)$ as

$$I(E) = \left| \int_{-\infty}^{\infty} A(t) e^{iEt/\hbar} dt \right|^2 \tag{2.116}$$

The conventional sinc spectrum is given by[75]

$$I_s(E) = \left| \frac{1}{2\pi} \int_0^T A(t) e^{iEt/\hbar} dt \right|^2, \tag{2.117}$$

where, T is the propagation time. $I_s(E)$ is an oscillatory function of energy E at time T. The energy resolution of the spectrum is given by

$$\Delta E = \frac{2\pi\hbar}{T}. \tag{2.118}$$

At $T \rightarrow \infty$, $I_s(E)$ behaves like a delta function.

Noises in disguise of unnecessary peaks are invoked in a finite time propagation. In order to reduce the noise in a finite time propagations, a window function is used either in the time domain or in the energy domain. The use of window function $w(t)$ can be helpful in eigenenergy calculation to get noise free spectra. In the Gaussian spectrum calculation method proposed by Zhang *et al.*[76] a Gaussian type window function ($w_g(T) = e^{-\alpha^2 t^2}$) is multiplied to the autocorrelation function at each time step before FT and the energy spectrum is evaluated as

$$I_g(E) = \left| \frac{1}{2\pi} \int_0^T e^{iEt/\hbar} A(t) w_g(t) dt \right|^2, \tag{2.119}$$

where α is an adjustable parameter. In this approach, the intensity decays exponentially from the spectral peaks. By increasing the value of α from zero the spectrum changes from sinc to Gaussian. However, a large value of α results a broaden spectrum.

Normalized Hanning window function $w_h(t)$ can also be multiplied with the autocorrelation function at each time step before FT to get a well resolved spectra.[75] The window function is expressed as

$$w_h(t) = \begin{cases} \frac{1}{T}[1 - \cos(2\pi t/T)], & \text{for } 0 \leq t \leq T \\ 0, & \text{for } t > T \end{cases} \tag{2.120}$$

Thus, eigenenergy spectrum is calculated as

$$I_h(E) = \left| \int_0^T e^{iEt/\hbar} A(t) w_h(t) dt \right|^2 . \tag{2.121}$$

The intensity of the energy spectrum depends on the choice of initial wave packet due to different overlaps with the eigenstates of the systems. The WFs corresponding to eigenstates with eigenenergies E_n can be computed by FT of the time evolved WF ($\Psi(t)$) as

$$\Psi(E_n) = \int_0^\infty \Psi(t) e^{iE_n t/\hbar} dt. \tag{2.122}$$

References

[1] Ho, T.; Rabitz, H. *J. Chem. Phys.* **1996**, *104*, 2584.

[2] Shepard, D. In *Proceedings of the 1968 23rd ACM National Conference*, ACM '68, pages 517, New York, NY, USA, 1968. ACM.

[3] Łukaszyk, S. *Comput. Mech.* **2004**, *33*, 299.

[4] Varandas, A. J. C. In *Advances in Chemical Physics;* John Wiley & Sons, Inc., 2007; pages 255.

[5] Aguado, A.; Paniagua, M. *J. Chem. Phys.* **1992**, *96*, 1265.

[6] Press, W. H.; Teukolsky, S. A.; Vetterling, W. T.; Flannery, B. P. *Numerical Recipes in Fortran 77;* Cambridge University Press, New York, 1992.

[7] Hankel, M.; Smith, S. C.; Allan, R. J.; Gray, S. K.; Balint-Kurti, G. G. *J. Chem. Phys.* **2006**, *125*, 164303.

[8] Manolopoulos, D. E. *J. Chem. Soc., Faraday Trans.* **1997**, *93*, 673.

[9] Quan, W.-L.; Song, Q.; Tang, B.-Y. *Chem. Phys. Lett.* **2007**, *437*, 165.

[10] Lin, S. Y.; Guo, H. *J. Chem. Phys.* **2003**, *119*, 11602.

[11] Lin, S. Y.; Guo, H. *J. Phys. Chem. A* **2004**, *108*, 2141.

[12] Lin, S. Y.; Sun, Z.; Guo, H.; Zhang, D. H.; Honvault, P.; Xie, D.; Lee, S.-Y. *J. Phys. Chem. A* **2008**, *112*, 602.

[13] Rao, T. R.; Goswami, S.; Mahapatra, S.; Bussery-Honvault, B.; Honvault, P. *J. Chem. Phys.* **2013**, *138*, 094318.

[14] Goswami, S.; Rao, T. R.; Mahapatra, S.; Bussery-Honvault, B.; Honvault, P. *J. Phys. Chem. A* **2014**, *118*, 5915.

[15] González-Lezana, T.; Honvault, P. *Int. Rev. Phys. Chem.* **2014**, *33*, 371.

[16] Martínez, R.; Sierra, J. D.; Gray, S. K.; González, M. *J. Chem. Phys.* **2006**, *125*, 164305.

[17] Maiti, B.; Kalyanaraman, C.; Panda, A. N.; Sathyamurthy, N. *J. Chem. Phys.* **2002**, *117*, 9719.

[18] Panda, A. N.; Sathyamurthy, N. *J. Chem. Phys.* **2005**, *122*, 054304.

[19] Mayneris, J.; Sierra, J. D.; González, M. *J. Chem. Phys.* **2008**, *128*, 194307.

[20] Lv, S.-J.; Zhang, P.-Y.; Han, K.-L.; He, G.-Z. *J. Chem. Phys.* **2010**, *132*, 014303.

[21] Gamallo, P.; Defazio, P.; González, M. *J. Phys. Chem. A* **2011**, *115*, 11525.

[22] Hu, M.; Xu, W.; Liu, X.; Tan, R.; Li, H. *J. Chem. Phys.* **2013**, *138*, 174305.

[23] Gamallo, P.; Akpinar, S.; Defazio, P.; Petrongolo, C. *J. Phys. Chem. A* **2014**, *118*, 6451.

[24] Bhattacharya, S.; Panda, A. N. *J. Phys. B: At. Mol. Opt. Phys.* **2009**, *42*, 085201.

[25] Xu, W.; Zhang, P. *J. Phys. Chem. A* **2013**, *117*, 1406.

[26] Zhang, J. Z. H. *Theory and Application of Quantum Molecular Dynamics;* World Scientific, 1999.

[27] Schatz, G. C.; Kuppermann, A. *J. Chem. Phys.* **1976**, *65*, 4642.

[28] McGuire, P.; Kouri, D. J. *J. Chem. Phys.* **1974**, *60*, 2488.

[29] Pack, R. T. *J. Chem. Phys.* **1974**, *60*, 633.

[30] Gray, S. K.; Balint-Kurti, G. G. *J. Chem. Phys.* **1998**, *108*, 950.

[31] Tal-Ezer, H.; Kosloff, R. *J. Chem. Phys.* **1984**, *81*, 3967.

[32] Chen, R.; Guo, H. *J. Chem. Phys.* **1996**, *105*, 3569.

[33] Chen, R.; Guo, H. *Comput. Phys. Commun.* **1999**, *119*, 19.

[34] Mandelshtam, V. A.; Taylor, H. S. *J. Chem. Phys.* **1995**, *102*, 7390.

[35] http://developer.amd.com/.

[36] Light, J. C.; Hamilton, I. P.; Lill, J. V. *J. Chem. Phys.* **1985**, *82*, 1400.

[37] Zanchet, A.; Roncero, O.; González-Lezana, T.; Rodríguez-López, A.; Aguado, A.; Sanz-Sanz, C.; Gómez-Carrasco, S. *J. Phys. Chem. A* **2009**, *113*, 14488.

[38] Lin, S. Y.; Guo, H. *Phys. Rev. A* **2006**, *74*, 022703.

[39] Sun, Z.; Lee, S.-Y.; Guo, H.; Zhang, D. H. *J. Chem. Phys.* **2009**, *130*, 174102.

[40] Colbert, D. T.; Miller, W. H. *J. Chem. Phys.* **1992**, *96*, 1982.

[41] Zhang, J. Z. H. *J. Chem. Phys.* **1991**, *94*, 6047.

[42] Meijer, A. J. H. M.; Goldfield, E. M.; Gray, S. K.; Balint-Kurti, G. G. *Chem. Phys. Lett.* **1998**, *293*, 270.

[43] Althorpe, S. C. *J. Chem. Phys.* **2001**, *114*, 1601.

[44] Lara, M.; Aguado, A.; Paniagua, M.; Roncero, O. *J. Chem. Phys.* **2000**, *113*, 1781.

[45] Miquel, I.; González, M.; Sayós, R.; Balint-Kurti, G. G.; Gray, S. K.; Goldfield, E. M. *J. Chem. Phys.* **2003**, *118*, 3111.

[46] Aslan, E.; Bulut, N.; Castillo, J. F.; Bañares, L.; Roncero, O.; Aoiz, F. J. *J. Phys. Chem. A* **2012**, *116*, 132.

[47] Skouteris, D.; Castillo, J. F.; Manolopoulos, D. E. *Comput. Phys. Commun.* **2000**, *133*, 128.

[48] Gamallo, P.; Huarte-Larrañaga, F.; González, M. *J. Phys. Chem. A* **2013**, *117*, 5393.

[49] Sato, K.; Takayanagi, T. *Chem. Phys.* **2015**, *450-451*, 74 .

[50] Jambrina, P. G.; Herráez-Aguilar, D.; Aoiz, F. J.; Sneha, M.; Jankunas, J.; Zare, R. N. *Nat. Chem.* **2015**, *7*, 661.

[51] Aldegunde, J.; Jambrina, P. G.; González-Sanchez, L.; Herrero, V. J.; Aoiz, F. J. *J. Phys. Chem. A* **2015**, *119*, 12245.

[52] Teixidor, M. M.; Varandas, A. J. C. *J. Chem. Phys.* **2015**, *142*, 014309.

[53] Zanchet, A.; Roncero, O.; Bulut, N. *Phys. Chem. Chem. Phys.* **2016**, *18*, 11391.

[54] Bulut, N.; Kłos, J.; Roncero, O. *J. Chem. Phys.* **2015**, *142*, 214310.

[55] Skouteris, D.; Castillo, J. F.; Manolopoulos, D. E. *Comput. Phys. Commun.* **2000**, *133*, 128.

[56] Schatz, G. C. *Chem. Phys. Lett.* **1988**, *150*, 92.

[57] Zhang, J. Z. H.; Miller, W. H. *J. Chem. Phys.* **1989**, *91*, 1528.

[58] Karplus, M.; Porter, R. N.; Sharma, R. D. *J. Chem. Phys.* **1965**, *43*, 3259.

[59] Truhlar, D. G.; Muckerman, J. T. In *Atom - Molecule Collision Theory*; Bernstein, R. B., Ed.; Springer US, 1979; pages 505.

[60] Henriksen, N. E.; Hansen, F. Y. *Theories of Molecular Reaction Dynamics;* Oxford, 2011.

[61] Aoiz, F. J.; Sáez-Rabanos, V.; Martínez-Haya, B.; González-Lezana, T. *J. Chem. Phys.* **2005**, *123*, 094101.

[62] Aoiz, F. J.; Herrero, V. J.; Sáez Rábanos, V. *J. Chem. Phys.* **1991**, *94*, 7991.

[63] Aoiz, F. J.; Verdasco, E.; Rábanos, V. S.; Loesch, H. J.; Menéndez, M.; Stienkemeier, F. *Phys. Chem. Chem. Phys.* **2000**, *2*, 541.

[64] Bañares, L.; Aoiz, F.; Honvault, P.; Bussery-Honvault, B.; Launay, J.-M. *J. Chem. Phys.* **2003**, *118*, 565.

[65] Nyman, G.; Wilhelmsson, U. *J. Chem. Phys.* **1992**, *96*, 5198.

[66] Gilibert, M.; Giménez, X.; Huarte-Larrañaga, F.; González, M.; Aguilar, A.; Last, I.; Baer, M. *J. Chem. Phys.* **1999**, *110*, 6278.

[67] Jambrina, P. G.; Aoiz, F. J.; Bulut, N.; Smith, S. C.; Balint-Kurti, G. G.; Hankel, M. *Phys. Chem. Chem. Phys.* **2010**, *12*, 1102.

[68] Panda, A. N.; Herráez-Aguilar, D.; Jambrina, P. G.; Aldegunde, J.; Althorpe, S. C.; Aoiz, F. J. *Phys. Chem. Chem. Phys.* **2012**, *14*, 13067.

[69] Bonnet, L.; Rayez, J.-C. *Chem. Phys. Lett.* **1997**, *277*, 183.

[70] Bonnet, L.; Rayez, J.-C. *Chem. Phys. Lett.* **2004**, *397*, 106.

[71] Truhlar, D. G.; Blais, N. C. *J. Chem. Phys.* **1977**, *67*, 1532.

[72] Tennyson, J.; Kostin, M. A.; Barletta, P.; Harris, G. J.; Polyansky, O. L.; Ramanlal, J.; Zobov, N. F. *Comput. Phys. Commun.* **2004**, *163*, 85.

[73] Dai, J.; Zhang, J. Z. H. *J. Chem. Phys.* **1996**, *104*, 3664.

[74] Feit, M. D.; J. A. Fleck, J.; Steiger, A. *J. Comp. Phys.* **1982**, *47*, 412 .

[75] Mahapatra, S.; Sathyamurthy, N. *J. Chem. Phys.* **1995**, *102*, 6057.

[76] Dai, J.; Zhang, J. Z. H. *J. Chem. Phys.* **1995**, *103*, 1491.

Chapter 3

Global Potential Energy Surfaces for $[HeHNe]^+$ and $[NeHNe]^+$ Systems and Bound States

---

This chapter introduces two proton-rare gas dimer molecular complexes, $[HeHNe]^+$ and $[NeHNe]^+$, and describes the full dimensional potential energy surfaces for these two systems. Nature of binding interactions between the rare gases and the hydrogen atom are explored, in addition to finding out the most stable structures and their characteristic features for each system. For both the systems, global analytical PESs are generated from *ab initio* energies for the first time. The bound vibrational states for $J = 0$ are also reported for the most stable structures of both the systems.

Part of the contents of this chapter are published in the following research articles:

- Koner, D.; Vats, A.; Vashishta, M.; Panda, A. N. *ab initio* Electronic Structure Investigation of Protonated Mixed Rare Gas Dimers $[NeHHe]^+$, $[ArHHe]^+$ and $[ArHNe]^+$. Comput. Theor. Chem. **2012**, *1000*, 19-25.

- Koner, D.; Panda, A. N. Quantum Dynamical Study of the He + NeH^+ Reaction on a New Analytical Potential Energy Surface. J. Phys. Chem. A **2013**, *117*, 13070-13078.

- Koner, D.; Barrios, L.; González-Lezana, T.; Panda, A. N. Scattering Study of the Ne + NeH^+ $(v_0 = 0, j_0 = 0) \rightarrow NeH^+$ + Ne Reaction on an *ab initio* Based Analytical Potential Energy Surface. J. Chem. Phys. **2016**, *144*, 034303.

3.1 INTRODUCTION

Rare gas dimers are weakly bound by van der Waals forces. However, presence of a proton highly stabilizes the system, e.g., He_2 dimer has a binding energy of 0.021 kcal/mol only,[1] whereas the dissociation process of $[HeHHe]^+$ to He and HeH^+ is endothermic by 13.24 kcal/mol.[2] Investigations on rare gas-hydrogen clusters have been the prime focus for many researchers for last few decades. Plentiful experimental as well as theoretical works have been reported in the literature for Rg_2H^+ and $[RgHRg']^+$ (Rg/Rg' = rare gas) type of molecules. Vibration spectra of linear $[ArHAr]^+$, $[KrHKr]^+$ and $[XeHXe]^+$ and their deuterated counterparts have been detected by Kunttu et al.[3,4] In an electron bombardment matrix isolation experiment of methanol-rare gas mixtures, Fridgen and Parnis reported the existence of mixed rare gas cations $[ArHKr]^+$, $[ArHXe]^+$ and $[KrHXe]^+$.[5] Computational studies on light rare gas-hydrogen clusters (Rg_2H^+, Rg = He, Ne and Ar) suggest a linear centrosymmetric $[RgHRg]^+$ geometry as the most stable one.[2,6–11] Analytic PESs for He_2H^+[11] and Ar_2H^+[10] have been generated and bound vibrational states of the most stable structures have also been predicted.[11,12] Electronic structure calculations of protonated mixed rare gases ($[RgHRg']^+$, Rg/Rg' = Ar, Kr and Xe) also suggested a linear configuration with the hydrogen in between the two rare gas atoms to be the most stable structure.[13–16] However, analytic PESs for $[HeHNe]^+$ and $[NeHNe]^+$ are not reported in the literature. Keeping in mind that both the systems might be important and relevant in rare gas chemistry, these two systems are explored and analytical PESs for these systems are constructed to study the possible reactive scattering phenomena.

3.2 THE $[HeHNe]^+$ SYSTEM

3.2.1 Electronic structure calculations

The electronic structure and bonding properties of $[HeHNe]^+$ are explored by using different high level *ab initio* methods and expensive basis sets with the ORCA[17] software. The *ab initio* methods which include Møller-Plesset perturbation theory through second order (MP2), quadratic configuration interaction including single and double substitutions (QCISD) and with perturbative triples correction (QCISD(T)), coupled cluster singles doubles methods (CCSD) and with perturbative triples correction (CCSD(T)) and coupled electron pair approximation (CEPA/1), and basis sets like Pople type 6-311G, augmented with several diffuse and polarization functions (d,p) and (3df,3pd), Dunning type correlation consistent polarized double, triple and quadrupole zeta basis sets (cc-pVnZ (n = D, T, Q)) and the augmented versions of the same (aug-cc-pVnZ (n = D, T, Q)) are used to optimize the electronic energy and geometry for the system. All the calculations are performed for the ground electronic state and the multireference property of the optimized structures is checked by calculating the T1-diagnostics at the CCSD level, which is much less than 0.02. Hence, it can be said that the system $[\mathrm{HeHNe}]^+$ does not have significant multiconfigurational character and the coupled cluster calculations are reliable for this system. The core electrons were kept frozen in all the calculations.

3.2.1.1 The global minimum

TABLE 3.1: Equilibrium bond lengths (in a.u.) for $[\mathrm{HeHNe}]^+$.

Bond	Basis set	Method					
		MP2	QCISD	CCSD	CEPA/1	QCISD(T)	CCSD(T)
HeH	6-311++G(d,p)	1.819	1.829	1.828	1.829	1.829	1.819
	6-311++G(3df,3pd)	1.811	1.822	1.821	1.819	1.820	1.829
	cc-pVDZ	1.793	1.799	1.799	1.798	1.799	1.800
	cc-pVTZ	1.820	1.832	1.835	1.832	1.832	1.831
	cc-pVQZ	1.802	1.808	1.809	1.811	1.809	1.808
	aug-cc-pVDZ	1.752	1.759	1.759	1.759	1.760	1.760
	aug-cc-pVTZ	1.806	1.815	1.816	1.818	1.814	1.812
	aug-cc-pVQZ	1.797	1.806	1.804	1.807	1.801	1.803
NeH	6-311++G(d,p)	2.083	2.074	2.073	2.072	2.075	2.082
	6-311++G(3df,3pd)	2.088	2.077	2.076	2.077	2.081	2.075
	cc-pVDZ	2.123	2.119	2.118	2.118	2.118	2.117
	cc-pVTZ	2.083	2.071	2.068	2.070	2.073	2.073
	cc-pVQZ	2.101	2.092	2.090	2.089	2.095	2.095
	aug-cc-pVDZ	2.217	2.213	2.211	2.211	2.213	2.212
	aug-cc-pVTZ	2.101	2.090	2.087	2.087	2.094	2.095
	aug-cc-pVQZ	2.108	2.097	2.097	2.096	2.104	2.102

Geometry optimization calculations for all the methods and the basis sets mentioned earlier yield a linear He-H-Ne configuration as the most stable geometry for the system. The bond lengths (R_{eq}) of the most stable structures obtained via different theoretical approaches are tabulated in Table 3.1. Unlike other protonated mixed rare gas dimers e.g., $[\text{ArHHe}]^+$, $[\text{ArHNe}]^+$,[18] $[\text{ArHKr}]^+$, $[\text{ArHXe}]^+$ and $[\text{KrHXe}]^+$,[5,13–16] the lighter rare gas atom in $[\text{HeHNe}]^+$ makes a shorter bond with hydrogen as compared to the heavier rare gas. As it is observed in Table 3.1, optimizations with the aug-cc-pVDZ basis set results the longest NeH bond and shortest HeH bond. Except aug-cc-pVDZ, both the bond lengths are similar for all the other basis sets with different methods.

The complex $[\text{HeHNe}]^+$ can dissociate either into Ne+HeH$^+$ or into He+NeH$^+$. CBS limit energies of the system are computed at optimized geometries using three different methods, CEPA/1, QCISD(T) and CCSD(T) with highly converging correlation consistent aug-cc-PVnZ (n = T, Q) basis sets. To measure the basis set superposition error, the counterpoise-correction (CP) method of Boys and Bernardi[19] is used. The CP corrected dissociation energies were calculated using the supermolecular approach:

$$D_e^{CP} = D_e - \Delta E_1 - \Delta E_2. \tag{3.1}$$

Here, $\Delta E_i (i = 1, 2)$ are the correction terms for the fragments of the complex, defined as the difference between the energies of the fragments at $[\text{HeHNe}]^+$ geometry with the total cluster basis set and fragment-centered basis set.

The dissociation energies for the two different dissociation channels are plotted in Figure 3.1. As can be seen in Figure 3.1(a), calculations with the cc-pVDZ basis set give the highest D_e for the Ne+HeH$^+$ dissociation channel, whereas aug-cc-pVDZ and 6-311++G(d,p) basis sets produce smaller D_e for the same channel compared to the other basis sets. The dissociation energies for the Ne+HeH$^+$ channel calculated at MP2 level with larger basis sets (e.g., cc-pVQZ and aug-cc-pVQZ) are comparable with the CCSD(T) values. In Figure 3.1(b), it is observed that aug-cc-pVDZ basis set gives significantly larger HeH bond dissociation energy, while 6-311++G(3df,3pd) results are comparable with expensive aug-cc-pVQZ basis set values. For both the dissociation channels, D_e calculated with CCSD(T) and QCISD(T) methods are very close to each

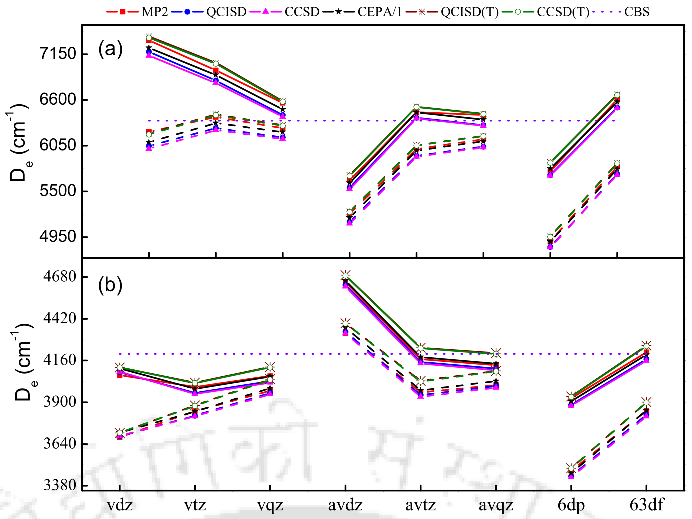

FIGURE 3.1: Counterpoise corrected (dashed lines) and uncorrected (solid lines) dissociation energies for the two dissociation channels of $[HeHNe]^+$, (a) $[HeHNe]^+ \rightarrow Ne + HeH^+$ and (b) $[HeHNe]^+ \rightarrow He + NeH^+$. Dashed horizontal lines represent the estimated CBS values at the CCSD(T) level. The abbreviations ‘vnz’ and ‘avnz’ (n = d, t, q) stand for ‘cc-pVnZ’ and ‘aug-cc-pVnZ’ (n = D, T, Q), respectively, and, ‘6df’ and ‘63df’ represent 6-311++G(d,p) and 6-311++G(3df,3pd) basis sets.

other. A comparison with the linear centrosymmetric He_2H^+ and Ne_2H^+ (see Ref. 2) shows that the lighter rare gas shows a longer and weaker bond with hydrogen, whereas the heavier rare gas forms a shorter and stronger bond with hydrogen than the corresponding bonds in the linear centrosymmetric cation. A similar situation can also be seen for other mixed rare gas-hydrogen clusters.[2,10,14,16,18]

As shown in Figure 3.1(a), CP uncorrected $He+NeH^+$ dissociation energies are closer to the CBS limit energy than the CP corrected energies. Calculations with CCSD(T) and QCISD(T) methods give almost the same equilibrium bond lengths and the dissociation energies, with all the basis sets, and CEPA/1 dissociation energy values are a bit smaller than CCSD(T) and QCISD(T) values. Results obtained from non-augmented Dunning’s basis sets are comparable with the augmented ones. While the dissociation energies obtained using cc-pVDZ, aug-cc-pVDZ and segmented 6-311++G(d,p) basis sets differ significantly from the others, 6-311++G(3df,3pd) produces reasonable results. Hereafter the CCSD(T) method with aug-cc-pVQZ basis set is chosen for further investigation of this system.

At the CCSD(T)/aug-cc-pVQZ level of theory, Mulliken population analysis shows that 62.9% of the total charge resides on hydrogen and the rest is distributed on He

(13.5%) and Ne (23.6%). Significant charge delocalization in the $[\mathrm{HeHNe}]^+$ system suggests a stronger binding interaction between the rare gas and hydrogen. Here it is to be mentioned that the Mayer bond orders estimated for the $[\mathrm{HeHNe}]^+$ system at CCSD(T)/aug-cc-pVQZ level are 0.32 and 0.36 for HeH and NeH bonds, respectively.

3.2.1.2 The local minima

Two other possible linear conformations, He-Ne-H and Ne-He-H, are explored in the present study and those have been found to be the local potential minima, alongside the most stable He-H-Ne configuration for the $[\mathrm{HeHNe}]^+$ system. The structures $[\mathrm{NeHeH}]^+$ and $[\mathrm{HeNeH}]^+$ are energetically higher by 5954.1 cm^{-1} and 4047.5 cm^{-1}, respectively, than the most stable $[\mathrm{HeHNe}]^+$ structure. These potential minima are characterized to be the true minima by computing the harmonic vibrational frequencies for those locally optimized geometries. All the four fundamental frequencies for each minimum are found to be real. Different parameters for the two local potential minima are tabulated in Table 3.2.

TABLE 3.2: Bond lengths (in a.u.), dissociation energies (in cm^{-1}) and charges computed at CCSD(T)/aug-cc-pVQZ level for the two local minima $[\mathrm{RgRg'H}]^+$.

Parameter	$[\mathrm{NeHeH}]^+$	$[\mathrm{HeNeH}]^+$
$R_{\mathrm{eq}}(\mathrm{RgRg'})$	4.127	4.770
$R_{\mathrm{eq}}(\mathrm{Rg'H})$	1.458	1.871
$D_e(\mathrm{RgRg'}+\mathrm{H}^+)$	16919.2	18825.8
$D_e(\mathrm{Rg}+\mathrm{Rg'H}^+)$	474.43	154.27
Charge on		
Ne	0.003	0.256
He	0.375	-0.003
H	0.623	0.746

Due to small amount of charge delocalization, the binding interactions between Ne and He in both the molecules are much larger compared to that in NeHe diatom (D_e = 14.5 cm^{-1}). Larger polarizability of Ne, in addition to a greater charge accumulation on He, results in a much stronger interaction between Ne and He. This leads to a smaller Ne-He bond length in $[\mathrm{NeHeH}]^+$. It is found that the Rg-H bond lengths in these two local minima are very close to those in RgH^+ diatoms. This findings are in good agreement with the previous study on $\mathrm{Ar_2H}^+$ by Qu et al. in which the Ar-Ar bond distance in $[\mathrm{ArArH}]^+$ is much smaller than argon dimer and the ArH bond length in $[\mathrm{ArArH}]^+$ is very close to that in ArH^+ diatom.[10]

3.2.2 Generation of the global PES

After getting an understanding of the possible potential minima, potential energies were computed for the atoms, diatoms and the triatom to construct the global PES for $[\mathrm{HeHNe}]^+$. A large number of *ab initio* energies were computed for different geometries of the diatoms (HeH^+, NeH^+ and HeNe) and for different arrangements of the triatom. All the electronic structure calculations were carried out in the ground electronic states of the fragments by using the CCSD(T) method with aug-cc-pVQZ basis set. The ORCA[17] software was used to perform all the *ab initio* electronic energy calculations.

For NeH^+, *ab initio* energies at 264 points were computed between 0.65 and 16 Å. Similarly, energies were calculated at 248 points between 0.47 and 16 Å for HeH^+. In both the cases, dense grids were set up around the equilibrium regions. As the interaction energy between Ne and He in HeNe is much less than the energies of NeH^+ and HeH^+ diatoms, *ab initio* energies were calculated at a large number of bond distances (344) in the range of 1.2 to 11 Å for construction of a smooth PES.

For the $[\mathrm{HeHNe}]^+$ triatom, electronic energy calculations were performed on a discrete grid based on internal coordinates ($R_{\mathrm{HeH}}, R_{\mathrm{NeH}}, R_{\mathrm{HeNe}}$ and θ), where R_i denotes the bond distance of the 'i' bond and θ is the Ne-H-He bond angle. The grid was set by varying R_{HeH} and R_{NeH} for a fixed θ values. The values of R_{NeH} were varied between 0.7 to 11.0 Å whereas R_{HeH} covered a range of 0.5 to 10.5 Å . The Ne-H-He bond angle was varied from 0° to 180° at an interval of 15°. Before setting up the R_i grids, constrained optimizations were performed for each θ and more points were taken into consideration around the constrained optimized geometries. Dense grids were also set up around the diatomic equilibrium geometries. To calculate the energies at $\theta = 0°$, $(R_{\mathrm{HeNe}}, R_{\mathrm{NeH}})$ and $(R_{\mathrm{HeNe}}, R_{\mathrm{HeH}})$ combinations were varied for He-Ne-H and Ne-He-H geometries, respectively. Finally, more than 20000 *ab initio* energies for the triatom were calculated covering all the important regions of the triatomic system.

TABLE 3.3: Parameters of the Aguado-Paniagua polynomial for the two body interaction energies ($V_i^{(2)}$).

Parameters	HeH^+	NeH^+	HeNe
c_0	1928.8647149280291	10010.896275848216	5622.97417024460
α_0	3.4928794652251156	3.3483677957690130	1.04573444442299
c_1	-15.581993278596640	-9.3447534825870378	-1.18521572026116
c_2	262.37466535009980	116.03550141257479	-413.012666796311
c_3	-5565.5510811043559	-2010.9890658935144	1707.33054915569
c_4	46961.836972713761	14127.141405578808	-36504.6922006954
c_5	-238939.83828430148	-59131.126310593238	311059.316641554
c_6	576489.63222197210	111805.30487240586	-1672221.15734755
c_7	-74460.272530127637	-8418.3470528068265	5633064.66936805
c_8	-2929374.5265850341	-374011.68900047976	-11582801.6645500
c_9	6281788.8629268110	655749.29223833478	13293260.4721444
c_{10}	-4311467.8458768912	-376266.85107707954	-6530813.73136487
$\beta^{(2)}$	0.86935966399465636	0.69348581311832036	0.751203362026533

The *ab initio* energies for all the diatoms were fitted to the Aguado-Paniagua functional form for two-body interactions and the triatomic *ab initio* energies were fitted to Aguado-Paniagua functional form for the 3B interaction energy. The expression of those functional forms are given in Eq. 2.17 and 2.18 (see Chapter 2). The order of all the polynomial functions was 10 (M = 10). For the 3B interaction energy fitting purposes, configurations with energies smaller than 60 kcal/mol (zero energy was set to the all atom dissociation limit energy for the system, i.e., He, Ne, H^+ are well separated) are used in the fitting procedure with a total number of 19605 *ab initio* energies. The Levenberg-Marquardt method for nonlinear multidimensional fitting was applied to determine the linear and nonlinear parameters of the functional form for the two and three body interaction energies. Finally, a smooth analytical potential energy surface for the $[HeHNe]^+$ is constructed. The linear and nonlinear parameters of the functional forms obtained from fitting are tabulated in Tables 3.3 and 3.4 for the diatoms and the triatom, respectively. The root mean square (rms) error in the fitting of three two-body interaction energies for the three diatoms NeH^+, HeH^+ and HeNe were 0.0044, 0.006 and 0.00021 kcal/mol, respectively. The rms error in the fitting of 3B interaction energies was 0.03 kcal/mol and the maximum energy deviation was 0.26 kcal/mol, compared to the *ab initio* data.

TABLE 3.4: Parameters of the Aguado-Paniagua polynomial for the three body interaction energies ($V^{(3)}$).

i	j	k	d_{ijk}	i	j	k	d_{ijk}
0	1	1	29.401388900327717	2	4	0	7177753.3496083068
0	1	2	-1296.9418664393650	2	4	1	33629699.920949832
0	1	3	22540.662563815556	2	4	2	83721866.197407231
0	1	4	-188728.36096246928	2	4	3	-479659380.66042233
0	1	5	353252.58814284584	2	4	4	-1942809393.1516564
0	1	6	-198033.87416499772	2	5	0	-43409993.335663222
0	1	7	-2348741.1963158376	2	5	1	-92848776.744525254
0	1	8	22024059.399422932	2	5	2	27726648.926211968
0	1	9	-62762616.314761110	2	5	3	1473654041.9685616
0	2	1	-1262.2055021852364	2	6	0	166780850.01279530
0	2	2	10891.265472271542	2	6	1	273559332.92902529
0	2	3	-604163.09943166596	2	6	2	-87845712.435403123
0	2	4	2812556.8189085838	2	7	0	-360512678.39584810
0	2	5	-2734332.1790066333	2	7	1	-399330337.35688132
0	2	6	7834135.6597158872	2	8	0	325395351.64491868
0	2	7	-55250233.748965532	3	0	1	-50808.951683938307
0	2	8	213362198.41857028	3	0	2	321953.13181340595
0	3	1	4767.3169888260527	3	0	3	178174.59078361743
0	3	2	649878.87506340654	3	0	4	10925844.423959505
0	3	3	5725762.2064002287	3	0	5	-66529418.086936906
0	3	4	-29994366.719448105	3	0	6	-56712781.722395808
0	3	5	-1435988.8212036870	3	0	7	393704577.39923900
0	3	6	-8955324.6702323575	3	1	0	41585.410172248565
0	3	7	-220826292.98946282	3	1	1	440154.37494582968
0	4	1	59559.623802076683	3	1	2	817939.43006925180
0	4	2	-13474517.372176750	3	1	3	18476147.901873346
0	4	3	-16977447.032129489	3	1	4	-34334757.901437141
0	4	4	182128917.73384547	3	1	5	188653655.91005239
0	4	5	132056362.84548485	3	1	6	-1832870226.7924368
0	4	6	207570202.81619227	3	2	0	-480395.94362830289
0	5	1	3288.7067881069001	3	2	1	-6389030.1186515102
0	5	2	104806492.78595266	3	2	2	-29342145.560721800
0	5	3	-52453054.194073260	3	2	3	-43814313.785489254
0	5	4	-626499826.06479275	3	2	4	75491663.994186610
0	5	5	-450478148.26489103	3	2	5	2428755406.3189230
0	6	1	-6754292.8138293549	3	3	0	3672726.3140310892
0	6	2	-398209843.67775339	3	3	1	47031199.535419323
0	6	3	405052346.46791804	3	3	2	161242455.16073567
0	6	4	908492214.71112490	3	3	3	-196218922.23477942
0	7	1	45557847.698509477	3	3	4	-771792141.45371330
0	7	2	737304344.77073050	3	4	0	-15201589.105899647
0	7	3	-632894894.80105162	3	4	1	-100209411.87289801

i	j	k	d_{ijk}	i	j	k	d_{ijk}
0	8	1	-117185257.20913310	3	4	2	109418540.09923045
0	8	2	-528230047.43367767	3	4	3	1157984991.5718584
0	9	1	108080824.22113840	3	5	0	24191367.018954642
1	0	1	-106.49101185808340	3	5	1	-153432901.11699903
1	0	2	2583.3118334952842	3	5	2	-1084400621.1198349
1	0	3	-40298.514777645796	3	6	0	-3060732.2872198583
1	0	4	418733.13925838965	3	6	1	420864266.62071389
1	0	5	-3026637.1574612018	3	7	0	-7048478.6771669025
1	0	6	19778303.907903410	4	0	1	512420.83950627758
1	0	7	-86740091.362687588	4	0	2	-2755802.6775338589
1	0	8	165786413.47268289	4	0	3	-7144385.2132045291
1	0	9	-62214097.362931266	4	0	4	20094553.808676954
1	1	0	125.74012133064285	4	0	5	165488707.26631927
1	1	1	4560.2210808189857	4	0	6	-272940106.86940044
1	1	2	-11279.076817675625	4	1	0	-370479.42370594107
1	1	3	702548.10256521031	4	1	1	-1705071.5697457660
1	1	4	-463447.96962474973	4	1	2	-2528388.1631883327
1	1	5	-6467963.9854645133	4	1	3	-28239316.999185029
1	1	6	58726042.897073373	4	1	4	-6421054.7280167937
1	1	7	-130703503.91998094	4	1	5	1284194784.8099380
1	1	8	-110707729.04224931	4	2	0	2851691.0969757666
1	2	0	-6918.0978008282918	4	2	1	15561882.283871844
1	2	1	-55807.200497740945	4	2	2	16286339.753729250
1	2	2	-564186.62994106906	4	2	3	-47404707.868829079
1	2	3	-7183130.2741509974	4	2	4	-2285014251.2586632
1	2	4	5948116.6461703954	4	3	0	-14322268.385460928
1	2	5	-66016702.116928674	4	3	1	-111390055.22025426
1	2	6	216405280.47579721	4	3	2	-174825853.14125437
1	2	7	-206290319.71715870	4	3	3	760961651.80980897
1	3	0	185011.47110412605	4	4	0	42375253.165770061
1	3	1	473444.49760805175	4	4	1	220871129.78179464
1	3	2	12317904.459616361	4	4	2	-180240795.07055447
1	3	3	57330500.890587978	4	5	0	-15585106.138677761
1	3	4	69481146.137937084	4	5	1	229960922.91196018
1	3	5	-86092304.002120048	4	6	0	-75397172.209207401
1	3	6	352325388.58172435	5	0	1	-3010386.1340469159
1	4	0	-2618335.3471910381	5	0	2	14670082.126917565
1	4	1	-6095565.8470616695	5	0	3	9592736.6952830814
1	4	2	-125785288.02159514	5	0	4	-118395889.85827667
1	4	3	-376320690.23881119	5	0	5	4444117.4649282582
1	4	4	-433122541.21593308	5	1	0	1950703.7660719184
1	4	5	-11013675.466494743	5	1	1	4319186.9931372842
1	5	0	21804357.006859083	5	1	2	6263767.8473505965
1	5	1	66840785.971975811	5	1	3	12348240.847091896
1	5	2	724789236.03364551	5	1	4	-516965678.57813221

i	j	k	d_{ijk}	i	j	k	d_{ijk}
1	5	3	1476341162.7529128	5	2	0	-9551591.2532756627
1	5	4	1032264771.6087192	5	2	1	2554298.6632750100
1	6	0	-110607621.12257834	5	2	2	150600874.14624885
1	6	1	-381135111.68742919	5	2	3	1077417621.6728218
1	6	2	-2158742254.6848145	5	3	0	26473528.319913082
1	6	3	-2339035892.1825480	5	3	1	45215806.813168898
1	7	0	335916964.09064275	5	3	2	-255463103.27244401
1	7	1	1029814917.3862942	5	4	0	-66080006.166879371
1	7	2	2531881400.9652524	5	4	1	-181767982.22723979
1	8	0	-561020794.03561461	5	5	0	23596007.917076141
1	8	1	-1059417799.4338503	6	0	1	10481025.826980447
1	9	0	396125911.92746419	6	0	2	-40176509.432312474
2	0	1	2940.2875753854887	6	0	3	24584384.262703493
2	0	2	-34949.999023874181	6	0	4	85983011.012536749
2	0	3	302082.35034684086	6	1	0	-6337682.2271359600
2	0	4	-3047795.3590782573	6	1	1	-10862453.169061266
2	0	5	5671308.4934995249	6	1	2	-17589571.987971280
2	0	6	28011097.507422958	6	1	3	120846547.86715606
2	0	7	3110779.0836296491	6	2	0	18183744.095359690
2	0	8	-269921790.74278897	6	2	1	-63916608.900251538
2	1	0	-2548.0870573869615	6	2	2	-436614715.74180472
2	1	1	-59217.277097843500	6	3	0	-11243616.652396157
2	1	2	-132834.51505271340	6	3	1	154343944.33187070
2	1	3	-4488533.7974142311	6	4	0	32036564.318107434
2	1	4	9460538.8857390787	7	0	1	-21446320.813172121
2	1	5	-31389119.783987246	7	0	2	52559214.100490682
2	1	6	-66197033.506211221	7	0	3	-38800760.026265062
2	1	7	1231404432.9806399	7	1	0	12613516.840444585
2	2	0	53231.931518235288	7	1	1	22452791.292191036
2	2	1	1104452.0266506213	7	1	2	13193283.349221652
2	2	2	6124676.3742512288	7	2	0	-19778996.460155182
2	2	3	21362722.580826093	7	2	1	84925552.593754753
2	2	4	7422802.8871864276	7	3	0	-16990346.864424918
2	2	5	-200405053.56715384	8	0	1	23951661.307416294
2	2	6	-1264012190.1642160	8	0	2	-26113122.994459428
2	3	0	-770232.96101471933	8	1	0	-14170534.844520021
2	3	1	-8803647.0810316056	8	1	1	-20050506.829071987
2	3	2	-42075800.559997357	8	2	0	10111792.400431175
2	3	3	-47628437.236839704	9	0	1	-11303017.513076708
2	3	4	598510218.86310804	9	1	0	6896980.4576004297
2	3	5	621350601.68473482	$\beta^{(3)}_{NeH}$			0.87007057935201182
$\beta^{(3)}_{HeH}$			1.1322876326557689	$\beta^{(3)}_{HeNe}$			0.89776363232028489

3.2.3 Global analytical PES

The contour plots of the analytical PES for six different He-H-Ne angles are shown in Figure 3.2. The change in the topology of the PES with respect to the He-H-Ne angle is clearly observed in the figure. A potential well can be seen for near-collinear arrangements of He-H-Ne and the deepest potential well is formed for $\angle$ HeHNe $= 180°$. This geometry corresponds to the equilibrium geometry of the $[\mathrm{HeHNe}]^+$ system. As the angle decreases, the well depth starts decreasing, and a barrier starts appearing at $\angle$ HeHNe $= 90°$.

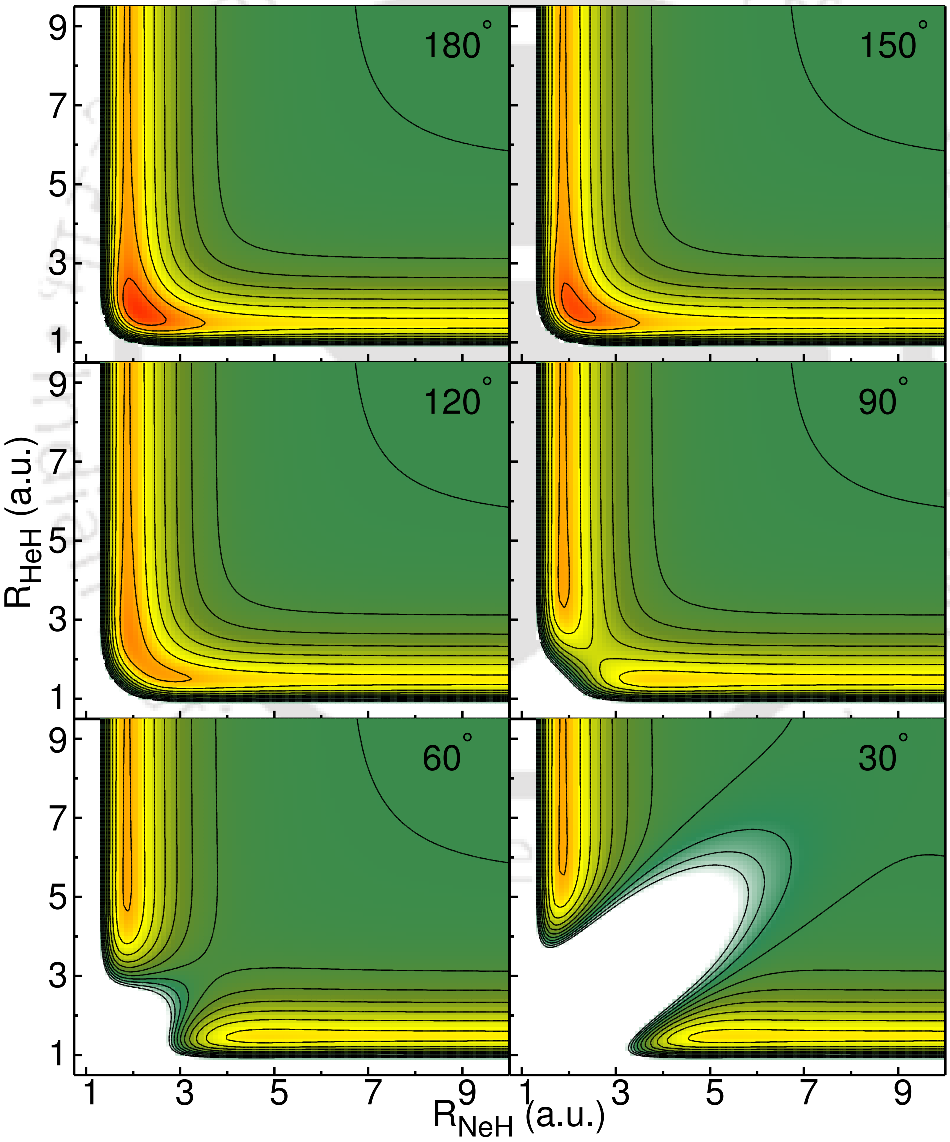

FIGURE 3.2: Contour plots of the analytical potential energy surface for six different He-H-Ne angles. The spacing between the contour lines is 7.5 kcal/mol.

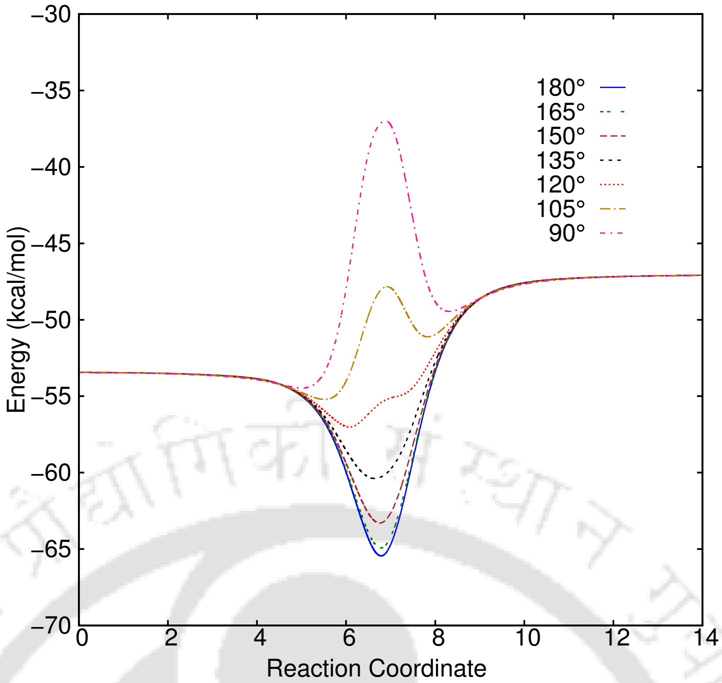

FIGURE 3.3: Minimum energy pathways for different He-H-Ne angles. Reaction coordinate has an arbitrary unit of length. Zero of energy is set to the all atom dissociation limit energy for the system.

In Figure 3.3, the minimum energy pathways for different He-H-Ne angles are plotted. The MEP for the collinear arrangement goes through the deepest potential energy well, which is the global minimum of the $[\mathrm{HeHNe}]^+$ system. The depth of the well is about 12.01 kcal/mol with respect to the He+NeH$^+$ asymptote and it is located at $R_{\mathrm{HeH}} = 1.804$ a.u. and $R_{\mathrm{NeH}} = 2.102$ a.u. The well depth decreases to 9.867 kcal/mol when the He-H-Ne angle becomes 150°. For 105°, a barrier is seen in the MEP and this barrier height increases for 90°. Harmonic vibrational frequencies for the most stable structure of $[\mathrm{HeHNe}]^+$ are calculated numerically by means of *ab initio* computation as well as from the analytical PES. The structural and energetic details of the equilibrium geometries for the diatoms and the triatomic system obtained via *ab initio* computations and calculated from the analytical PES are tabulated in Table 3.5 along with the harmonic vibrational frequencies of the triatom at the equilibrium geometry. The fundamental modes with degenerate energies correspond to the bent vibrational modes and the highest stretching frequency corresponds to the asymmetric stretching mode, where two bonds vibrate simultaneously with opposite atomic motions (while one bond is elongating the other is contracting). A very good agreement between the parameters obtained from *ab initio* computation and from the analytical PES is quite obvious in Table 3.5.

TABLE 3.5: Equilibrium bond lengths (in a.u.) and energies (in kcal/mol) at equilibrium geometries of diatoms and triatom and harmonic vibrational frequencies (in cm^{-1}) of the triatom at the most stable geometry. Zero of energy is the same as Figure 3.3.

		ab initio	analytical PES
HeH$^+$	R_{eq}	1.464	1.464
	Energy	-47.066	-47.066
NeH$^+$	R_{eq}	1.872	1.872
	Energy	-53.433	-53.433
HeNe	R_{eq}	5.696	5.684
	Energy	-0.0484	-0.0485
[HeHNe]$^+$	R_{eq}(HeH)	1.804	1.804
	R_{eq}(NeH)	2.102	2.102
	∠HeHNe	180.0	180.0
	Energy	-65.447	-65.447
	Harmonic vibrational frequencies	853.8, 853.8, 855.8, 1602.5	848.8, 848.8, 856.0, 1605.3

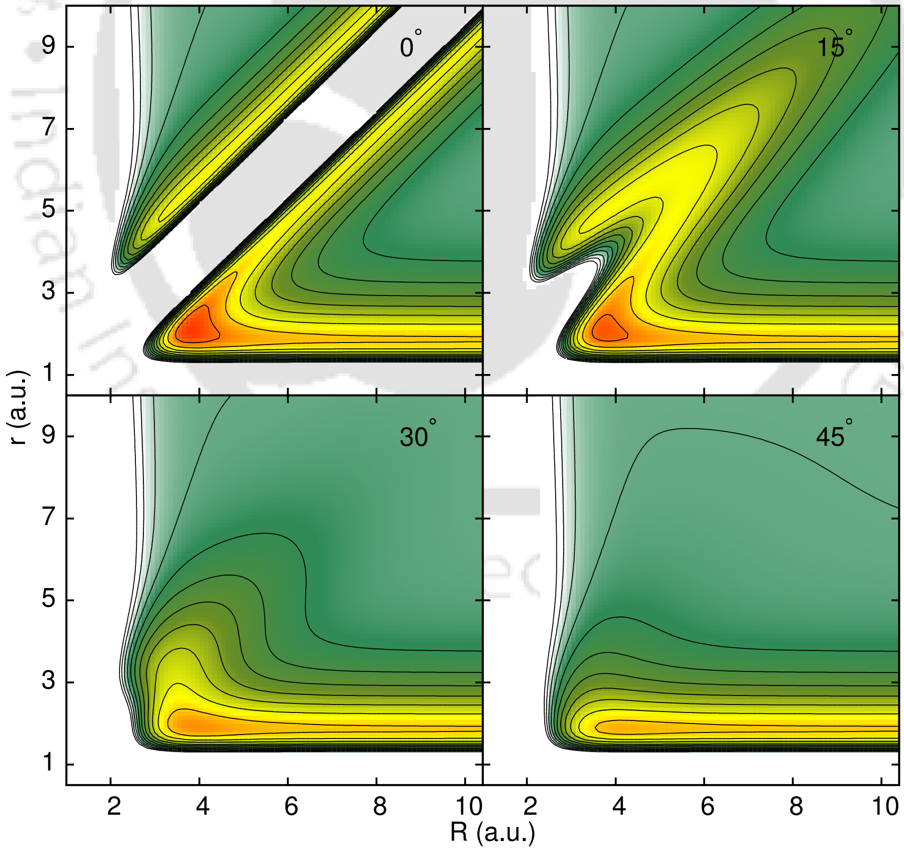

FIGURE 3.4: Contour diagrams of the analytical PES in reactant Jacobi coordinates for the He+NeH$^+$ reactive system for different θ. The spacing between the contour lines is 7.5 kcal/mol.

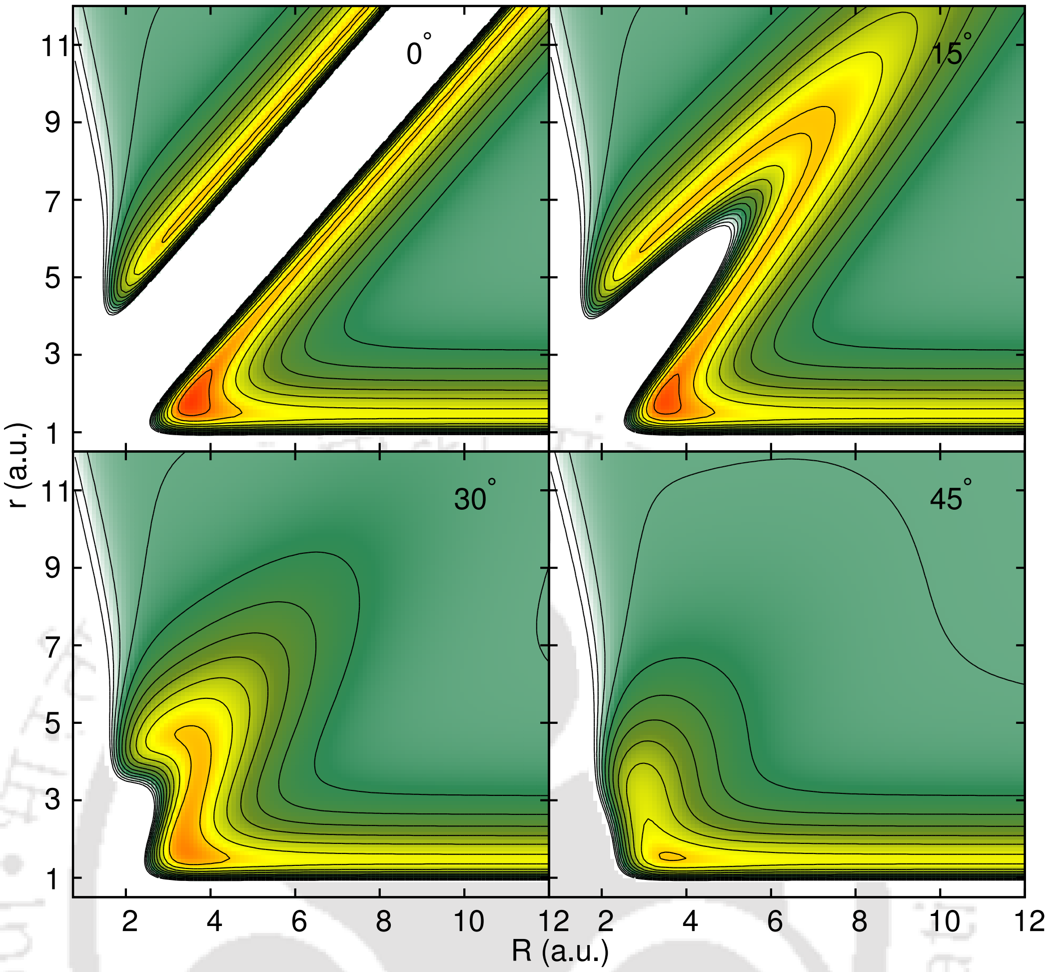

FIGURE 3.5: Same as Figure 3.4 but in terms of Ne+HeH$^+$ reactant Jacobi coordinates.

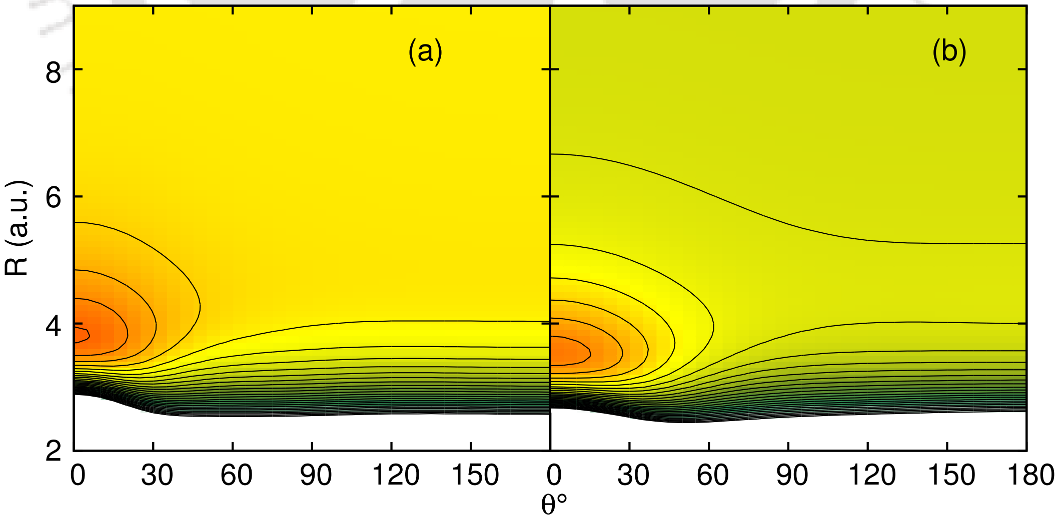

FIGURE 3.6: Contour diagrams of the analytical PES in reactant Jacobi coordinates. r is kept constant at r_{eq}. (a) He+NeH$^+$ system, r_{eq} = 1.872 a.u. (b) Ne+HeH$^+$ system, r_{eq} = 1.464 a.u. The spacing between the contour lines is 2.5 kcal/mol.

In Figures 3.4, 3.5 and 3.6, the contour diagrams of the analytical PES are presented in reactant Jacobi coordinates for the two reactive collision systems. It is clear from these figures that both the He+NeH$^+$ and Ne+HeH$^+$ systems prefer collinear and near-collinear paths for a reactive collision. While the He + NeH$^+$ $\rightarrow$ Ne + HeH$^+$ reaction has a late barrier (barrier height corresponds to the endothermicity of the reaction), Ne + HeH$^+$ $\rightarrow$ He + NeH$^+$ reaction is exothermic and barrierless in nature. For larger attacking angles, both the reactions fail to occur.

The energies obtained from the analytical PES for different geometries which include short range and long range and potential well regions are plotted along with their *ab initio* counterparts in Figure 3.7. As can be seen in Figure 3.7, there is an excellent agreement between the *ab initio* and analytical energies. Hence, it is worth mentioning that the analytical surface successfully describes the asymptotic regions as well as the interaction regions of the [HeHNe]$^+$ system with high accuracy. To further check the accuracy of the analytical PES, *ab initio* energies of 422 randomly distributed points are calculated and compared with the analytical values. Figure 3.8 shows the difference between the *ab initio* and analytical energies with respect to the total energies for those random points. The largest deviation has been found to be 0.083 kcal/mol and the rms error is less than 0.023 kcal/mol.

As mentioned earlier, two local potential minima corresponding to collinear He-Ne-H and Ne-He-H configurations were characterized by *ab initio* calculations. Those two minima are also found in the analytical PES. The local minimum [HeNeH]$^+$ is energetically 4050.9 cm^{-1} higher than the most stable structure. This is in excellent agreement with the *ab initio* energy difference (4047.5 cm^{-1}) between the local minimum [HeNeH]$^+$ and the global minimum. The HeNe and NeH$^+$ bond lengths in [HeNeH]$^+$ are 4.822 and 1.871 a_0, respectively. The HeNe and HeH$^+$ bond distances for the second local minimum [NeHeH]$^+$ are 4.128 and 1.458 a_0, respectively. This local minimum is located at 5959.1 cm^{-1} high in energy with respect to the global minimum and it is close to the *ab initio* value 5954.1 cm^{-1}.

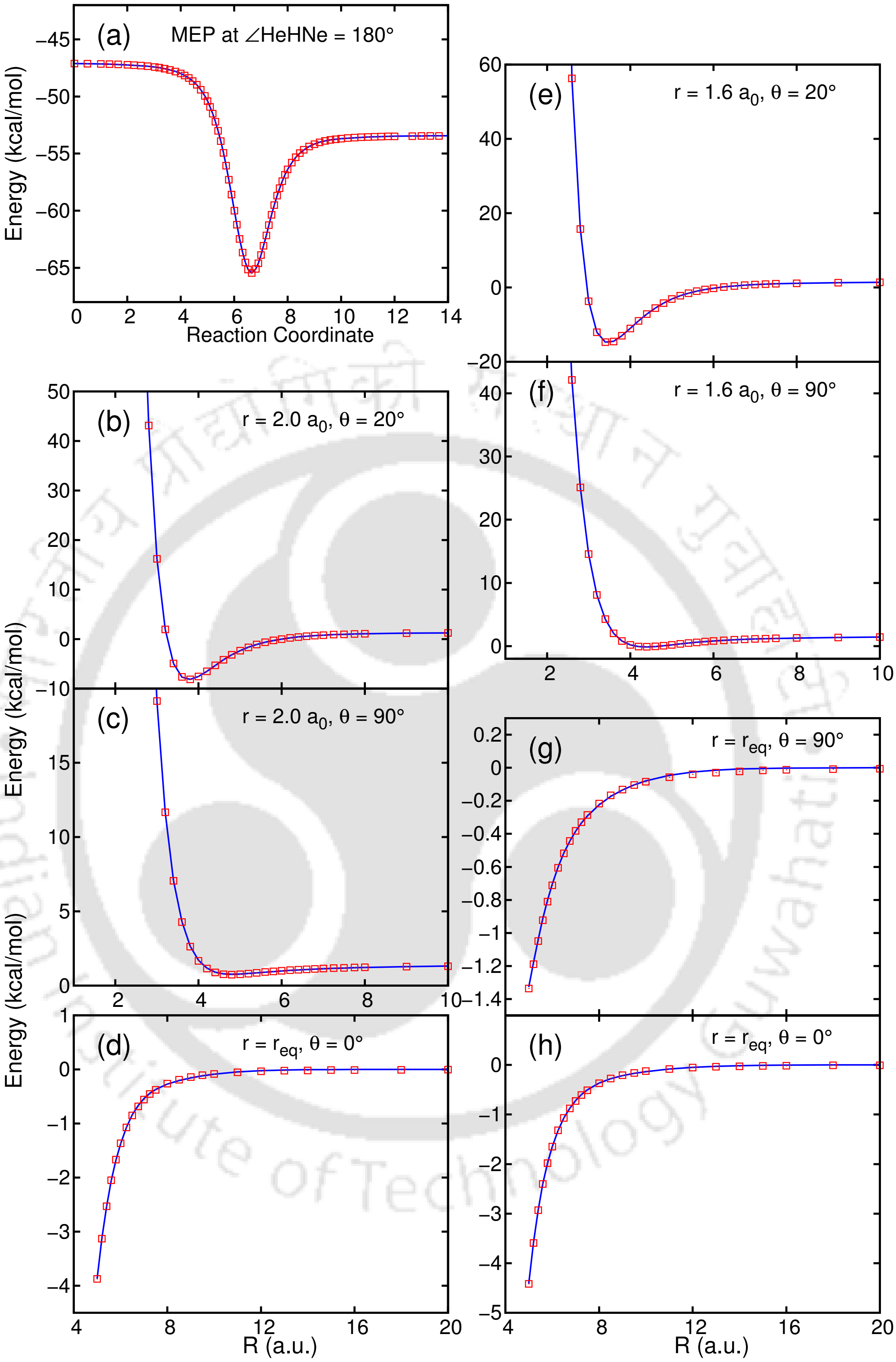

FIGURE 3.7: Comparison between *ab initio* energies (square points) and analytical energies (solid lines): (a) along the collinear MEP as presented in Figure 3.3, (b, c, d) in He+NeH$^+$ reactant Jacobi coordinates and (e, f, g, h) in Ne+HeH$^+$ reactant Jacobi coordinates. Zero of energy for (a) is the same as defined in Figure 3.3 and it corresponds to the reactant asymptote for the others.

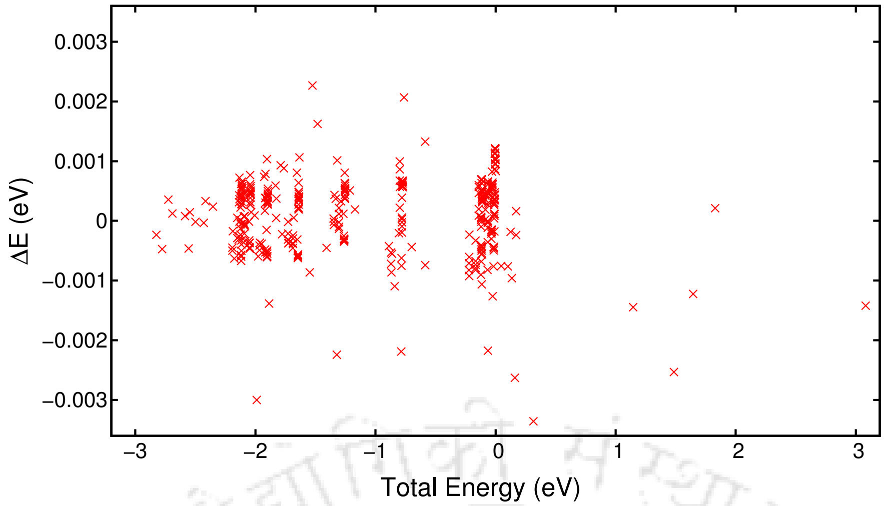

FIGURE 3.8: ΔE, the differences in energies between analytical and *ab initio* values, are plotted against total *ab initio* energy at some random configurations. Zero is set at all atom dissociation limit.

3.2.4 Bound states of $[\mathrm{HeHNe}]^+$ complex

As discussed already, a potential well presents on the ground electronic PES of the $[\mathrm{HeHNe}]^+$ system for collinear and near-collinear arrangements of He-H-Ne. The minimum of the potential well is located energetically 0.521 eV below the He+NeH$^+$ asymptote. This potential well can support a number of bound and quasibound states of the $[\mathrm{HeHNe}]^+$ complex. As determination of the bound states is useful for future experimental studies, the eigen states of the $[\mathrm{HeHNe}]^+$ complex are computed for the $J = 0$ state by using the DVR3D program of Tennyson et al.[20] In addition, a TDWP propagation technique was also used to compute the bound states. The DVR Hamiltonian was formed in the scattering coordinates with 64 and 42 radial Gauss-Laguerre quadrature grid points along R and r coordinates, respectively and 48 Gauss-Legendre quadrature points along the θ coordinate. Total six bound vibrational states are obtained below the dissociation level of the complex and the energies of these six states are tabulated in Table 3.6. The energetically lowest state is lying at 0.2546 eV above the global minimum of the system. The TDWP methodology to calculate the eigen energy spectra is discussed in detail in Chapter 2. The TDWP calculations were carried out in the reactant Jacobi coordinates (R, r, θ) of He+NeH$^+$ system. The initial wave packet was placed at $R = 3.5$ a_0 and $r = 2.0$ a_0 with width parameters $\partial_R = 0.3$ a_0 and $\partial_r = 0.25$ a_0. Split operator technique was employed to propagate the $\Psi(0)$ for 80000 time steps with $\Delta t = 5.0$ a.u. The R and r grids ranged from 0.2 to 16.1 a_0 with 160 points and from 0.3 to 16 a_0 with 144 points, respectively. The angular coordinate consisted of 120 Gauss-Legendre quadrature points. The Hanning window function was used to get a smooth and well resolved spectra. The energy spectrum for $J = 0$ is plotted in Figure 3.9. Total six bound vibrational states as well as a few quasi bound states can be observed in Figure 3.9. The maxima of the energy spectrum correspond to the energies of the eigen states and those are tabulated in Table 3.6 along with the DVR3D results. Both the TIQM and TDQM approaches used here produce the same result for this system.

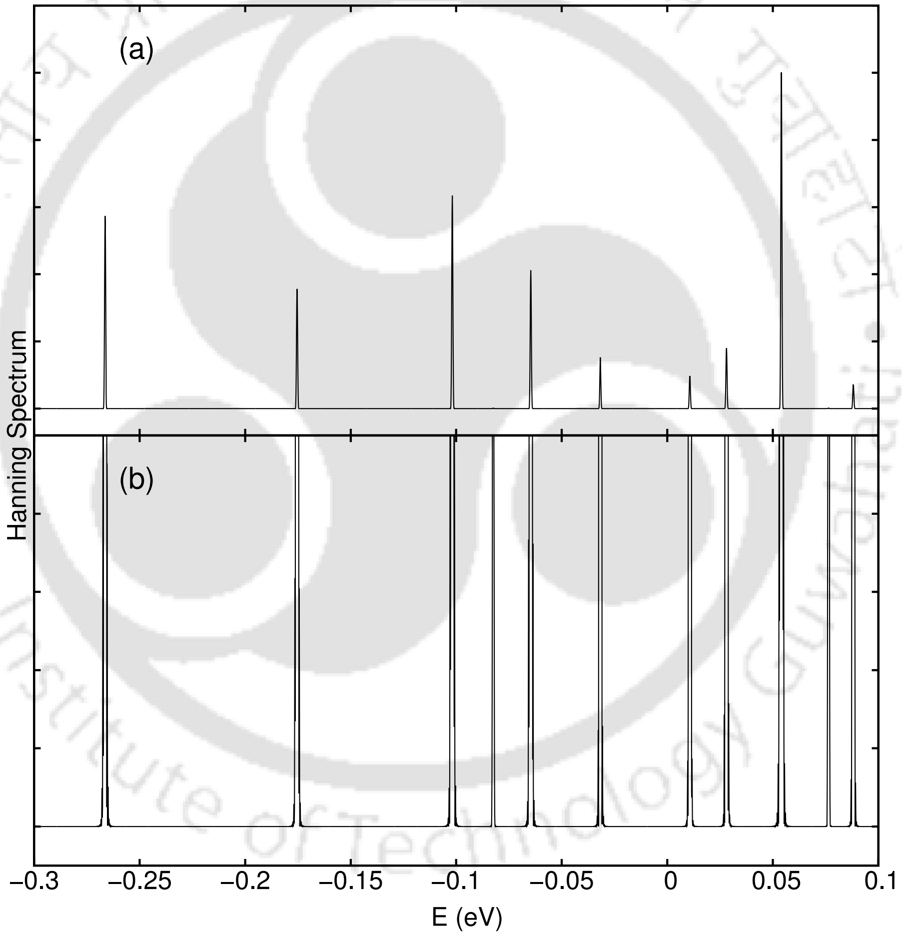

FIGURE 3.9: Eigenvalue spectrum of the $[\mathrm{HeHNe}]^+$ complex obtained from TDWP calculation by using the Hanning window function, showing the bound and quasi-bound states. (a) spectrum, (b) zoomed version of (a). Zero of energy corresponds to He+NeH$^+$ asymptote.

Table 3.6: Energies (in eV) of the bound states of the $[\text{HeHNe}]^+$ complex for $J = 0$, obtained from DVR3D and TDWP calculations. Energy of the He+NeH^+ asymptote is taken as zero.

n	Energy		n	Energy	
	DVR3D	TDWP		DVR3D	TDWP
1	-0.2664	-0.2664	4	-0.0825	-0.0825
2	-0.1754	-0.1754	5	-0.0647	-0.0647
3	-0.1019	-0.1019	6	-0.0317	-0.0317

3.3 THE $[\text{NeHNe}]^+$ SYSTEM

3.3.1 Electronic structure calculations

Ne2H^+ system was earlier explored by Kim and Lee at various levels of theory and CCSD(T)/aug-cc-pVQZ level was concluded to be a very good choice for this system.[2] The same level of theory is applied in this thesis to obtain a global *ab initio* based PES for this system. All the electronic structure calculations were performed by using the Gaussian 09 software.[21] T1 diagnostics value, which is much smaller than 0.02 for this system, makes coupled cluster calculation reliable for this system.

3.3.1.1 The global minimum

Geometry optimization produces a linear centrosymmetric Ne-H-Ne structure with both the NeH bond lengths of 2.156 a_0 as the global minimum for this system. The minimum is confirmed by harmonic vibrational frequencies calculations. Linear centrosymmetric structures were also found as the global minimum for other protonated rare gas dimers e.g., He_2H^+,[2,11] Ar_2H^+, Kr_2H^+ and Xe_2H^+.[5,10,13,14] The global minimum is stable by 70.036, 69.941 and 16.603 kcal/mol with respect to the all atom dissociation limit of the system (i.e., $\text{Ne+H}^+\text{+Ne}$ asymptote), $\text{Ne}_2\text{+H}^+$ asymptote and Ne+NeH^+ asymptote, respectively. Mulliken population analysis performed by ORCA[17] shows a positive charge of 0.178 on each Ne atom and 0.643 on the hydrogen atom. The Mayer bond order of the NeH bond is found to be 0.307.

3.3.1.2 The local minimum and the transition state

A second minimum for the system was also reported for a linear Ne-Ne-H structure by Kim and Lee.[2] However, serious doubt was raised about the real existence of this local minimum because the barrier height for conversion between $[\text{NeNeH}]^+$ and $[\text{NeHNe}]^+$ was found to be reduced to a large extent with the inclusion of core correlation effect. A similar structure was explored as a local minimum for Ar_2H^+ system at the QCISD/6-311++G(3df, 3pd) level of theory by Qu et al.[10] In this study, a stable linear Ne-Ne-H configuration is also found with the bond lengths of 5.0 and 1.87 a_0, for NeNe and NeH, respectively. The Ne-Ne bond dissociation energy for this geometry is 0.774 kcal/mol, which is much larger than that of the neon dimer. Mulliken population analysis shows 74.3 % and 25.2 % of the total positive charge on the hydrogen atom and the adjacent Ne atom, respectively. Thus, partial charge delocalization yields a stronger interaction between the rare gas atoms in $[\text{NeNeH}]^+$.

Like the Ar_2H^+ system,[10] a transition state is also found for the Ne_2H^+ system. The transition state for this system is a bent structure with NeNe bond length of 5.038 a_0, NeH bond length of 1.87 a_0 and an angle of 146.41° between these two bonds. The structure is only 4.4 cm^{-1} higher in energy compared to the $[\text{NeNeH}]^+$ minimum.

3.3.2 Generation of the global PES

Using dense grids around all the important regions of the diatomic potentials, energies at 317 points were computed between 1 and 100 a_0 for NeH^+ and energies at 332 different geometries were evaluated between 2 and 36 a_0 for Ne_2 molecule. Spline interpolation technique was used to get the analytical PES for the diatoms. By doing so, an excellent agreement between the *ab initio* and analytical data has been achieved in the long range interaction part of the diatomic potentials. Later, *ab initio* energies were computed at 110 and 86 randomly sampled points for NeH^+ and Ne_2, respectively and those are compared with interpolated data. The rms deviations of 2.4×10^{-4} kcal/mol and 5×10^{-5} kcal/mol are found for NeH^+ and Ne_2, respectively.

For the triatomic system, electronic energy calculations were carried out on a grid set up using the internal coordinate system, R_1, R_2 and θ. Here R_1 and R_2 are the two Ne-H bond lengths and θ is the Ne-H-Ne angle. Angle θ was varied from 5° to 180° with a uniform spacing of 5° and for each θ, grids were set up for R_1 and R_2 covering regions ranging 1.4 - 20 a_0. Before setting up the R_i grids, constrained optimizations were performed for each θ and more points were taken into consideration around the constrained optimized geometries. Dense grid was also set up for each R_i around their diatomic equilibrium geometry. For $\theta = 0°$, R_1 and R_2 are Ne-Ne and Ne-H bond lengths, respectively. Finally, *ab initio* energies at more than 23000 points were calculated for the triatomic system, which were scattered over all the regions including the important potential well and asymptotic regions for the system.

3B interaction energies were calculated from the triatomic *ab initio* energies and fitted to the Aguado-Paniagua functional form given in Eq. 2.18 (see Chapter 2). Considering the symmetry of the system, ABA type, the fitting resulted in 2 nonlinear and 140 linear parameters for $M = 10$. Energies below 70 kcal/mol (zero was set at all atom dissociation level) were used for the fitting of 3B interaction energies, which results in inclusion of 22537 number of *ab initio* energies. The Levenberg-Marquardt method for nonlinear multidimensional fitting was applied to determine the linear and nonlinear parameters. The parameters thus obtained are tabulated in Table 3.7. The rms error for the overall fitting was 0.026 kcal/mol and the maximum energy deviation was 0.43 kcal/mol. The point of maximum deviation corresponds to a configuration having the two NeH bond distances of 1.5 and 1.6 a.u. with ∠ NeHNe = 165°.

TABLE 3.7: Parameters of the Aguado-Paniagua polynomial for the three body interaction energies ($V^{(3)}$). Here, $d_{ijk} = d_{ikj}$.

i	j	k	d_{ijk}	i	j	k	d_{ijk}
0	1	1	53.071003106215812	2	2	3	107952.92793097142
0	1	2	-651.81129888756220	2	2	4	14144.483422396414
0	1	3	4325.7773110321941	2	2	5	1284315.2851971590
0	1	4	-13573.586668782424	2	2	6	2286118.6967905504
0	1	5	14454.585134774818	2	3	3	1529766.3849390750
0	1	6	34742.462682351274	2	3	4	-2802020.8856470385

i	j	k	d_{ijk}	i	j	k	d_{ijk}
0	1	7	-109185.09193854770	2	3	5	520699.20613647444
0	1	8	67653.739619045431	2	4	4	-2008178.8644883225
0	1	9	8343.2759016146883	3	0	1	793.42671243306472
0	2	2	2489.6919324429637	3	0	2	-8885.9248220824902
0	2	3	1041.7694879017199	3	0	3	3333.5904069095704
0	2	4	-38420.075863668026	3	0	4	-162976.78928976890
0	2	5	111503.02131810467	3	0	5	482127.46466156386
0	2	6	65779.104613187286	3	0	6	1697657.5538350940
0	2	7	-1049100.7703201575	3	0	7	-3195978.3506104900
0	2	8	1527761.3519931249	3	1	1	29572.594475388891
0	3	3	-30679.570433755140	3	1	2	-64390.733326686270
0	3	4	8449.4515631181876	3	1	3	252145.14031606331
0	3	5	281432.44415681693	3	1	4	-1497692.2526150546
0	3	6	-981194.47244129691	3	1	5	54083.150886512267
0	3	7	1391518.7972256471	3	1	6	8434765.5220825560
0	4	4	366521.23029072280	3	2	2	143231.53050347266
0	4	5	-170325.82368410294	3	2	3	986537.86166326795
0	4	6	-1193844.2428007429	3	2	4	-2426517.7532641487
0	5	5	-153408.71895971580	3	2	5	-6600304.3293650467
1	0	1	-5.8522721751503077	3	3	3	466671.51029411191
1	0	2	73.741057155486345	3	3	4	-739243.22072474053
1	0	3	473.89061011496892	4	0	1	-484.97101509290451
1	0	4	-9924.3672028315341	4	0	2	19389.417284579176
1	0	5	33193.322577209066	4	0	3	111999.95128440647
1	0	6	7188.2138545766456	4	0	4	-623684.75244675716
1	0	7	-201826.06321431519	4	0	5	652844.27225332451
1	0	8	352559.16031813051	4	0	6	-3311580.4498963794
1	0	9	-215449.26944888197	4	1	1	9848.0383495962051
1	1	1	556.52543525994520	4	1	2	-110727.84750843747
1	1	2	-4989.6485367035730	4	1	3	1026705.9346197858
1	1	3	26728.905179199144	4	1	4	-3219882.2227872377
1	1	4	-63354.771006018345	4	1	5	7481319.4451027121
1	1	5	-71728.927950921105	4	2	2	298828.59947676450
1	1	6	212242.91605888377	4	2	3	449692.06723180192
1	1	7	931809.47207822767	4	2	4	-20440808.493268516
1	1	8	-1423438.2457749769	4	3	3	43242179.860918522
1	2	2	41914.808041759417	5	0	1	-16690.931812688534
1	2	3	-41909.121526804411	5	0	2	-49424.592612036475
1	2	4	-113825.29301324481	5	0	3	354328.83144929167
1	2	5	312941.96440920082	5	0	4	-1286977.5362286940
1	2	6	478541.94585471641	5	0	5	6021828.3200764339
1	2	7	-2750080.6650076341	5	1	1	29600.555407363063
1	3	3	172336.82697896665	5	1	2	-370471.39338720957
1	3	4	106408.95898420559	5	1	3	4494973.8839001479
1	3	5	-771286.79711408447	5	1	4	-10726362.990844145

i	j	k	d_{ijk}	i	j	k	d_{ijk}
1	3	6	1276293.2826818586	5	2	2	-5883726.2516646478
1	4	4	-3046795.6524720690	5	2	3	4503846.7504064888
1	4	5	5263619.3680815743	6	0	1	34352.954164054448
2	0	1	-39.242831559850842	6	0	2	-354126.34791806905
2	0	2	-1115.1125406753661	6	0	3	1675541.5155915204
2	0	3	11215.214593812520	6	0	4	-6473163.6617297810
2	0	4	-21776.550383127968	6	1	1	3326.8916743204172
2	0	5	45192.796120063715	6	1	2	-1233860.4417850666
2	0	6	-130635.73781592425	6	1	3	16451598.025033951
2	0	7	-536671.49707303802	6	2	2	-20769155.337159246
2	0	8	1326603.7056133337	7	0	1	126675.54187841264
2	1	1	91.144580649965064	7	0	2	-422957.83427982638
2	1	2	-7488.8531595656477	7	0	3	1079300.0330368560
2	1	3	125990.83191542540	7	1	1	783988.74152241717
2	1	4	-284071.22252200852	7	1	2	-3820443.3903748491
2	1	5	-189879.36881566310	8	0	1	13385.721594617236
2	1	6	1701303.5190600508	8	0	2	-441443.71007282333
2	1	7	-4262810.0935674291	8	1	1	7032521.4494804181
2	2	2	-219543.14837477379	9	0	1	-1068103.5681705740
$\beta^{(3)}_{Ne_2}$			0.74906438215787674	$\beta^{(3)}_{NeH}$			0.85637249766504331

3.3.3 Global analytical PES

The contour maps of the analytical PES for four different internal bond angles are presented in Figure 3.10. As the Ne atom approaches to the NeH$^+$ ion in a near collinear path, interactions between the atoms become stronger and a potential well is formed. The potential well reaches its deepest value at a linear Ne-H-Ne configuration, which is the global minimum for the system, located 16.606 kcal/mol below the Ne+NeH$^+$ asymptote and 69.943 kcal/mol below the Ne$_2$+H$^+$ asymptote. This most stable geometry for the Ne$_2$H$^+$ system has been characterized by harmonic frequencies calculated via *ab initio* calculation. The details of the equilibrium geometries for NeH$^+$, Ne$_2$ and Ne$_2$H$^+$ systems and harmonic vibrational frequencies computed via *ab initio* calculations and obtained from the analytical PES are tabulated in Table 3.8. The fundamental modes with degenerate energies correspond to the bent vibrational modes, the largest frequency corresponds to the asymmetric stretching mode and the lowest one corresponds to the symmetric stretching mode. An excellent agreement between the *ab initio* and the analytical results is obvious in Table 3.8.

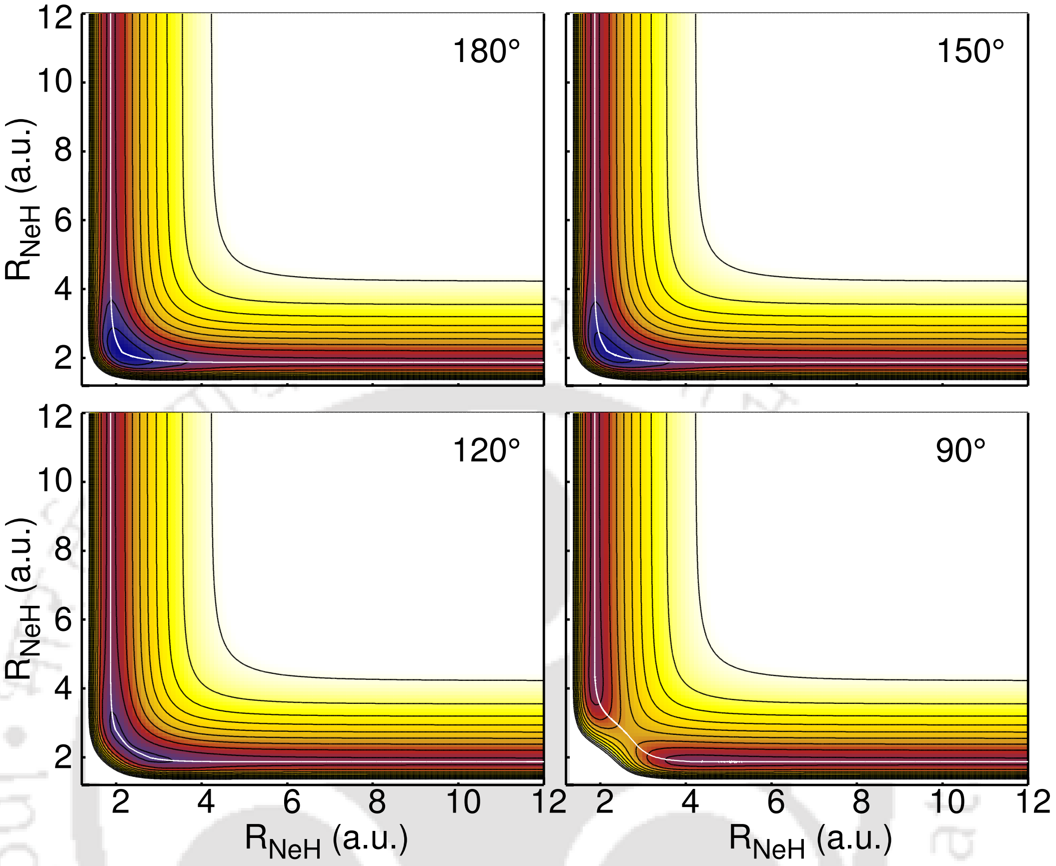

FIGURE 3.10: Contour plots of the analytical PES of Ne_2H^+ system for four different Ne-H-Ne angles. The spacing between the contour lines is 6 kcal/mol. The energy of the Ne+NeH$^+$ reactant asymptote is set as zero. The white lines appearing in the low energy region correspond to the MEPs for different Ne-H-Ne angles.

TABLE 3.8: Equilibrium bond lengths (in a.u.) and energies (in kcal/mol) at equilibrium geometries of diatoms and triatom and harmonic vibrational frequencies (in cm^{-1}) of the triatom at most stable geometry. Energies of the atoms are set as zero.

		ab initio	analytical PES
NeH$^+$	R_{eq}	1.872	1.872
	Energy	-53.433	-53.433
Ne$_2$	R_{eq}	5.845	5.845
	Energy	-0.0952	-0.0952
[NeHNe]$^+$	R_{eq}(NeH)	2.156	2.156
	∠NeHNe	180.0	180.0
	Energy	-70.036	-70.038
	Harmonic vibrational frequencies	513.7,818.5, 818.5,1588.9	514.5,794.7, 794.7,1587.2

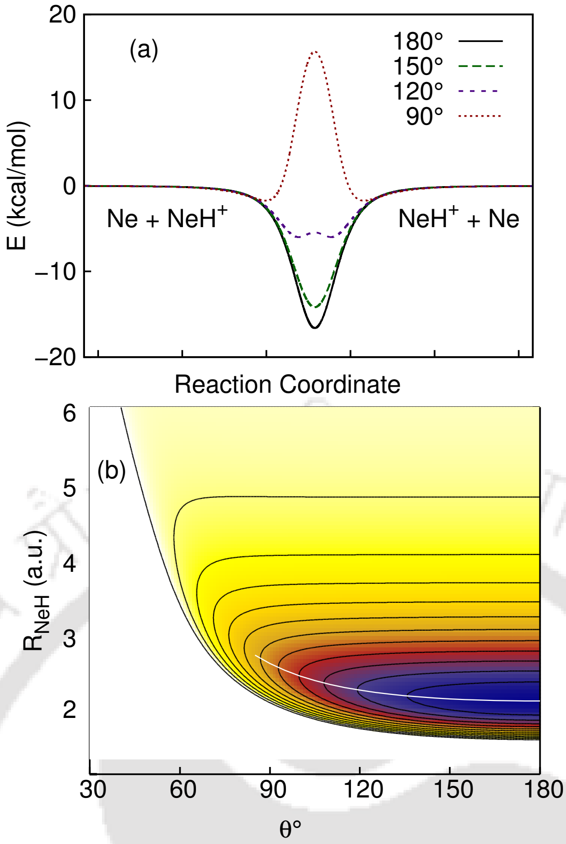

FIGURE 3.11: (a) MEPs connecting Ne + NeH$^+$ reactants with NeH$^+$ + Ne products, for different ∠ NeHNe angles. Reaction coordinate here is defined as the distance covered while the reaction is taking place along the MEP and it is in arbitrary units. (b) Contour plot of the analytical PES with equal NeH bonds for different ∠ NeHNe. The white line represents the MEP along ∠ NeHNe with equal NeH bond distances, i.e., it connects the central points of the MEPs of (a).

The minimum energy paths (MEPs) for different Ne-H-Ne angles are highlighted with white lines in Figure 3.10. These MEPs for different angles of approach are presented in Figure 3.11(a). As can be seen, like [HeHNe]$^+$, for the collinear and near-collinear geometries there exists a potential well. However, the depth of the potential well decreases when the ∠ NeHNe becomes smaller and a barrier appears for small Ne-H-Ne angles. In Figure 3.11(b), contour plot of the interaction potential is presented for different ∠ NeHNe values with equal NeH$^+$ distances. The white line in this figure represents the path of evolvement of the minimum as a function of ∠ NeHNe. It is clear that for small ∠ NeHNe values, the barrier height crosses the all atom dissociation level for the system.

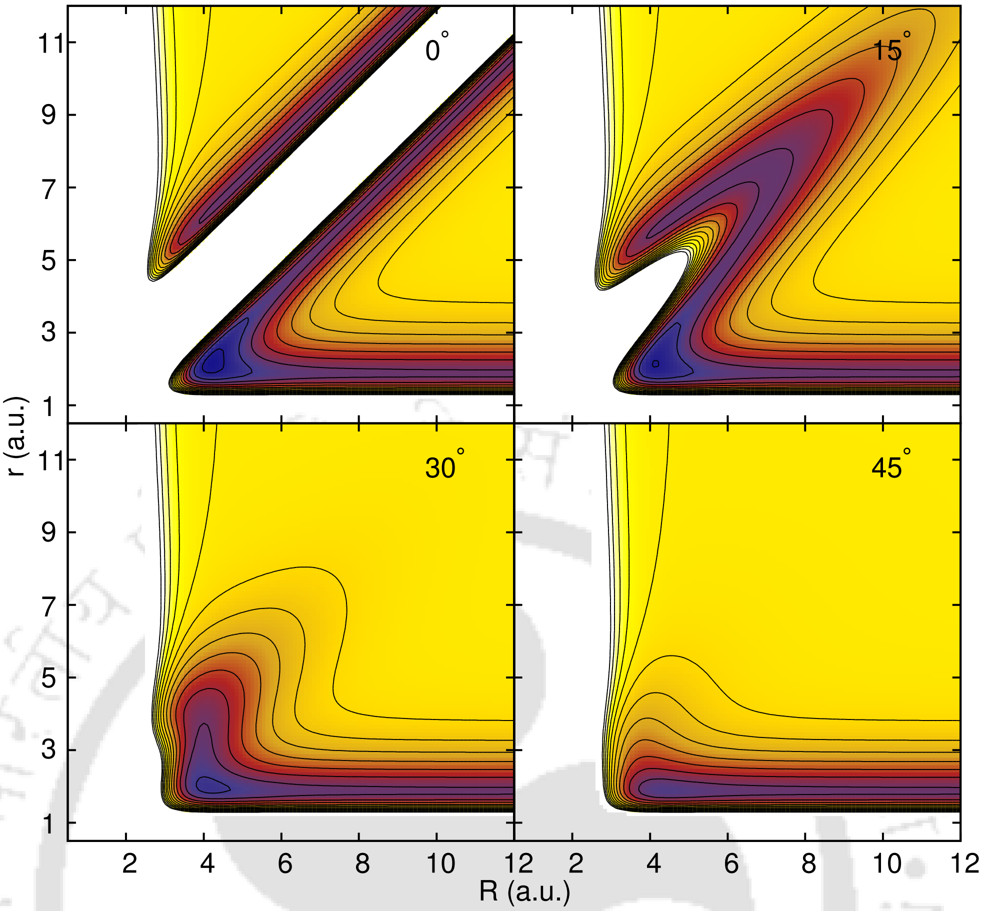

FIGURE 3.12: Contour diagrams of the analytical PES in reactant Jacobi coordinates for the Ne+NeH$^+$ reactive system for different θ values. The spacing between the contour lines is 7.5 kcal/mol.

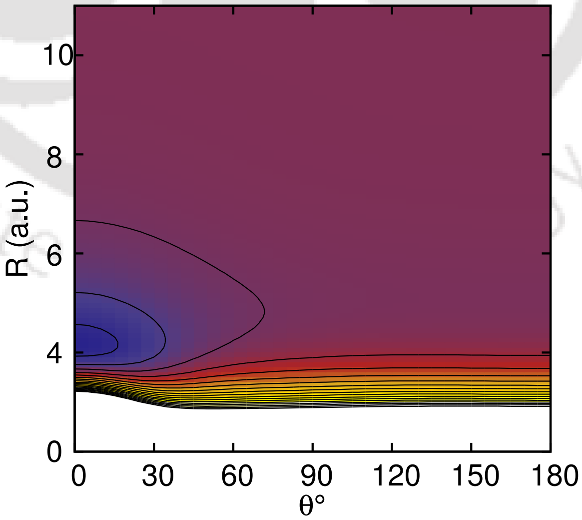

FIGURE 3.13: Contour diagrams of the analytical PES in reactant Jacobi coordinates for the Ne+NeH$^+$ reactive system. r is kept constant at $r_{eq} = 1.8716\ a_0$. The spacing between the contour lines is 5.0 kcal/mol.

In Figures 3.12 and 3.13 the contour maps of the analytical PES is presented in reactant Jacobi coordinates for Ne+NeH$^+$ reactive systems. It can be seen from these figures that the proton transfer reaction between the two Ne atoms is preferably collinear and barrierless. The reaction can not occur for large attacking angles.

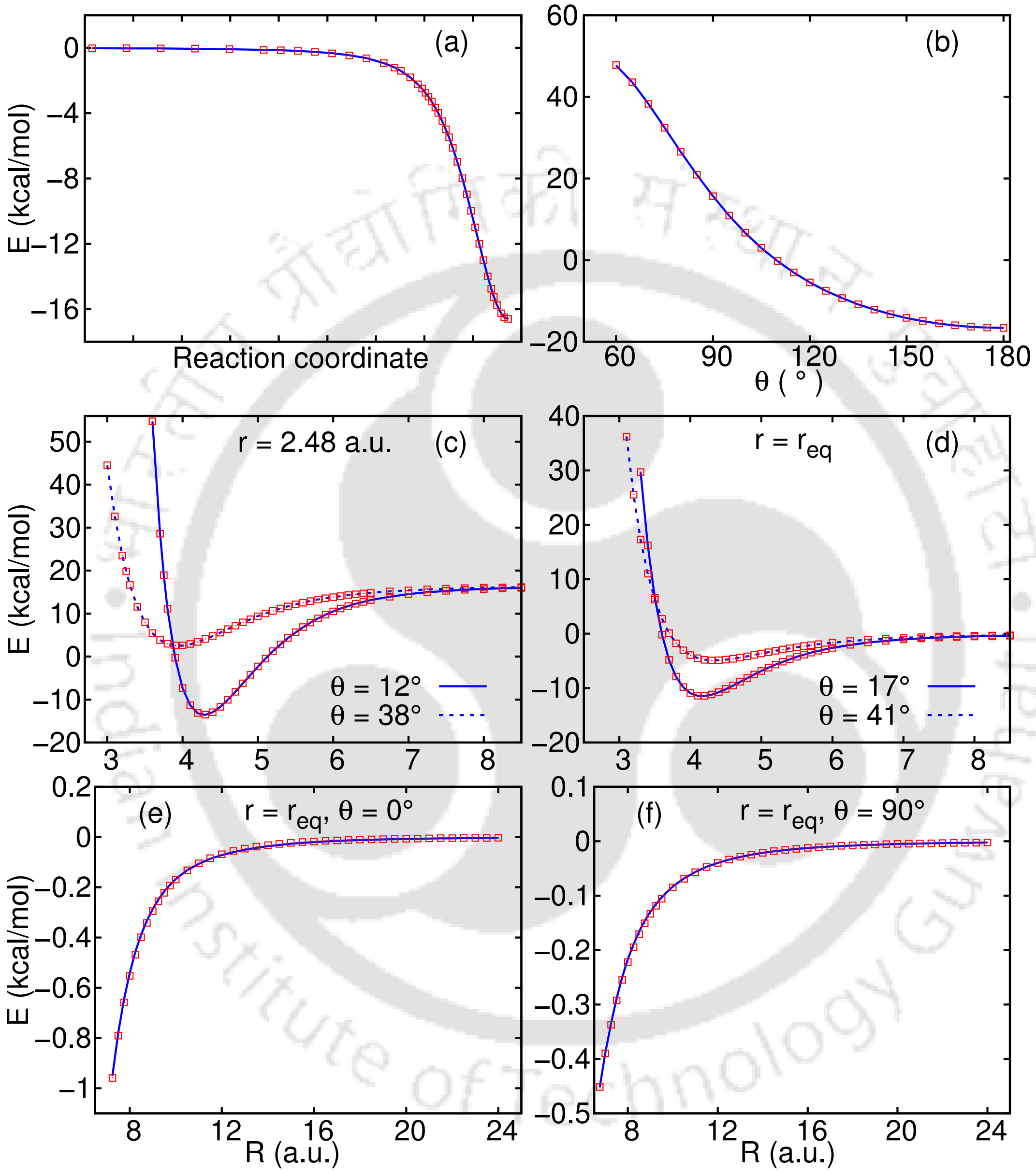

FIGURE 3.14: Comparison between analytical energies (lines) and *ab initio* energies (square points): (a) along the MEP for ∠ NeHNe = 180°; (b) along the white line in Fig. 2(b); (c,d) at different **R** values with fixed r = 2.48 a.u. and r_{eq} (1.8716 a.u.) and θ = 12°, 38°, 17° and 41°; (e,f) at long range interaction region for two different θ values. Reaction coordinate in (a) is the same as in Figure 3.11

The energies obtained from the analytical PES for different configurations including short range and long range regions are plotted along with their *ab initio* counterparts in Figure 3.14. It is quite clear from Figure 3.14 that there is an excellent agreement between the *ab initio* and analytical energies over all the regions of the surface. Finally, energies of 776 random configurations were computed by means of *ab initio* calculations and compared with those obtained from the analytical PES. The rms deviation of the energies was found to be 0.025 kcal/mol while the maximum energy deviation was 0.182 kcal/mol. The differences between analytical and *ab initio* energies for these random configurations are plotted with respect to total energies in Figure 3.15. For most of the geometries, there are very small differences between the analytical and *ab initio* energies. It is quite clear from Figure 3.14 and Figure 3.15 that the analytical PES successfully describes the global *ab initio* PES for Ne_2H^+ system.

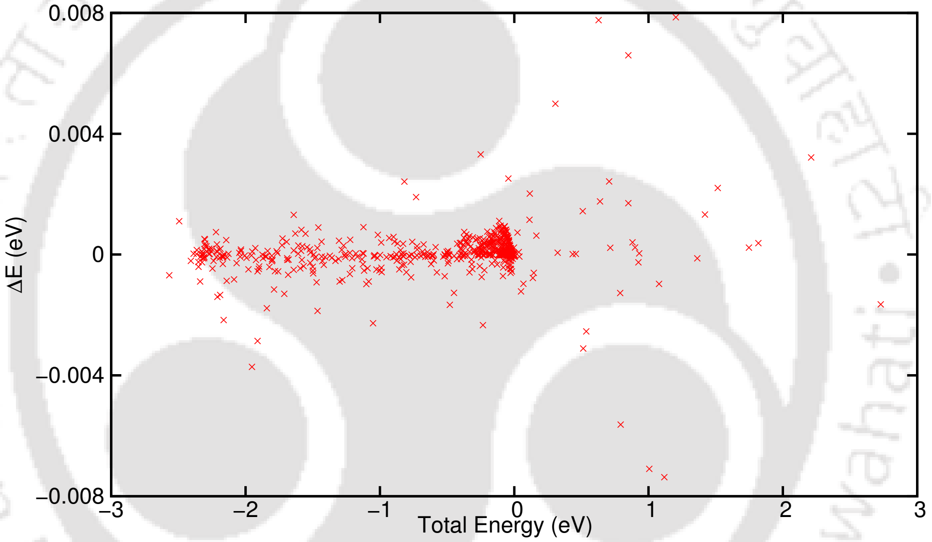

FIGURE 3.15: ΔE, the differences in energies between analytical and *ab initio* values, are plotted against total *ab initio* energy at some random configurations. Zero is set at all-atomic dissociation limit.

The existence of a second minimum for the linear $[NeNeH]^+$ geometry is also found in the analytical PES. The minimum is located 0.7668 kcal/mol below the $Ne+NeH^+$ asymptote with Ne-H and Ne-Ne bonds being 5.01 a.u. and 1.87 a.u. long, respectively. However, the barrier height for conversion between $[NeNeH]^+$ and $[NeHNe]^+$ found from the analytical PES is very small (< 1.0 cm^{-1}). Here, it is worth mentioning that the RMS error of the fitted surface is 0.026 kcal/mol (≈ 9.0 cm^{-1}).

3.3.4 Bound states of $[\mathrm{NeHNe}]^+$ complex

For an HLH type system like $[\mathrm{NeHNe}]^+$, it is interesting to look at the vibrational states of the complex. Vibrational calculations for $J = 0$ are carried out in scattering coordinates using the 3D discrete variable representation (DVR) method with the DVR3D program of Tennyson et al.[20] The radial Gauss-Laguerre quadrature grids consist of 72 and 48 points along R and r coordinates, respectively. For θ, a grid of 42 Gauss-Legendre points was used. Total 37 bound states are found for $J = 0$ below the dissociation level, out of which 22 well-converged low-lying vibrational states are reported in Table 3.9. The lowest level obtained from the DVR calculations lies 0.2277 eV above the global minimum, making the zero-point energy of $[\mathrm{NeHNe}]^+$ as 0.2277 eV.

TABLE 3.9: Calculated energies (in eV) of 22 low lying vibrational states of the $[\mathrm{NeHNe}]^+$ complex for $J = 0$, obtained from DVR3D and TDWP calculations. Energy of the Ne+NeH$^+$ asymptote is taken as zero.

n	Energy		n	Energy	
	DVR3D	TDWP		DVR3D	TDWP
1	-0.4924	-0.4924	12	-0.1966	-0.1967
2	-0.4358	-0.4358	13	-0.1779	-0.1780
3	-0.3804	-0.3804	14	-0.1761	-0.1764
4	-0.3266	-0.3266	15	-0.1602	-0.1605
5	-0.3144	-0.3144	16	-0.1489	-0.1493
6	-0.3031	-0.3031	17	-0.1360	-0.1370
7	-0.2745	-0.2745	18	-0.1304	-0.1318
8	-0.2669	-0.2669	19	-0.1232	-0.1234
9	-0.2487	-0.2487	20	-0.1149	-0.1158
10	-0.2243	-0.2243	21	-0.1120	-0.1123
11	-0.2213	-0.2213	22	-0.1018	-0.1031

In addition to using the DVR3D code, TDWP propagations was also carried out for initial WPs located in the well region of the PES, which was followed by Fourier transformation of the autocorrelation function to generate the spectral density. The method is discussed in detail in Chapter 2. The TDWP calculations were carried out in the reactant Jacobi coordinates (R, r, θ) of Ne+NeH$^+$ system. The initial wave packet was placed at $R = 4.25\ a_0$ and $r = 2.16\ a_0$ with width parameters $\partial_R = 0.3\ a_0$ and $\partial_r = 0.25\ a_0$. Split operator technique was employed to propagate the $\Psi(0)$ for 100000 time steps with $\Delta t = 5.0$ a.u. The R and r grids ranged from 0.2 to 22.0 a_0 with 398 points and from 0.3 to 22.3 a_0 with 368 points, respectively. The angular coordinate consisted of 96 Gauss-Legendre quadrature points. A Gaussian window function was used to get a smooth and well resolved spectra. The pseudospectrum, ranging from -0.5 eV to 0.5 eV, for $J = 0$ is plotted in Figure 3.16. The energies of the 22 low lying bound states are tabulated in Table 3.9. It is quite clear from the Table 3.9 that there is an excellent agreement between the results obtained by two different methods for the first 22 vibrational states.

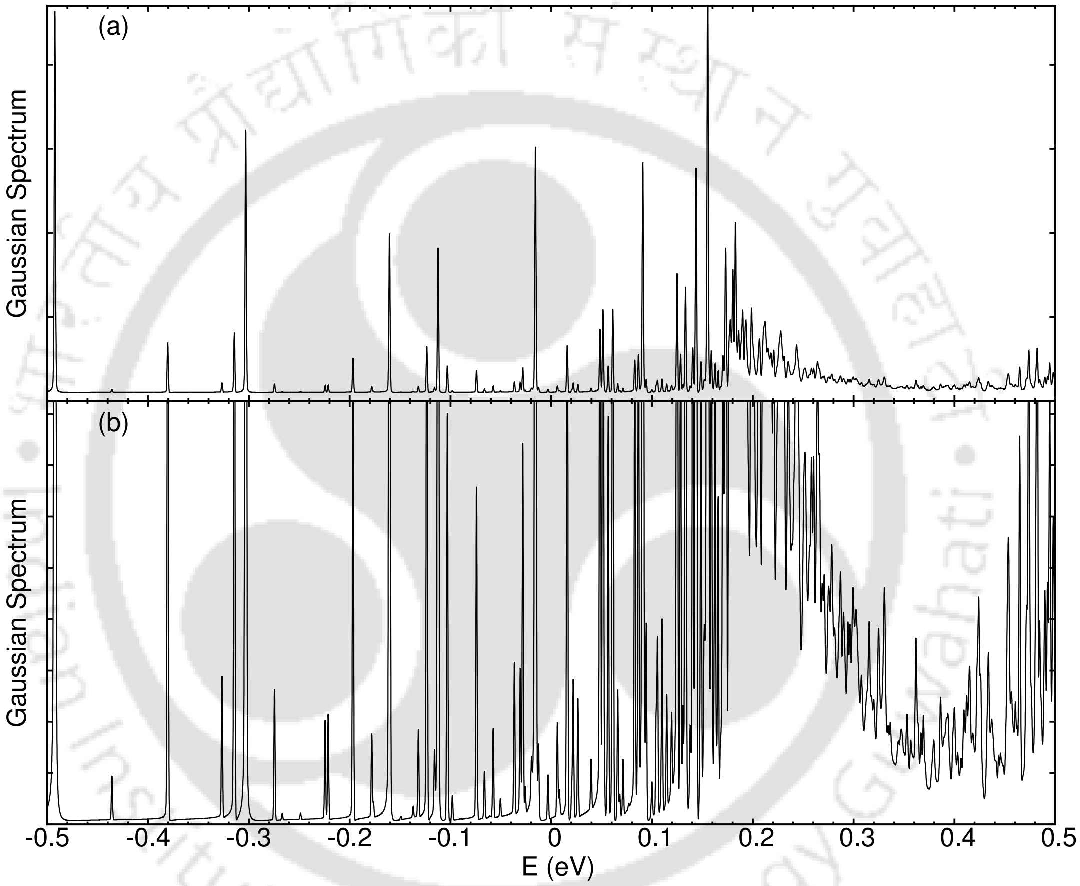

FIGURE 3.16: Eigenvalue spectrum of the $[NeHNe]^+$ complex obtained from TDWP calculation by using the Gaussian window function, showing the bound and quasi-bound states. (a) spectrum, (b) zoomed version of (a). Zero of energy corresponds to $Ne+NeH^+$ asymptote.

3.4 CONCLUSIONS

Electronic structure and binding properties of two different rare gas-hydrogen containing systems $[HeHNe]^+$ and $[NeHNe]^+$ have been explored via *ab initio* calculations with computationally expensive CCSD(T) method and the aug-cc-pVQZ basis set. Global analytical PESs with high accuracy have been constructed for the ground electronic states of both the systems for the first time. A linear configuration with the hydrogen atom located in between the two rare gas atoms is found to be the most stable structure for each of the systems. Excellent agreements between the analytic and *ab initio* energies are found in the strong interaction region as well as asymptotic regions for both the PESs. For collinear and near-collinear arrangements, the MEPs for the proton transfer process contain a potential well. Bound vibrational states are also computed for the most stable structures of these systems for $J = 0$ and the number of bound eigen states are found to be 6 and 37 for $[\mathrm{HeHNe}]^+$ and $[\mathrm{NeHNe}]^+$, respectively. The computed global analytical PESs for these two systems are used in the next three chapters to study the reactive scattering dynamics.

References

[1] Cybulski, S. M.; Toczylowski, R. R. *J. Chem. Phys.* **1999**, *111*, 10520.

[2] Kim, S. T.; Lee, J. S. *J. Chem. Phys.* **1999**, *110*, 4413.

[3] Kunttu, H.; Seetula, J.; Räsänen, M.; Apkarian, V. A. *J. Chem. Phys.* **1992**, *96*, 5630.

[4] Kunttu, H. M.; Seetula, J. A. *Chem. Phys.* **1994**, *189*, 273.

[5] Fridgen, T. D.; Parnis, J. M. *J. Chem. Phys.* **1998**, *109*, 2155.

[6] Milleur, M. B.; Matcha, R. L.; Hayes, E. F. *J. Chem. Phys.* **1974**, *60*, 674.

[7] Matcha, R. L.; Milleur, M. B.; Meier, P. F. *J. Chem. Phys.* **1978**, *68*, 4748.

[8] Rosenkrantz, M. E. *Chem. Phys. Lett.* **1990**, *173*, 378.

[9] Filippone, F.; Gianturco, F. A. *Europhys. Lett.* **1998**, *44*, 585.

[10] Qu, J. Y.; Li, W.; Guo, R.; Zhao, X. S. *J. Chem. Phys.* **2002**, *117*, 2592.

[11] Panda, A. N.; Sathyamurthy, N. *J. Phys. Chem. A* **2003**, *107*, 7125.

[12] Li, W.; Qu, J. Y.; Zhao, X. S. *Chin. J. Chem. Phys.* **2002**, *15*, 188.

[13] Lundell, J. *J. Mol. Struct.* **1995**, *355*, 291.

[14] Fridgen, T. D.; Parnis, J. M. *J. Chem. Phys.* **1998**, *109*, 2162.

[15] Beyer, M.; Lammers, A.; Savchenko, E. V.; Niedner-Schatteburg, G.; Bondybey, V. E. *Phys. Chem. Chem. Phys.* **1999**, *1*, 2213.

[16] Lundell, J.; Pettersson, M.; Räsänen, M. *Phys. Chem. Chem. Phys.* **1999**, *1*, 4151.

[17] Neese, F. *ORCA, An Ab Initio, DFT and Semiempirical SCF-MO Package;* Max-Planck Institute for Bioinorganic Chemistry, Mülheim a. d. Ruhr, Germany, 2010.

[18] Koner, D.; Vats, A.; Vashishta, M.; Panda, A. N. *Comput. Theor. Chem.* **2012**, *1000*, 19 .

[19] Boys, S. F.; Bernardi, F. *Mol. Phys.* **1970**, *19*, 553.

[20] Tennyson, J.; Kostin, M. A.; Barletta, P.; Harris, G. J.; Polyansky, O. L.; Ramanlal, J.; Zobov, N. F. *Comput. Phys. Commun.* **2004**, *163*, 85.

[21] Frisch, M. J.; Trucks, G. W.; Schlegel, H. B.; Scuseria, G. E.; Robb, M. A.; Cheeseman, J. R.; Scalmani, G.; Barone, V.; Mennucci, B.; Petersson, G. A.; Nakatsuji, H.; Caricato, M.; Li, X.; Hratchian, H. P.; Izmaylov, A. F.; Bloino, J.; Zheng, G.; Sonnenberg, J. L.; Hada, M.; Ehara, M.; Toyota, K.; Fukuda, R.; Hasegawa, J.; Ishida, M.; Nakajima, T.; Honda, Y.; Kitao, O.; Nakai, H.; Vreven, T.; Montgomery, Jr., J. A.; Peralta, J. E.; Ogliaro, F.; Bearpark, M.; Heyd, J. J.; Brothers, E.; Kudin, K. N.; Staroverov, V. N.; Kobayashi, R.; Normand, J.; Raghavachari, K.; Rendell, A.; Burant, J. C.; Iyengar, S. S.; Tomasi, J.; Cossi,

M.; Rega, N.; Millam, J. M.; Klene, M.; Knox, J. E.; Cross, J. B.; Bakken, V.; Adamo, C.; Jaramillo, J.; Gomperts, R.; Stratmann, R. E.; Yazyev, O.; Austin, A. J.; Cammi, R.; Pomelli, C.; Ochterski, J. W.; Martin, R. L.; Morokuma, K.; Zakrzewski, V. G.; Voth, G. A.; Salvador, P.; Dannenberg, J. J.; Dapprich, S.; Daniels, A. D.; Farkas, Ö.; Foresman, J. B.; Ortiz, J. V.; Cioslowski, J.; Fox, D. J. *Gaussian∼09 Revision D.01;* Gaussian Inc. Wallingford CT 2013.

Chapter 4

The He + $NeH^+ \rightarrow HeH^+$ + Ne Reaction

A real wave packet based time-dependent, time-independent quantum mechanical and quasiclassical trajectory methods are employed to study the dynamics of He + $NeH^+ \rightarrow HeH^+$ + Ne reaction on an analytical PES based on *ab initio* energies. Total reaction probabilities and ICSs have been calculated for the title reaction with the reactants in ground ro-vibrational, first excited rotational and first excited vibrational states. TDQM calculations have been performed within both the CC and CS frameworks and the importance of inclusion of Coriolis coupling in the QM calculations is discussed. The QCT results are computed by following both the GB and HB approaches. A few collision energies are chosen in the moderate to high energy regions to investigate the state-to-state dynamics starting from ground ro-vibrational reactant state. TIQM and QCT methods are applied to calculate the product ro-vibrational distributions and DCSs at those selected energies. Different mechanisms associated with the process are also investigated as a function of the collision energy.

Parts of the contents of this chapter are published in the following research article:

- Koner, D.; Barrios, L.; González-Lezana, T.; Panda, A. N. Wave Packet and Statistical Quantum Calculations for the He + $NeH^+ \rightarrow HeH^+$ + Ne Reaction on the Ground Electronic State. J. Chem. Phys. **2014**, *141*, 114302.

4.1 INTRODUCTION

Reactive scattering studies of various atom-molecular ionic systems in gas phase, occurring in interstellar clouds, planetary ionospheres and thermonuclear experiments in plasma physics are one of the most interesting areas of research. Hydrogen and light rare gases are amongst the most abundant elements of the universe. The systems containing rare gases and hydrogen element, e.g., protonated rare gas species, play an important role in interstellar chemistry and in different cosmological phenomena.[1–4] Thus the simple proton transfer reactions $\mathrm{Rg} + \mathrm{H}_2^+ \rightarrow \mathrm{RgH}^+ + \mathrm{H}$ (Rg = He, Ne, and Ar) have drawn much attention for a long time and numerous investigations have been carried out experimentally as well as theoretically on these reactions in the past few decades.[5–21] Recently, the reverse reaction for Rg = He, i.e., $\mathrm{HeH}^+ + \mathrm{H} \rightarrow \mathrm{He} + \mathrm{H}_2^+$ has been studied theoretically via TIQM, TDWP and QCT methods.[22–24] In addition to HeH_2^+ system, $\mathrm{He}_2\mathrm{H}^+$ system, a complex containing two rare gas atoms and a proton has also been studied theoretically, which includes calculations of reactive scattering attributes for $\mathrm{He} + \mathrm{HeH}^+ \rightarrow \mathrm{HeH}^+ + \mathrm{He}$ by means of TDQM and QCT methods.[25–28] All these triatomic systems are found to display a global potential energy minimum for a collinear configuration. Numerous sharp oscillations observed in the reaction probability curves indicate that the atom-molecular ion reactive collisions for these systems are either mediated by resonances or follow complex-forming paths. Differences observed between CS approximated results and exact results suggest that inclusion of Coriolis coupling in the QM simulations is of paramount importance for these type of bimolecular complex-forming scattering systems. Therefore, besides being relevant in the atmospheric and interstellar chemistry, the dynamics of such processes are of fundamental importance. However, dynamical studies of the mixed rare gas cationic hydrides containing light rare gases (He, Ne and Ar) are scarce in literature. In this Chapter, results of a detailed computational study on the dynamics of $\mathrm{He} + \mathrm{NeH}^+ \rightarrow \mathrm{HeH}^+ + \mathrm{Ne}$ reaction are presented.

A schematic potential energy profile of reactants, products, and the minimum for the title reaction is shown in Figure 4.1. Some selective reactants and products rovibrational states are also depicted in the same picture. It is clear from the figure that the reaction is endothermic (by 0.293 eV) with reactants in the ground ro-vibrational states, but vibrational excitation of the reactant makes the process exothermic. As shown in Figure 4.1 there exists a potential energy well (of maximum depth 0.521 eV with respect to the reactant asymptote) along the minimum energy path. The minimum of the potential energy well corresponds to a collinear He-H-Ne geometry with NeH and HeH bond distances of 2.102 and 1.804 bohr, respectively.

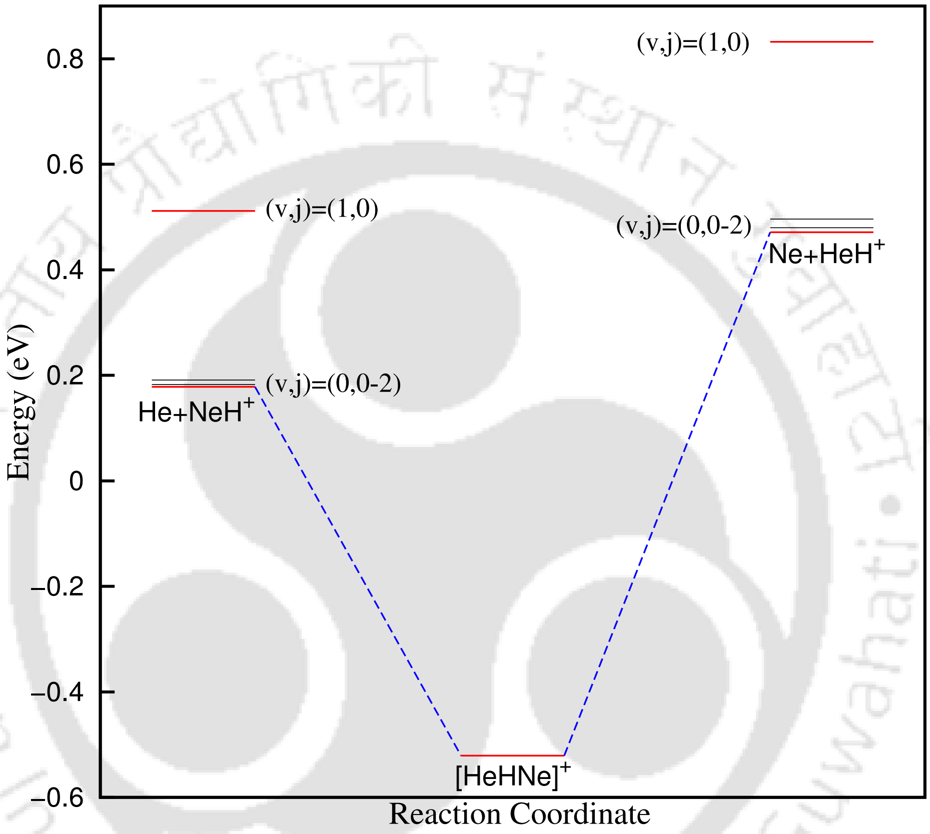

FIGURE 4.1: Schematic potential energy profile of reactants and products for the He + $NeH^+ \rightarrow HeH^+$ + Ne reaction. Energy of He+NeH^+ asymptote is set as zero.

4.2 METHODS

The title reaction is investigated here by using three different methodologies, TDQM, TIQM and QCT. Details of the theoretical formalisms of different approaches are discussed in Chapter 2. In the TDQM approach employed here, the initial WP is formed in reactant Jacobi coordinates and propagated via CRWP method within both CS and CC formulations. Damping functions used in the TDQM calculation has the form of

TABLE 4.1: Numerical parameters used in the TDQM simulations (All parameters are given in atomic units).

Number of R grid points	220
Number of r grid points	150
Number of angular grid points	120
R_{min}	0.2
r_{min}	0.5
δR	0.1
δr	0.12
Centre of initial wave packet	14.0
Damping coefficients along R and r	0.001, 0.001
Starting points of damping along R and r	15.5, 13.22
Analysis point along r	12.98
Number of Chebyshev iterations	30000

Eq. 2.46. Different initial state specific total reaction probabilities are computed within a collision energy range 0.0005-0.5 eV by calculating the total flux of the energy dependent WP going through a fixed surface. The TDQM calculations were performed using a Fortran code developed by us and parallelized using MPI as well as OPENMP algorithm. Many test runs were carried out to check the convergence of each parameter used in the TDWP studies. The final parameters used in the TDQM calculations are given in Table 4.1. For $v = 0$, the values of $J_{\max}$ are 67 and 74 for TDQM-CS and TDQM-CC calculations, respectively, while for $v = 1$, $J_{\max} = 91$ was enough for both the TDQM-CS and TDQM-CC calculations to converge the integral cross sections within the above mentioned energy range.

The calculations of reaction probabilities including all K states for high J values are highly computationally demanding. However, for the title reaction, converged total reaction probabilities are obtained using truncated helicity basis. In Figure 4.2, the convergence of the TDQM-CC reaction probabilities with respect to $K_{\max}$ (maximum value of K) is shown for different initial reactant states at large J values. For $v = 0$ and 1, $J = 50$ and 70 respectively, are chosen to investigate the $K_{\max}$ dependence on total reaction probabilities. As can be seen in Figures 4.2a and 4.2b, very small differences appear between the reaction probabilities obtained using $K_{\max} = 7$ and 11. Considering the computational cost and time factor as well as accuracy of the calculations, $K_{\max} = \min(J, 7)$ were used for all $v = 0$ calculations. However, for $v = 1$, a large number of

J's were needed to converge the cross sections within the investigated energy range. As it is observed in Figure 4.2c, $K_{\max} = 11$ results slightly overestimate the probabilities obtained using $K_{\max} = 7$. But reaction probabilities obtained by using $K_{\max} = 11$ and 13 are literally having the same values. Hence, $K_{\max} = 11$ was used for $J > 50$ calculations and $K_{\max} = \min(J, 7)$ were used in rest of the calculations.

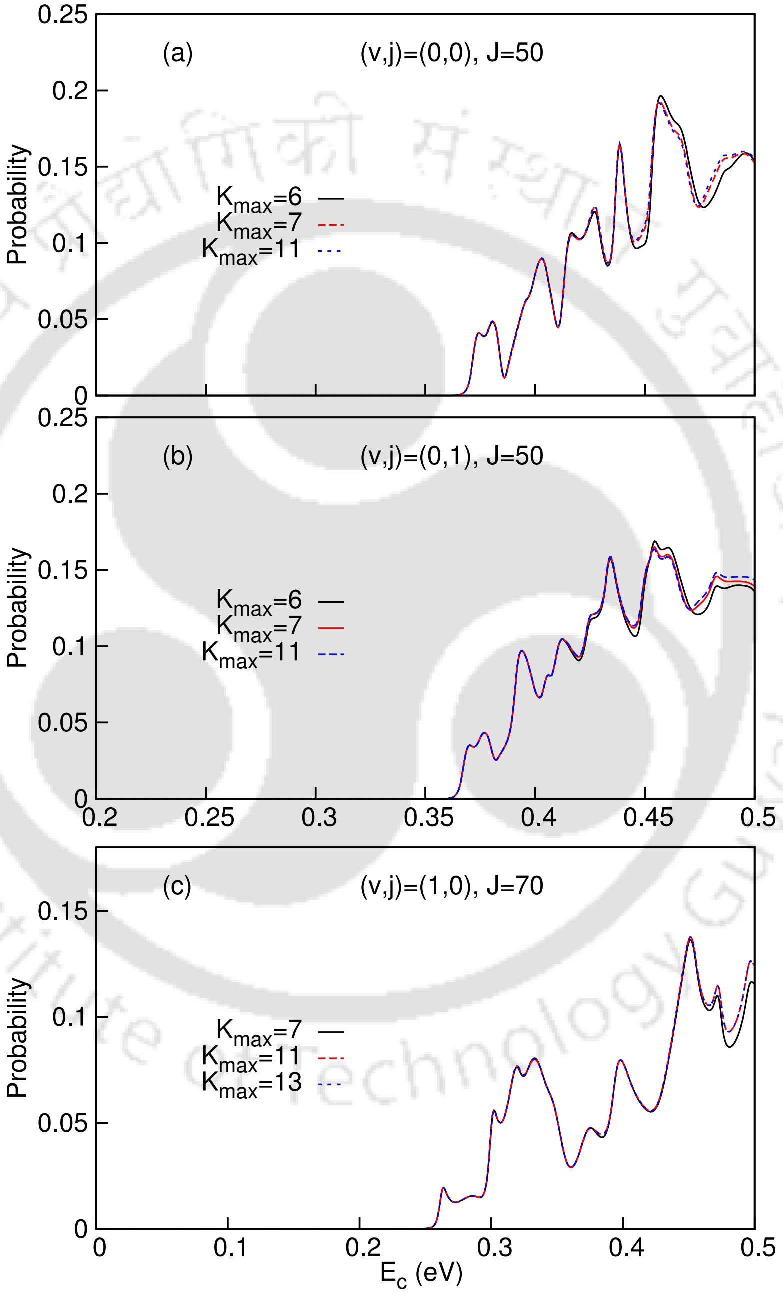

FIGURE 4.2: Dependence of total reaction probabilities on the $K_{\max}$ values. (a,b,c) Results are shown for three different initial states and for two different J values.

As mentioned already, all the TIQM calculations are performed using the ABC code

TABLE 4.2: Numerical parameters employed in the TIQM calculations.

Maximum hyperradius ($\rho_{\max}/a_0$)	30	$E_c \leq 0.01$ eV
	25	0.01 eV $< E_c \leq 0.5$ eV
	22	$E_c > 0.5$ eV
Number of log derivative propagation sectors (n_{sec})	290	$E_c \leq 0.01$ eV
	234	0.01 eV $< E_c \leq 0.5$ eV
	200	$E_c > 0.5$ eV
Maximum rotational quantum number ($j_{\max}$)	30	
Maximum internal energy ($e_{\max}$/eV)	2.0	
Helicity truncation parameter ($K_{\max}$)	$\min(11, J)$	$E_c \leq 0.6$ eV
	$\min(15, J)$	$E_c > 0.6$ eV

developed by Manolopoulos and co-workers.[29] Many test runs are performed to converge the state-to-state reaction probabilities with respect to different initial parameters. The optimal values of the parameters used to obtain the TIQM results reported here are listed in Table 4.2. Optimal values of the parameters $e_{\max}$ and $j_{\max}$ as mentioned in Table 4.2 define the coupled-channel basis set for $J = 0$ with 261 basis functions. The number of basis functions in the truncated helicity basis set for $J \geq 11$ with $K_{\max} = 11$ is 2224 and for $J \geq 15$ with $K_{\max} = 15$ is 2327.

QCT studies are performed only for the He + NeH$^+$($v = 0, j = 0$) $\rightarrow$ Ne + HeH$^+$(v', j') reaction. As mentioned already, these QCT calculations are carried out using a newly developed code by us which uses a fourth-order Runge-Kutta method for numerical integration. A fixed time step of 2 a.u. was used which guaranteed conservation of the total energy and the angular momentum up to eighth and ninth decimal places, respectively. For all the trajectories, the He atom was separated initially from the center of mass of NeH$^+$ molecule by a distance of 30 a.u. Trajectory calculations were stopped when the distance between He and H atoms exceeded 35 a.u. or distance between Ne and H atoms exceeded 30 a.u. Product internal states have been assigned using both HB and GB formulations. J-sampling technique is used to calculate ICSs and DCSs at particular collision energies by running batches of 2000000 - 5000000 trajectories. In addition, total and vibrational state resolved reaction probabilities have been computed for $J = 0$ and 50, and total ICSs have been computed as a function of collision energy. The method of moments expansion in Legendre polynomials approach is used to calculate probabilities and ICSs as a function of collision energy.[30]

4.3 RESULTS AND DISCUSSION

This section reports the final state averaged results for three different initial states, (v, j) = (0, 0), (0, 1) and (1, 0) and the state-to-state results for the initial state (v, j) = (0, 0). In addition to discussing the results, the mechanistic pathways followed by the reaction are also looked into.

4.3.1 Initial state selected dynamics

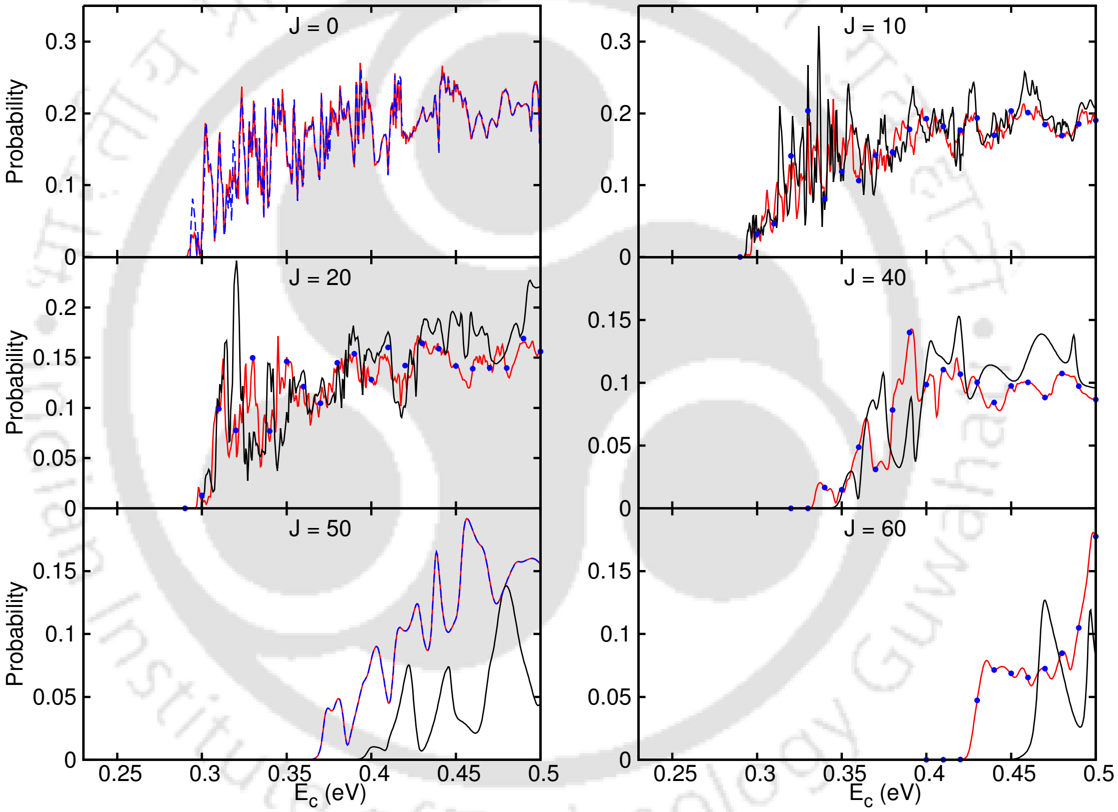

FIGURE 4.3: Total reaction probabilities plotted as a function of collision energy for He + $NeH^+(v = 0, j = 0) \rightarrow HeH^+$ + Ne reaction for few selected J values obtained from the following methods: TIQM (- - / •), TDQM-CC (—), TDQM-CS (—).

4.3.1.1 Total reaction probabilities

Different initial-state selected TDQM and TIQM total reaction probabilities for few selected Js are plotted in Figures 4.3 and 4.4, for reactants in ground ro-vibrational and

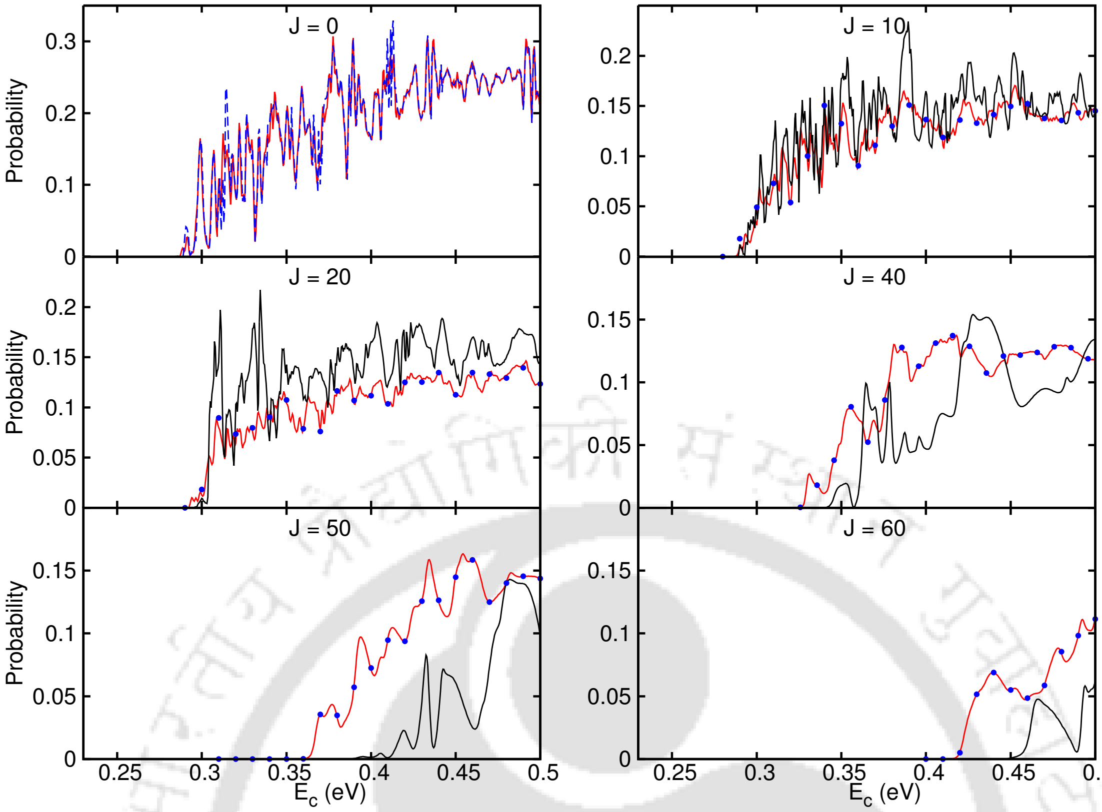

FIGURE 4.4: Same as Figure 4.3 for He + $NeH^+(v = 0, j = 1) \rightarrow HeH^+ + Ne$.

excited rotational states, respectively. Excellent agreements observed between TDQM-CC and TIQM results suggest that both sets of the results are well converged and accurate. As can be seen in Figures 4.3 and 4.4, both the CC and CS probabilities exhibit dense oscillations for low J values, which may be an indication of an intermediate complex getting formed in the deep potential well during the reaction. Such dense oscillatory total reaction probabilities have been seen for many other bimolecular complex forming reactions.[8,10,13,14,21,25,27,31–38] For larger J values, the peaks in the probability curves become broader. The other significant observation is that the amplitudes of the oscillations are larger for the CS probabilities than those in the CC results. CC probability for a particular value of J is calculated by summing over the probabilities of all the individual K states included in the CC calculation. As a result, the resonance features of the individual K-dependent probabilities are diminished in the resultant CC probabilities. As it is seen in Figure 4.3, the reaction has a threshold of ~ 0.29 eV for ground ro-vibrational state of the reactants. The threshold increases for higher J values due to the increase of centrifugal potential. For $v = 0$ reactions, the CC probabilities

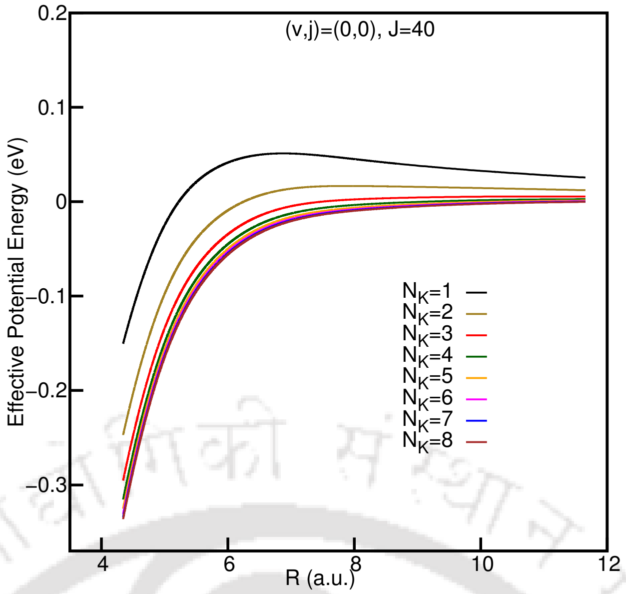

FIGURE 4.5: Effective potential energy profiles for the He + NeH$^+$ reaction at $J = 40$. Horizontal axis corresponds to the collinear minimum energy path. N_K is the number of K states used.

for larger J values (e.g., $J = 50$, 60) have smaller threshold energies than the corresponding thresholds in CS probabilities. The N_K-dependent effective potential energy profiles, plotted in Figure 4.5, address this difference. Here, N_K is the number of K states included in QM-CC calculations. The effective potential energies ($E(R, r)$) for a particular J and N_K are calculated as

$$E(R, r) = \frac{F}{2\mu_R R^2} + V(R, r), \tag{4.1}$$

where F is the smallest eigenvalue obtained by diagonalizing the centrifugal tridiagonal matrix of Eq. 2.24. $V(R, r)$ is the potential energy of the system along the collinear minimum energy path. As the angular kinetic energy decreases with the increase in K (see Eq. 2.24), the term F, described in Eq. 4.1 also decreases. This results in a lower effective potential energy. Thus, more the number of K states included in the CC calculations, less is the value of the effective potential energy and this feature is reflected in Figure 4.5. On the other hand, in the CS calculations, N_K is always equal to one and the centrifugal barrier is independent of N_K.

In Figures 4.3 and 4.4 , the similarities between CC and CS reaction probabilities for low J values ($J = 10$) are quite clear but differences increase with the increase of

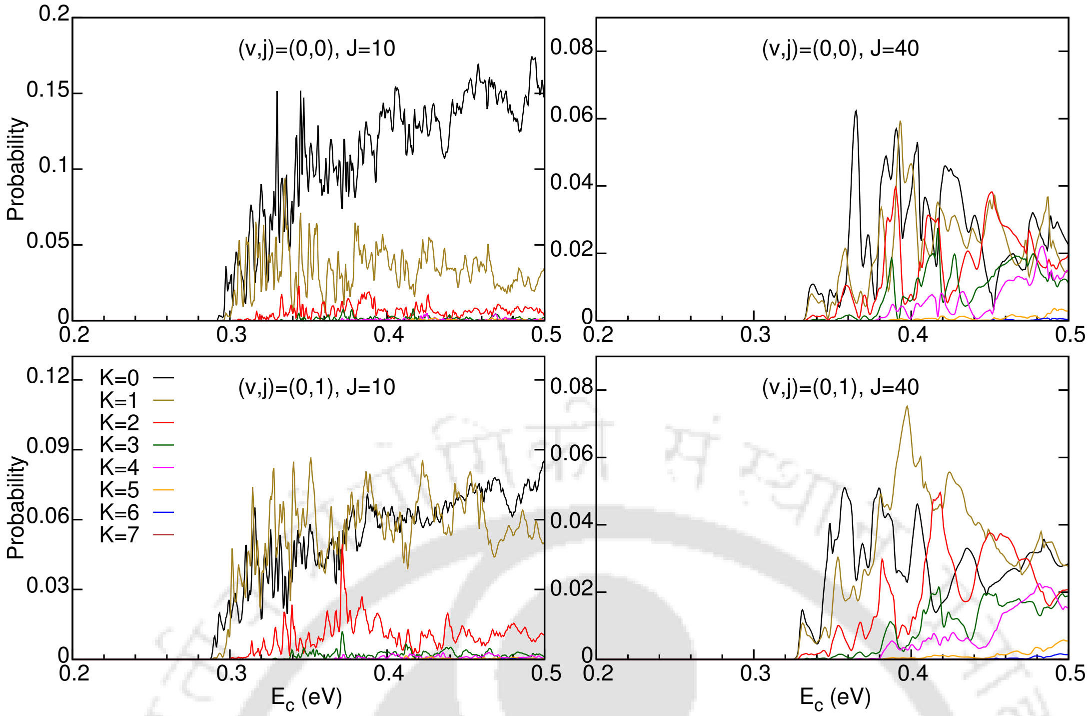

FIGURE 4.6: K-dependent total reaction probabilities for two different ro-vibrational and J states obtained from TDQM-CC calculations.

total angular momentum. These findings are in accordance with the results for other atom-molecular ion systems[8,21,32] for which it has been observed that Coriolis coupling becomes more important as the value of J increases.

The contributions of each K state to the total CC reaction probabilities for $(v, j) = (0, 0)$ and $(v, j) = (0, 1)$ and $J = 10$, 40 are presented in Figure 4.6. It is obvious from this figure that for $(v, j) = (0, 0)$ and (0, 1) and $J = 10$, the major part of the reaction probabilities comes from first three K states and the contributions from larger K states are negligibly small. However, for $J = 40$, the initial WP is channeled to larger K states to overcome the centrifugal barrier and more number K states contribute significantly to the reaction probabilities. In the CS calculations, the out of plane rotations of molecule are restricted and only one K state (here $K = 0$) is included during quantum calculations. As a result, it can be seen in Figure 4.3 that there are no significant differences between the CS and CC reaction probabilities for $(v, j) = (0, 0)$ and $J = 10$, where major share of the CC reaction probabilities comes from $K = 0$ state. However, it is seen in Figure 4.4 that the differences between CS and CC reaction probabilities increase a bit for $(v, j) = (0, 1)$ and $J = 10$, where $K = 0$ and 1 states have almost similar contribution

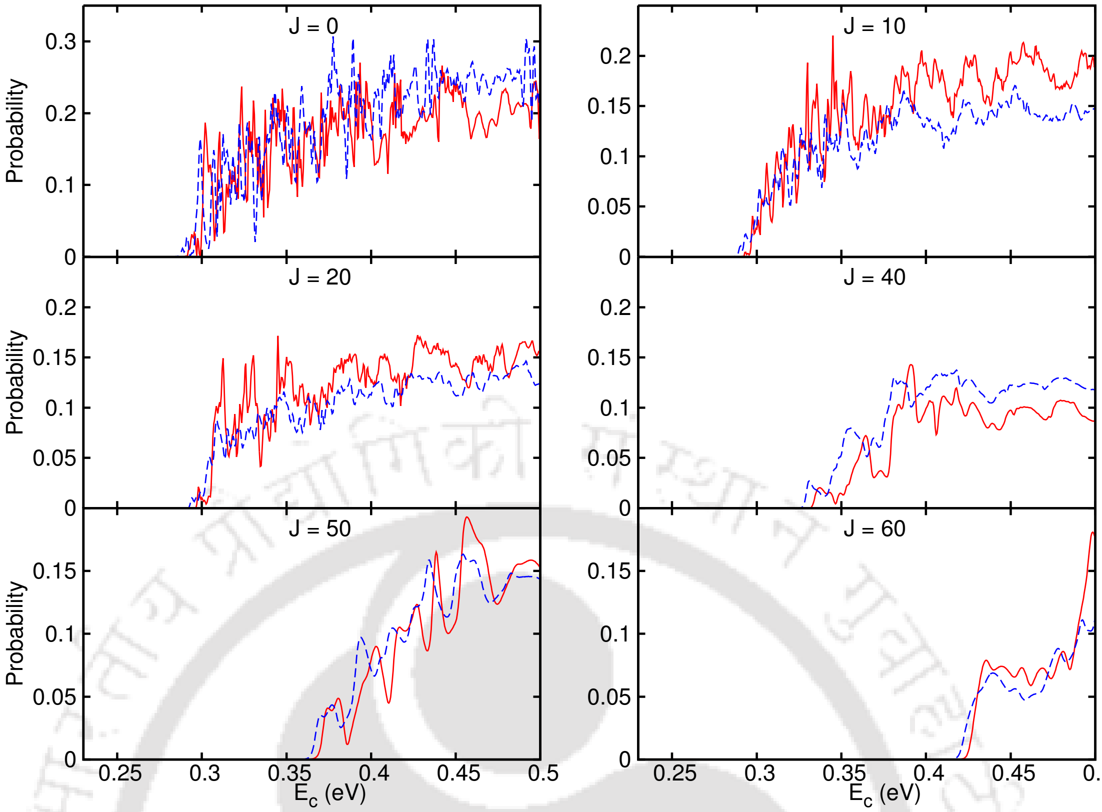

FIGURE 4.7: Comparison between (v, j) = (0, 0) and (0, 1) TDQM-CC total reaction probabilities.

to the total CC reaction probability.

Effect of rotational excitation of the reactants on the title reaction is presented in Figure 4.7. The overall behavior of the reaction probabilities is similar for both the initial states, which is in accordance with many other endothermic reactions.[8,10,13,14,32,34,35] The thresholds for the probabilities for $(v, j) = (0, 1)$ are smaller than corresponding $(v, j) = (0, 0)$ probabilities due to increment in internal energy for the rotationally excited reactants. A comparison in magnitudes of the probabilities at different collision energies for both the initial states does not show any special trend. It is seen that the reaction probabilities for $J = 0$ and $(v, j) = (0, 1)$ are very much comparable to the corresponding $(v, j) = (0, 0)$ probabilities near the threshold regions, but at higher collision energies $(v, j) = (0, 1)$ probabilities are slightly larger than the $(v, j) = (0, 0)$ probabilities. Probabilities for (v, j) = (0, 1) are larger and smaller for J = 40 and J = 10, 20, respectively, than the results for (v, j) = (0, 0) case. But the probabilities for J = 50 and 60 for both the initial states are comparable to each other. It seems that

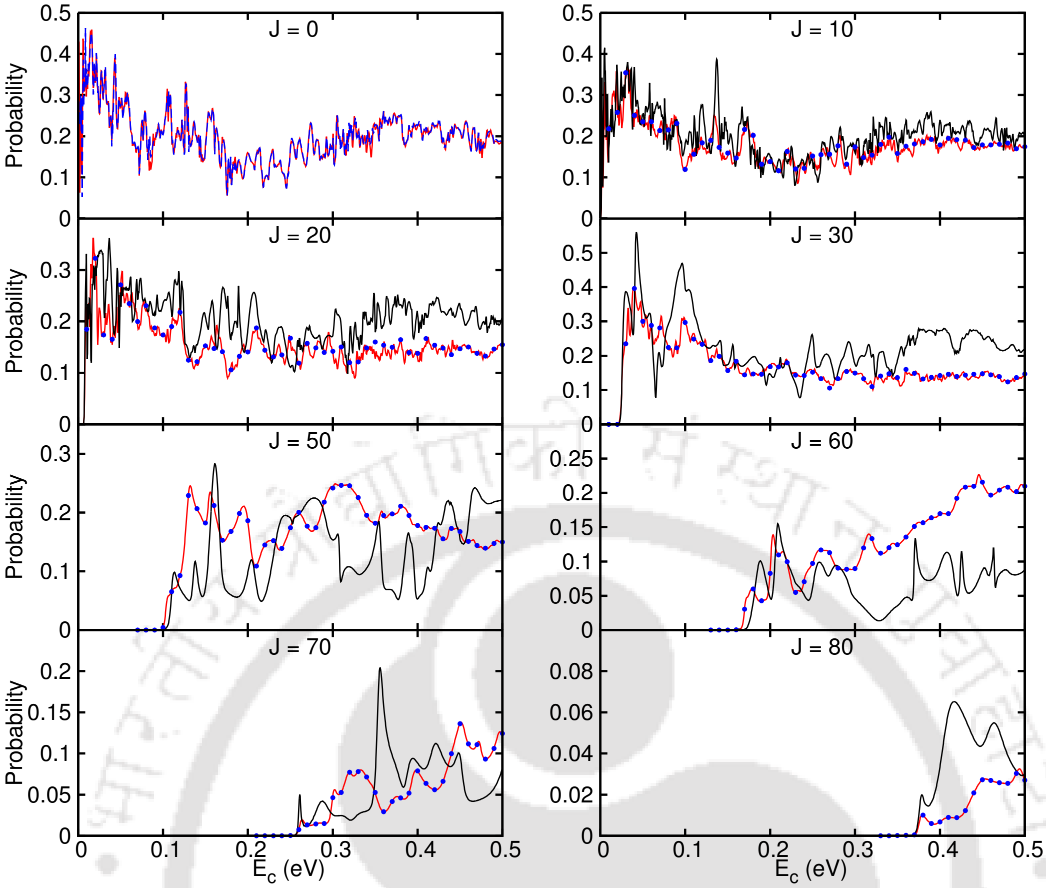

FIGURE 4.8: Same as Figure 4.3 for He + NeH$^+$($v = 1, j = 0$) → HeH$^+$ + Ne.

the rotational excitation of the reactants to its first excited state has less effect on the reaction probabilities.

In Figure 4.8, total reaction probabilities computed via TDQM-CC, TDQM-CS and TIQM approaches are presented for a few selected Js for He + NeH$^+$($v = 1, j = 0$) $\rightarrow$ HeH$^+$ + Ne reaction. It is clear in Figure 4.8 that TIQM results agree quite well with the TDQM-CC results in almost entire collision energy range. Vibrational excitation of the reactants is found to enhance the title reaction to a large extent. As is seen in Figure 4.1, vibrational excitation makes the reaction thermodynamically exothermic, which results in a strong enhancement in the reaction probabilities. For $(v, j) = (1, 0)$ the reaction probabilities for lower J values start without any threshold, which is typical for barrierless exothermic reactions and processes with reactants in vibrationally excited states.[21,33,36–38] Differences between the CC ans CS results for larger Js are clearly noticeable in Figure 4.8.

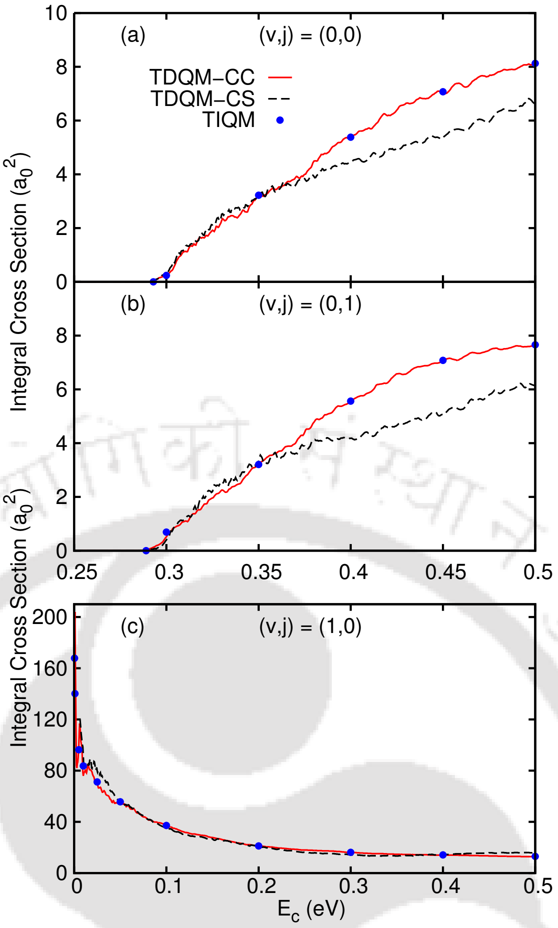

FIGURE 4.9: Total integral reaction cross sections for He + NeH$^+$ → HeH$^+$ + Ne reaction for different initial reactant states computed via TDQM-CC, TDQM-CS and TIQM approaches.

4.3.1.2 Total integral cross sections and opacity functions

The total integral cross sections (ICSs) calculated using TDQM and TIQM approaches are plotted in Figures 4.9a, 4.9b and 4.9c for $(v, j) = (0, 0)$, (0, 1) and (1, 0), respectively. An excellent agreement between the TDQM-CC and TIQM ICSs can be seen in Figure 4.9. The resonances observed in QM reaction probabilities are mostly diminished (except for the $(v, j) = (1, 0)$, ICSs in the low energy region) in the cross section curves due to J-averaging effect. The cross sections for $(v, j) = (0, 0)$ increase steadily within the investigated energy range, as is the case for other endothermic reactions.[8,10,13,14,32,34,35] CC ICSs for $(v, j) = (0, 0)$ and (0, 1) are a bit smaller than the results obtained using CS around the threshold region but are considerably larger than the CS ones at higher collision energies. It is already mentioned in Chapter 3 that the collinear path is the most preferable path for the He + NeH^+ reaction. In the CS calculations, the molecule is confined to rotate only in the molecular plane and out-of-plane rotations of the reactant molecule are restricted within this approximations. Thus, in the CS calculations, there are more chances for head-on collisions between the reactants and this results in larger CS cross sections near threshold regions. Coriolis coupling between different K-states opens up more dissociation channels for the complex to break and form the products. This leads to larger cross sections in case of QM-CC than the results in CS at high collision energies. This is seen for many other reactions also.[8,9,21] Thus, at higher collision energies, Coriolis coupling effect promotes the reactivity for the title reaction. The ICSs for $(v, j) = (1, 0)$ are very high at low collision energies and the magnitude decreases sharply with the increase in collision energy and remains almost constant with further increase in collision energy. Similar observations were reported for other barrierless exothermic processes[21,33,36] and for reactions with reactants in their vibrationally excited states in late barrier type surfaces.[10,13,34,35] In the present system, the barrier corresponds to the reaction endothermicity. It can be seen in Figure 4.9c that some resonance peaks survive the partial wave summation and appear at very low energies in the ICS curve for $(v, j) = (1, 0)$. This is a clear indication of indirect mechanism(s) associated with the process.

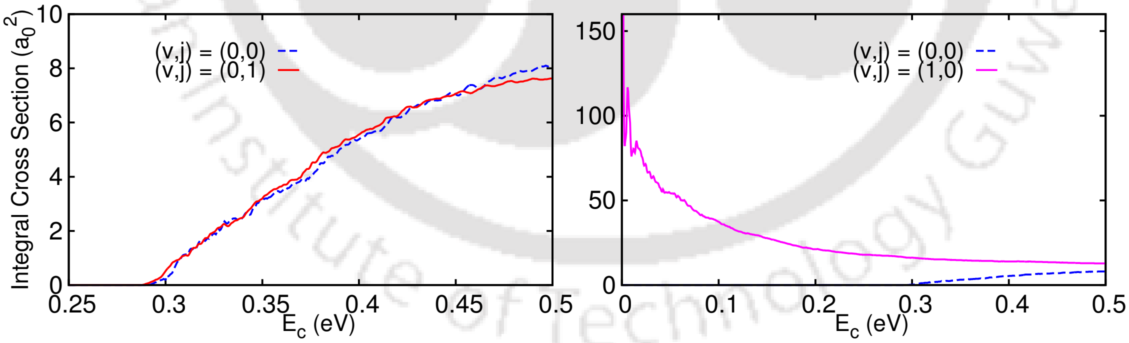

FIGURE 4.10: Comparison between TDQM-CC ICSs for different initial reactant states for He + $NeH^+ \rightarrow HeH^+$ + Ne reaction.

Figure 4.10 shows the effect of rotational and vibrational excitations on the cross sections. No special trend is found, when the cross sections between the $(v, j) = (0, 0)$ and $(v, j) = (0, 1)$ results are compared at collision energies upto 0.47 eV. However, minor differences appear at high energies ($E_c > 0.47$ eV) between the ICSs for $(v, j) = (0, 0)$

and (0, 1), and this seems to increase with increase in energies. A similar situation was observed in case of He + H_2^+ reaction cross sections.[10] As the reaction becomes exothermic due to vibrational excitations of the reactants, the reaction cross sections for $(v, j) = (1, 0)$ are very different compared to $(v, j) = (0, 0)$ reaction cross sections. Vibrational excitations greatly enhances the magnitudes of the ICSs in the whole energy range.

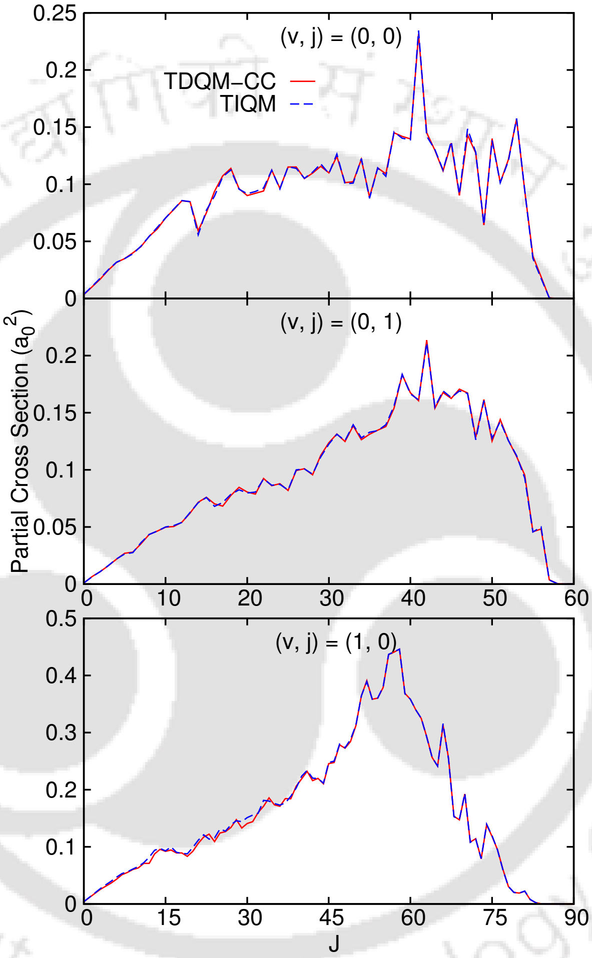

FIGURE 4.11: Partial waves contributions to the total integral cross sections plotted as a function of total angular momentum for the title reaction for different initial reactant states at $E_c = 0.4$ eV.

The opacity functions, reaction probabilities as a function J at particular collision energies, are plotted as $(2J + 1)P^J(E_c)$ in Figure 4.11. There is an excellent agreement between TDQM-CC and TIQM results. As it is seen, a large number of partial waves were needed to converge the cross sections for $(v, j) = (1, 0)$. Oscillating feature of the opacity functions indicates involvement of indirect mechanism for the title reaction.

4.3.2 State-to-state dynamics

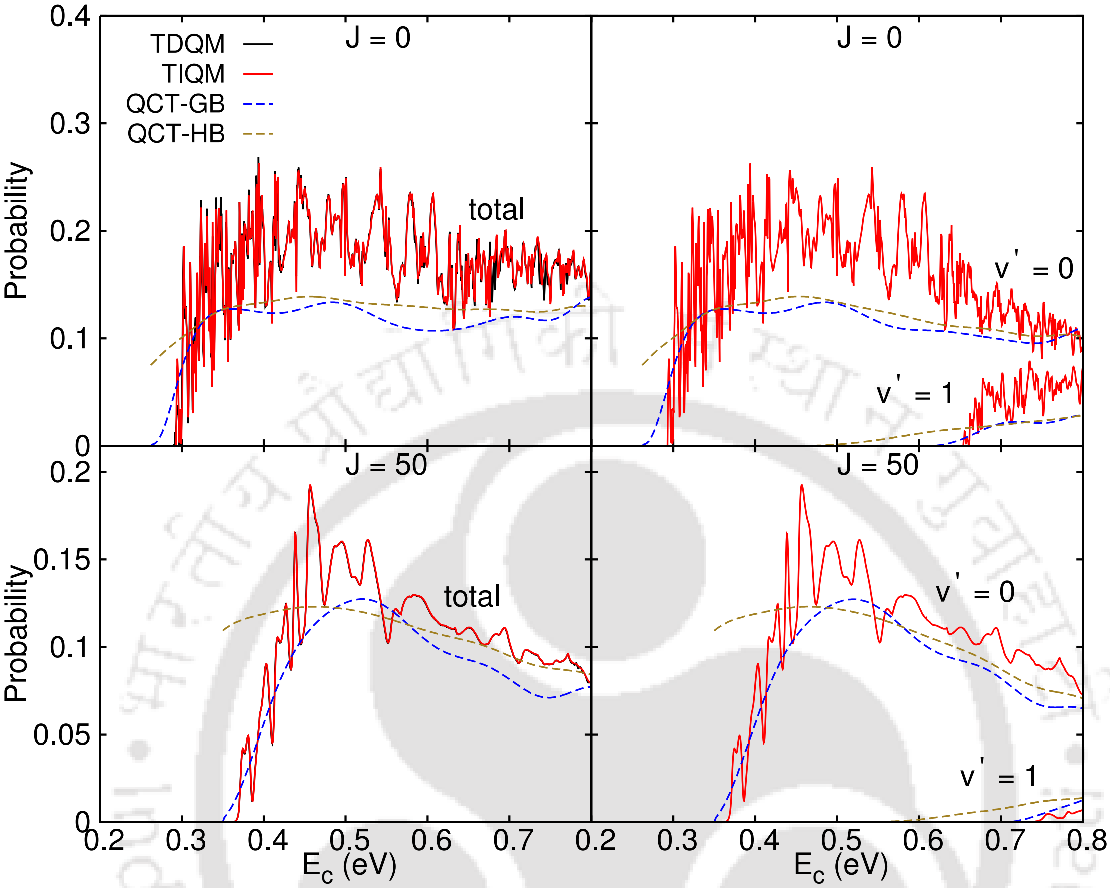

FIGURE 4.12: Total and vibrational state-resolved reaction probabilities for two different J values plotted as a function of collision energies obtained from different methods.

The title reaction is investigated at state-to-state level for $(v, j) = (0, 0)$ initial reactant state via TIQM and QCT calculations. A few selected collision energies covering low, moderate and high regions are chosen to explore the state-to-state dynamics. The excellent agreement between the TIQM and TDQM final state averaged results is already mentioned. Accuracy of the QCT approach in exploring the title reaction is also checked by calculating reaction probabilities for $J = 0$ and 50, as well as ICSs as a function of collision energy within the range 0.2 - 0.8 eV. In Figure 4.12, total and product vibrational state-resolved reaction probabilities for the title reaction for $(v, j) = (0, 0)$ and $J = 0$, 50 obtained from QCT calculations are plotted along with the QM probabilities. The QCT-GB results reproduce the overall shape of the QM results quite satisfactorily. However, the probabilities computed following HB approach differ significantly from the

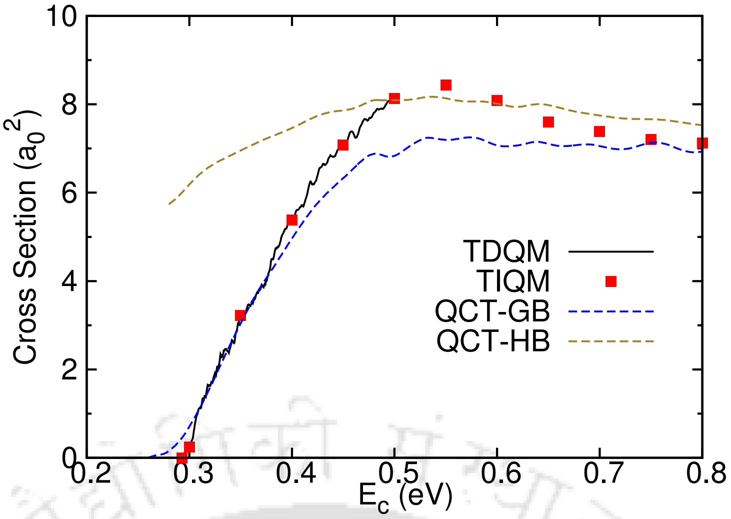

FIGURE 4.13: Total integral cross sections plotted as a function of collision energies calculated by means of different theoretical approaches.

corresponding QM ones in the threshold region, similar to this kind of observations noticed for many other systems.[39–41] The resonance features of the QM probabilities can not be reproduced via QCT calculation because of inherent limitations associated with QCT methodology. In QM approach, all the regions of the phase space are described by the WF, and thus probabilities with resonances can be obtained. But in QCT, a Monte Carlo sampling is done over the phase space and the results obtained from QCT calculations are computed as the averaged values. However, resonance peaks have been observed in QCT probabilities for F + OH system due to appearance of a large number of *trapped* trajectories.[42]

A comparison between the QCT and QM total ICSs is presented in Figure 4.13. QCT-GB approach successfully reproduces the QM ICSs near the threshold region but differences can be seen at E_c = 0.45 - 0.65 eV range. QCT-HB approach fails to describe the threshold region but reproduces the average behavior of the QM ICSs for $E_c \geq 0.5$ eV. Similar observations were made for many other endothermic reactions.[41,43–45]

4.3.2.1 Rotational distributions

TIQM and QCT product rotational distributions at E_c = 0.35, 0.5, 0.65 and 0.8 eV are presented in Figure 4.14. The overall shapes of the QCT distributions fairly agree with the QM distributions at all E_cs. However, neither of the QCT binning methods

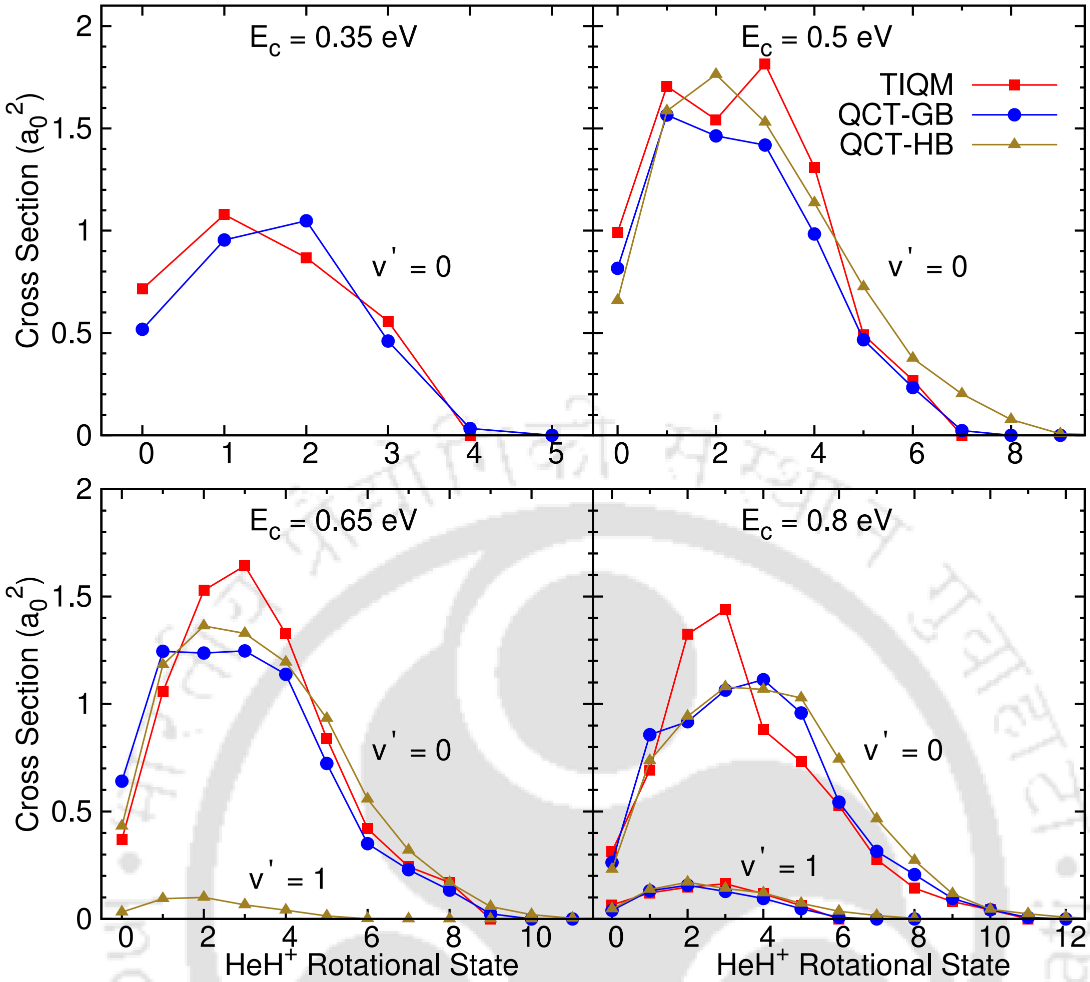

FIGURE 4.14: TIQM and QCT product rotational state distributions for the He + NeH$^+$($v = 0, j = 0$) $\rightarrow$ HeH$^+$(v', j') + Ne reaction calculated at different collision energies. QCT results obtained following both HB and GB approaches are plotted.

is able to reproduce the correct distribution around the maxima of the QM results for $v' = 0$. QCT-HB results at $E_c = 0.35$ eV are not plotted in Figure 4.14 because at this energy QCT-HB approach fails to calculate the correct ICSs (See Figure 4.13, QCT-HB results differ to a large extent from the exact QM results). At $E_c = 0.35$ eV, QCT-GB method successfully reproduces the average behavior of the TIQM distribution, which is related to the excellent agreement between QCT-GB and QM ICSs at that energy (See Figure 4.13). Rotational distribution for $v' = 0$ at $E_c = 0.5$ eV shows a better agreement of QCT-HB results than that of QCT-GB with TIQM distributions for low product rotational states and around the maximum. Although the QCT-HB and QM ICSs are nearly indistinguishable at $E_c = 0.5$ eV, QCT-HB distribution is little hotter than its QM counterpart. As can be seen in Figure 4.14, HeH$^+$ with $v' = 1$

is formed only via QCT-HB methods at $E_c = 0.65$ eV, though this state is quantum mechanically closed. Rotational state resolved cross sections for $v' = 1$ calculated via different methods at $E_c = 0.8$ eV agree quite well. It is quite obvious in Figure 4.14 that the rotational distributions obtained from QCT-GB method have excellent agreements with QM distributions for higher j' values at all E_cs reported here. Formation of the products with rotational states beyond allowed quantum states can be seen in QCT-HB results, whereas those states are suppressed by following the GB approach.

4.3.2.2 Differential cross sections

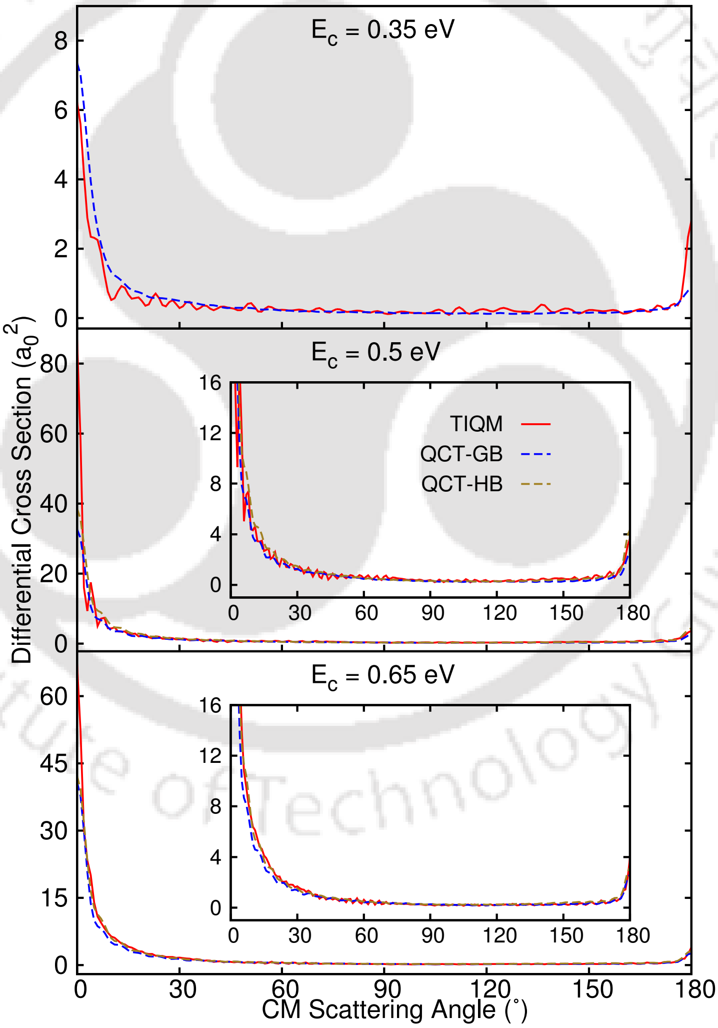

FIGURE 4.15: Total differential cross sections calculated for He + NeH$^+$($v = 0, j = 0$) → HeH$^+$ + Ne reaction at $E_c = 0.35$ (top), 0.5 (middle) and 0.65 eV (bottom). The insets in the middle and bottom panels show the zoomed versions of the DCSs.

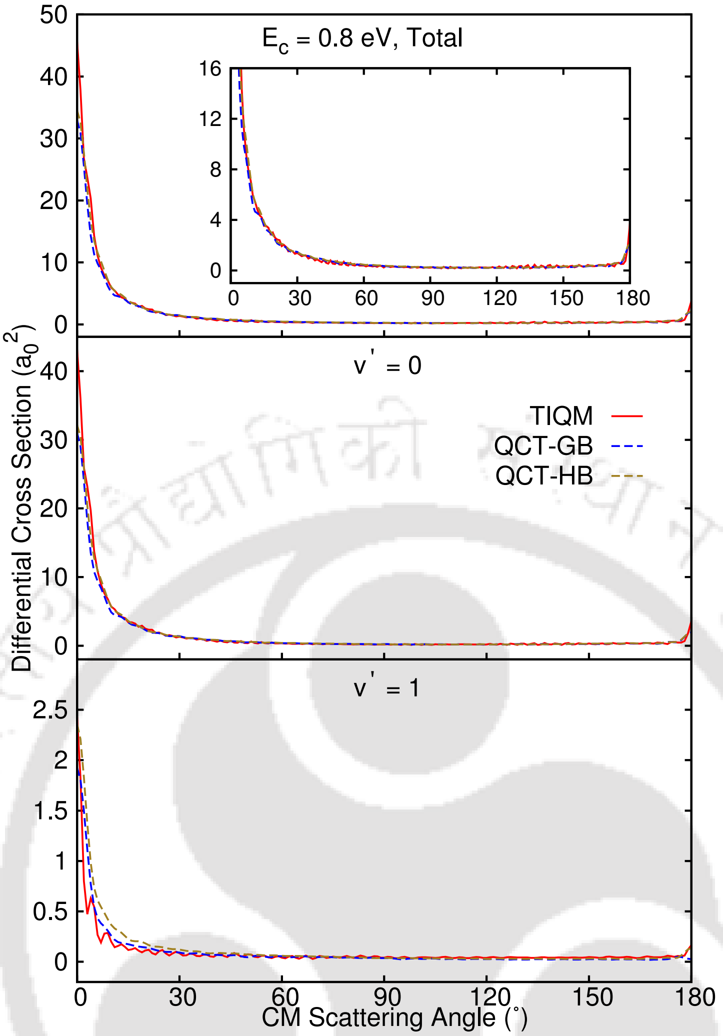

FIGURE 4.16: Total and vibrational state resolved differential cross sections for the He + NeH$^+$($v = 0, j = 0$) $\rightarrow$ HeH$^+$(v') + Ne reaction at $E_c = 0.8$ eV. The inset in the top panel shows the zoomed versions of the DCSs.

Total differential cross sections obtained by means of TIQM, QCT-GB and QCT-HB at three different values of collision energy with reactants in ground ro-vibrational state are presented in Figure 4.15. It is observed in Figure 4.15 (top) that at $E_c = 0.35$ TIQM DCS shows a forward peak, which is almost double in magnitude of the backward peak. However, QCT-GB DCS is totally asymmetric and the products clearly favor a forward scattering. The intensity of the forward peak of the QCT-GB DCS is greater than the TIQM one, whereas reverse is true for the backward peak. As can be seen in Figure 4.15 (middle and bottom panels), the overall shapes of the DCS curves obtained from all the methods at $E_c = 0.5$ and 0.65 eV are similar in nature with a marked preference for the forward direction. At these energies, both the QCT approaches produce similar results and the backward peaks of the QCT DCSs are in an excellent agreement with the TIQM one. However, the forward peaks of the TIQM DCSs at E_c = 0.5 and 0.65 eV are $\sim$ 2 times larger than corresponding QCT DCSs.

In Figure 4.16, total and vibrational state resolved TIQM and QCT DCSs calculated at 0.8 eV are plotted. All the DCS curves are asymmetric in nature with intense peaks at $\sim 0°$. Both the QCT GB and HB approaches successfully describe the overall behavior of the TIQM DCSs. However, the forward and backward peaks of the total DCSs computed via QCT approaches slightly underestimate the TIQM ones, and, as products with v' = 0 state contributes more to the total DCSs, similar observations are noticed for v' = 0 results. For v' = 1, peaks observed at $\sim 0°$ and $\sim 180°$ in the QCT-HB DCSs are in good agreement with the exact results. The clear preference of the products to get forward scattered with a predominant peak at $\sim 0°$, as observed in the DCS plots, indicates that the overall dynamics is not governed by intermediate complex formation with longer lifetimes.

4.3.3 Understanding the reaction mechanisms

As discussed in Chapter 3, and also can be seen in Figure 4.1, the PES of the He+NeH$^+$ reactive system contains a potential well of depth $\sim$ 0.521 eV from the reactant asymptote. Although the potential well is shallow, dense oscillatory structures are observed in the QM reaction probabilities at low energies for small values of J (see Figure 4.3). This finding suggests the possibility of formation of an intermediate complex in the potential well during reaction, and the reaction to be a resonance mediated one. However, the resonances appeared in the QM probabilities are almost washed out in the QM ICSs (see Figure 4.9). Apart from this, TIQM and QCT DCSs calculated at different energies are asymmetric in nature and show prominent forward peaks at $\sim 0°$ (see Figures 4.15 and 4.16). These indicate that direct mechanisms may also play an important role during the reaction, though the involvement of indirect paths can not be ruled out. QCT studies are always helpful to investigate the mechanistic pathways for a reaction. In the present case, QCT-GB calculations successfully reproduce overall features of most of the TIQM results. Hence, rigorous QCT-GB studies are carried out to look into the

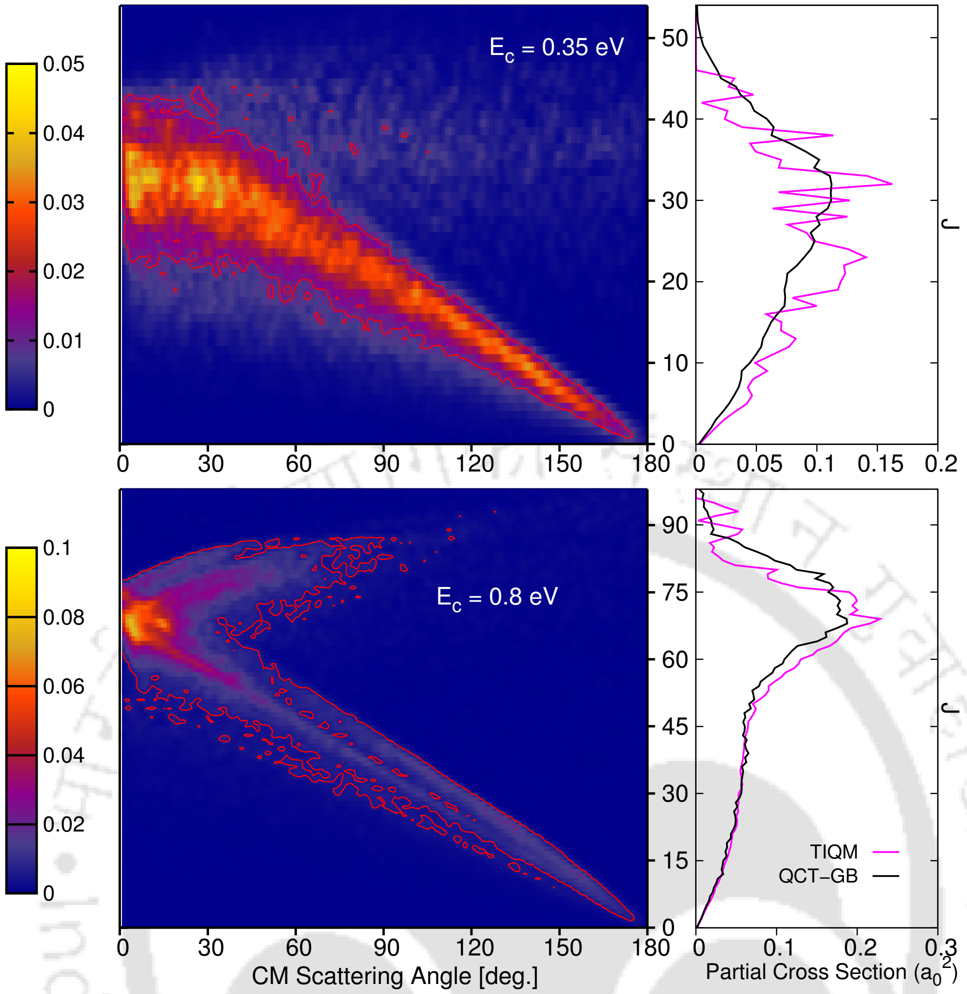

FIGURE 4.17: (left) Normalized classical deflection function, $D_r(J,\theta)$, for the He + NeH$^+$ $(v=0, j=0) \rightarrow$ HeH$^+$ + Ne reaction at $E_c = 0.35$ eV (top) and $E_c = 0.8$ eV (bottom). The solid red contour lines have magnitudes of 0.01 and 0.005 in the top and bottom panels, respectively. Enclosed areas inside the solid red lines indicate $(J-\theta)$ pairs contributing maximum to the cross sections. (right) Partial cross sections for the title reaction at $E_c = 0.35$ eV (top) and $E_c = 0.8$ eV (bottom) calculated by means of TIQM and QCT-GB methods.

microscopic details in order to reveal the underlying mechanisms for the title reaction. For this purpose, two different collision energies, 0.35 eV and 0.8 eV, are chosen.

The normalized classical deflection function, $D_r(J,\theta)$, a function of both J and scattering angle (θ), represents the correlation between angular distribution of products and orbital angular momentum or impact parameter. $D_r(J,\theta)$ is defined here as in Ref. 46:

$$D_r(J,\theta) = \frac{1}{\sigma_{\text{tot}}}\frac{\pi}{k^2}(2J+1)\frac{N_r(J,\theta)}{N_{\text{tot}}(J)}\ \frac{1}{\Delta\theta}. \tag{4.2}$$

A normalized Gaussian function, $G(\theta - \theta_i)$, where θ_i is the scattering angle for the i-th trajectory, is used during the $N_r(J, \theta)$ calculation to get a smoothed $D_r(J, \theta)$ function.

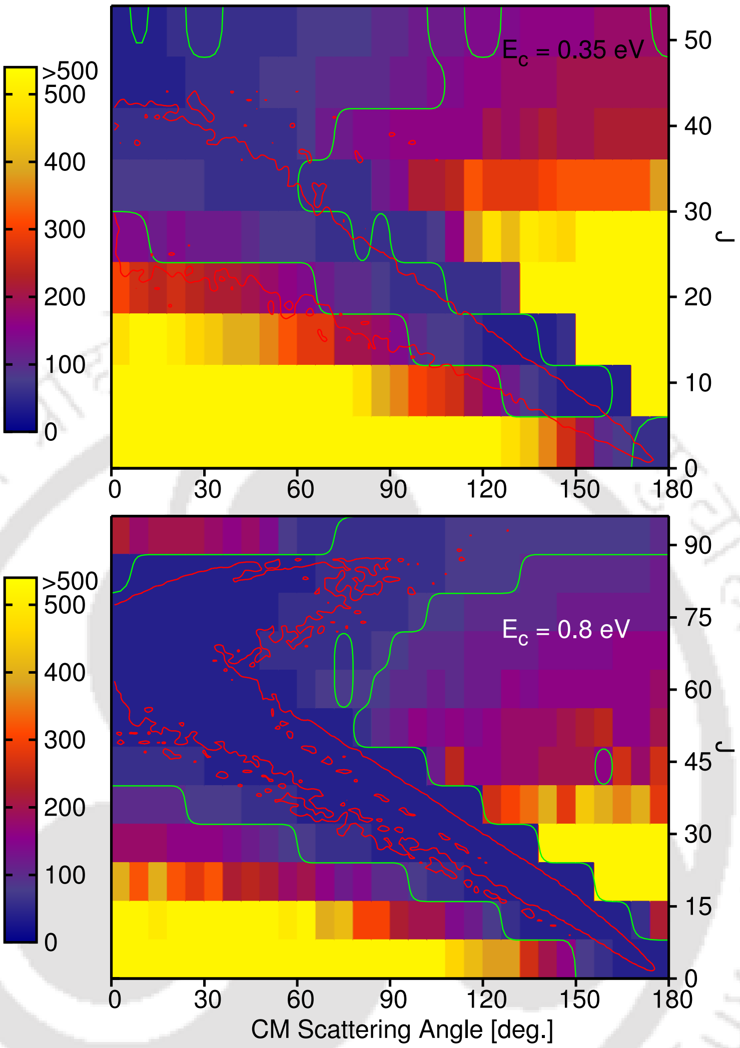

FIGURE 4.18: Average collision time, $\tilde{\tau}$, plotted as a function of CM scattering angle (θ) and J. The solid green contour lines represent a $\tilde{\tau}$ value of 75 fs. The areas marked with the solid red lines are the same as appeared in the top and bottom panels of Figure 4.17.

Figure 4.17 presents the $D_r(J, \theta)$ function (shown in left panels) and the partial cross sections, $\pi/k^2(2J + 1)P_r(J)$, (shown in right panels) at E_c = 0.35 eV and 0.8 eV. Partial cross sections calculated following QCT-GB approach (solid black lines) are in a good accord with TIQM (solid magenta lines) partial cross sections. The largest value of the total angular momentum (denoted as $J_{\max}$) are 55 and 99 for E_c = 0.35 eV and 0.8 eV, respectively. These $J_{\max}$ values correspond to the maximum impact parameter ($b_{\max}$) of 4.42 a.u. and 5.24 a.u., for E_c = 0.35 eV and 0.8 eV, respectively.

The areas inside the red solid lines represent the $(J - \theta)$ pairs for which the reaction occurs predominantly. At $E_c = 0.35$ eV, the plot shows that the larger the J, more forward is the scattering angle. However, the distribution becomes wider for large Js ($J \approx 20 - 40$). For those Js, products are formed with a wider range of scattering angles ($\theta \approx 0 - 60^\circ$) in the forward direction. At $E_c = 0.8$ eV, two distinct bands with opposite slopes are seen: The first band ranges from $\sim 180^\circ$ and small Js to 0° and large Js. The scattering angle is inversely proportional to J in this band. The second band covers a wider range of scattering angles ($\theta \approx 0 - 90^\circ$), but over a narrower range of very large total angular momentum ($J \approx 70 - 85$).

To analyze the distribution of scattering angles with respect to Js as shown in Figure 4.17, a parameter collision time (τ) is defined. For a particular trajectory τ is defined as the time elapsed between the *first* entry time of the trajectory into a certain criteria and the *last* exit time from that criteria. The criteria considered here is the sum of three inter-atomic distances have to be less than a cutoff value of 5 Å. A small value of τ corresponds to a direct path whereas a comparatively large value indicates a trapped trajectory or formation of an intermediate complex. Trapped or complex forming trajectories are observed for this reaction for trajectories with $\tau > 75$ fs. This sort of trajectories will be discussed later in this section.

In Figure 4.18, average collision times, defined as $\tilde{\tau} = 1/N_r(J,\theta) \times \sum \tau_i$ for the reactive trajectories, scattered at different angles and for different Js, are shown as contour plots at $E_c = 0.35$ eV and 0.8 eV. The area inside red contour lines are the same as described in Figure 4.17. The trajectories located inside the green contour lines in Figure 4.18 have $\tilde{\tau} < 75$ fs, and most of them follow a direct path for the reaction. As observed in Figure 4.18, most of the trajectories follow direct paths at $E_c = 0.8$ eV. However, at $E_c = 0.35$ eV, indirect dynamics has some role to play. The contributions of the reactive trajectories with collision time τ to the ICS (σ_τ) are plotted as solid blue lines in Figure 4.19 at $E_c = 0.35$ eV and 0.8 eV. Normalized cumulative distributions (σ_c) of the ICSs with respect to collision time are plotted as dashed red lines in the

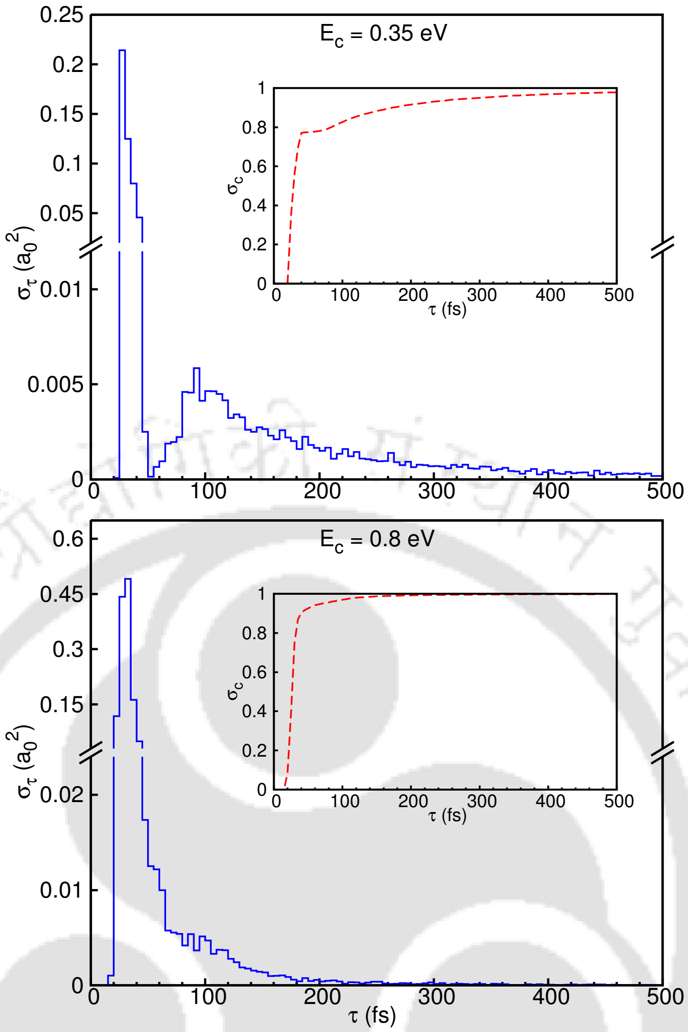

FIGURE 4.19: ICS vs collision time plot at two different collision energies for the He + NeH$^+$ ($v = 0, j = 0$) $\rightarrow$ HeH$^+$ + Ne reaction. (Inset) Normalized cumulative distribution of the ICSs with respect to collision time.

insets of Figure 4.19. σ_c is defined as

$$\sigma_c(\tau) = \frac{1}{\sigma_{\text{tot}}} \int_0^{\tau} \sigma_\tau d\tau. \tag{4.3}$$

Two distinct maxima at $\sim$ 30 fs and $\sim$ 95 fs can be seen in the ICS vs collision time plot (solid blue line) for $E_c = 0.35$ eV. The first maximum, at $\sim$ 30 fs, relates to the direct dynamics pathways for the reaction, whereas the second maximum appearing at $\sim$ 95 fs hints at the indirect dynamics paths. The cumulative distribution shows that $\sim$ 80% of the contribution is coming from direct trajectories ($\tau < 75$ fs) for $E_c = 0.35$ eV. It can also be seen that there are few trajectories with $\tau > 500$ fs, and those trajectories contribute only $\sim$ 2% to the ICS. The distribution of ICSs for $E_c = 0.8$ eV decreases

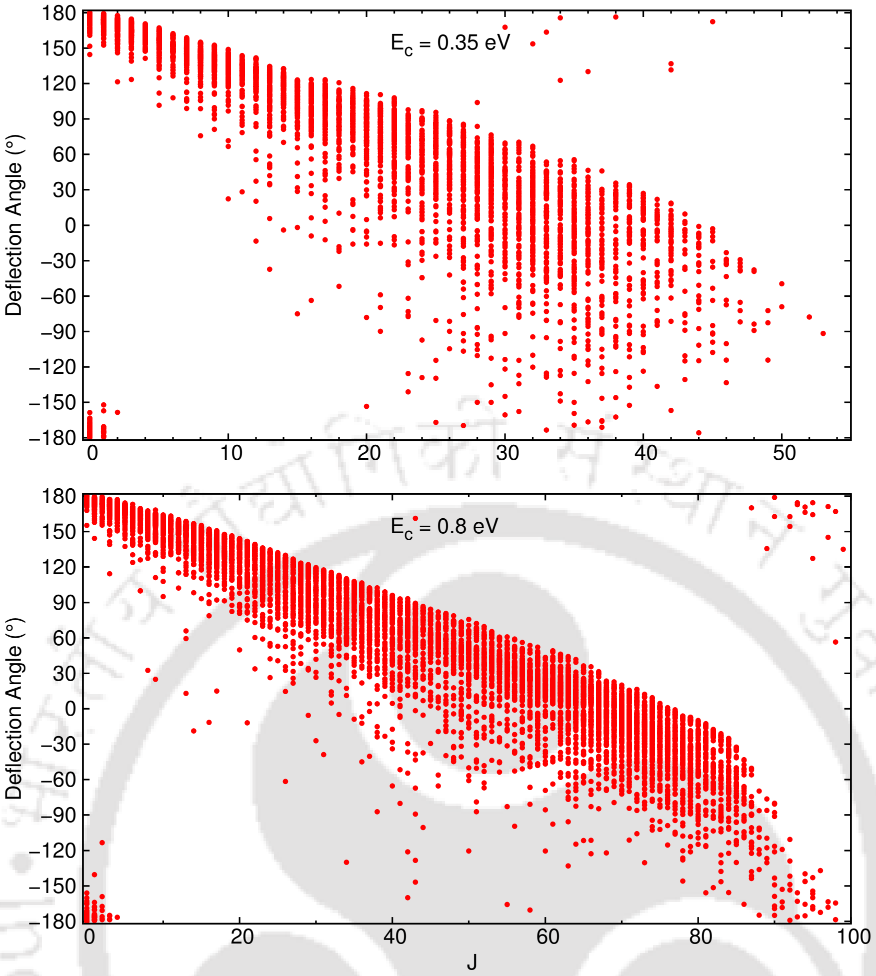

FIGURE 4.20: Deflection angle vs J plot for the direct trajectories ($\tau < 75$ fs) at $E_c =$ 0.35 eV and 0.8 eV.

smoothly after the maximum appeared at ∼ 35 fs. As can be seen in the cumulative distribution function plotted in Figure 4.19 for $E_c = 0.8$ eV, ∼ 95% of the reaction proceeds via direct mechanisms. It is found that at $E_c = 0.8$ eV, trajectories with $\tau > 500$ fs contribute less than 0.2% to the ICS.

In order to explore the mechanistic pathways related to direct trajectories, deflection angle (θ_d) ranging from $-180°$ to $180°$ are calculated for the reactive trajectories with $\tau < 75$ fs at $E_c = 0.35$ eV and 0.8 eV. In Figure 4.20, deflection angle is plotted for different Js for few of those trajectories having large weightage in GB calculations. As can be seen in Figure 4.20, the trajectories with small impact parameters (low Js) follow a mechanism where He atom strikes the NeH$^+$ diatom directly and then, the product HeH$^+$ gets rebound in the backward direction with a large scattering angle ($\theta_d \approx 120° - 180°$). A small fraction of those trajectories with very small impact parameters are farside scattered ($\theta_d \approx -180°$), where the y-component of the product relative velocity vector is negative. It is to be noted that the center of mass of the reactant diatom and the free He atom lie in the yz plane with the relative velocity vector along the positive z-axis and R_y, the y component of the vector $\mathbf{R}$, which is directed from He to center of mass of NeH^+, is ≤ 0 (see the intial arrangement of the reactive system in Chapter 2, Figure 2.2). For the trajectories with moderate b (or J) values, the He atom makes a glancing collision with NeH^+ diatom and HeH^+ scattered at sideway directions ($\theta_d \approx 45° - 120°$). The trajectories with comparatively large impact parameters (or Js) form forward scattered products ($\theta_d \approx 0° - 45°$), which indicates a spectator-stripping mechanism,[47] where glancing blow type collisions between NeH^+ and He atom strips the proton so suddenly that little deflection of the products occur. However, there are some trajectories with comparatively larger J values for which farside scattering occur in forward direction ($0° > \theta_d \gtrsim -45°$). The trajectories with very large Js predominantly show farside scattering covering wide range of θ_d. Attractive nature of the PES for the present system are mainly responsible for this type of farside scattering.

In order to analyze the types of trajectories involved in indirect dynamics pathways for the title reaction, four selected reactive trajectories associated with indirect pathways are presented in Figure 4.21. The trajectories depicted in Figure 4.21 (a) and (b) show two typical complex-forming trajectories with large lifetimes. As can be seen in panel (a), a long-lived collision-complex with lifetime of $\sim$ 233 fs formed in the potential well region of the PES. In panel (b), the collision-complex has a lifetime of $\sim$ 95.3 fs. Although τ is not exactly the lifetime of the collision-complex, for a tightly bound complex (as it is for the trajectories represented in Figure 4.21 (a) and (b)), τ can be approximated as the lifetime of the complex. The trajectories shown in Figure 4.21 (c) and (d) are examples of two long-lived trajectories. For these trajectories, after the first collision, the reactant or the product diatom (if product is formed) is exited internally (either vibrationally or rotationally or both vibrationally and rotationally), and there is too small translational energy left to allow dissociation, and thus forming a weakly bound collision complex. This type of trajectories are called *roaming* trajectories.[48,49] Both the reactive and nonreactive trajectories may be trapped in the roaming region of the PES for a system for a long time to produce roaming trajectories. It is found that for

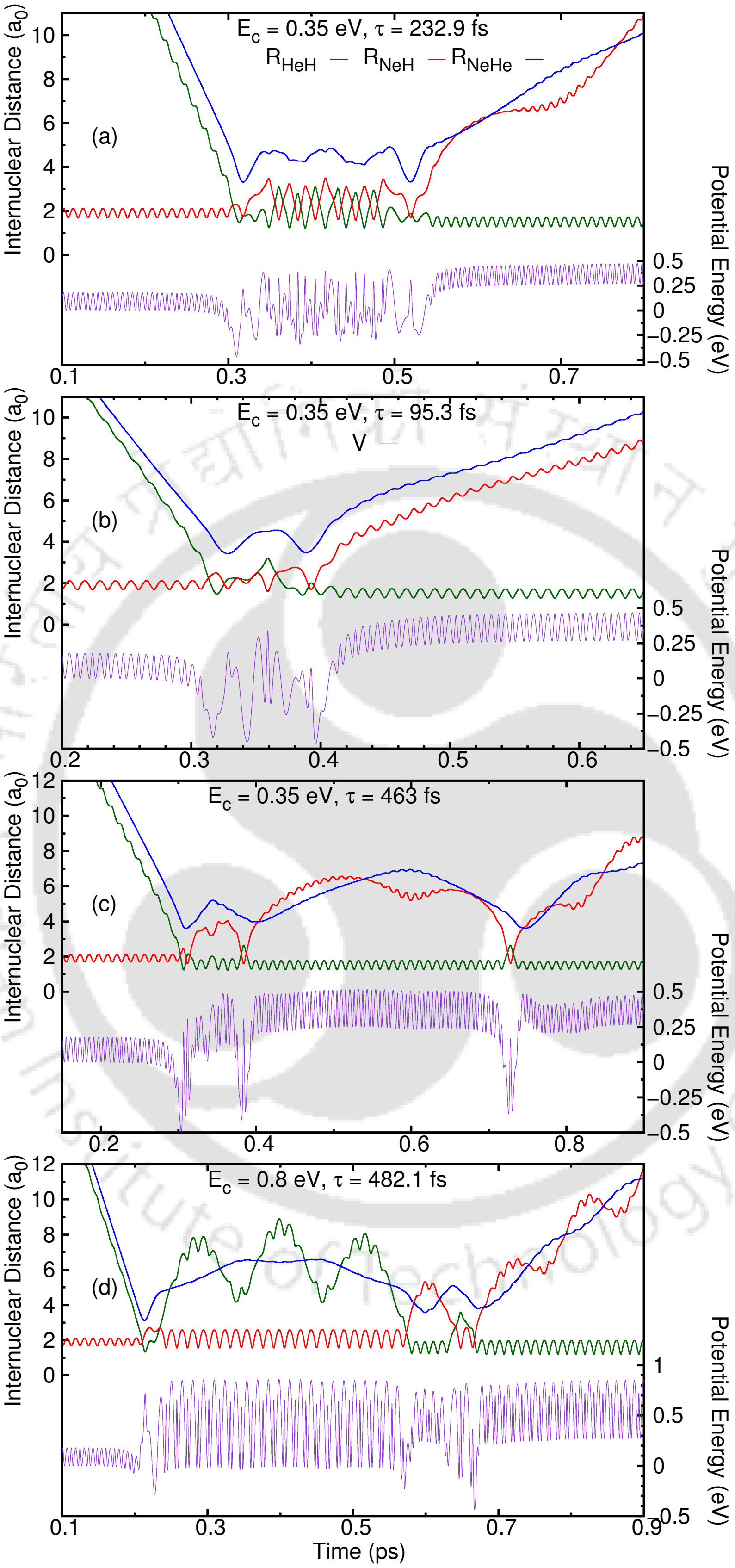

FIGURE 4.21: Time evolution of both the inter-particle distances and the potential energy measured with respect to the He + NeH$^+$ asymptote for four representative complex-forming trajectories at E_c = 0.35 and 0.8 eV. Associated collision times are mentioned.

the present case most of the longly lived trajectories are roaming type trajectories. The smallest rotational period τ_{rot} of the intermediate complex formed in a complex forming trajectory is estimated from the equilibrium geometry of the [HeHNe]$^+$ complex, i.e., the collinear [HeHNe]$^+$, as $\tau_{\text{rot}} = 2\pi I/L\hbar$. Here I is the moment of inertia of [HeHNe]$^+$, and L is the orbital angular momentum. τ_{rot} values are estimated to be 296 fs and 149 fs at 0.35 eV and 0.8 eV, respectively. It is found that very few reactive trajectories have collision times larger than τ_{rot} and among those most are roaming trajectories. Hence, it can be concluded that the reaction is mainly governed by direct dynamics and complex-forming mechanisms have comparatively less effect on this reaction.

4.4 CONCLUSIONS

In this chapter, TDWP and TIQM methods have been applied to compute different initial reactant ro-vibrational state selected total reaction probabilities and total ICSs for the He + NeH$^+$ reaction on the ground electronic state. The state-to-state dynamics of this reaction is also studied for ground ro-vibrational reactant state by means of TIQM and QCT calculations. Dense resonance structures observed in the probability curves for low values of J in the low energy region are mostly washed out in the ICSs curves. For all the three combinations of initial states, noticeable differences are observed between TDQM-CC and TDQM-CS results, although differences are smaller for smaller J values. These observations indicate the importance of inclusion of Coriolis coupling in the quantum mechanical studies for the title reaction. Vibrational excitation of the reactants strongly enhances the reaction, while rotational excitation has small effect on the reaction. QCT-GB results are in a fair agreement with TIQM state-to-state results. DCSs for the reaction are asymmetric in nature and show pronounced forward peaks at $\theta \approx 0°$. Different mechanistic pathways for the title reaction have been explored via rigorous QCT calculations. The reaction is mainly direct. Both nearside and farside scatterings have been observed for the reactive trajectories with direct mechanisms. Indirect dynamics influences the reaction at low energies. Significant number of complex-forming (short-lived as well as long-lived including roaming) trajectories are found for the title reaction at low collision energies.

References

[1] Croswell, K. *The Alchemy of the Heavens: Searching for Meaning in the Milky Way;* New York: Anchor Books/Doubleday, 1995.

[2] Zygelman, B.; Stancil, P. C.; Dalgarno, A. *Astrophys. J.* **1998**, *508*, 151.

[3] Ferrière, K. M. *Rev. Mod. Phys.* **2001**, *73*, 1031.

[4] Lepp, S.; Stancil, P. C.; Dalgarno, A. *J. Phys. B: At. Mol. Opt. Phys.* **2002**, *35*, R57.

[5] Palmieri, P.; Puzzarini, C.; Aquilanti, V.; Capecchi, G.; Cavalli, S.; de Fazio, D.; Aguilar, A.; Giménez, X.; Lucas, J. M. *Mol. Phys.* **2000**, *98*, 1835.

[6] Panda, A. N.; Sathyamurthy, N. *J. Chem. Phys.* **2005**, *122*, 054304.

[7] Tang, X. N.; Xu, H.; Zhang, T.; Hou, Y.; Chang, C.; Ng, C. Y.; Chiu, Y.; Dressler, R. A.; Levandier, D. J. *J. Chem. Phys.* **2005**, *122*, 164301.

[8] Lv, S.-J.; Zhang, P.-Y.; Han, K.-L.; He, G.-Z. *J. Chem. Phys.* **2010**, *132*, 014303.

[9] Zhao, J.; Luo, Y. *J. Phys. Chem. A* **2012**, *116*, 2388.

[10] de Fazio, D.; de Castro-Vitores, M.; Aguado, A.; Aquilanti, V.; Cavalli, S. *J. Chem. Phys.* **2012**, *137*, 244306.

[11] Zhang, T.; Qian, X.-M.; Tang, X. N.; Ng, C. Y.; Chiu, Y.; Levandier, D. J.; Miller, J. S.; Dressler, R. A. *J. Chem. Phys.* **2003**, *119*, 10175.

[12] Xiao, J.; Yang, C.-L.; Tong, X.-F.; Wang, M.-S.; Ma, X.-G. *J. Phys. Chem. A* **2011**, *115*, 1486.

[13] Gamallo, P.; Defazio, P.; González, M. *J. Phys. Chem. A* **2011**, *115*, 11525.

[14] Gamallo, P.; Huarte-Larrañaga, F.; González, M. *J. Phys. Chem. A* **2013**, *117*, 5393.

[15] Gamallo, P.; Martínez, R.; Sierra, J. D.; González, M. *Phys. Chem. Chem. Phys.* **2014**, *16*, 6641.

[16] Maiti, B.; Kalyanaraman, C.; Panda, A. N.; Sathyamurthy, N. *J. Chem. Phys.* **2002**, *117*, 9719.

[17] Qian, X.-M.; Zhang, T.; Chiu, Y.-H.; Levandier, D. J.; Miller, J. S.; Dressler, R. A.; Ng, C. Y. *J. Chem. Phys.* **2003**, *118*, 2455.

[18] Panda, A. N.; Althorpe, S. C. *Chem. Phys. Lett.* **2006**, *419*, 245 .

[19] Dressler, R. A.; Chiu, Y.; Levandier, D. J.; Tang, X. N.; Hou, Y.; Chang, C.; Houchins, C.; Xu, H.; Ng, C.-Y. *J. Chem. Phys.* **2006**, *125*, 132306.

[20] Liu, X.; Liu, H.; Zhang, Q. *Chem. Phys. Lett.* **2011**, *507*, 24 .

[21] Hu, M.; Xu, W.; Liu, X.; Tan, R.; Li, H. *J. Chem. Phys.* **2013**, *138*, 174305.

[22] de Fazio, D. *Phys. Chem. Chem. Phys.* **2014**, *16*, 11662.

[23] Gamallo, P.; Akpinar, S.; Defazio, P.; Petrongolo, C. *J. Phys. Chem. A* **2014**, *118*, 6451.

[24] Esposito, F.; Coppola, C. M.; Fazio, D. D. *J. Phys. Chem. A* **2015**, *119*, 12615.

[25] Bhattacharya, S.; Panda, A. N. *J. Phys. B: At. Mol. Opt. Phys.* **2009**, *42*, 085201.

[26] Liang, J.-J.; Yang, C.-L.; Wang, L.-Z.; Zhang, Q.-G. *J. Chem. Phys.* **2012**, *136*, 094307.

[27] Xu, W.; Zhang, P. *J. Phys. Chem. A* **2013**, *117*, 1406.

[28] Wu, D.; Guo, M.; Wang, Y.; Yin, S.; Sun, Z.; Hoffmann, M. R. *Theor. Chem. Acc.* **2014**, *133*, 1552.

[29] Skouteris, D.; Castillo, J. F.; Manolopoulos, D. E. *Comput. Phys. Commun.* **2000**, *133*, 128.

[30] Aoiz, F. J.; Sáez-Rabanos, V.; Martínez-Haya, B.; González-Lezana, T. *J. Chem. Phys.* **2005**, *123*, 094101.

[31] Guo, H. *Int. Rev. Phys. Chem.* **2012**, *31*, 1.

[32] Aslan, E.; Bulut, N.; Castillo, J. F.; Bañares, L.; Roncero, O.; Aoiz, F. J. *J. Phys. Chem. A* **2012**, *116*, 132.

[33] Xu, W.; Li, W.; Lv, S.; Zhai, H.; Duan, Z.; Zhang, P. *J. Phys. Chem. A* **2012**, *116*, 10882.

[34] Aguado, A.; Paniagua, M.; Lara, M.; Roncero, O. *J. Chem. Phys.* **1997**, *107*, 10085.

[35] González-Sánchez, L.; Vasyutinskii, O.; Zanchet, A.; Sanz-Sanz, C.; Roncero, O. *Phys. Chem. Chem. Phys.* **2011**, *13*, 13656.

[36] Rao, T. R.; Goswami, S.; Mahapatra, S.; Bussery-Honvault, B.; Honvault, P. *J. Chem. Phys.* **2013**, *138*, 094318.

[37] Lin, S. Y.; Guo, H. *J. Phys. Chem. A* **2004**, *108*, 2141.

[38] Lin, S. Y.; Guo, H. *Phys. Rev. A* **2006**, *74*, 022703.

[39] Bañares, L.; Aoiz, F.; Honvault, P.; Bussery-Honvault, B.; Launay, J.-M. *J. Chem. Phys.* **2003**, *118*, 565.

[40] Bañares, L.; Aoiz, F. J.; Honvault, P.; Launay, J.-M. *J. Phys. Chem. A* **2004**, *108*, 1616.

[41] Panda, A. N.; Herráez-Aguilar, D.; Jambrina, P. G.; Aldegunde, J.; Althorpe, S. C.; Aoiz, F. J. *Phys. Chem. Chem. Phys.* **2012**, *14*, 13067.

[42] Gómez-Carrasco, S.; González-Sánchez, L.; Aguado, A.; Roncero, O.; Alvariño, J. M.; Hernández, M. L.; Paniagua, M. *J. Chem. Phys.* **2004**, *121*, 4605.

[43] Nyman, G.; Wilhelmsson, U. *J. Chem. Phys.* **1992**, *96*, 5198.

[44] Gilibert, M.; Giménez, X.; Huarte-Larrañaga, F.; González, M.; Aguilar, A.; Last, I.; Baer, M. *J. Chem. Phys.* **1999**, *110*, 6278.

[45] Jambrina, P. G.; Aoiz, F. J.; Bulut, N.; Smith, S. C.; Balint-Kurti, G. G.; Hankel, M. *Phys. Chem. Chem. Phys.* **2010**, *12*, 1102.

[46] Menéndez, M.; Castillo, J. F.; Martínez-Haya, B.; Aoiz, F. J. *Phys. Chem. Chem. Phys.* **2015**, *17*, 25471.

[47] Truhlar, D. G.; Muckerman, J. T. In *Atom - Molecule Collision Theory*; Bernstein, R. B., Ed.; Springer US, 1979; pages 505.

[48] Bowman, J. M. *Mol. Phys.* **2014**, *112*, 2516.

[49] Mauguière, F. A.; Collins, P.; Ezra, G. S.; Farantos, S. C.; Wiggins, S. *Chem. Phys. Lett.* **2014**, *592*, 282.

Chapter 5

The Ne + HeH$^+$ → NeH$^+$ + He Reaction

In this chapter, the dynamics of Ne + HeH$^+$ → NeH$^+$ + He reaction is reported by carrying out time-independent quantum mechanical, time-dependent real wave packet and quasiclassical trajectory calculations. Total reaction probabilities and ICSs have been calculated for the title reaction with the reactants in ground ro-vibrational, first excited rotational and first excited vibrational states. TDQM calculations have been performed within both the CC and CS frameworks. Initial state selected rate constants for the title reaction are computed between 20 and 1000 K. ICSs and rate constant are also calculated by following the Langevin capture model. A few collision energies are chosen to investigate the state-to-state dynamics for the title reaction for ground ro-vibrational reactant state. TIQM and QCT methods are applied to calculate the ro-vibrational distributions and DCSs. Different mechanisms associated to this reaction are investigated as a function of the collision energy.

Parts of the contents of this chapter are published in the following research articles:

- Koner, D.; Barrios, L.; González-Lezana, T.; Panda, A. N. Quantum, Statistical, and Quasiclassical Trajectory Studies For the Ne + HeH$^+$ → NeH$^+$ + He Reaction on the Ground Electronic State. J. Phys. Chem. A **2015**, *119*, 12052.
- Koner, D.; Barrios, L.; González-Lezana, T.; Panda, A. N. State-to-State Dynamics of the Ne + HeH$^+$(v = 0, j = 0) → NeH$^+$(v', j') + He Reaction. J. Phys. Chem. A **2016** *doi:10.1021/acs.jpca.5b11477.*

5.1 INTRODUCTION

Hydrogen and helium, the two most abundant elements of our galaxy, are the results of primordial nucleosynthesis, which played an important role in the early universe evolution scenario.[1–4] In a series of chemical reactions, these elements formed the first molecular ionic system of the universe, HeH^+,[2,5] which was then followed by formation of H_2^+,[5] Other two light rare gases neon and argon are also present in a considerable amount in the ISM.[6–9] In fact, neon is the fifth most abundant element in our solar system.[10] Reactive collisions are thus possible in the ISM environment among the light rare gases, proton (H^+), HeH^+ and H_2^+. Dynamics of reactions involving light rare gas atoms (He, Ne and Ar) and hydrogen molecular ion has been studied widely in the last few decades.[11–27] The first active chemical reaction $HeH^+ + H \rightarrow He + H_2^+$, in our universe[5] has been studied recently in the ultra cold to hyperthermal region via TIQM, TDWP and QCT methods by different groups.[28–30] The $He + HeH^+ \rightarrow HeH^+ + He$ reaction has also been widely studied theoretically by TDQM and QCT approaches.[31–34] This type of proton transfer process is either mediated by resonances or follow complex-forming mechanisms due to the presence of potential energy well along the reaction path, which results in numerous resonances in the corresponding reaction probabilities. Most of these atom-molecular ion reactions are barrierless and can take place at very low temperatures. Therefore, besides a fundamental relevance on the dynamics of such processes, their study can also provide useful knowledge regarding the evolution of the ISM. The $Ne + HeH^+ \rightarrow NeH^+ + He$ reaction was studied by Glosík *et al.*[35] experimentally by using selected ion flow tube apparatus, and the rate constant at 300 K has been reported to be $1.25\pm0.625\times10^{-9}$ cm^3 s^{-1}. ISM. A DIM PES was constructed by Matcha *et al.*[36] for the collinear $[HeHNe]^+$ system. However, reactive scattering study of this reaction by means of theoretical calculations has not been reported in the literature.

In this Chapter, a detailed theoretical study for the $Ne + HeH^+ \rightarrow NeH^+ + He$ reaction is reported based on the analytical PES discussed in Chapter 3. A schematic potential energy profile for the process is shown in Figure 5.1. Different ro-vibrational states of reactants and products are also presented in the same figure. As it is seen, the reactive process is barrierless and exothermic by 0.293 eV. The PES is characterized by a potential well with maximum depth of ∼ 0.8 eV (with respect to the reactant asymptote) for a collinear He-H-Ne configuration (∠HeHNe = 180°), with values of the internuclear distances of $R_{\mathrm{NeH}} = 2.102$ a.u. and $R_{\mathrm{HeH}} = 1.804$ a.u.

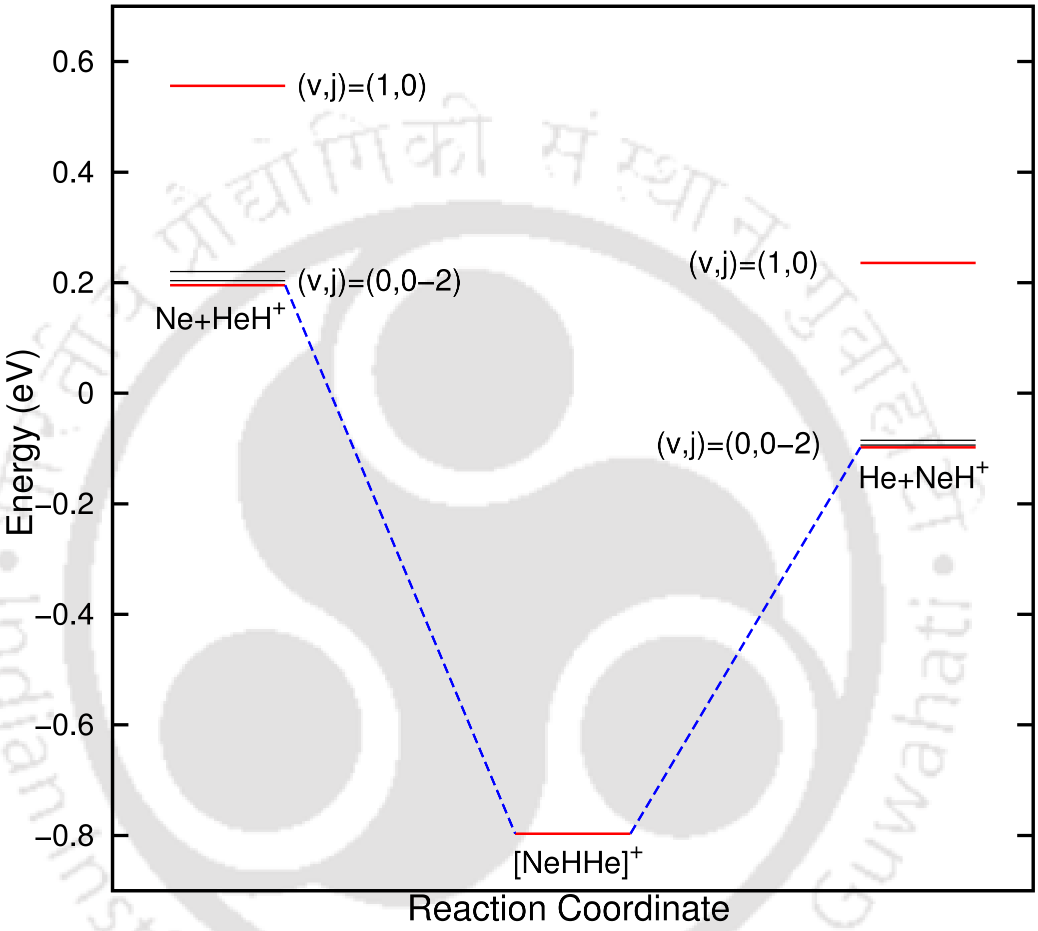

Figure 5.1: Schematic potential energy profile of reactants and products for the Ne + $HeH^+ \rightarrow NeH^+$ + He reaction. Energy of Ne+HeH^+ asymptote is set as zero.

5.2 METHODS

TDQM, TIQM and QCT methodologies have been used to explore the initial state selected as well as state-to-state dynamical attributes for the title reaction. Details of the TDQM methodology associated to the TDQM code used here is discussed in Chapter 2. In brief, TDSE is solved numerically following CRWP method and the total reaction probabilities have been computed by calculating the flux. The title reaction is investigated by Coriolis coupled TDQM calculations and also under CS approximation scheme within a collision energy range 0.001 - 0.5 eV. TDQM parameters were converged by running several test runs. The converged parameters used in the TDQM calculations are tabulated in Table 5.1

TABLE 5.1: Parameters used in the TDQM calculations (All parameters are given in atomic units).

Number of R grid points	310
Number of r grid points	132
Number of angular grid points	130
R_{min}	0.2
r_{min}	0.5
δR	0.09
δr	0.13
Centre of initial wave packet	15.0
Starting points of damping along R and r	19.0, 12.59
Analysis point along r	12.46
Number of Chebyshev iterations	22000

In Figure 5.2, total reaction probabilities calculated including different numbers of helicity terms are plotted for different initial states and $J = 60$. It is clear that a value of $K_{\max} = 9$ is sufficient to get converged results for the present case. As the CC calculations are computationally expensive, for $(v, j) = (0,\ 1)$ and $(1,\ 0)$, exact total reaction probabilities were calculated for all the Js less than 40 and for some selected Js (45, 50, 55, ..., $J_{\max}$) thereafter. A 'J-shifting' approximation, discussed in Chapter 2, was then applied to calculate the probabilities for the remaining Js.

All the TIQM calculations are carried out using the ABC code of Manolopoulos and coworkers.[37] Initial state selected total reaction probabilities for few selected Js and total ICSs at few selected energies have been calculated to compare with the TDQM results. For computing the state-to-state attributes, TIQM calculations are performed at the following specific energies: 0.005, 0.01, 0.05, 0.1, 0.2, 0.3, 0.4 and 0.5 eV. Many test runs are performed to converge the results with respect to different initial parameters. The optimal parameters used for the final set of calculations for different energy regimes are listed in Table 5.2. Convergence between three and five decimal figures for the state-to-state reaction probabilities has been reached using this set of parameters. It can be

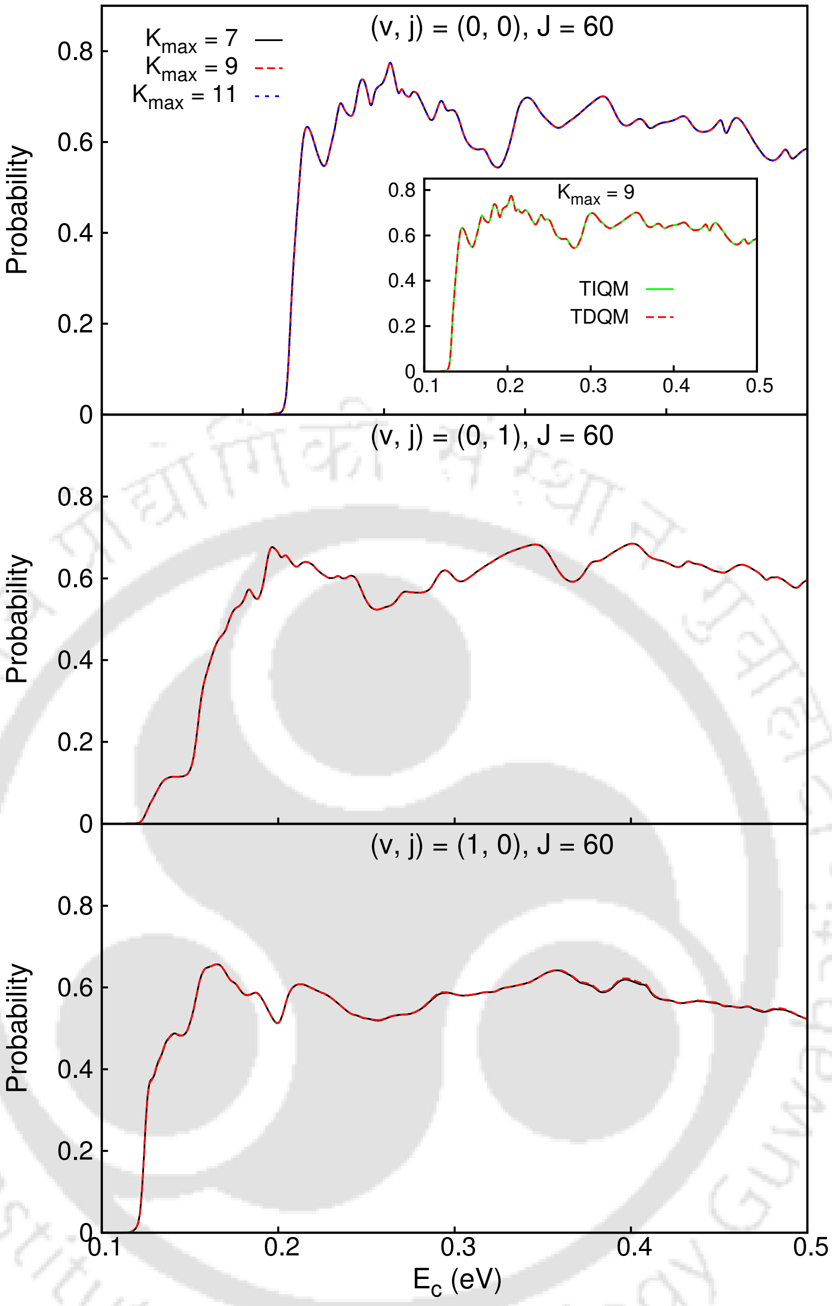

FIGURE 5.2: Convergence of the TDQM reaction probability values with respect to the K_{max} value plotted for different initial states and $J = 60$. Inset in the top panel shows the comparison between TIQM and TDQM probabilities for $J = 60$ and $(v, j) = (0, 0)$ with $K_{\mathrm{max}} = 9$.

seen in 5.2 that a value of $K_{\mathrm{max}} = 9$ is sufficient to converge the TIQM total reaction probabilities. Hence, although a value of $K_{\mathrm{max}} = 18$ is used to calculate the state-to-state dynamical attributes, a value of $K_{\mathrm{max}} = 9$ is used to calculate the total attributes (computed for different initial states to compare with the TDQM results).

Table 5.2: Numerical parameters employed in the TIQM calculations.

Maximum hyperradius ($\rho_{\max}$/bohr)	30 ($E_c \le 0.01$ eV) 25 ($E_c > 0.01$ eV)
Number of log derivative propagation sectors ($n_{\rm sec}$)	326 ($E_c \le 0.01$ eV) 264 ($E_c > 0.01$ eV)
Maximum rotational quantum number ($j_{\max}$)	30
Maximum internal energy ($e_{\max}$/eV)	1.8
Helicity truncation parameter ($K_{\max}$)	min($18, J$) (state-to-state) min($9, J$) (state-averaged)

In the QCT approach, the set of Hamilton's first-order differential equations of motion are numerically integrated with standard Monte Carlo sampling of the initial conditions. The methodological details has been explained thoroughly in Chapter 2. A fixed time step of 2 a.u. is used in the integrations, which guaranteed conservation of the total energy and the angular momentum up to eighth and ninth decimal places, respectively. Histogram binning method is used to calculate the total reaction probabilities and ICSs. J-dependent total reaction probabilities were computed by running a batch of 20000 trajectories at each collision energy. Total ICSs at different collision energies (E_c) for different initial states are calculated by following the b-sampling method as

$$\sigma_{v,j}(E_c) = \pi b^2_{\max} \frac{N_r(E_c)}{N_{\rm tot}(E_c)}, \tag{5.1}$$

where N_r and $N_{\rm tot}$ are the number of reactive and total trajectories, respectively, and $b_{\max}$ is the maximum value of impact parameter for a reactive trajectory at a particular collision energy. For a particular collision energy $b_{\max}$ is calculated by running a small batch of trajectories (2000 - 10000s). Batches of 40000 trajectories were calculated at each collision energy to determine the ICSs.

As mentioned earlier, a few collision energies have been chosen to investigate the state-to-state dynamics for the title reaction starting from ground ro-vibrational state of the reactants. DCSs and ro-vibrational distributions are calculated by means of QCT calculations at different collision energies by running batches of 300000 - 600000 trajectories. A J-sampling technique (discussed in Chapter 2) is used rather than continuous impact parameter sampling to calculate ICSs and DCSs at a particular collision energy. To assign the product internal states, both the HB and GB approaches are followed.

5.3 RESULTS AND DISCUSSION

This section reports the final state averaged results for three different initial states, (v, j) = (0, 0), (0, 1) and (1, 0) obtained from TDQM-CC, TDQM-CS, TIQM and QCT-HB calculations, and the state-to-state results for the reactants in the state (v, j) = (0, 0) obtained from TIQM, QCT-HB and QCT-GB calculations. In addition to discussing the results, the mechanistic pathways followed by the reaction at different collision energies are also explored.

5.3.1 Initial state selected dynamics

5.3.1.1 Total reaction probabilities

Initial state-selected TDQM-CC total reaction probabilities for some selected J values are plotted as a function of collision energy in Figure 5.3. At low values of the total angular momentum, e.g., $J \approx 10$ the reaction probabilities starts at the minimum E_c considered here. The situation changes as J increases, and for $J > 20$, a clear threshold for the reaction due to the corresponding centrifugal barriers is manifested. The numerous existing sharp resonances for low values of J, with widths typically ~ 0.001 eV, may have their origin in the PES well, which can trap the collision-complex for a certain time. These probabilities reach values close to 1 in the low-energy range and then gradually decrease with increase in collision energy. This type of behavior has been observed for other barrierless exothermic reactions.[27,29,38–42] However, in the case of $(v, j) = (0, 0)$, an increasing behavior of the probabilities is noticed in the high-energy regime for small J values. For $J > 40$, probability curves become remarkably smoother as resonances are much broader.

Similar calculations were performed for the reaction initiated from either rotationally or vibrationally excited HeH$^+$, and the corresponding results are shown in Figure

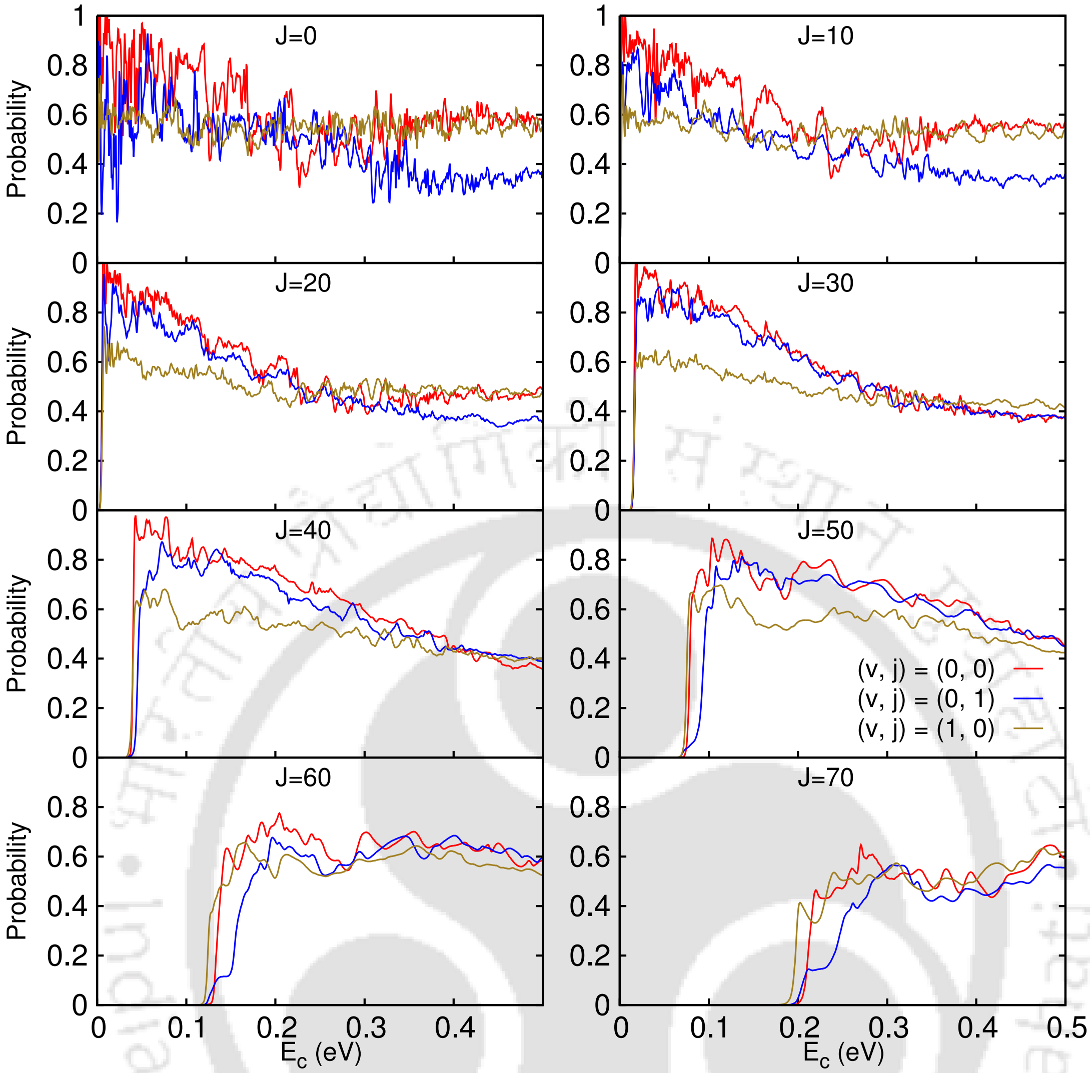

FIGURE 5.3: TDQM-CC total reaction probabilities for Ne + HeH$^+$ → NeH$^+$ + He reaction for different initial reactants ro-vibrational states for some selected J values.

5.3. The probabilities for $(v, j) = (0, 1)$ follow a similar pattern to that of $(v, j) = (0, 0)$, that is, very high values at lower-energy region and then a gradual decrease with energy. But for J = 0 - 20, there are significant differences in magnitudes between the probabilities for (v, j) = (0, 0) and (0, 1), thus showing an average reduction of the reaction for the case of rotationally excited reactants. Such an inhibition of the reactivity by rotational excitation of the reactants has been reported for many other barrierless exothermic processes.[41,42] As shown in Chapter 3, the minimum-energy path for the reaction corresponds to a collinear or near-collinear approach of the reactants. Rotationally excited reactants disrupt this preferred orientation for the collision, and as a result, reactivity decreases when the process is initiated from HeH$^+$ $(v = 0, j = 1)$.

Figure 5.3 also shows noticeable differences with respect to the case $(v, j) = (1, 0)$, which for smaller J values have quite different patterns than the probabilities for $(v, j) = (0, 0)$. Probabilities for vibrationally excited reactants are almost invariant, oscillating within 0.5 and 0.65, with respect to the collision energy in the whole region. The probabilities for $(v, j) = (1, 0)$ are smaller than that for $(v, j) = (0, 0)$, up to $J = 50$, in the low-energy region, but become similar at high collision energies. Thus, the vibrational excitation of the reactant molecules reduces the reactivity of the title collision to a large extent in the low-energy region.

A comparison between the total reaction probabilities for some selected J values calculated via the TDQM-CC, TDQM-CS, TIQM and QCT-HB methods is presented in Figures 5.4, 5.5 and 5.6 for the title reaction with the reactants in $(v, j) = (0, 0)$, $(0, 1)$ and $(1, 0)$ states, respectively. An excellent agreement between TIQM (blue dashed lines and filled circles) and TDQM-CC results can be seen in the entire energy regimes (except at ultra low energies). The QM results display a marked oscillatory character, although the average performed over the K states in the CC calculations smooths somehow the corresponding TDQM-CC probabilities. Interestingly differences between CS and CC approaches become significant as the total angular momentum becomes larger, thus suggesting that Coriolis coupled states cannot be ignored within the QM framework for sufficiently high values of J. Differences observed in the threshold values of the CC and CS probabilities for high values of J can be correlated to lowering of centrifugal barriers in the effective potentials by having more number of K states in the CC calculations (only a single K state, here $K = 0$, is included in the CS calculations). Some TDQM probabilities are found to have values greater than 1 in the low collision energy regime, a feature also observed in the literature for barrierless exothermic reactions studied via TDWP methods.[27,38,40,43] This may result either from poor absorption of the WP by the absorbing potential at the end of the grid or insufficient number of Chebyshev iteration steps (a large number of iteration steps are required to converge the probabilities at low energies, which was not possible in this case due to use of computationally affordable finite grid). Many test runs were performed by varying the absorption parameters, and no better convergence was found for the present grid. Probably a finer grid and propagation of the WP upto sufficiently long time are needed for a complete convergence

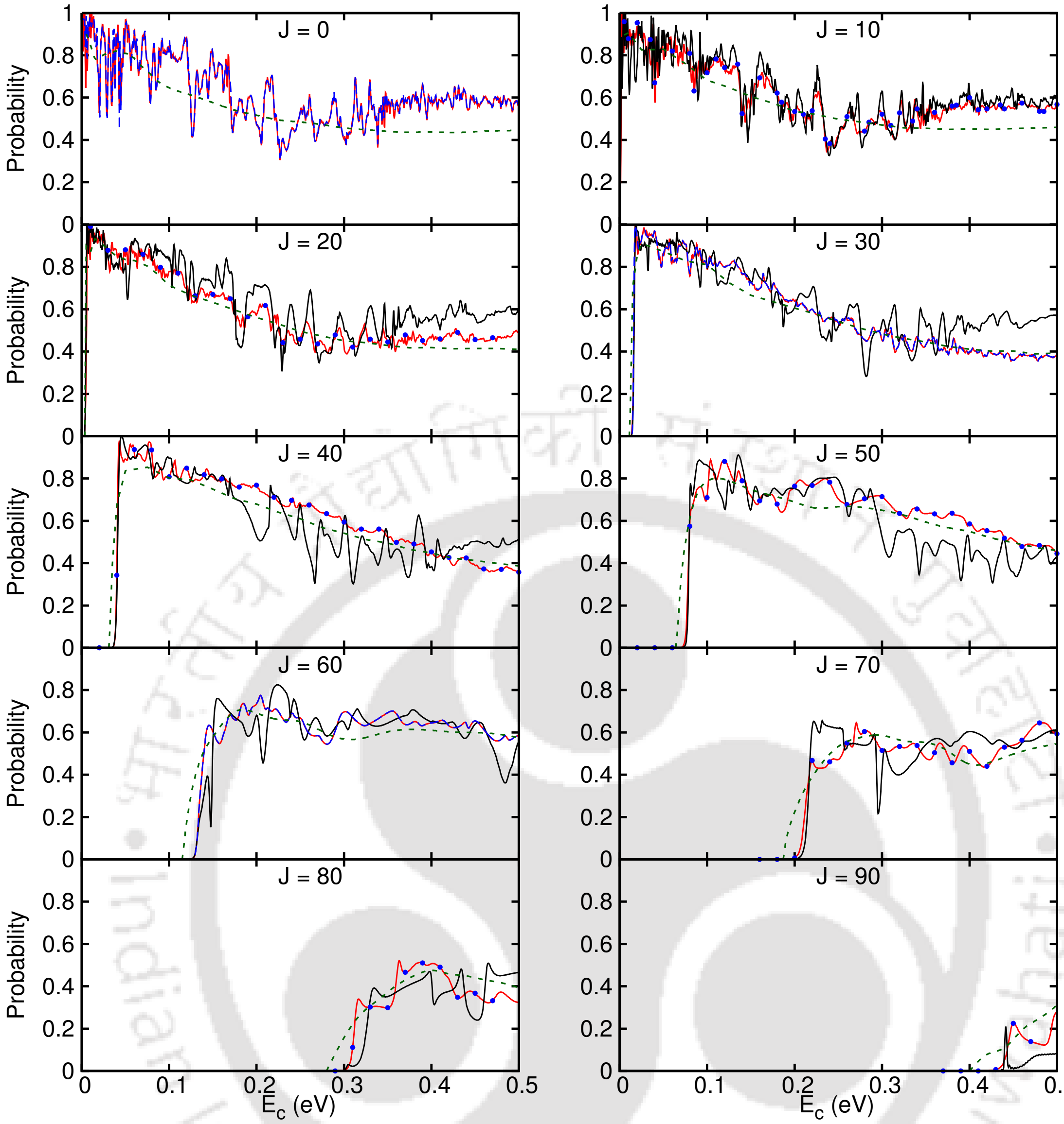

FIGURE 5.4: Total reaction probabilities for Ne + HeH$^+$($v = 0, j = 0$) → NeH$^+$ + He reaction for some selected J values obtained from the following methods: TIQM (- - / •), TDQM-CC (—), TDQM-CS (—), QCT-HB (- -).

of the total reaction probabilities at cold and ultra cold regions. In the ICSs calculations, the value of those probabilities were assumed to be ‘one’.

Figures 5.4, 5.5 and 5.6 also show that the total reaction probabilities calculated by means of QCT-HB calculations successfully reproduce the average behavior of QM probabilities, for all the cases. As expected, resonance structure of the reaction probabilities could not be reproduced via classical calculations. QCT probabilities have lower thresholds than the quantum probabilities for larger J values, which may be due to the

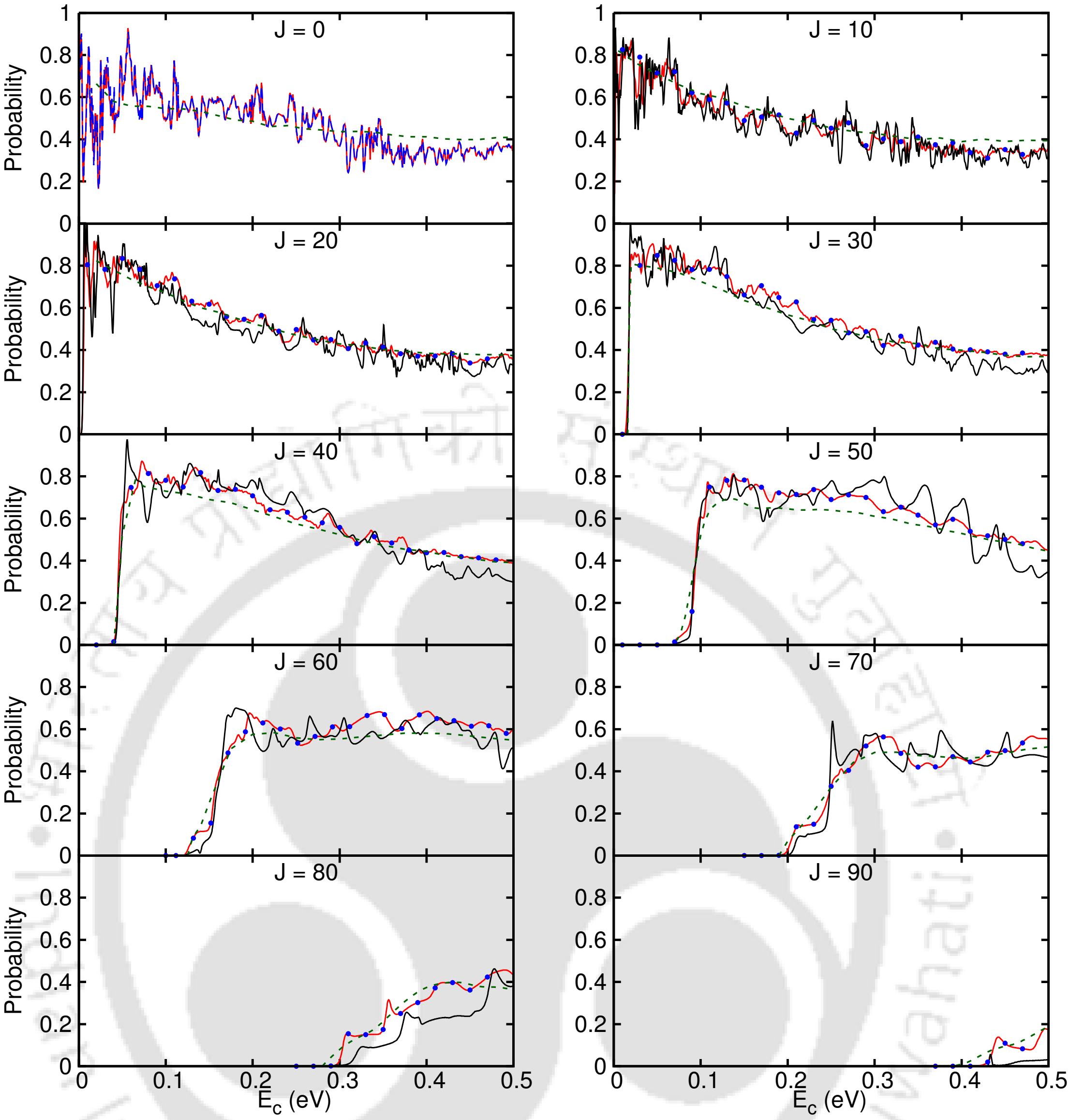

FIGURE 5.5: Same as Figure 5.4 for Ne + HeH$^+$$(v = 0, j = 1) \rightarrow$ NeH$^+$ + He.

noninclusion of the zero point energy (ZPE) correction for the products with lesser vibrational energy than that of the ground vibrational state. In the case of $(v, j) = (0, 0)$, for a significant amount of reactive trajectories ($\sim$ 18%), the products NeH$^+$ have energies less than the ZPE. However, this is reduced to ($\sim$ 5%) for $(v, j) = (1, 0)$ reactant state. As it is observed, the QCT probabilities are closer to CC than the CS results. In the CS method, out-of-plane rotations of the reagent molecule are restricted, but no such approximation exists in case of QCT calculations; this may be the reason for the good agreement between the QCT and QM-CC reaction probabilities. Despite this average accord with the QM results, QCT probabilities display some discrepancies such as the case of J = 0 - 20 for (v, j) = (0, 0) beyond E_c = 0.35 eV or reaction probabilities of J

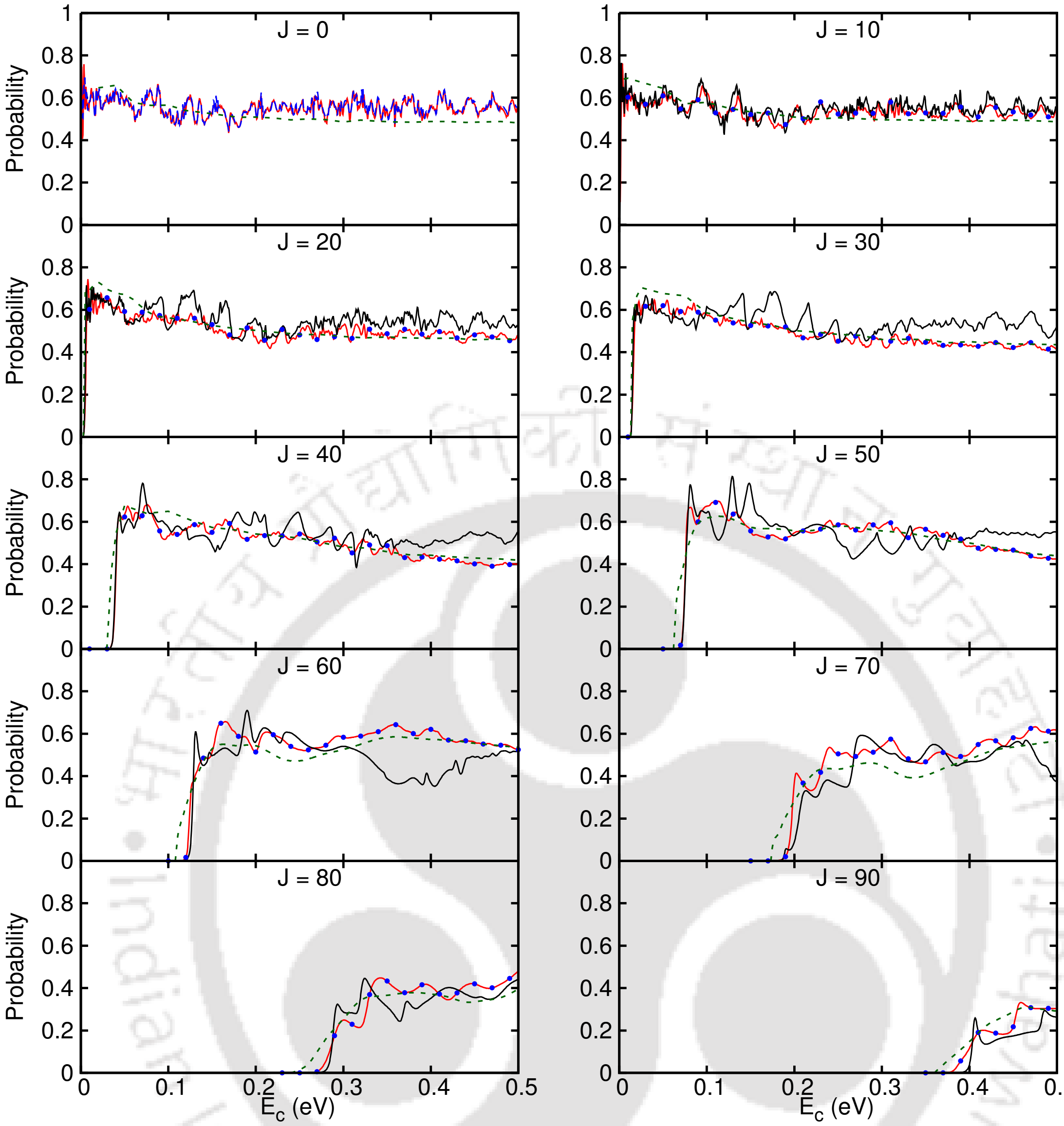

FIGURE 5.6: Same as Figure 5.4 for Ne + HeH$^+$($v = 1, j = 0$) → NeH$^+$ + He.

= 10 - 30 for (v, j) = (1, 0) at low energies.

An estimation of the lifetime of the collision complexes, calculated from the average width of the resonances appeared in (v, j) = (0, 0) CC probabilities at low energies (E_c = 0.005 - 0.05 eV) shows that the average lifetime is ∼ 0.12 ps. In classical calculations, instead of determining the lifetime of the the collision complexes, collision time (τ) of a trajectory is defined as the time elapsed between the first entry time of the trajectory into a certain criteria and the last exit time from that criteria. In our case, we considered the criteria that the sum of three atomic distances is less than a cutoff value of 5 Å. Here, it is worth mentioning that τ is not exactly the lifetime of the complex, but closely related to the lifetime of the complex. The average collision time is found to be ~ 0.1 ps at low translational energies (E_c = 0.005 - 0.05 eV) for (v, j) = (0, 0), which compares well with the corresponding QM ones.

5.3.1.2 Total integral cross sections

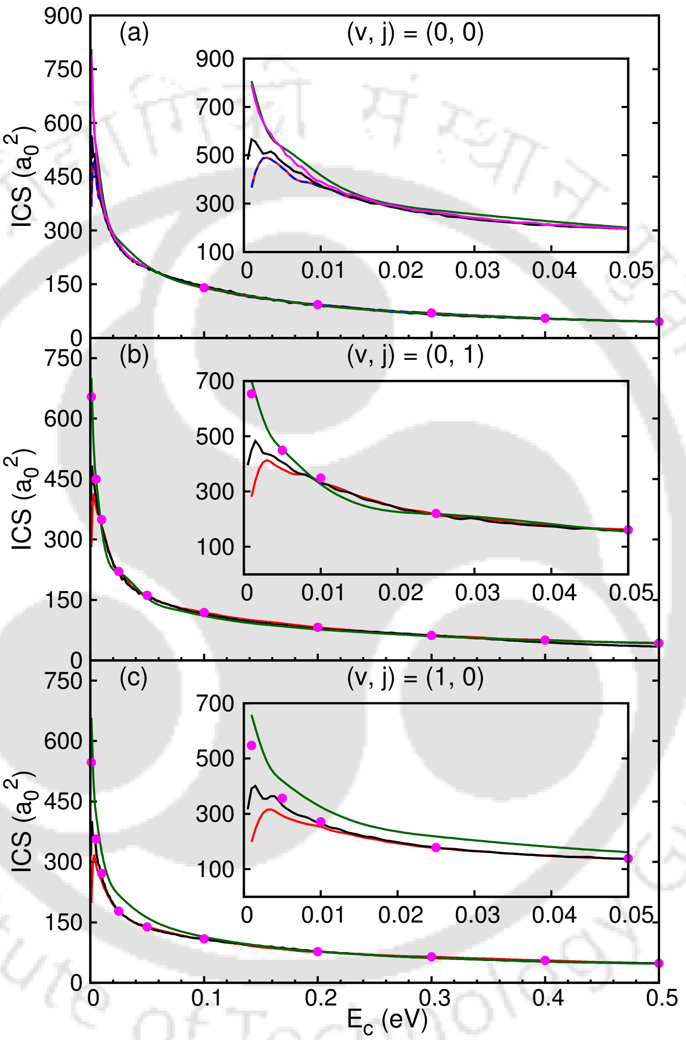

FIGURE 5.7: Initial state selected total integral cross sections as a function of collision energy for Ne + HeH$^+$ → NeH$^+$ + He reaction obtained from interpolated TDQM-CC (—), exact TDQM-CC (- -), TDQM-CS (—), TIQM (— / •) and QCT-HB (—) calculations. Zoomed versions for E_c = 0.001 - 0.05 are shown in the insets.

Total ICSs for the title reaction for different initial reactant states calculated using different methods are presented in Figure 5.7. To compute the QM ICS for the investigated energy range, reaction probabilities were calculated up to J = 96 for (v, j) = (0, 0) and

(0, 1) and up to $J = 100$ for $(v, j) = (1, 0)$, for both the QM-CS and QM-CC calculations. All the TDQM-CC reaction probabilities for $(v, j) = (0, 0)$ for different J values were obtained from exact QM calculations, but for the excited reactant ro-vibrational states TDQM-CC probabilities beyond $J \geqslant 40$, only some selected values (45, 50, 55, ..., $J_{\max}$) were computed with the exact QM treatment. Given the smooth dependence with collision energy observed in general for reaction probabilities at such large total angular momenta, the remaining J probabilities were estimated from the known probabilities via a J-shifting method as described in Chapter 2. To check the accuracy of this approach, TDQM-CC reaction probabilities were also computed for $(v, j) = (0, 0)$ using the J-shifting method and the resultant ICSs are plotted along with the exact TDQM-CC cross sections (those calculated from exact TDQM-CC probabilities) in Figure 5.7a. Literally there is no difference between the interpolated and the exact cross sections for $(v, j) = (0, 0)$, hence, J-shifting technique is used for the excited ro-vibrational states. For the sake of simplicity, interpolated TDQM-CC results will be called as TDQM-CC results from now onwards. All the methods employed here produce finite cross sections at the lowest collision energy considered here, i.e., $E_c = 0.001$ eV. ICSs are very large at low collision energies and decrease rapidly with increment in translational energy up to ~ 0.25 eV but decrease slowly beyond that point. The overall behavior of the cross sections is similar to other barrierless exothermic reactions.[27,28,38–43] As seen in Figure 5.7, the oscillatory structure of quantum reaction probabilities is greatly reduced in the QM ICS plots due to the partial waves averaging effect.

As can be seen in Figure 5.7a, for the ground ro-vibrational reactant state, there are no remarkable differences between the reaction cross sections obtained using different methods, except at really low collision energies. Although the CS and CC probabilities for $(v, j) = (0, 0)$ and (1, 0) (see Figures 5.7a and 5.7c) certainly differ at low E_c, agreement between the cross sections obtained from the CC and CS methods is reasonably good. It seems that CC has less effect on average quantities for $j = 0$. For rotationally excited reactant state, CS results slightly underestimate the CC ICSs above ~ 0.3 eV (see Figure 5.7b). Thus, it is clear that CC promotes the reactivity of the rotationally excited reactants. It is seen for all the initial states that TDQM-CS cross sections are slightly larger than the TDQM-CC ones in the ultra low-energy region.

An excellent agreement is seen between the TDQM-CC and TIQM ICSs beyond $E_c \approx$ 0.015 eV. However, in all the cases, both the CC and CS ICSs obtained from TDQM calculations are significantly smaller compared to corresponding TIQM ones in the low energy regime. In a contrary to the TDQM results, no declining behavior of the TIQM ICSs has been seen in the ultra low energy regime with decrease in collision energy. As mentioned previously, it is always cumbersome to converge probabilities in this regime with TDWP calculations, which require very large grids, long propagation time, and precise damping procedures of the WP to conclude anything about the behavior of the reaction attributes, whereas TIQM calculations can provide a correct description of the reaction attributes at very low energies.

Total ICSs have been calculated for the Ne + $HeH^+(v = 0, j = 0) \rightarrow NeH^+$ + He reaction using the TIQM method in the energy range from 0.001 to 0.05 eV with an energy spacing of 0.0005 eV and plotted in the inset of Figure 5.7a along with the ICSs obtained from other methods. As opposed to the results obtained by means of the TDQM approach, no trace of a maximum below $E_c \approx 0.01$ eV is obtained in the TIQM ICSs. This suggests that such a feature corresponds in fact to an artifact due to the above mentioned deficiencies of the TDWP approach at the low-energy regime. Maxima like in the present TDQM results have been found in previous time-independent investigations on similar reactions such as $H+HeH^+$.[28] Another example is Ne + $H_2^+ \rightarrow NeH^+$ + H, where differences between the TDQM and TIQM cross sections were attributed to possible inaccuracies in the wave packet technique at very low collision energy.[19,20] These deficiencies seem to be as well the most likely reason for the discrepancies between both techniques in the ICSs shown in Figure 5.7a. However, an excellent agreement between the TIQM and the TDQM cross sections observed at larger energies in Figures 5.7a, 5.7b and 5.7c suggests that TDQM method provides the correct description of the process in moderate to high energy region.

Figure 5.7 shows that QCT results successfully reproduce the overall qualitative behavior of the QM cross sections for all the reactant states. In the low energy regime, although the TDQM results exhibit a maximum peak at ∼ 0.003 eV, the QCT results show a similar behavior like the correct TIQM results. QCT results are in a good accord with the TIQM results in the entire investigated energy regime for $(v, j) = (0,\ 0)$ and $(0,\ 1)$. For the Ne + HeH$^+$$(v = 1, j = 0)$ reactive system (see Figure 5.7c) the QCT approach yields cross sections that slightly overestimate the QM results at the lower energies ($E_c < 0.11$ eV).

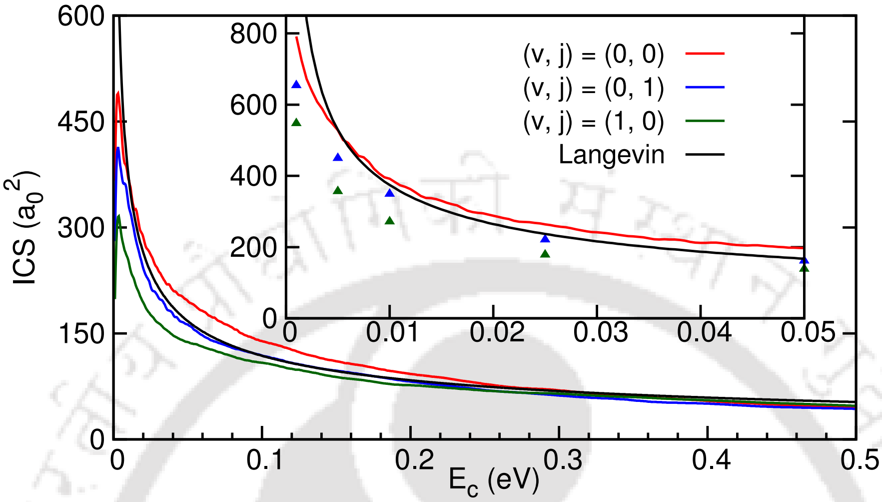

FIGURE 5.8: Comparison between different initial state selected ICSs as a function of collision energy for Ne + HeH$^+$ → NeH$^+$ + He reaction obtained from TDQM-CC and TIQM (inset) calculations. The Langevin ICSs are also shown.

QM-CC cross sections for different initial ro-vibrational states are compared in Figure 5.8. The figure shows that the cross sections for excited ro-vibrational states are different than the results for the ground state: differences are large in the low-energy region and small in the high-energy regime. Cross sections for $(v, j) = (0,\ 1)$ are smaller than $(v, j) = (0,\ 0)$ cross sections in the entire energy range. ICSs for $(v, j) = (1,\ 0)$ start being smaller than those for the reaction from the ground ro-vibrational state at low collision energies but become larger beyond $E_c \approx 0.35$ eV. Substantial decrease in the ICSs at low collision energies with vibrational excitation has also been observed for exothermic C+OH reaction.[44] Inhibition of reactivity due to rotational excitation is seen for many other exothermic reactions,[39,41,42] which may be related to orientation effect of the reactants. Similarities among the cross sections for different initial ro-vibrational states in the high-energy region is also common for exothermic reactions with no barrier along their collision paths.[39,41,42,44]

The ICSs for a barrierless exothermic reaction can be calculated by the Langevin capture model,[45,46] which expresses the ICS for a reaction between an ion and a neutral species as

$$\sigma_{\text{Lang}}(E_c) = 2\pi \left(\frac{C_4}{E_c}\right)^{1/2}, \tag{5.2}$$

where $C_4 = \frac{1}{2}\frac{q^2\alpha}{(4\pi\epsilon_0)^2}$. α denotes the dipole polarizability of the neutral reactant, and ϵ_0 is the vacuum electric constant. α for Ne atom has been calculated at CCSD(T)/aug-cc-pVQZ level numerically to be 2.60918 a.u. using the ORCA software,[47] which agrees quite well with values from literature.[48–50] The Langevin cross sections, also shown in Figure 5.8, are in a fairly good agreement with the QM-CC results, especially for (v, j) = (0, 1) between $E_c = 0.02$ - 0.22 eV. It is worth mentioning at this point that a proper description of the long-range part of the potential is required to have accurate estimation of cross sections for ionic reactions. However, the long-range part of the PES used in the present set of calculations may not be accurate enough to account for the cross sections in the low-energy region. This could be the reason for the deviation of QM ICSs from the Langevin behavior at the low energies. Moreover, anisotropy of the PES can lead to a nonuniform variation of the potential at large R for different θ values and affects the observables. Hence, the actual capture cross sections for this reaction may not coincide with the simple Langevin capture results.

5.3.1.3 Rate constants

Initial state selected rate constants estimated from QM and QCT ICSs are plotted in Figure 5.9. After showing a rapid early rise, the rate constants remain almost invariant with respect to temperature. No significant differences can be seen between CC and CS rate constants for all the cases, except at very cold regions. QCT calculations successfully reproduce the overall behavior of QM rate constants, and for $(v, j) = (0, 0)$, the agreement between QM and QCT rate constants is good. For $(v, j) = (1, 0)$, QCT rate constants overestimate the QM results.

It is already seen that present TDQM results are inaccurate in the low-energy regime, while TIQM results successfully describe the low-energy region. In Figure 5.10, the initial state resolved rate constants calculated from accurate QM-CC ICSs (TIQM ICSs used in $E_c = 0.001$ - 0.05 eV and TDQM-CC ICSs used in $E_c = 0.05$ - 0.5 eV)

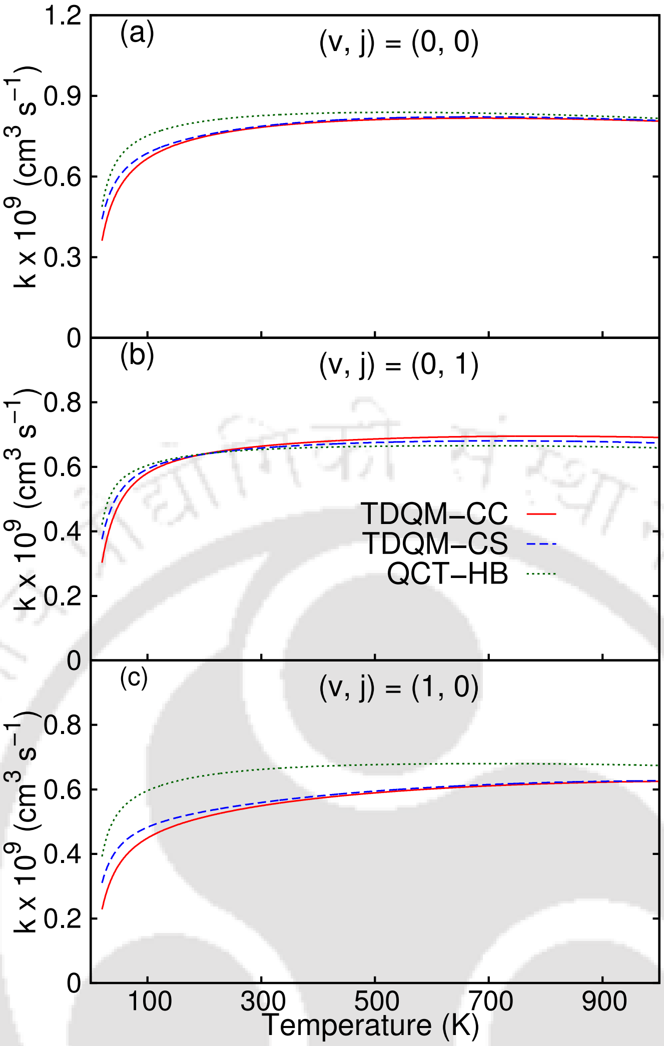

FIGURE 5.9: Temperature dependence of the initial state selected rate constants for the Ne + HeH^+ → NeH^+ + He reaction.

are compared with the available experimental result. Figure 5.10 shows that QM rate constants for all the states follow a similar pattern, but the rate is reduced to a large extent by vibrational or rotational excitation. At 300 K, the QM-CC rate constant for (v, j) = (0, 0) is 0.8×10^{-9} cm^3 s^{-1}, which is within the error bar of experimental rate constant measured to be $1.25\pm0.625\times10^{-9}$ cm^3 s^{-1} by Glosík *et al.*[35] Here it is noteworthy that the computed rate constants are Boltzmann-averaged over collision energies only, but not over the ro-vibrational energies. Quantum dynamical calculations are very expensive for $j > 0$ for these type of ion-molecule reactions, so the initial state-selected rate constants are only reported here. Rate constant for this type of barrierless exothermic reactions can be calculated using the Langevin capture model as[45,46]

$$k_{\rm Lang}(T) = 2\pi \left(\frac{2C_4}{\mu_R}\right)^{1/2}. \tag{5.3}$$

As it is clear from the above expression, $k_{\rm Lang}(T)$ is temperature-independent. For the title reaction, the value of the Langevin rate constant is 0.728×10^{-9} cm^3 s^{-1} , which is consistent with the usual value for this kind of processes. $k_{\rm Lang}(T)$ is also plotted in Figure 5.10. Result from the simple Langevin model is also within the error bar of the experimental results and agrees quite well with the QM results. $k_{\rm Lang}(T)$ lies in between (v, j) = (0, 0) and (0, 1) rate constants, closer to (0, 1) rate constants than those for (0, 0). It is reiterated at this point that a proper description of the long-range interactions for an ion-molecule system is necessary to calculate the rate constants at low temperatures.

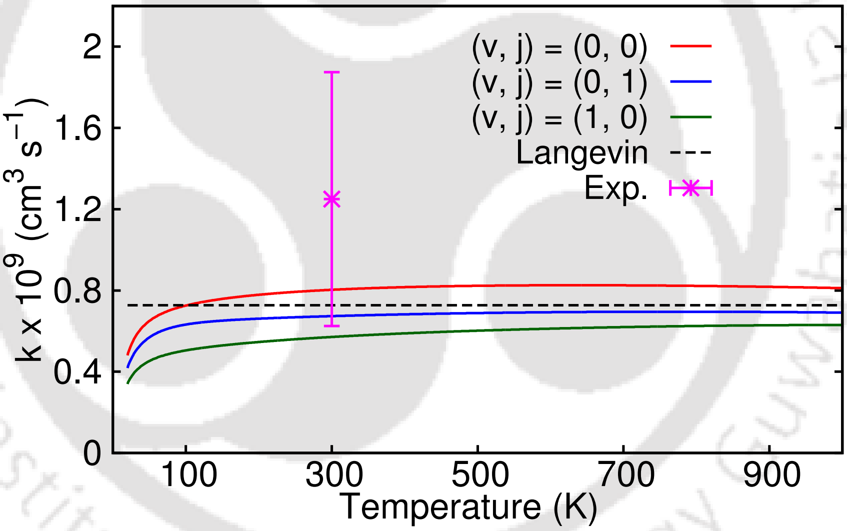

FIGURE 5.10: Comparison between different initial state selected rate constants computed from exact QM-CC ICSs (see text) and Langevin rate constant (black dashed line). The only available experimental rate constant (magenta point with error bar) at 300 K [Ref: 35] is also shown.

5.3.2 State-to-state dynamics

State-to-state dynamics of the title reaction is investigated for $(v, j) = (0, 0)$ initial reactant state via TIQM and QCT calculations at a few selected collision energies covering low, moderate and high energy regions. Overall good agreement found between the

TIQM and QCT final state averaged results for $(v, j) = (0,\ 0)$ supports the reliability of QCT method for the present case.

5.3.2.1 State-to-state cross sections

TABLE 5.3: Total and vibrationally-resolved cross sections for the Ne + HeH$^+$($v = 0, j = 0$) $\rightarrow$ NeH$^+$(v') + He reaction for different values of the collision energy computed by means of the TIQM, TDQM-CC and QCT methods. Units are in a$_0^2$.

$E_c = 0.01$ eV	σ_{tot}	$\sigma_{v'=0}$	$\sigma_{v'=1}$	$\sigma_{v'=2}$
TIQM	391.67	391.67		
TDQM-CC	368.75			
QCT-GB	419.06	419.03	0.03	
QCT-HB	417.28	368.39	48.89	
$E_c = 0.1$ eV	σ_{tot}	$\sigma_{v'=0}$	$\sigma_{v'=1}$	$\sigma_{v'=2}$
TIQM	139.81	126.85	12.96	
TDQM-CC	139.81			
QCT-GB	142.34	131.45	10.89	
QCT-HB	140.41	120.27	20.14	
$E_c = 0.3$ eV	σ_{tot}	$\sigma_{v'=0}$	$\sigma_{v'=1}$	$\sigma_{v'=2}$
TIQM	69.42	56.31	13.11	
TDQM-CC	69.35			
QCT-GB	67.53	54.42	13.11	
QCT-HB	67.64	51.64	15.36	0.64
$E_c = 0.5$ eV	σ_{tot}	$\sigma_{v'=0}$	$\sigma_{v'=1}$	$\sigma_{v'=2}$
TIQM	45.14	32.05	11.17	1.92
TDQM-CC	44.78			
QCT-GB	45.57	32.30	11.47	1.80
QCT-HB	45.00	30.33	12.55	2.12

Vibrational state resolved values of ICSs at few specific energies are shown in Table 5.3. The comparison between the TIQM and the TDQM total cross sections reveals that the only noticeable differences exist at the lowest energy under consideration, $E_c = 0.01$ eV. For the other cases, 0.1, 0.3, and 0.5 eV, both TDQM and TIQM approaches yield to almost identical ICSs. Again, it is at $E_c = 0.01$ eV, where QCT results deviate significantly from the TIQM cross section (in particular between 6 and 7%) and despite the total ICSs calculated by means of GB and HB approaches disagreeing in less than 0.5 Å^2, the two binning procedures used in the QCT method produce different results for the formation of vibrationally excited NeH$^+$($v' = 1$): almost negligible for the former version and 13.69 Å^2 for the QCT-HB. At E_c = 0.3 eV, excited NeH$^+$($v' = 2$) are obtained only from the QCT-HB method.

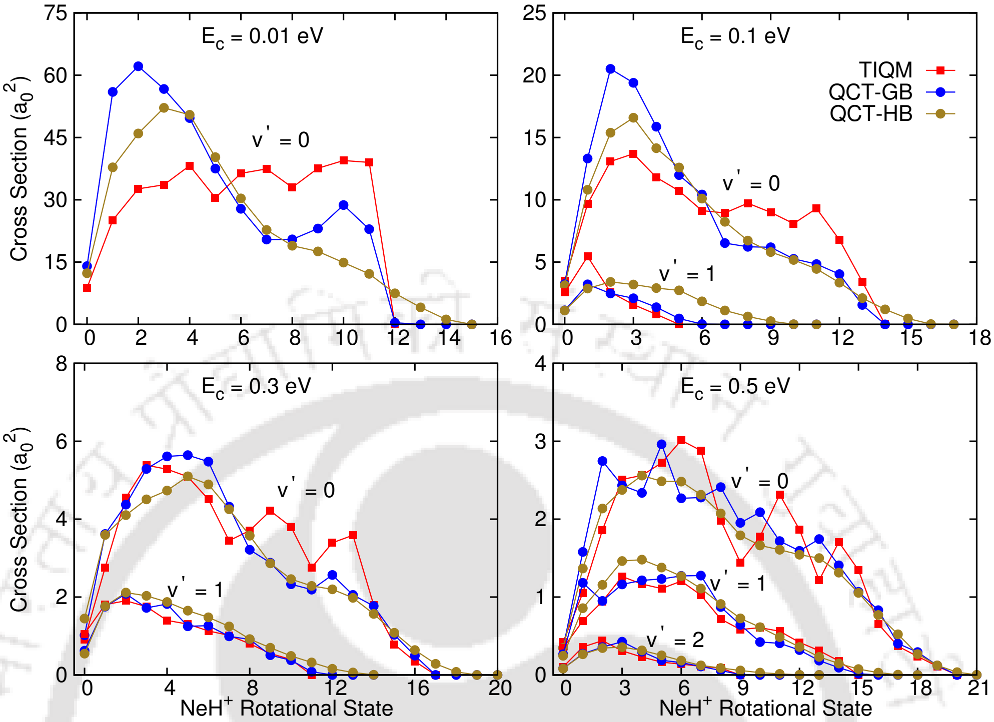

FIGURE 5.11: Rotational distribution of the NeH$^+$ for the Ne + HeH$^+$($v = 0, j = 0$) $\rightarrow$ NeH$^+$(v', j') + He reaction.

A much finer detail on the dynamics of the title reaction is obtained with the rotational distributions. State-to-state cross sections for the Ne + HeH$^+$($v = 0, j = 0$) $\rightarrow$ NeH$^+$(v', j') + He reaction were calculated at different values of the collision energy by means of TIQM, QCT-GB and QCT-HB methods. Results are presented in Figure 5.11. NeH$^+$($v' = 0$) is the only one energetically accessible at E_c = 0.01 eV. Qualitative differences can be found, between the QCT and the TIQM results: both QCT calculations yield cross sections with preference for low rotational states, with maximum values for the j' = 2 - 3, which is at odds with the TIQM calculation. The situation does not really change significantly when the collision energy is increased to E_c = 0.1 eV, since rotational distributions obtained from QCT and TIQM exhibit noticeable differences, especially for the NeH$^+$($v' = 0$) state. At much higher values of collision energies, such as 0.3 and 0.5 eV, as shown in Figure 5.11, rotational cross sections obtained with TIQM and QCT methods display an overall agreement not observed for the lower collision energies discussed above. QCT-HB rotational distributions are on an average smoother than the other and show rotationally hot NeH$^+$, which are quantum mechanically closed. Similar result found for some other processes in previous studies.[51–53]

5.3.2.2 Differential cross sections

The angular distribution at $E_c = 0.01$ eV obtained by means of the TIQM and QCT approaches are compared in Figure 5.12. It is clear from the figure that the dynamics of the title reaction at that specific energy corresponds to a process in which the forward scattering direction of $\theta \approx 0°$ is clearly favored. The TIQM DCSs shows a marked preference along that particular direction with a peak that is ~ 7.5 times larger than the angular cross section along the backward scattering direction of $\theta \approx 180°$. The QCT results reproduce successfully this feature, especially the QCT-HB version, whereas the QCT-GB yields some slight overestimation of the forward scattering peak.

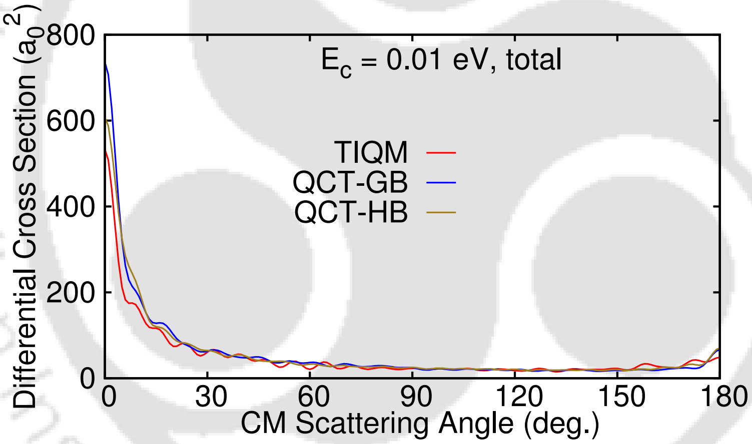

FIGURE 5.12: Total differential cross sections for the Ne + HeH$^+$($v = 0, j = 0$) $\rightarrow$ NeH$^+$ + He reaction at $E_c = 0.01$ eV.

In Figure 5.13, total and vibrational state resolved DCSs for the title reaction for $(v, j) = (0, 0)$ initial state are plotted for $E_c = 0.1$ and 0.3 eV. The same is plotted for $E_c = 0.5$ eV in Figure 5.14. At $E_c = 0.1$ eV, the total TIQM DCSs exhibit a forward-to-backward ratio of ~ 14. Despite the QCT results displaying the correct asymmetry between the peaks along the $\theta \approx 0°$ and $\theta \approx 180°$ scattering directions, the maximum for the forward direction is noticeably smaller than the TIQM distribution. The origin of such a discrepancy is in the Ne + HeH$^+$($v = 0, j = 0$) $\rightarrow$ He + NeH$^+$($v' = 0$) process (see left-middle panel of Figure 5.13), responsible for much of the reaction at this energy.

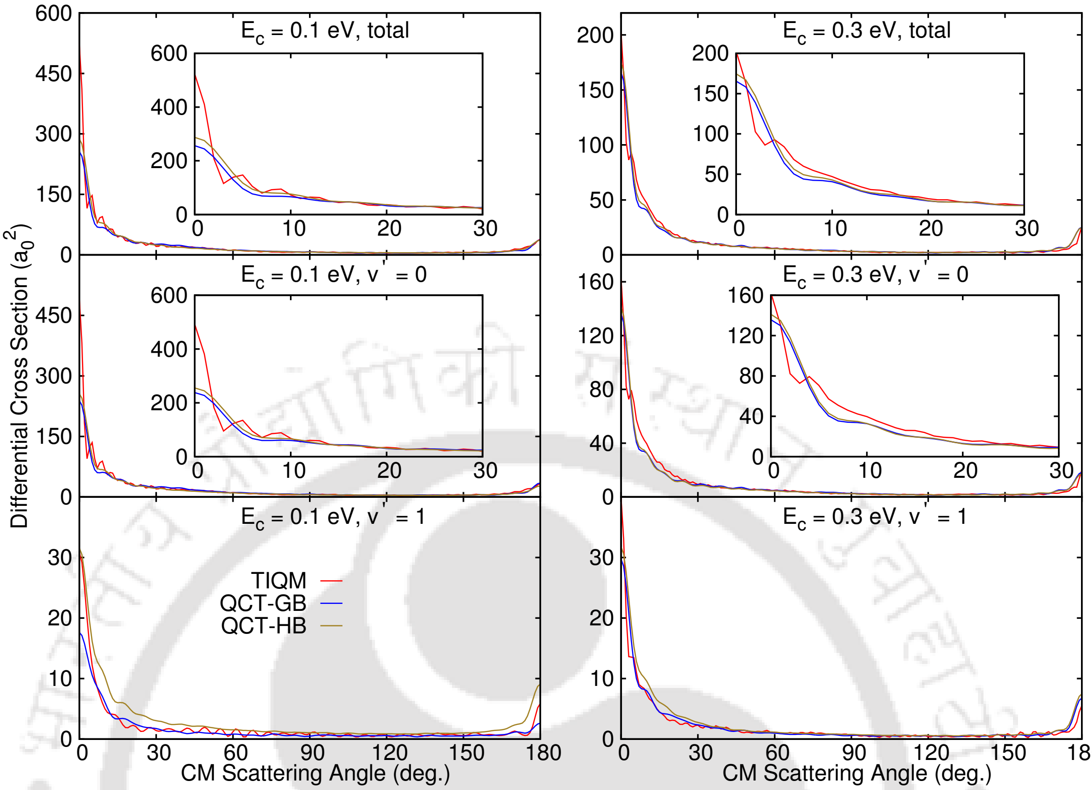

FIGURE 5.13: Total and vibrational state resolved DCSs for the Ne + HeH$^+$($v = 0, j = 0$) $\rightarrow$ NeH$^+$(v') + He reaction at E_c = 0.1 and 0.3 eV.

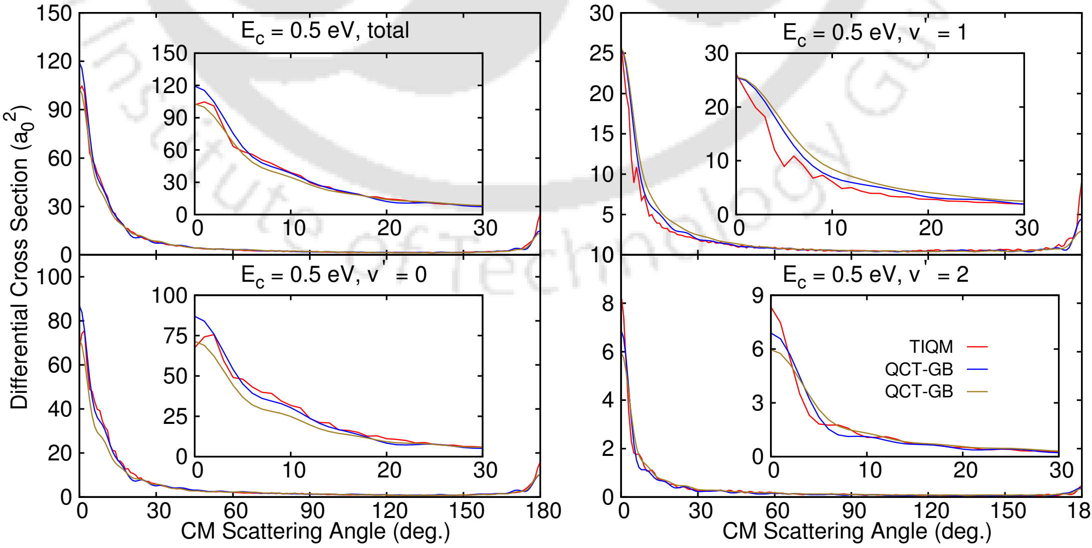

FIGURE 5.14: Total and vibrational state resolved DCSs for the Ne + HeH$^+$($v = 0, j = 0$) $\rightarrow$ NeH$^+$(v') + He reaction at E_c = 0.5 eV.

The production of vibrationally excited NeH^+, on the contrary, much less important (see bottom panel of Figure 5.13), produces DCSs with a smaller asymmetry with a better comparison among the predictions of the different theoretical approaches. The QCT-HB distribution gives a reasonably good reproduction of the TIQM result. The increase in the collision energy comprises certain variation in the DCSs as well. As observed for the rotational distributions at $E_c = 0.3$ eV, TIQM and QCT methods seem to describe the same overall dynamical features (see Figure 5.13 right panels). Thus, for this energy, DCSs obtained by means of these two methods are in a remarkably good agreement both for the total distribution starting from $HeH^+(v = 0, j = 0)$ and for those distributions corresponding to final vibrational state resolved cases. A similar situation is found for $E_c = 0.5$ eV, an energy at which the agreement between QCT and TIQM results is almost perfect (see Figure 5.14).

The preference for a specific scattering direction, with a predominant peak along $\theta \approx 0^\circ$ in this case, observed in the exact QM DCSs, can be interpreted as an indication that the overall dynamics of the $Ne + HeH^+(v = 0, j = 0) \rightarrow NeH^+ + He$ reaction is not governed by complex-forming mechanisms. According to previous studies, structured rotational distributions and nearside farside oscillations in the sideways scattering direction in DCSs can be indications of the presence of resonances. This has been illustrated, for instance, for the case of the F+HD[54] and $F+H_2$.[55] In particular, present TIQM results show some resemblance to the DCSs obtained for $F + HD(j = 0, 1) \rightarrow HF(v' = 2) + D$, with pronounced backward scattering at certain energies and an oscillating profile over the angular range far from the $\theta \approx 0^\circ$ and $\theta \approx 180^\circ$ regions. Rotational cross sections for the same state-to-state process are also similar to those reported here. It is worth noticing, however, before concluding that both sets of results correspond to the same resonance-mediated process, which, in principle, PESs governing $F+H_2$ and $Ne+HeH^+$ reactions show substantial differences. Whereas the long-lived reactive resonances observed for the former collision correspond to quasi-bound states trapped at the van der Waals wells located in the exit channel, for the present case it is the intermediate potential well between reactants ($Ne+HeH^+$) and products ($He+NeH^+$) that may support quasi-bound states for a three-body collision complex.

5.3.3 Understanding the reaction mechanisms

Looking at the good accord found between the QCT and TIQM cross sections, it can be said that although for the low-energy regime noticeable differences for both rotational distributions and DCSs could suggest the relevance of QM effects, as the collision energy increases the QCT approach becomes a valid alternative to the exact calculation. In particular essential features such as the peak through the $\theta \approx 0^\circ$ scattering direction in the angular distribution are perfectly reproduced. Encouraged by the good agreement observed with the QM results, the QCT-GB method was employed to delve into the underlying dynamical mechanisms of the title reaction. In particular, the normalized classical deflection function, $D_r(J, \theta)$ is calculated for this process for $(v, j) = (0, 0)$ state. $D_r(J, \theta)$ is a function of both J and scattering angle (θ) representing the correlation between angular distribution of products and orbital angular momentum or impact parameter, and defined in Chapter 4, Eq. 4.2.

The deflection functions were obtained with batches of 2×10^6 and 5×10^6 trajectories run at two different collision energies, 0.005 and 0.5 eV, respectively, in an attempt to explore both the low and high-energy regimes. The partial cross sections, $\pi/k^2(2J + 1)P_r(J)$, are plotted against J at these two collisions energies in right panels of Figure 5.15. There is an excellent agreement between the TIQM (solid magenta lines) and QCT-GB (solid black lines) partial cross sections for $E_c = 0.5$ eV and only slight discrepancies for the highest partial waves for 0.005 eV, with maxima at $J \approx 20$ for $E_c = 0.005$ eV and at $J \approx 70$ for 0.5 eV. The largest values of the total angular momentum (denoted as $J_{\max}$) are 23 and 96 for $E_c = 0.005$ and 0.5 eV, respectively. These $J_{\max}$ values correspond to the maximum impact parameter ($b_{\max}$) of 14.34 bohr for $E_c = 0.005$ eV and 5.89 bohr for $E_c = 0.5$ eV. Values of the $D_r(J, \theta)$ function at both energies are shown in left panels of Figure 5.15. The areas inside the red solid lines represent the (J, θ) pairs for which the reaction occurs predominantly. Two distinct bands with opposite slopes are seen inside these areas: For the first band, which ranges from $\theta \sim 165^\circ$ and small J values to 0° and large J, the scattering angle varies inversely as J. The second band covers a wider range of θ (ranging from 0° to $\sim 120^\circ$), but over a narrower range of very large J values.

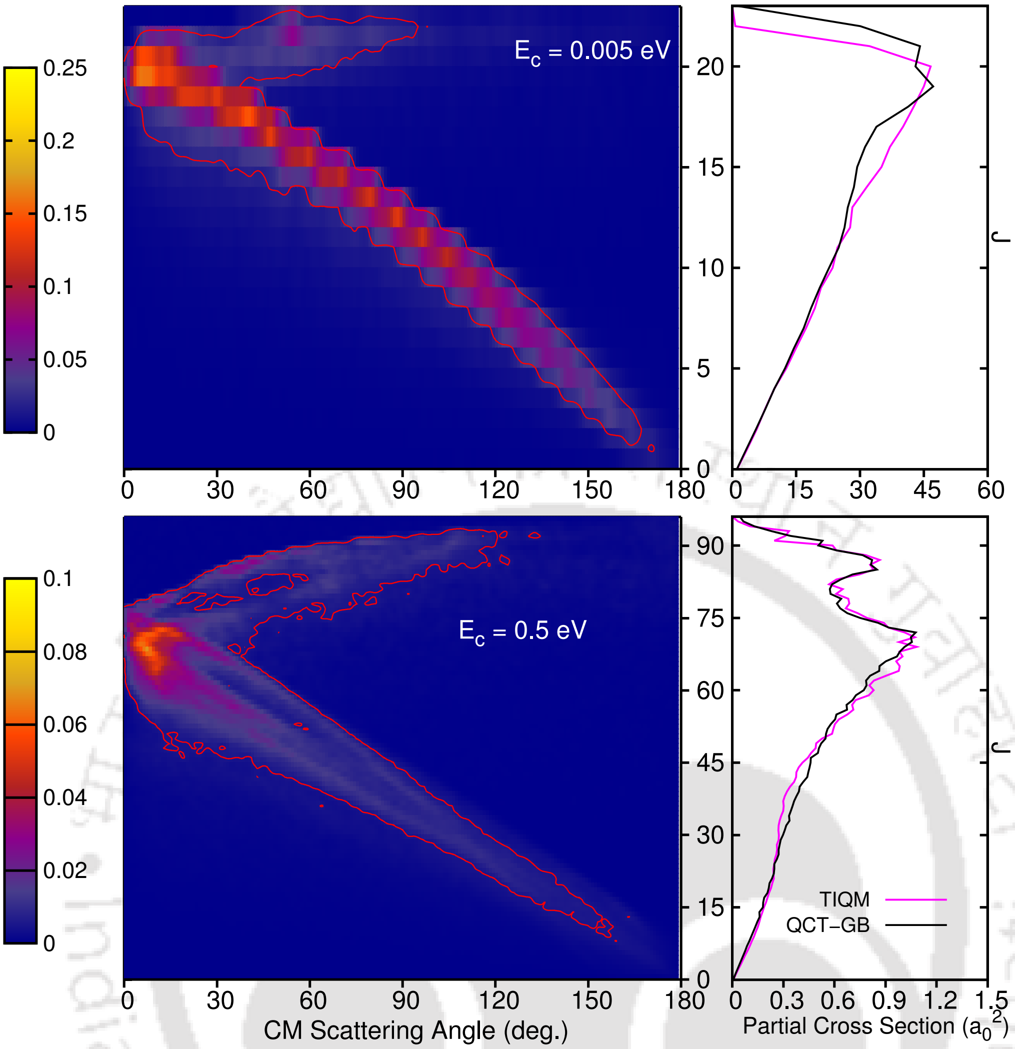

FIGURE 5.15: (left) Normalized classical deflection function, $D_r(J,\theta)$, for the Ne + HeH$^+$($v = 0, j = 0$) $\rightarrow$ NeH$^+$ + He reaction at $E_c = 0.005$ eV (top) and $E_c = 0.5$ eV (bottom). The solid red contour lines have magnitudes of 0.02 and 0.005 in the top and bottom panels, respectively. Enclosed areas inside the solid red lines indicate $J-\theta$ pairs contributing maximum to the cross sections. (right) Partial cross sections for the title reaction at $E_c = 0.005$ eV (top) and 0.5 eV (bottom) calculated by means of TIQM and QCT-GB methods.

The above results showing the correlation between scattering angles and the associated mechanisms can be analyzed in terms of collision time (τ). The value of τ for a trajectory gives an indication of the nature of the trajectory: A small value of τ corresponds to a direct path, whereas a comparatively large value indicates formation of an intermediate complex. In the present QCT calculations, this complex-forming mechanism is usually observed for the trajectories with $\tau > 75$ fs. In Figure 5.16, average collision times, defined as $\tilde{\tau} = 1/N_r(J,\theta) \times \sum \tau_i$ for the reactive trajectories, scattered at different angles and for different J values, are shown as contour plots at $E_c = 0.005$ and

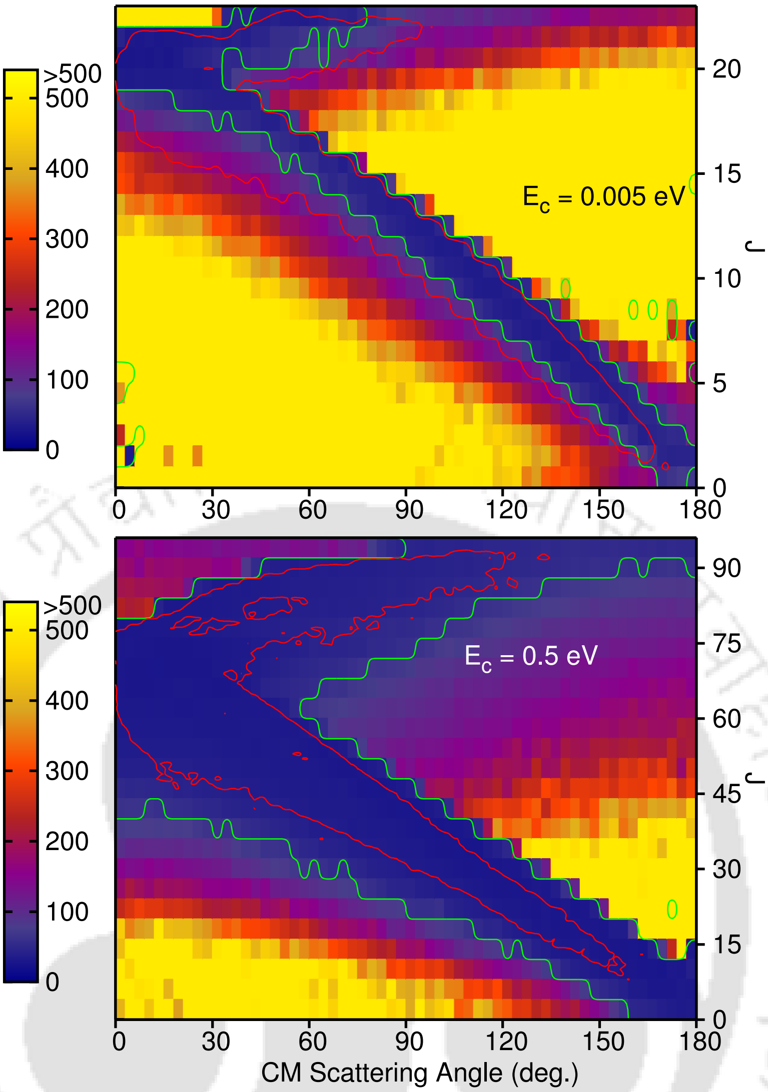

FIGURE 5.16: Average collision time $\tilde{\tau}$ plotted as a function of CM scattering angle (θ) and J. Green contour line represents $\tilde{\tau}$ = 75 fs. The areas marked with the solid red lines are the same as appeared in the top and bottom panels of Figure 5.15

0.5 eV. The area inside the red contour lines on the $J-\theta$ plane is the same area shown in Figure 5.15, while trajectories with $\tilde{\tau} < 75$ fs, that is, the trajectories following a direct path for the reaction, are located inside the green contour lines. The trajectories with small impact parameters (low J) indicate head-on collisions where NeH$^+$ gets scattered at large scattering angles ($\theta \approx 180°$). In those trajectories with moderate b values, the Ne atom makes a glancing collision with the HeH$^+$ diatom, and the product NeH$^+$ is scattered at sideway directions ($\theta \approx 90°$). The trajectories with high-impact parameters (large J) and forward scattered products indicate a spectator-stripping mechanism,[56] in which the Ne atom strips the proton so suddenly that little deflection of the products occur, and NeH$^+$ are scattered at small scattering angles ($\theta \approx 0°$). Since the b

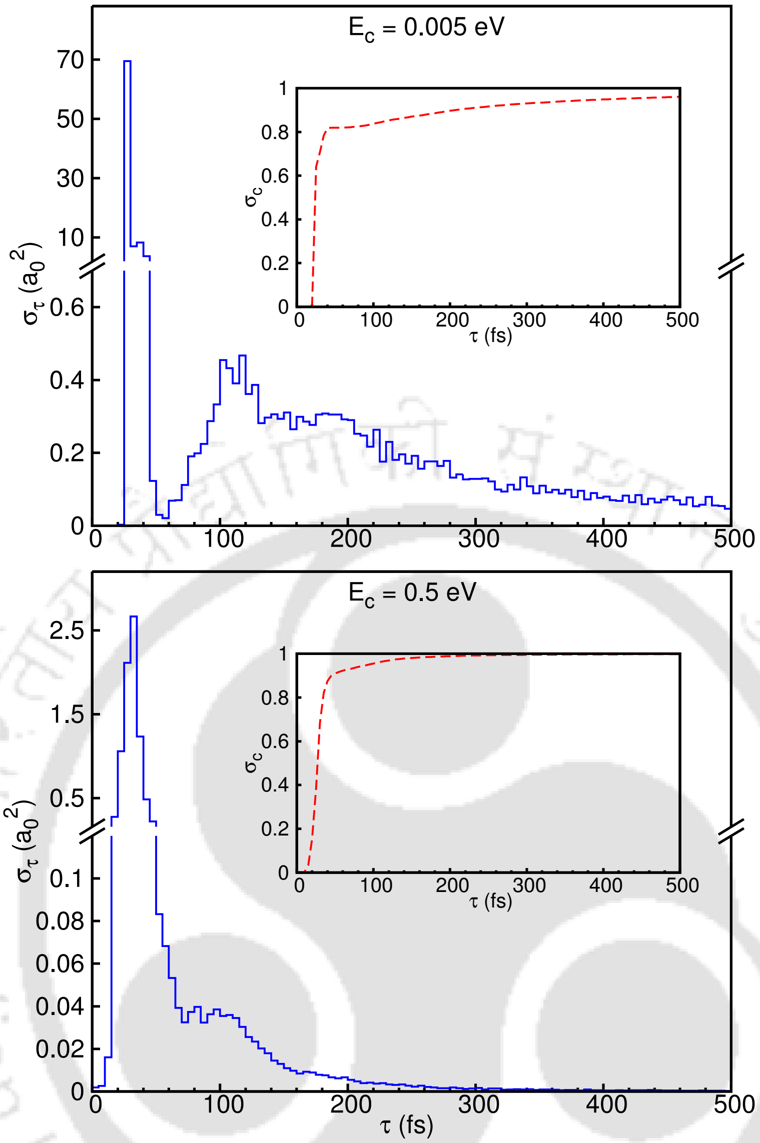

FIGURE 5.17: Total ICS vs collision time plot at two different collision energies for the Ne + HeH$^+$ ($v = 0, j = 0$) $\rightarrow$ NeH$^+$ + He reaction. (Inset) Cumulative distribution of the ICS (σ_c) with respect to collision time.

value is very large in this case, these trajectories contribute more to the cross section. Trajectories associated with these three reaction pathways are mostly scattered into the nearside, that is, into the same hemisphere as the incoming atom. However, as observed in Figure 5.16, for the trajectories with very large J, scattering of the products occurs at a wider range of θ ($\theta \approx 0° - 120°$). Most of the trajectories in this region are direct and correspond to farside scattered products, where the y-component of the product relative velocity vector is negative. Attractive forces are mainly responsible for these negative deflections.

The contributions of the reactive trajectories to the total ICSs with respect to the collision time τ are presented as solid blue lines in Figure 5.17 at $E_c = 0.005$ eV and 0.5 eV. The cumulative distribution of the ICS with respect to collision time (as described in Chapter 4, Eq. 4.3) are also plotted as dashed red lines in the insets of Figure 5.17. Two distinct maxima at ~ 30 fs and ~ 110 fs can be seen in the ICS vs collision time plot (solid blue line) for $E_c = 0.005$ eV. The first maximum, at ~ 30 fs, relates to the direct dynamics pathways for the reaction, whereas the second maximum appearing at ~ 110 fs hints at the indirect paths. The cumulative distribution shows that although $\sim 82\%$ of the reaction follows direct dynamics, complex-forming dynamics plays an important role for $E_c = 0.005$ eV. A small fraction of reactive trajectories are having significantly long collision times with $\tau > 500$ fs. As can be seen in the bottom panel of Figure 5.17, the distribution of total ICSs for $E_c = 0.5$ eV decays smoothly after the maximum appeared at ~ 35 fs. The cumulative distribution function for $E_c = 0.5$ eV shows that $\sim 93\%$ of the reaction proceeds via direct mechanisms at this energy and almost all the reactive trajectories have collision times < 300 fs.

Three representative trajectories showing the formation of collision-complexes are presented in Figure 5.18, at the two collision energies. The corresponding collision times for these trajectories, while the complex intermediates are formed inside the potential well, are long. However, there are some trajectories where reactants or the products are loosely bound and form a weak collision complex, as shown in the middle panel of Figure 5.18, but with a long lifetime. These trajectories can be assigned as *roaming* trajectories.[57,58] The smallest rotational period τ_{rot} of the complex is estimated from the equilibrium geometry of the collision-complex, that is, the collinear $[\text{HeHNe}]^+$, as $\tau_{\text{rot}} = 2\pi I / L\hbar$. Here I is the moment of inertia of $[\text{HeHNe}]^+$, and L is the orbital angular momentum. τ_{rot} values are estimated to be 624 and 152 fs at 0.005 and 0.5 eV, respectively. For most of the indirect trajectories it is found that $\tau_{\text{rot}} > \tau$, which makes the reaction nonstatistical.

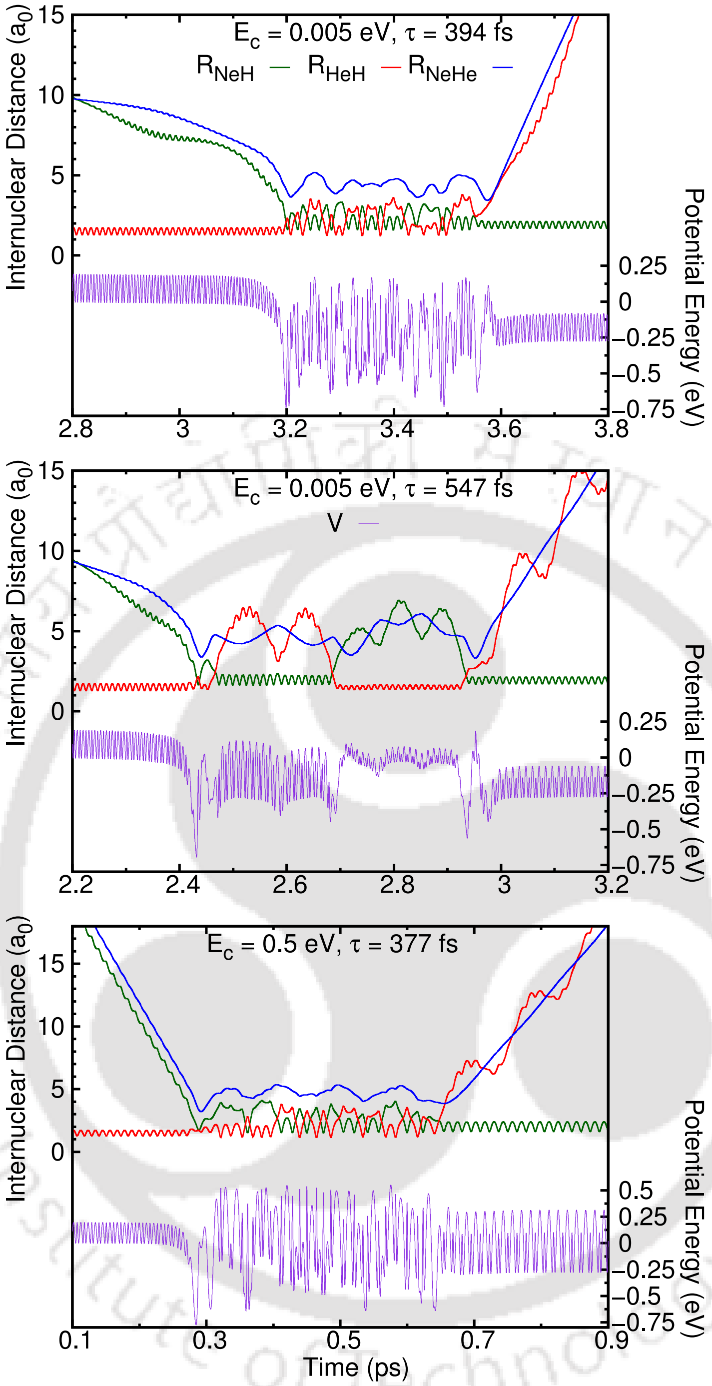

FIGURE 5.18: Time evolution of both the inter-particle distances and the potential energy measured with respect to the Ne + HeH^+ asymptote for three representative complex-forming trajectories. Associated collision times are mentioned.

5.4 CONCLUSIONS

Initial state selected reactive scattering studies for the exothermic atom-molecular ion type Ne + HeH^+ (v, j) → NeH^+ + He reaction have been performed via TDWP, TIQM methods and by means of QCT calculations. Numerous resonances seen in the QM probability curves for small J values indicate presence of metastable states of the intermediate collision-complex formed during the reaction. Rotational or vibrational excitation of the reactants significantly decreases the reactivity of the reaction in the low-energy regime. Minor discrepancies are found between the QM-CC and QM-CS ICSs for $j = 0$ reactant state at most of the investigated energies. However, for excited rotational reactant state, CC has been found to promote the reaction. Except at ultra low energies, TDQM-CC results are in a excellent agreement with the corresponding TIQM results. The calculated ICSs show that the TDQM study yields remarkably different results at the low-energy regime in comparison of with the TIQM method. The QCT results are overall in a good accord with the TIQM results. This highlights QCT as an efficient method to study this reaction. Simple Langevin capture model can also describe the reaction well. A good agreement between the experimental and theoretically calculated rate constants has been achieved in this work.

The state-to-state dynamics of the Ne + HeH^+ $(v = 0, j = 0) \rightarrow \mathrm{NeH}^+(v', j')$ + He reaction has been studied in detail by means of a TIQM method in combination with QCT-GB and QCT-HB approaches at specific values of the collision energy. The agreement between the quasi-classical and exact TIQM rotational distributions is excellent as the energy increases. Marked preference for the forward-scattering direction manifested by both the exact and QCT angular distributions suggests that the overall dynamics of the title process is far to be entirely attributed to a typical complex-forming mechanism. An analysis using the classical trajectories shows that the reaction is dominated by direct mechanisms producing both nearside and farside scattered products, although a small fraction of trajectories form collision complexes.

References

[1] Croswell, K. *The Alchemy of the Heavens: Searching for Meaning in the Milky Way;* New York: Anchor Books/Doubleday, 1995.

[2] Zygelman, B.; Stancil, P. C.; Dalgarno, A. *Astrophys. J.* **1998**, *508*, 151.

[3] Ferrière, K. M. *Rev. Mod. Phys.* **2001**, *73*, 1031.

[4] Lepp, S.; Stancil, P. C.; Dalgarno, A. *J. Phys. B: At. Mol. Opt. Phys.* **2002**, *35*, R57.

[5] Dalgarno, A. *Faraday Discuss.* **2006**, *133*, 9.

[6] Yao, Y.; Wang, Q. D. *Astrophys. J.* **2006**, *641*, 930.

[7] Barlow, M. J.; Swinyard, B. M.; Owen, P. J.; Cernicharo, J.; Gomez, H. L.; Ivison, R. J.; Krause, O.; Lim, T. L.; Matsuura, M.; Miller, S.; Olofsson, G.; Polehampton, E. T. *Science* **2013**, *342*, 1343.

[8] Bochsler, P.; Petersen, L.; Möbius, E.; Schwadron, N. A.; Wurz, P.; Scheer, J. A.; Fuselier, S. A.; McComas, D. J.; Bzowski, M.; Frisch, P. C. *Astrophys. J. Suppl. Ser.* **2012**, *198*, 13.

[9] Park, J.; Kucharek, H.; Möbius, E.; Leonard, T.; Bzowski, M.; Sokół, J. M.; Kubiak, M. A.; Fuselier, S. A.; McComas, D. J. *Astrophys. J.* **2014**, *795*, 97.

[10] Asplund, M.; Grevesse, N.; Sauval, A. J.; Scott, P. *Annu. Rev. Astron. Astrophys.* **2009**, *47*, 481.

[11] Palmieri, P.; Puzzarini, C.; Aquilanti, V.; Capecchi, G.; Cavalli, S.; de Fazio, D.; Aguilar, A.; Giménez, X.; Lucas, J. M. *Mol. Phys.* **2000**, *98*, 1835.

[12] Panda, A. N.; Sathyamurthy, N. *J. Chem. Phys.* **2005**, *122*, 054304.

[13] Tang, X. N.; Xu, H.; Zhang, T.; Hou, Y.; Chang, C.; Ng, C. Y.; Chiu, Y.; Dressler, R. A.; Levandier, D. J. *J. Chem. Phys.* **2005**, *122*, 164301.

[14] Lv, S.-J.; Zhang, P.-Y.; Han, K.-L.; He, G.-Z. *J. Chem. Phys.* **2010**, *132*, 014303.

[15] Zhao, J.; Luo, Y. *J. Phys. Chem. A* **2012**, *116*, 2388.

[16] de Fazio, D.; de Castro-Vitores, M.; Aguado, A.; Aquilanti, V.; Cavalli, S. *J. Chem. Phys.* **2012**, *137*, 244306.

[17] Zhang, T.; Qian, X.-M.; Tang, X. N.; Ng, C. Y.; Chiu, Y.; Levandier, D. J.; Miller, J. S.; Dressler, R. A. *J. Chem. Phys.* **2003**, *119*, 10175.

[18] Xiao, J.; Yang, C.-L.; Tong, X.-F.; Wang, M.-S.; Ma, X.-G. *J. Phys. Chem. A* **2011**, *115*, 1486.

[19] Gamallo, P.; Defazio, P.; González, M. *J. Phys. Chem. A* **2011**, *115*, 11525.

[20] Gamallo, P.; Huarte-Larrañaga, F.; González, M. *J. Phys. Chem. A* **2013**, *117*, 5393.

[21] Gamallo, P.; Martínez, R.; Sierra, J. D.; González, M. *Phys. Chem. Chem. Phys.* **2014**, *16*, 6641.

[22] Maiti, B.; Kalyanaraman, C.; Panda, A. N.; Sathyamurthy, N. *J. Chem. Phys.* **2002**, *117*, 9719.

[23] Qian, X.-M.; Zhang, T.; Chiu, Y.-H.; Levandier, D. J.; Miller, J. S.; Dressler, R. A.; Ng, C. Y. *J. Chem. Phys.* **2003**, *118*, 2455.

[24] Panda, A. N.; Althorpe, S. C. *Chem. Phys. Lett.* **2006**, *419*, 245 .

[25] Dressler, R. A.; Chiu, Y.; Levandier, D. J.; Tang, X. N.; Hou, Y.; Chang, C.; Houchins, C.; Xu, H.; Ng, C.-Y. *J. Chem. Phys.* **2006**, *125*, 132306.

[26] Liu, X.; Liu, H.; Zhang, Q. *Chem. Phys. Lett.* **2011**, *507*, 24 .

[27] Hu, M.; Xu, W.; Liu, X.; Tan, R.; Li, H. *J. Chem. Phys.* **2013**, *138*, 174305.

[28] de Fazio, D. *Phys. Chem. Chem. Phys.* **2014**, *16*, 11662.

[29] Gamallo, P.; Akpinar, S.; Defazio, P.; Petrongolo, C. *J. Phys. Chem. A* **2014**, *118*, 6451.

[30] Esposito, F.; Coppola, C. M.; Fazio, D. D. *J. Phys. Chem. A* **2015**, *119*, 12615.

[31] Bhattacharya, S.; Panda, A. N. *J. Phys. B: At. Mol. Opt. Phys.* **2009**, *42*, 085201.

[32] Liang, J.-J.; Yang, C.-L.; Wang, L.-Z.; Zhang, Q.-G. *J. Chem. Phys.* **2012**, *136*, 094307.

[33] Xu, W.; Zhang, P. *J. Phys. Chem. A* **2013**, *117*, 1406.

[34] Wu, D.; Guo, M.; Wang, Y.; Yin, S.; Sun, Z.; Hoffmann, M. R. *Theor. Chem. Acc.* **2014**, *133*, 1552.

[35] Glosík, J.; Twiddy, N. D.; Javahery, G.; Ferguson, E. E. *Int. J. Mass Spectrom. Ion Processes* **1991**, *109*, 75.

[36] Matcha, R. L.; Pettitt, B. M.; Meier, P. F.; Pendergast, P. *J. Chem. Phys.* **1978**, *69*, 2264.

[37] Skouteris, D.; Castillo, J. F.; Manolopoulos, D. E. *Comput. Phys. Commun.* **2000**, *133*, 128.

[38] Martínez, R.; Sierra, J. D.; Gray, S. K.; González, M. *J. Chem. Phys.* **2006**, *125*, 164305.

[39] Bulut, N.; Castillo, J. F.; Aoiz, F. J.; Bañares, L. *Phys. Chem. Chem. Phys.* **2008**, *10*, 821.

[40] Sun, Z.; Zhang, C.; Lin, S.; Zheng, Y.; Meng, Q.; Bian, W. *J. Chem. Phys.* **2013**, *139*, 014306.

[41] Rao, T. R.; Goswami, S.; Mahapatra, S.; Bussery-Honvault, B.; Honvault, P. *J. Chem. Phys.* **2013**, *138*, 094318.

[42] Goswami, S.; Rao, T. R.; Mahapatra, S.; Bussery-Honvault, B.; Honvault, P. *J. Phys. Chem. A* **2014**, *118*, 5915.

[43] Xu, W.; Li, W.; Lv, S.; Zhai, H.; Duan, Z.; Zhang, P. *J. Phys. Chem. A* **2012**, *116*, 10882.

[44] Bulut, N.; Zanchet, A.; Honvault, P.; Bussery-Honvault, B.; Bañares, L. *J. Chem. Phys.* **2009**, *130*, 194303.

[45] Gioumousis, G.; Stevenson, D. P. *J. Chem. Phys.* **1958**, *29*, 294.

[46] Drake, G. W. F. *Handbook of Atomic, Molecular, and Optical Physics;* Springer, 2006.

[47] Neese, F. *ORCA, An Ab Initio, DFT and Semiempirical SCF-MO Package;* Max-Planck Institute for Bioinorganic Chemistry, Mülheim a. d. Ruhr, Germany, 2010.

[48] Kumar, A.; Meath, W. J. *Can. J. Chem.* **1985**, *63*, 1616.

[49] Maroulis, G.; Thakkar, A. J. *Chem. Phys. Lett.* **1989**, *156*, 87.

[50] Christiansen, O.; Jørgensen, P. *Chem. Phys. Lett.* **1993**, *207*, 367.

[51] Bañares, L.; Aoiz, F.; Honvault, P.; Bussery-Honvault, B.; Launay, J.-M. *J. Chem. Phys.* **2003**, *118*, 565.

[52] Bañares, L.; Aoiz, F. J.; Honvault, P.; Launay, J.-M. *J. Phys. Chem. A* **2004**, *108*, 1616.

[53] Panda, A. N.; Herráez-Aguilar, D.; Jambrina, P. G.; Aldegunde, J.; Althorpe, S. C.; Aoiz, F. J. *Phys. Chem. Chem. Phys.* **2012**, *14*, 13067.

[54] De Fazio, D.; Aquilanti, V.; Cavalli, S.; Aguilar, A.; Lucas, J. M. *J. Chem. Phys.* **2008**, *129*, 064303.

[55] Sokolovski, D.; De Fazio, D.; Cavalli, S.; Aquilanti, V. *Phys. Chem. Chem. Phys.* **2007**, *9*, 5664.

[56] Truhlar, D. G.; Muckerman, J. T. In *Atom - Molecule Collision Theory*; Bernstein, R. B., Ed.; Springer US, 1979; pages 505.

[57] Bowman, J. M. *Mol. Phys.* **2014**, *112*, 2516.

[58] Mauguière, F. A.; Collins, P.; Ezra, G. S.; Farantos, S. C.; Wiggins, S. *Chem. Phys. Lett.* **2014**, *592*, 282.

Chapter 6

The Ne + NeH$^+$ → NeH$^+$ + Ne Reaction

In this chapter, initial state selected dynamics of the Ne + NeH$^+$ → NeH$^+$ + Ne reaction are reported by carrying out quantum mechanical studies on the ground electronic state. Total reaction probabilities as well as total integral cross sections have been calculated for ground ro-vibrational, first excited rotational and first excited vibrational states of the reactants. Coriolis couplings between the adjacent helicity states are taken into account in the QM calculations. Thermally average rate constants for this reaction are calculated for different initial reactant states and compared with the Langevin rate constant for this reaction. In order to investigate the resonances found in the QM ICSs in the low energy region, quasiclassical simulations have been carried out for the reaction at few collision energies.

Part of the contents of this chapter are published in the following research articles:

- Koner, D.; Barrios, L.; González-Lezana, T.; Panda, A. N. Scattering Study of the Ne + NeH$^+$ $(v_0 = 0, j_0 = 0)$ → NeH$^+$ + Ne Reaction on an *ab initio* Based Analytical Potential Energy Surface. J. Chem. Phys. **2016**, *144*, 034303.

6.1 INTRODUCTION

Protonated rare gas dimers (Rg_2H^+) have attracted the interest of the scientific community for a long time. With an introduction of ionic species e.g., proton in the chemically inert rare gas dimers (Rg_2), electrons are partly delocalized and a distinct charge separation enables covalent or charge induced electrostatic interactions. Thus in Rg_2H^+, the binding becomes much stronger compared to neutral Rg_2, which are bound entirely by weak van der Waal forces. The existence of Rg_2H^+ have been investigated by various groups experimentally as well as theoretically from late sixties. Ferguson *et al.*[1] and Adams *et al.*[2] reported the existence of Rg_2H^+ (Rg = He, Ne, Ar) using the flowing afterglow technique. Kunttu *et al.*[3,4] explored $Rg_2H(D)^+$ (Rg = Ar, Kr, Xe) in Ar, Kr and Xe matrices doped with hydrogen halides and detected the vibration spectra of the bound states. A lot of computational studies have also been carried out on Rg_2H^+ system via *ab initio* or density functional theory methods.[5–10] Most of the works suggest a linear centrosymmetric configuration as the most stable structure. Potential energy surfaces have been generated on the ground electronic state for He_2H^+[11,12] and Ar_2H^+[10] systems. However, reactive scattering studies have been performed only for the $He + HeH^+ \rightarrow HeH^+ + He$ reaction by means of TDWP[13–15] and QCT[12] methods. These studies indicate the reaction as a complex-forming one, and it is found that Coriolis coupling has significant effect on the reaction dynamics.

A DIM PES for the collinear $Ne+NeH^+$ proton transfer process was developed by Matcha *et al.*[16] Electronic structure of the Ne_2H^+system has been explored theoretically by Kim *et al.*,[8] but the dynamics of the $Ne + NeH^+ \rightarrow NeH^+ + Ne$ reaction has not been studied yet. Investigation on this process may be relevant for understanding the evolution of our solar system, because hydrogen and neon are the most and fifth most abundant elements, respectively, in our solar system,[17] and proton-rare gas collisions occur in interstellar medium and planetary ionospheres.[18–20] It is worth mentioning here that NASA's Lunar Atmosphere and Dust Environment Explorer spacecraft's Neutral Mass Spectrometer confirms the existence of neon in lunar exosphere, which mainly comes from solar wind.[21] Besides this, the system $[NeHNe]^+$ is an example of 'heavy-light-heavy' (HLH) system, where quantum effects like tunneling and reactive resonances play important roles in the dynamics, and thus the reaction also has fundamental importance. In this Chapter, the scattering dynamics of the Ne + $NeH^+ \rightarrow NeH^+$ + Ne reaction has been investigated by means of QM calculations. Classical simulations have been performed for few low collision energies to understand the dynamics of this process in the low energy region.

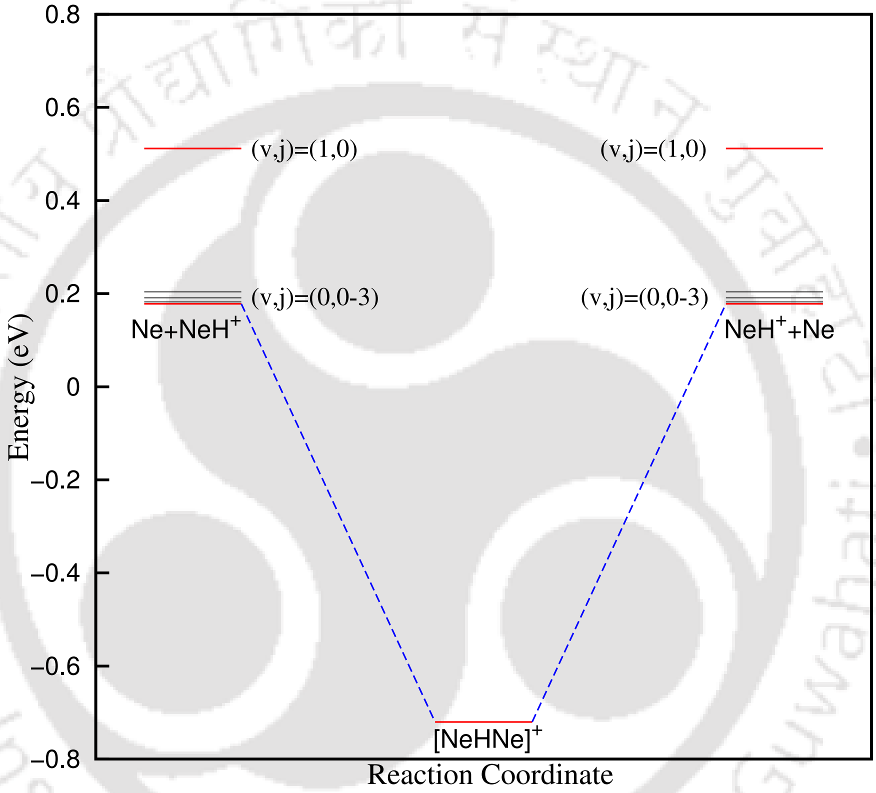

FIGURE 6.1: Schematic potential energy profile of reactants and products for the Ne + $NeH^+ \rightarrow NeH^+$ + Ne reaction. Energy of Ne+NeH^+ asymptote is set as zero.

A schematic potential energy profile of reactants and products for the Ne + $NeH^+ \rightarrow NeH^+$ + Ne reaction is shown in Figure 6.1 along with the global minimum of Ne_2H^+ system. Some selective reactants and products ro-vibrational states are also shown in the same picture. The reaction is thermoneutral with reactants in the ground ro-vibrational states. However, rotational or vibrational excitation of the reactant makes the process exothermic. As can be seen in Figure 6.1, there exists a potential energy well (of depth 0.72 eV with respect to the Ne+NeH^+ asymptote) along the reaction path. The global minimum of the Ne_2H^+ system corresponds to a collinear centrosymmetric Ne-H-Ne configurations with both the NeH bond distances of 2.156 bohr. As it is seen in Chapter 3, the potential well can accommodate a large number of bound and quasibound states.

6.2 METHODS

Two different methodologies, TDQM and TIQM, have been used to study the reactive scattering phenomenon for the title reaction. Details of the TDQM methodology used and implemented in the developed TDQM code is discussed elaborately in Chapter 2. In the TDQM approach, TDSE is solved by propagating the initial WP on a grid following CRWP method. Damping functions expressed in Eq. 2.47, 2.49 have been used in the TDQM calculations. Collision energy resolved initial state selected total reaction probabilities for different partial waves ($P^J_{v,j}(E_c)$) are computed by calculating the total flux in the product channel. All the parameters used in the TDQM calculations to get converged probabilities for the title reactive scattering system are tabulated in Table 6.1.

Table 6.1: Numerical parameters employed in the TDQM calculations (All parameters are given in atomic units).

Number of R grid points	406
Number of r grid points	148
Number of angular grid points	120
R_{min}	0.2
r_{min}	0.5
δR	0.06
δr	0.12
Centre of initial wave packet	15.0
Starting points of damping along R and r	17.5, 13.1
Analysis point along r	12.98
Number of Chebyshev iterations	50000

Coriolis couplings between different K states have been taken into account in the TDQM calculations. In Figure 6.2, total reaction probabilities calculated including different numbers of helicity terms are plotted for three different Js for $(v, j) = (0, 0)$. It is obvious from Figure 6.2 that a value of $K_{\max} = 7$ is sufficient to get converged results for the present case. Total reaction probabilities are also calculated for $(v, j) = (0, 0)$ reactant state using the CS approximation to compare with the exact CC results and to

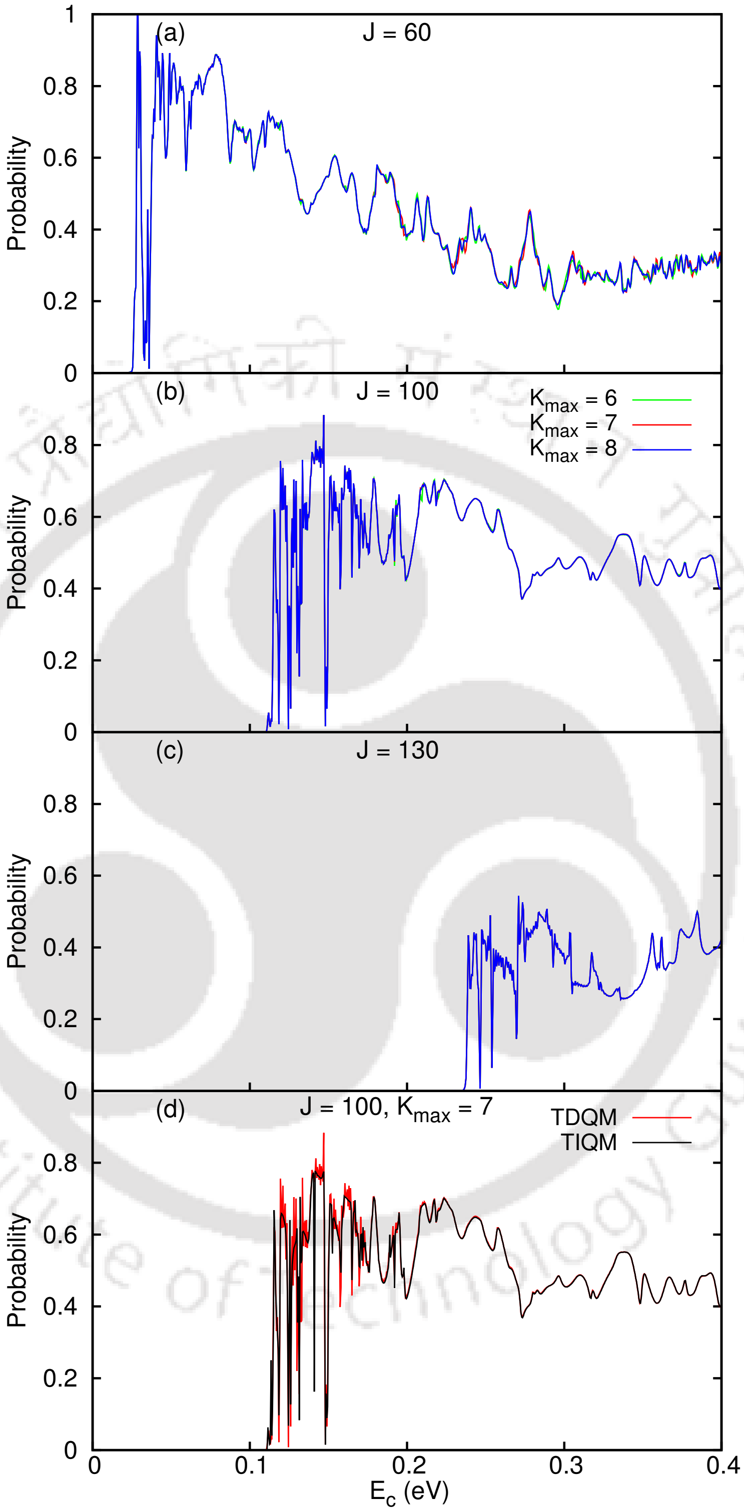

FIGURE 6.2: Convergence of reaction probability values with respect to the $K_{\max}$ value. Top three panels show the TDQM results for $J = 60$, 100 and 130 for $(v, j) = (0, 0)$. The bottom panel shows a comparison of the TDQM results with the TIQM for $J = 100$ and $K_{\max} = 7$.

TABLE 6.2: Numerical parameters employed in the TIQM calculations.

Maximum hyperradius (ρ_{max}/bohr)	30 ($E_c \leq 0.01$ eV)
	25 ($E_c > 0.01$ eV)
Number of log derivative propagation sectors	430 ($E_c \leq 0.01$ eV)
	340 ($E_c > 0.01$ eV)
Maximum rotational quantum number (j_{max})	30
Maximum internal energy (e_{max}/eV)	2.1
Helicity truncation parameter (K_{max})	$\min(7, J)$
Number of basis functions	$386 (J = 0)$
	2586 ($J \geq 7$)

find out the validity of the approximation to study this system. A large number of Js ($\sim$ 160) were needed to compute the total integral cross sections (ICSs) upto $E_c = 0.4$ eV. As the CC calculations are computationally expensive, exact CC probabilities are calculated for all the Js up to 75 and then, for each fifth J afterwards, i.e., for 80, 85, 90,..., J_{max}. A J-shifting technique is employed to compute the CC reaction probabilities for all the remaining Js, for which the variations of reaction probabilities with collision energy are assumed to be relatively smoother. The interpolation procedure is discussed in Chapter 2.

In presence of a potential well in the PES for the title reactive system, it was cumbersome to converge the TDQM reaction probabilities at very low energies ($E_c <$ 0.04 eV). It was also not possible to propagate the WP efficiently and accurately for a sufficiently long time because of finite sized grid used in the calculations and the poor absorption of the WP by the damping function. Here it is worth mentioning that all the parameters of the damping function were extensively checked by varying those for a wide range of values, yet it was impossible to get a proper convergence at very low energies for the present grid (the largest manageable). For this reason, TIQM method have been followed to compute the total reaction probabilities up to 0.05 eV collision energy for the title reaction. The ABC code developed by Manolopoulos and co-workers[22] is used to perform all the TIQM calculations. Separate calculations are performed for each combination of J and triatomic parities. The final set of parameters used in the TIQM calculations are tabulated in Table 6.2. In Figure 6.2 (bottom panel), total reaction probabilities for $J = 100$ obtained from TDQM and TIQM calculation with a K_{max} value of 7 are presented. Excellent agreement between the TDQM and TIQM results confirms that $K_{\max} = 7$ is sufficient to reproduce converged total reaction probabilities for the title reaction.

6.3 RESULTS AND DISCUSSION

6.3.1 Total reaction probabilities

Total reaction probabilities as a function of collision energy for the ground ro-vibrational reactant state and for some selective Js obtained from TDQM-CC, TDQM-CS, TIQM calculations are shown in Figure 6.3. TDQM probabilities are plotted in the collision energy range 0.05 - 0.4 eV for all the Js except for $J = 0$ ($E_c = 0.001$ - 0.4 eV). For $J = 0$, the agreement between TIQM and TDQM results is very good over all the energy region, except at ultra low energies and this shows that the TDQM results are well converged with respect to the set of grid parameters used. For $J > 0$, and $E_c > 0.05$ eV, TIQM probabilities were calculated at few energy points (plotted with blue filled circle) to compare with the TDQM results. An excellent matching between the TIQM and TDQM-CC probabilities is quite clear in Figure 6.3 for all the Js. It is also observed in Figure 6.3 that the reaction probability curves for smaller Js (J = 0, 10, 20, 30, 40) follow a similar average pattern, i.e., these probabilities are remarkably large at low energies and these large values gradually decrease to a minimum as E_c increases. For $E_c \approx 0.15$ - 0.4 eV, the average of the less oscillatory probabilities form a dome like shape and this is followed by an uprising behavior of the average of probabilities towards the end of the energy range. Reaction probability curves for J = 50, 70, 90 and 110 show, on an average, a declining behavior in almost the entire energy range after reaching the maximum value near the threshold region.

With the reactant in its ground ro-vibrational state, the title reaction is thermoneutral in nature and there is no barrier along the MEP (see Figure 6.1). Reaction probabilities for small Js thus start at very low collision energies, as shown in Figure 6.3. As the value of J increases, centrifugal barrier height increases and the reaction fails to occur for collision energies less than the barrier height. This results in appearance of thresholds in the reaction probabilities for larger Js. However, by including the CC

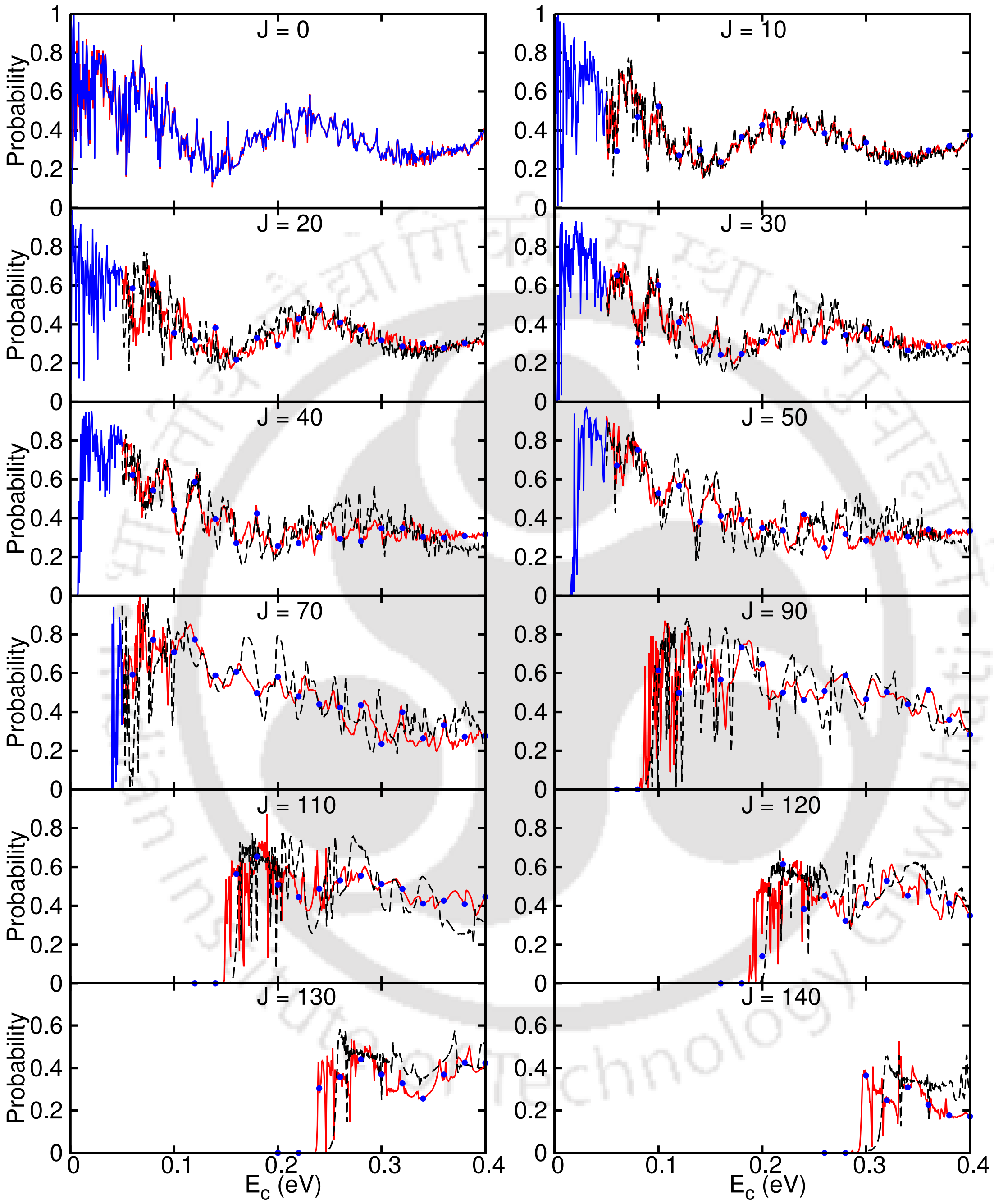

FIGURE 6.3: Total reaction probabilities obtained from TDQM-CS (- -), TDQM-CC (—) and TIQM (— / •) calculations plotted as a function of collision energy for the Ne + NeH$^+$($v = 0, j = 0$) → NeH$^+$ + Ne reaction for few selected J values.

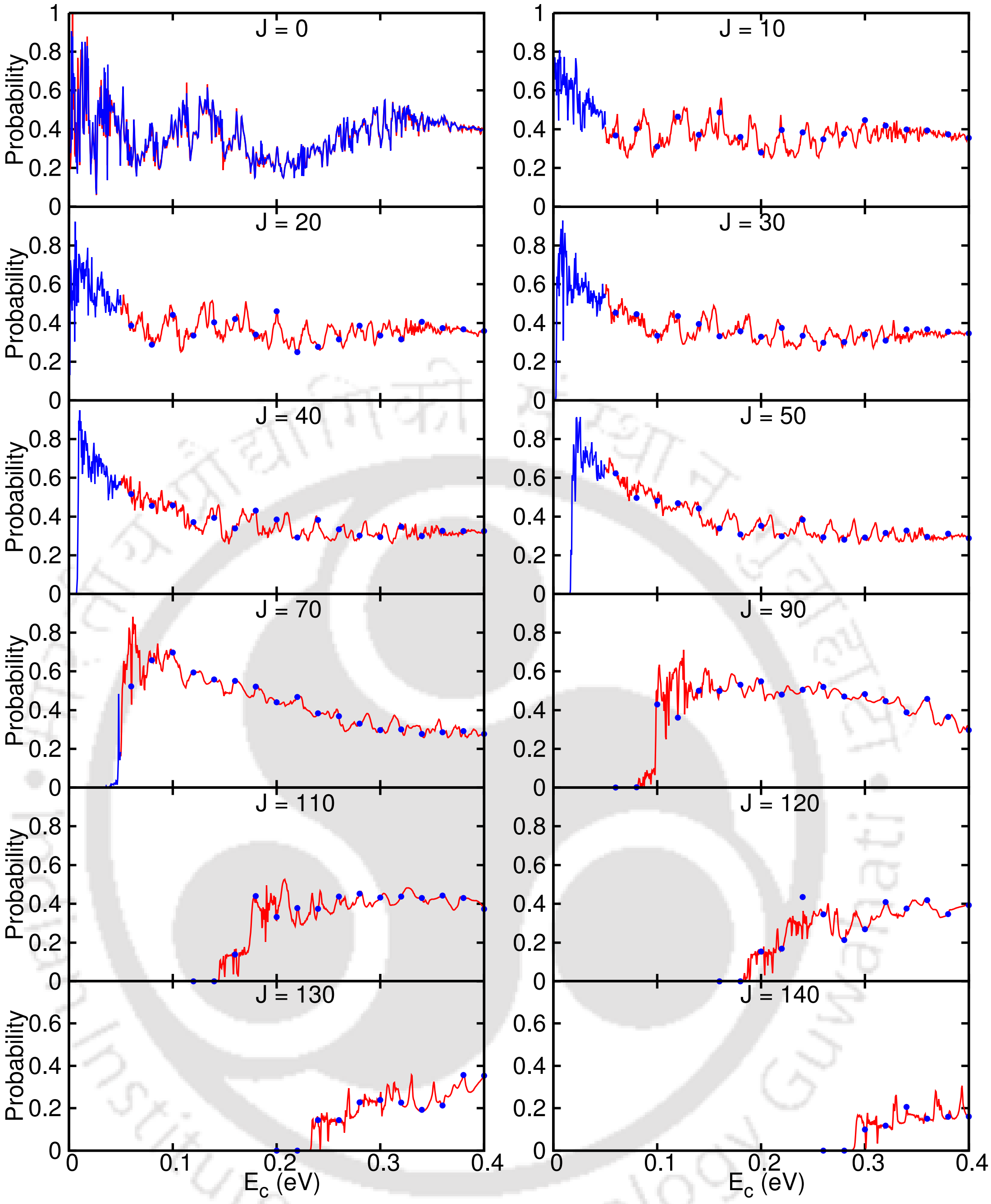

FIGURE 6.4: Total reaction probabilities obtained from TDQM-CC (—) and TIQM (— / •) calculations plotted as a function of collision energy for the Ne + NeH$^+$($v = 0, j = 1$) → NeH$^+$ + Ne reaction for few selected J values.

terms in the calculations, the centrifugal barrier height decreases as it depends on $K_{\max}$ and thus the threshold energies for the CC probabilities become relatively smaller than the corresponding CS probabilities (this is quite clear for larger Js). Minor differences can be seen between CC and CS reaction probabilities for small Js (J = 0, 10, 20, 30), whereas differences are quite large for the larger Js, i.e., J = 40, 50, 70, ..., 130 and 140.

The most important feature of the probability curves in Figure 6.3 is their strong oscillatory behavior. Numerous sharp resonances are observed, particularly for smaller Js and for collision energies not too far from thresholds. The amplitudes of the peaks decrease with the increase in collision energy. As discussed in the previous section, a potential well of depth $\sim$ 0.72 eV is present in the PES for collinear $[\mathrm{NeHNe}]^+$ configuration, which is the most stable structure for the present system. It is seen from the eigen spectrum plotted in Figure 3.16 in Chapter 3 that the potential well supports many metastable states of the $[\mathrm{NeHNe}]^+$ complex near the threshold region and above the dissociation limit of the complex. Those may contribute to the oscillating feature of the reaction probabilities for the title reaction. As can be seen, the resonances are very narrow at low energies, which suggests the formation of collision complexes with long lifetimes in this region. The lifetimes of the metastable states are computed to be $\sim$0.7 ps, from the average width of resonances appearing in the probability curves for smaller Js at around $\sim$ 0.005 eV of E_c. At this point, a batch of 10^6 classical trajectories have been calculated for the Ne + $\mathrm{NeH}^+(v = 0, j = 0) \rightarrow \mathrm{NeH}^+$ + Ne reaction at E_c = 0.005 eV and the collision times (τ) as defined in Chapter 4 are calculated for those trajectories with a cut off value of 5.5 Å. For the reactive trajectories, the average value of τ is found to be $\sim$0.6 ps (close to the QM value), which corresponds to formation of intermediate collision-complexes with long lifetimes. However, the resonance features become less prominent as the peaks become broader with the increase in collision energies. This suggests the shortening of lifetime of the collision complexes at higher energies. These broad peaks may be related to classical periodic orbits of the system. The same is quite clear for the larger values of J and it is apparent that the reaction follows a direct path for larger Js at higher collision energies. However, dense resonances are still quite obvious for the larger Js near the threshold region.

Total reaction probabilities computed by means of TDQM-CC and TIQM calculations for the title reaction with the reactants in first excited rotational state and in first excited vibrational state are plotted for few selected Js in Figures 6.4 and 6.5, respectively. Whereas a very good agreement is observed between the results obtained from both the QM methods for (v, j) = (0, 1) and $J = 0$, the results are in fairly good agreement with each other in the case of (v, j) = (1, 0) and $J = 0$. In the case of (v, j) =

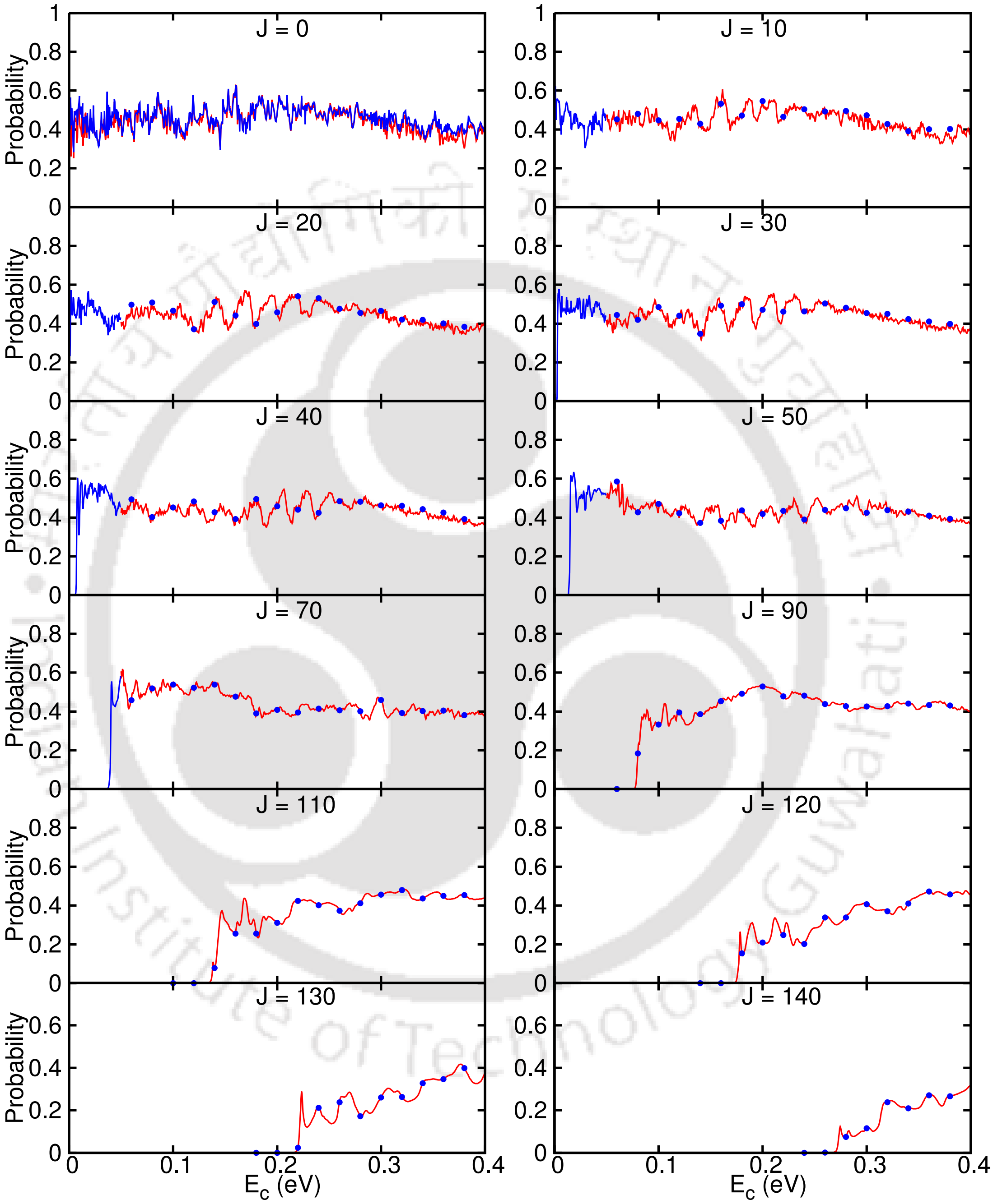

FIGURE 6.5: Same as Figure 6.4 for Ne + NeH$^+$($v = 1, j = 0$) $\rightarrow$ NeH$^+$ + Ne.

(1, 0) and $J = 0$, the TDQM results differ slightly from the corresponding TIQM results at ultra low and very high energies. For $J > 0$, TDQM results are in a good accord with the TIQM results (presented by filled blue circles) in the entire energy range for both $(v, j) = (0, 1)$ and (1, 0) initial states, except the minor differences noticed at high collision energies for $(v, j) = (1, 0)$ and $J = 10$, 20, 30 and 40. As it is seen in Figure 6.4, average of the probabilities for (v, j) = (0, 1) follow similar patterns like $(v, j) = (0, 0)$; for Js upto 90, probabilities are large at low energies and gradually decrease with increase in energy, and for J = 110, 120, 130 and 140 the probabilities increase with increase in energy. Dense resonances can also be seen in the probability curves (v, j) = (0, 1) for low values of J in the low energy region. However, the amplitude of the oscillations are somewhat less than those observed for $(v, j) = (0, 0)$. Complex forming mechanism may still play a significant role for the title reaction with the reactants in first excited rotational state.

It is obvious in Figure 6.5 that the average behavior of the probability curves for (v, j) = (1, 0) and J = 0 - 90 is completely different than those of (v, j) = (0, 0) and (0, 1). The probabilities for (v, j) = (1, 0) and J = 0 - 100 oscillate around $\sim$ 0.4 and have magnitudes in between $\sim$ 0.25 and $\sim$ 0.6 in the entire energy region. Similar behavior is also observed for the Ne + HeH$^+$$(v = 1, j = 0)$ → He + NeH$^+$ reaction (see Chapter 5). However, probabilities for J = 110 - 140 and (v, j) = (1, 0) follow an average behavior similar to that of (v, j) = (0, 0). It can be seen in Figure 6.5 that the reaction probabilities for $(v, j) = (1, 0)$ is comparatively less oscillatory compared to the results of (v, j) = (0, 0) and (0, 1). The probability curves for comparatively larger values of J and $(v, j) = (1, 0)$ are very smooth. Broad oscillations can be seen in the average of the probabilities for $(v, j) = (1, 0)$ and J = 10, 20, 30, 40 and 50 at E_c = 0.12 - 0.25 eV. It can be said that an increase in the internal energy of the reactants by vibrational excitation makes the collision complex weaker and short-lived, thus leading to relatively smoother probability curves.

Figure 6.6 compares the total reaction probabilities calculated for different initial ro-vibrational states. While the probabilities for (v, j) = (0, 1) and J = 10, 20 and 30 are smaller than the corresponding (v, j) = (0, 0) results in the low energy region, the trend

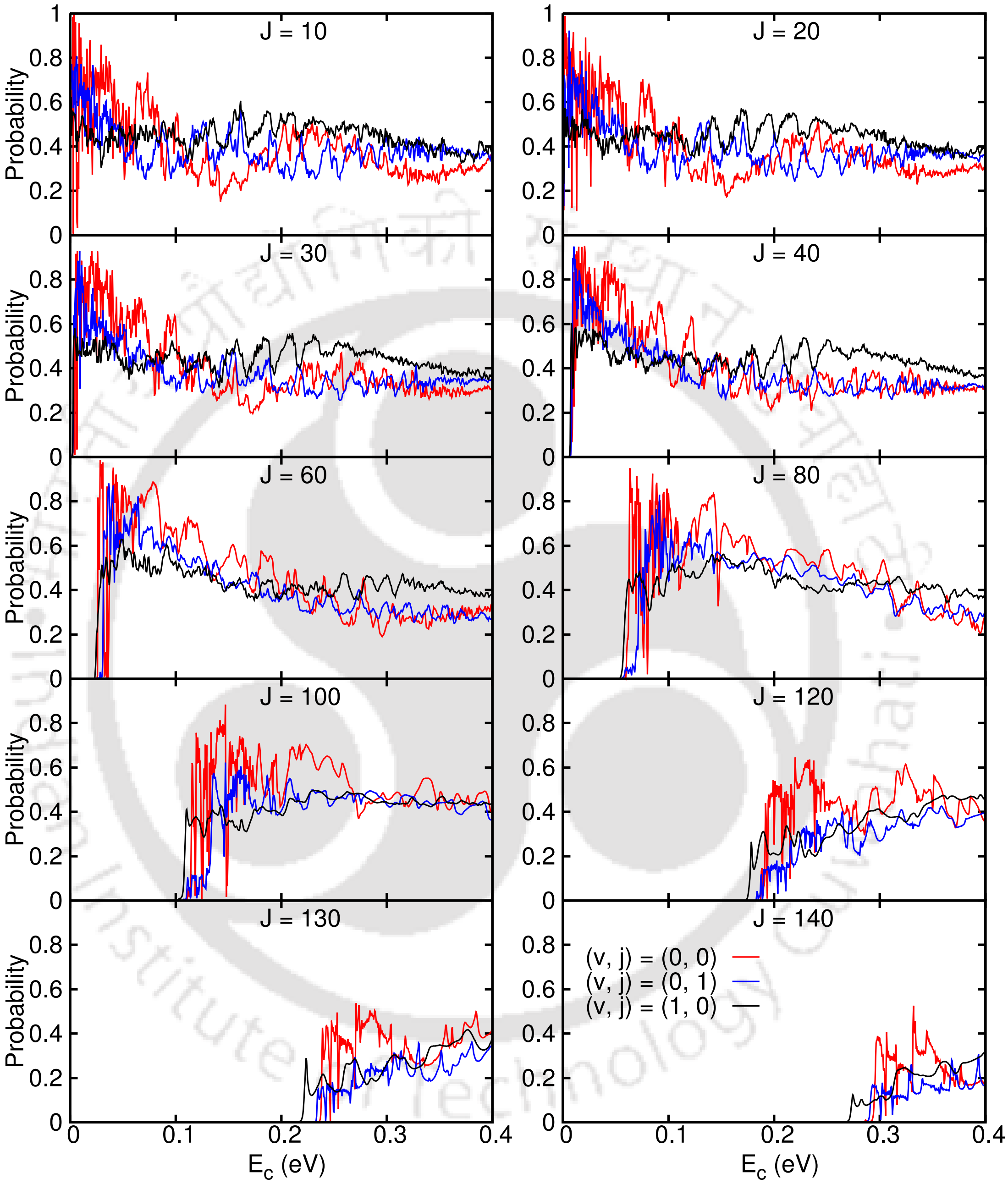

FIGURE 6.6: Comparison between different initial state selected total reaction probabilities for Ne + NeH$^+$ → NeH$^+$ + Ne reaction for few selected J values. Probabilities at $E_c = 0.001$ - 0.05 eV are calculated via TIQM calculations and probabilities at rest of the energies are calculated via TDQM-CC calculations.

reverses in the high energy region. For $J = 40$, 60 and 80, $(v, j) = (0, 1)$ probabilities are smaller than corresponding $(v, j) = (0, 0)$ ones at $E_c < 0.3$ eV and both $(v, j) = (0, 1)$ and (0, 0) probabilities are pretty close at high energies. The probabilities for $(v, j) = (0, 1)$ and $J = 100$ - 140 are smaller than corresponding $(v, j) = (0, 0)$ probabilities in almost entire energy region. As it is seen in Figure 6.6, the probabilities for $(v, j) = (1, 0)$ and $J = 0$ - 80 are smaller at low and moderate collision energies, but larger at high collision energies than corresponding $(v, j) = (0, 0)$ probabilities. A substantial decrease in the threshold for the $(v, j) = (1, 0)$ probabilities for larger values of J is clearly seen compared to $(v, j) = (0, 0)$ probabilities. Vibrational excitation enhances the internal energy of the reactants and the centrifugal barrier appeared for larger values of J is overcome by the reactants to form product at comparatively low collision energies.

6.3.2 Integral cross sections

In Figure 6.7, total ICSs for the Ne + $NeH^+ \rightarrow NeH^+$ + Ne reaction for different initial states obtained from TDQM and TIQM calculations are plotted as a function of E_c. The whole energy range in this figure can be divided into two sub-regimes, the low-energy region below 0.05 eV and the moderate to high-energy region beyond 0.05 eV. As has been mentioned before, because of the finite-sized grids and improper absorbing of the WP at the grid edges, difficulties arose in converging the TDWP calculations below 0.04 eV and TIQM approach becomes the accurate method to investigate the overall dynamics in the low-energy region. It can be seen in Figure 6.7 that the TDQM calculations highly underestimate the reaction cross sections at low energies. Probably propagation of the WP for a much longer time would produce improved results. It is seen that for all the initial states, the reaction cross section starts with a very large value in the low-energy region, and then rapidly decreases with increase in E_c. Beyond $E_c = 0.02$ eV, ICSs decrease progressively but very slowly with energy. At high collision energies, the ICSs remain almost invariant with respect to E_c. This behavior of the ICSs is very typical of barrierless exothermic or thermoneutral reactions.[13,14,23–29] Blue filled circles in Figure 6.7 refer to the TIQM cross sections at few selected energies in the moderate and high-energy region. As it is observed, these TIQM ICSs are in an

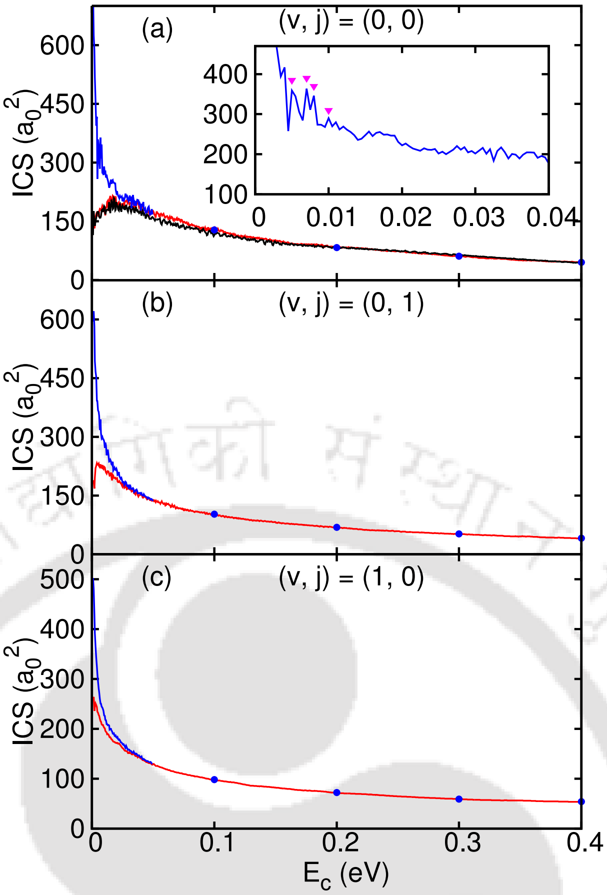

FIGURE 6.7: Initial state selected total ICSs as a function of collision energy for Ne + NeH$^+$ → NeH$^+$ + Ne reaction obtained from TIQM (- - / ●), TDQM-CC (—) and TDQM-CS (—) calculations. For (v, j) = (0, 0) state, the low-energy region is zoomed in the inset and few selected resonance peaks are marked with filled magenta triangles.

excellent agreement with the TDQM-CC ICSs. For $(v, j) = (0, 0)$, the CS approximation clearly underestimates the exact results for $E_c < \sim 0.2$ eV. Inclusion of CC allows the reactants to undergo out of plane rotations necessary to excite the vibrational modes of the collision complex formed during the reaction leading to efficient evolvement into products. In the CS approach where the molecular rotation is confined to the molecular plane, the dissociation pathways are limited leading to smaller cross sections. However, at high energies, the reaction may adopt a direct mechanism path and hence, CC is observed to have less effect on the reaction mechanism. Similar situation is also noted for the Ne + HeH$^+$$(v = 0, j = 0)$ → NeH$^+$ + He reaction (see Chapter 5). Inclusion of CC in the QM calculations was found to enhance the reactivity for a similar type reaction, He + HeH$^+$$(v = 0, j = 0)$ → HeH$^+$ + He.[14]

The interesting feature in the low-energy region of the ICSs for (v, j) = (0, 0) state

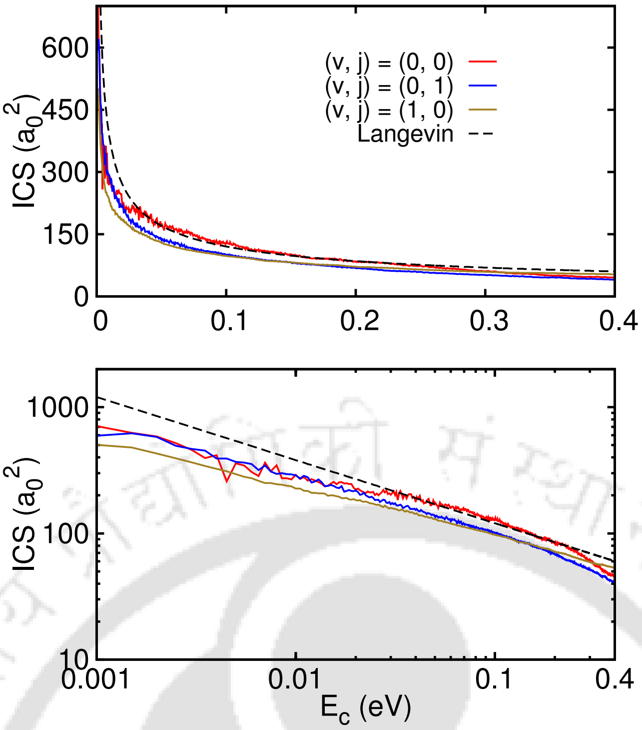

FIGURE 6.8: Comparison between different initial state selected exact QM ICSs. The cross sections at E_c = 0.001 - 0.05 eV are obtained from TIQM probabilities and ICSs at rest of the energies are obtained from TDQM-CC probabilities. In the bottom panel both the ICSs and collision energies are plotted in log-scale

is the presence of sharp but small oscillations which have survived the J-averaging as shown in the inset. Similar observations have been made in systems like He+H_2^+,[30] Ne+H_2^+,[31,32] H+HeH$^+$[29,33] and He+HeH$^+$[13,14] etc. As has been discussed already, the potential well supports many metastable states above the dissociation limit of the complex leading to manifestation of resonances. The power spectrum computed using the TDWP method, as shown in Figure 3.16 in Chapter 3 also supports this idea. In what follows, four resonance peaks in the ultra low-energy region (E_c = 0.005, 0.007, 0.008 and 0.01 eV) of the ICS curve have been identified, and these are marked as filled magenta triangles in the inset of Figure 6.7a. These resonance peaks are investigated in a more detailed manner and discussed in the next section.

Effect of reactant vibrational or rotational excitations have been presented in Figure 6.8. ICSs for (v, j) = (0, 1) and (v, j) = (0, 0) are pretty close to each other at $E_c <$ 0.015 eV. At E_c = 0.015 eV, the (v, j) = (0, 1) ICSs start to decrease with respect to (v, j) = (0, 0) ICSs with increase in energy and remain smaller upto E_c = 0.4 eV. Inhibition of reactivity due to rotational excitation is seen earlier for many exothermic reactions,[23,27,28] which may be related to orientation effect of the reactants. With regard to vibrational excitation, the ICS values clearly underestimate the $(v, j) = (0,\ 0)$ results in the low and moderate energies. Similar trend is also noticed for the exothermic Ne + HeH$^+$ → NeH$^+$ + He (see Chapter 5) and C+OH[34] reactions. However, in the high-energy region, $(v, j) = (1,\ 0)$ ICSs are a bit higher than the $(v, j) = (0,\ 0)$ ICSs.

According to Langevin's capture model,[35,36] the ICSs for a barrierless reaction between an ion and a neutral species can be expressed as $\sigma(E_c) = 2\pi \left(\frac{C_4}{E_c}\right)^{1/2}$ where C_4 is written as $C_4 = \frac{1}{2}\frac{q^2\alpha}{(4\pi\epsilon_0)^2}$. α is the dipole polarizability of the neutral reactant and ϵ_0 is vacuum permittivity. C_4 for the neon atom is calculated from the PES by comparing the potential computed at large R values (20 - 30 a.u.) with $-C_4/R^4$ and then, by averaging over different initial orientations of the reactants. This yields a value of 2.6974 a.u. for α of the Ne atom which is close to the experimental value of 2.67 a.u.[37,38] For comparison purpose, α has also been calculated at CCSD(T)/aug-cc-pVQZ level numerically to be 2.5933 a.u. using the Gaussian 09 software.[39] The ICSs for the title reaction using $C_4 = 1.3487$ a.u. and computed by employing the above stated formula is also depicted in Figure 6.8. The QM ICSs show the same overall behavior like Langevin ICSs in the entire energy region, except at low energies where a significant deviation is seen between the QM ICSs and the capture cross sections. This may stem from the inherent limitation of Langevin's model as the model assumes an isotropic interaction between the reactants.

6.3.3 Analysis of resonance peaks in the ICSs

The resonance peaks marked as filled magenta triangles in the low energy region for $(v, j) = (0,\ 0)$ are investigated by analyzing partial cross-sections and DCSs at those energies obtained from TIQM calculations. Here, it is worth mentioning that TIQM calculations were performed for those set of energies with values of $K_{\max} = 12$ and 7, and a value of $K_{\max} = 7$ was found to be sufficient to converge the state-to-state TIQM results in this low-energy region.

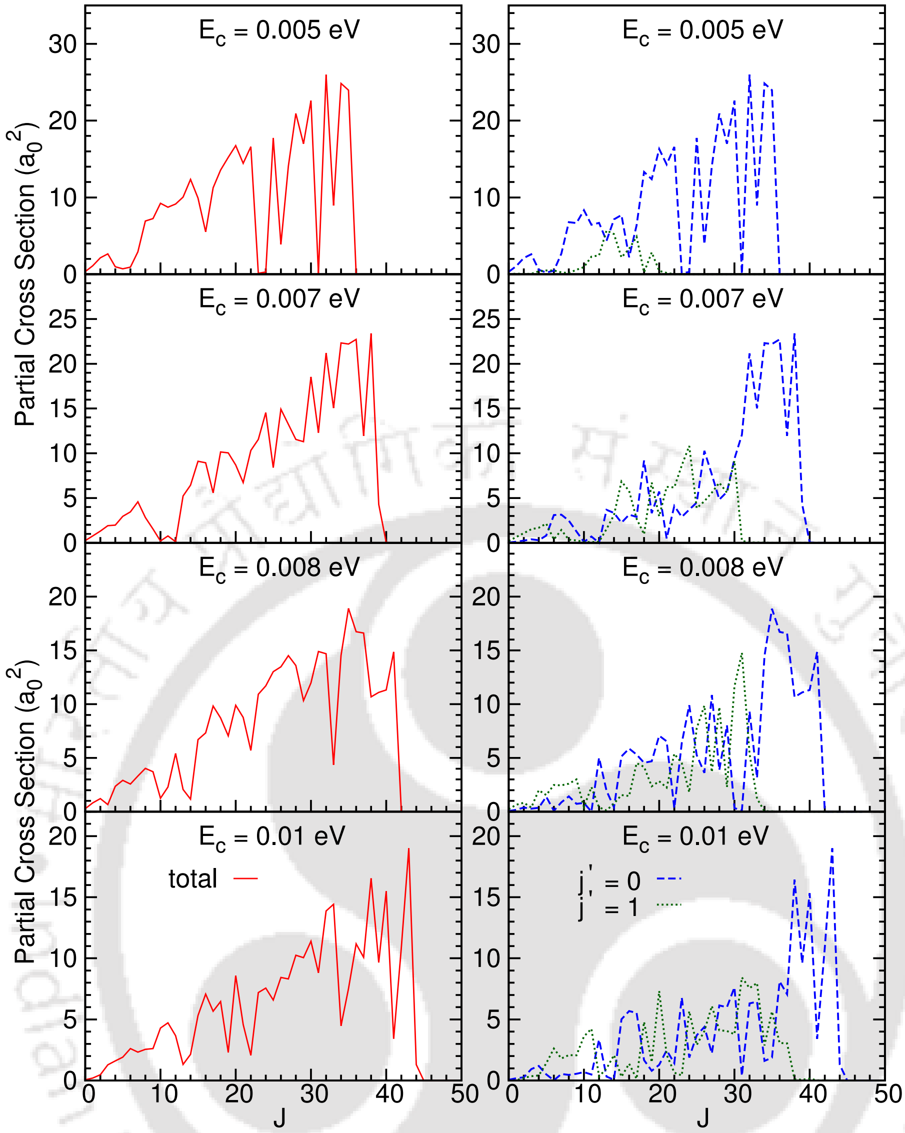

FIGURE 6.9: Partial cross section obtained by means of TIQM calculation at four low values of collision energies marked as filled magenta triangles in Figure 6.7a inset. (left panels) total ones, (right panels) for different product rotational states.

The partial cross section ($\pi/k^2(2J+1)P^J$) at those energies obtained from TIQM calculations are plotted in Figure 6.9. Particular observations in Figure 6.9 are again the oscillatory structure of the partial cross sections showing the contributions of different Js, which are almost zero for some partial waves and are extremely significant for some values of J. In Figure 6.9 right panels, it can be seen that some particular values of J contribute to a particular product rotational state for different energies. Significant contributions to the total ICSs coming from different combinations of Js for a particular collision energy has previously been noticed for Ne+H$_2^+$ reactive scattering.[32] It was suggested that this behavior is related to the selection rules for a particular transition for that process.[32] In the present case, the complicated structure of the eigenvalue spectrum as shown in Figure 3.16 in Chapter 3 in conjunction with the special behavior of partial cross sections lends support to the importance of resonances in this reaction.

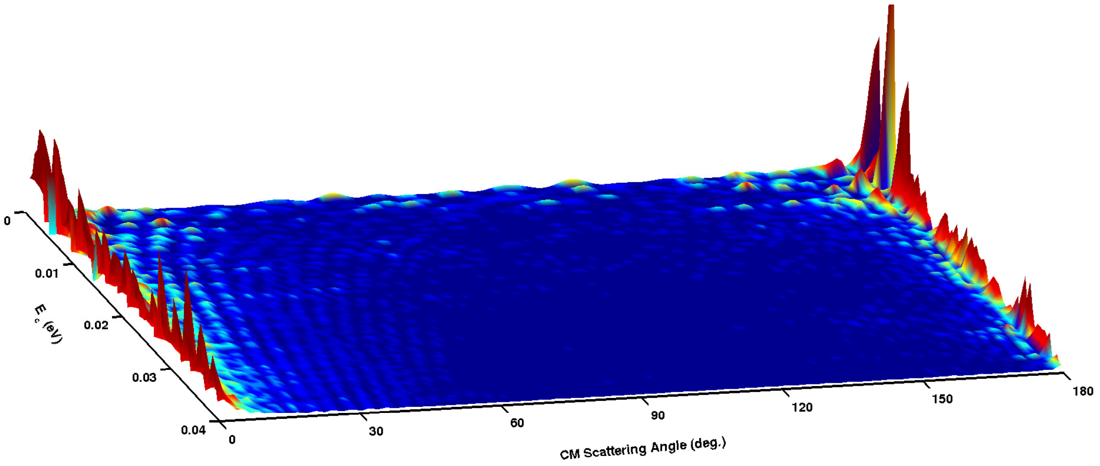

FIGURE 6.10: TIQM differential cross sections (z-axis) for the Ne + NeH$^+$($v = 0, j = 0$) $\rightarrow$ NeH$^+$ + Ne reaction as a function of collision energies in the low energy-region.

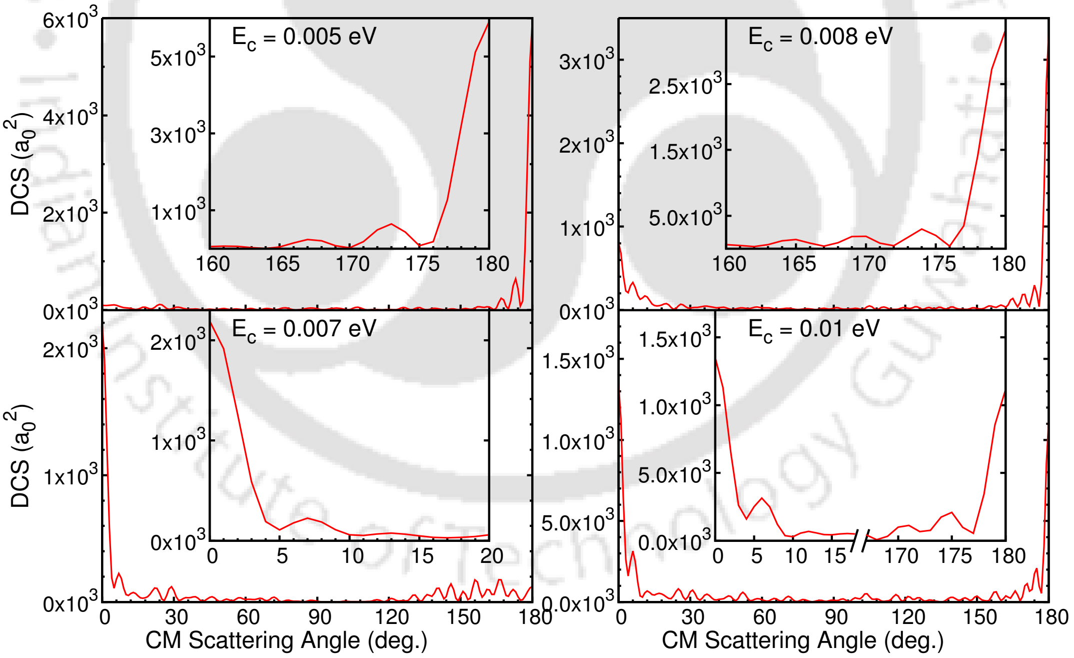

FIGURE 6.11: Differential cross sections obtained by means of TIQM calculations at four collision energies marked as filled magenta triangles in Figure 6.7a inset.

Differential cross sections computed in the low energy region by means of TIQM calculations are presented in Figure 6.10 for E_c = 0.001 - 0.04 eV. Sharp oscillatory structures of the DCSs can be seen at ultra low energies. As it is seen in Figure 6.10, the pattern of the DCSs change in a nonmonotonic way with increase in collision energy. In Figure 6.11, DCSs are plotted for few selected E_cs (marked as filled magenta triangles in Figure 6.7a inset). The DCS curves for $E_c = 0.005$, 0.007 and 0.008 eV are totally asymmetric with a prominent peak close to one extreme end. For $E_c = 0.005$ eV, DCSs have very high magnitudes at $\theta \approx 180°$. While the reaction predominantly favors forward scattered products ($\theta \approx 0°$) for $E_c = 0.007$ eV, a reverse situation can be seen (i.e., prominent peak at $\theta \approx 180°$) for $E_c = 0.008$ eV. Nearly symmetric pattern of angular distribution is obvious for $E_c = 0.01$ eV. Such a drastic change in the DCSs with minor alteration of collision energy can be correlated with the resonances appeared in the low-energy region of the ICSs. Similar situation was also observed in previous studies on the Ne+H_2^+[32] and F+H_2[40] systems. It was suggested that Feshbach resonances play important role for those systems. In the present case, nearly symmetric angular distributions are noticed for few E_cs indicating the presence of stable intermediate-complex for this reaction at those energies.

In order to get a glimpse of the reaction in the low-energy region, classical mechanical simulations have been performed at few selected collision energies (marked as filled magenta triangles in Figure 6.7a). Theoretical details of the classical simulation methodologies are discussed in Chapter 2. A uniform J-sampling method is used to investigate the process at a particular energy, and 10^6 number of trajectories have been calculated at each collision energy. QCT-GB method was found to perform poorly for this reaction. Hence, HB approach is followed to assign the product states. The collision time defined earlier in this section has been calculated for each trajectory. τ gives a direct indication about the nature of a trajectory. In the present case, a trajectory with a value of $\tau <\sim 85$ fs is found to be a direct trajectory. A single collision occurs between the reactants for those direct trajectories. However, it is observed that a large number of reactive as well as nonreactive trajectories get trapped in the potential well of the PES to form short- and long-lived collision complexes. There are many trajectories with long lifetimes for which internally excited reactants or products are loosely bound and roam in a large region as a result of having insufficient translational energy to allow them to break apart. Being a heavy-light-heavy system, those roaming trajectories may be associated with stable periodic orbits in classical mechanics and can be correlated to HLH type resonances in QM.[41,42]

ICSs obtained from quasiclassical simulations for the Ne + $NeH^+(v = 0, j = 0) \rightarrow NeH^+$ + Ne reaction are tabulated in Table 6.3. Significant differences seen between the QM and QCT ICSs are because of vibrationally adiabatic nonreactive trajectories. As observed in case of H^++H_2 and H^++D_2 systems, an adiabatic correction may produce better results.[43] Contributions of the indirect trajectories to the total cross sections (σ_{com}) are calculated and reported in Table 6.3. It is found that the indirect trajectories contribute $> 50\%$ to the total cross section at 0.005, 0.007, 0.008 and 0.01 eV of collision energies. Average collision times for the reactive trajectories at a particular E_c, defined as $\tilde{\tau} = 1/N_r \times \sum \tau_i$ are also tabulated in Table 6.3. In the present case, values of $\tilde{\tau}$ are too large making the complexes to forget about the initial states. Therefore, it can be concluded that the Ne + $NeH^+(v = 0, j = 0) \rightarrow NeH^+$ + Ne reaction is strongly governed by indirect mechanisms including complex-forming mechanism (formation of stable or short-lived intermediate complexes) at low collision energies.

TABLE 6.3: Classical simulation results for the Ne + $NeH^+(v = 0, j = 0) \rightarrow NeH^+$ + Ne reaction at few selected collision energies. TIQM ICS values are also given.

E_c	TIQM-ICS (a_0^2)	QCT-ICS (a_0^2)	$\sigma_{\text{com}}(a_0^2)$	$\tilde{\tau}(fs)$
0.005	359.03	352.04	186.8	605.4
0.007	363.54	308.77	159.8	544.3
0.008	346.28	291.54	150.2	541.8
0.01	290.30	268.23	134.5	520.8

6.3.4 Rate constants

Temperature dependent thermal rate constants for the title reaction have been computed from the exact QM cross sections for a wide range of temperatures and the results are represented in Figure 6.12. Rate constant for a barrierless reaction between an ion and a neutral species can also be calculated by using Langevin's capture model as[35,36] $k_{\text{Lang}}(T) = 2\pi \left(\frac{2C_4}{\mu_R}\right)^{1/2}$. Such a rate constant is temperature independent and for most of the reactions, $k_{\text{Lang}}(T)$ has a magnitude $\approx 10^{-9}$ cm^3 s^{-1}. In the present case, $k_{\text{Lang}}(T)$ has been calculated as 0.4627 $\times 10^{-9}$ cm^3 s^{-1} and is plotted in Figure 6.12.

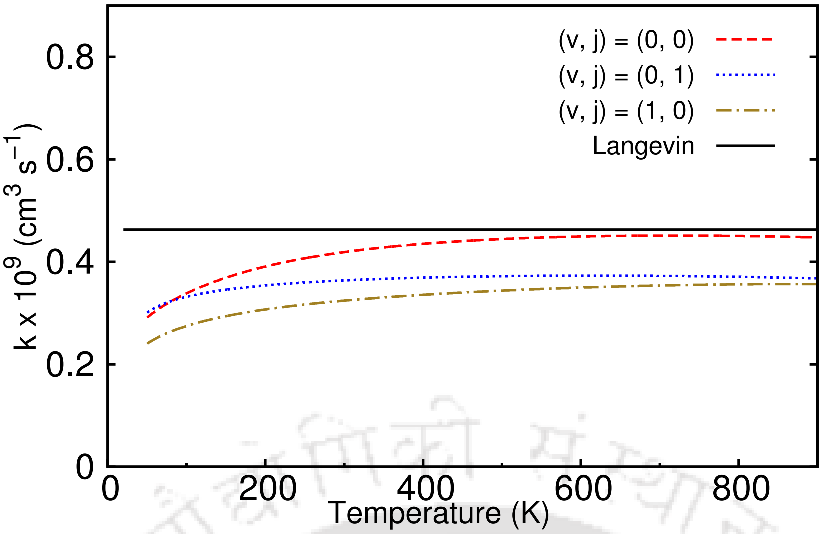

FIGURE 6.12: Temperature dependence of the rate constants for different initial states for the Ne + NeH$^+$ → NeH$^+$ + Ne reaction. Rate constant obtained by following Langevin model is shown as solid line.

It can be seen that the QM rate constant is almost invariant at high temperatures and as the temperature decreases QM $k(T)$ shows a declining trend. All the initial state specific rate constants are smaller than $k_{\text{Lang}}(T)$ at all the temperatures. However, Rate constants for $(v, j) = (0, 0)$ are in good agreement with $k_{\text{Lang}}(T)$ at high temperatures. In view of the requirements for a sufficiently large asymptotic distance in time independent approaches and the difficulties found for time dependent techniques to treat the low energy regime, one has to be very careful in the analysis of the behavior of rate constants at low temperatures, before extracting any definitive conclusion. It is to be mentioned that in the QM rate constant calculation, the minimum collision energy (E_{min}) was 0.001 eV, a value which perhaps should be even decreased for an accurate description of $k(T)$ when the temperature under study is low. Rate constants for $(v, j) = (0, 1)$ and $(1, 0)$ are smaller than $(v, j) = (0, 0)$ ones in almost entire temperature range reported here. However, at ultra low temperatures, $(v, j) = (0, 1)$ rate constant is slightly larger than corresponding $(v, j) = (0, 0)$ results.

6.4 CONCLUSIONS

The Ne + NeH$^+$ → NeH$^+$ + Ne reaction has been studied by means of TDQM and TIQM methodologies for different initial reactant states. Both, CC and CS approaches are followed in the TDQM calculations. Although TDQM methods fails to reproduce correct results at very low energies, an overall excellent agreement is found between TDQM-CC and TIQM results in moderate and high energy regions. Dense oscillatory structures are observed in the total reaction probability curves for low Js and for (v, j) = (0, 0). Those resonances survive the partial wave summation and appear in the total ICS curve. Analysis of the QM results indicates that the reaction is mediated by resonances as well as complex-forming mechanisms in the low energy region. A set of quasiclassical simulations have been performed at few selected low collision energies. Presence of numerous trapped and roaming trajectories for this reaction suggests that a major portion of the reaction occurs via indirect mechanisms. Rotational excitation of the reactant diatom inhibits the reaction. Vibrational excitation of the reactants is found to inhibit the reaction at low and moderate energies and promote the reaction at high energies. Initial state selected thermally average rate constants for the reaction are calculated for a wide range of temperatures. At high temperatures, rate constants for (v, j) = (0, 0) are found to be in excellent agreement with the rate constant calculated by following the Langevin capture model.

References

[1] Fehsenfeld, F. C.; Schmeltekopf, A. L.; Ferguson, E. E. *J. Chem. Phys.* **1967**, *46*, 2802.

[2] Adams, N. G.; Bohme, D. K.; Ferguson, E. E. *J. Chem. Phys.* **1970**, *52*, 5101.

[3] Kunttu, H.; Seetula, J.; Räsänen, M.; Apkarian, V. A. *J. Chem. Phys.* **1992**, *96*, 5630.

[4] Kunttu, H. M.; Seetula, J. A. *Chem. Phys.* **1994**, *189*, 273.

[5] Lundell, J. *J. Mol. Struct.* **1995**, *355*, 291.

[6] Fridgen, T. D.; Parnis, J. M. *J. Chem. Phys.* **1998**, *109*, 2162.

[7] Lundell, J.; Pettersson, M.; Räsänen, M. *Phys. Chem. Chem. Phys.* **1999**, *1*, 4151.

[8] Kim, S. T.; Lee, J. S. *J. Chem. Phys.* **1999**, *110*, 4413.

[9] Gianturco, F. A.; Filippone, F. *Comput. Phys. Commun.* **2002**, *145*, 78.

[10] Qu, J. Y.; Li, W.; Guo, R.; Zhao, X. S. *J. Chem. Phys.* **2002**, *117*, 2592.

[11] Panda, A. N.; Sathyamurthy, N. *J. Phys. Chem. A* **2003**, *107*, 7125.

[12] Liang, J.-J.; Yang, C.-L.; Wang, L.-Z.; Zhang, Q.-G. *J. Chem. Phys.* **2012**, *136*, 094307.

[13] Bhattacharya, S.; Panda, A. N. *J. Phys. B: At. Mol. Opt. Phys.* **2009**, *42*, 085201.

[14] Xu, W.; Zhang, P. *J. Phys. Chem. A* **2013**, *117*, 1406.

[15] Wu, D.; Guo, M.; Wang, Y.; Yin, S.; Sun, Z.; Hoffmann, M. R. *Theor. Chem. Acc.* **2014**, *133*, 1552.

[16] Matcha, R. L.; Milleur, M. B.; Meier, P. F. *J. Chem. Phys.* **1978**, *68*, 4748.

[17] Asplund, M.; Grevesse, N.; Sauval, A. J.; Scott, P. *Annu. Rev. Astron. Astrophys.* **2009**, *47*, 481.

[18] Zygelman, B.; Stancil, P. C.; Dalgarno, A. *Astrophys. J.* **1998**, *508*, 151.

[19] Ferrière, K. M. *Rev. Mod. Phys.* **2001**, *73*, 1031.

[20] Lepp, S.; Stancil, P. C.; Dalgarno, A. *J. Phys. B: At. Mol. Opt. Phys.* **2002**, *35*, R57.

[21] http://sservi.nasa.gov/articles/nasas-ladee-spacecraft-finds-neon-in-lunar-atmosphere/.

[22] Skouteris, D.; Castillo, J. F.; Manolopoulos, D. E. *Comput. Phys. Commun.* **2000**, *133*, 128.

[23] Bulut, N.; Castillo, J. F.; Aoiz, F. J.; Bañares, L. *Phys. Chem. Chem. Phys.* **2008**, *10*, 821.

[24] Xu, W.; Li, W.; Lv, S.; Zhai, H.; Duan, Z.; Zhang, P. *J. Phys. Chem. A* **2012**, *116*, 10882.

[25] Sun, Z.; Zhang, C.; Lin, S.; Zheng, Y.; Meng, Q.; Bian, W. *J. Chem. Phys.* **2013**, *139*, 014306.

[26] Hu, M.; Xu, W.; Liu, X.; Tan, R.; Li, H. *J. Chem. Phys.* **2013**, *138*, 174305.

[27] Rao, T. R.; Goswami, S.; Mahapatra, S.; Bussery-Honvault, B.; Honvault, P. *J. Chem. Phys.* **2013**, *138*, 094318.

[28] Goswami, S.; Rao, T. R.; Mahapatra, S.; Bussery-Honvault, B.; Honvault, P. *J. Phys. Chem. A* **2014**, *118*, 5915.

[29] de Fazio, D. *Phys. Chem. Chem. Phys.* **2014**, *16*, 11662.

[30] de Fazio, D.; de Castro-Vitores, M.; Aguado, A.; Aquilanti, V.; Cavalli, S. *J. Chem. Phys.* **2012**, *137*, 244306.

[31] Gamallo, P.; Defazio, P.; González, M. *J. Phys. Chem. A* **2011**, *115*, 11525.

[32] Gamallo, P.; Huarte-Larrañaga, F.; González, M. *J. Phys. Chem. A* **2013**, *117*, 5393.

[33] Gamallo, P.; Akpinar, S.; Defazio, P.; Petrongolo, C. *J. Phys. Chem. A* **2014**, *118*, 6451.

[34] Bulut, N.; Zanchet, A.; Honvault, P.; Bussery-Honvault, B.; Bañares, L. *J. Chem. Phys.* **2009**, *130*, 194303.

[35] Gioumousis, G.; Stevenson, D. P. *J. Chem. Phys.* **1958**, *29*, 294.

[36] Drake, G. W. F. *Handbook of Atomic, Molecular, and Optical Physics;* Springer, 2006.

[37] Orcutt, R. H.; Cole, R. H. *J. Chem. Phys.* **1967**, *46*, 697.

[38] Hohm, U.; Kerl, K. *Mol. Phys.* **1990**, *69*, 803.

[39] Frisch, M. J.; Trucks, G. W.; Schlegel, H. B.; Scuseria, G. E.; Robb, M. A.; Cheeseman, J. R.; Scalmani, G.; Barone, V.; Mennucci, B.; Petersson, G. A.; Nakatsuji, H.; Caricato, M.; Li, X.; Hratchian, H. P.; Izmaylov, A. F.; Bloino, J.; Zheng, G.; Sonnenberg, J. L.; Hada, M.; Ehara, M.; Toyota, K.; Fukuda, R.; Hasegawa, J.; Ishida, M.; Nakajima, T.; Honda, Y.; Kitao, O.; Nakai, H.; Vreven, T.; Montgomery, Jr., J. A.; Peralta, J. E.; Ogliaro, F.; Bearpark, M.; Heyd, J. J.; Brothers, E.; Kudin, K. N.; Staroverov, V. N.; Kobayashi, R.; Normand, J.; Raghavachari, K.; Rendell, A.; Burant, J. C.; Iyengar, S. S.; Tomasi, J.; Cossi, M.; Rega, N.; Millam, J. M.; Klene, M.; Knox, J. E.; Cross, J. B.; Bakken, V.; Adamo, C.; Jaramillo, J.; Gomperts, R.; Stratmann, R. E.; Yazyev, O.; Austin, A. J.; Cammi, R.; Pomelli, C.; Ochterski, J. W.; Martin, R. L.; Morokuma, K.; Zakrzewski, V. G.; Voth, G. A.; Salvador, P.; Dannenberg, J. J.; Dapprich, S.; Daniels, A. D.; Farkas, Ö.; Foresman, J. B.; Ortiz, J. V.; Cioslowski, J.; Fox, D. J. *Gaussian~09 Revision D.01;* Gaussian Inc. Wallingford CT 2013.

[40] Sokolovski, D.; De Fazio, D.; Cavalli, S.; Aquilanti, V. *Phys. Chem. Chem. Phys.* **2007**, *9*, 5664.

[41] Gómez-Carrasco, S.; González-Sánchez, L.; Aguado, A.; Roncero, O.; Alvariño, J. M.; Hernández, M. L.; Paniagua, M. *J. Chem. Phys.* **2004**, *121*, 4605.

[42] Skodje, R. T. *Annu. Rev. Phys. Chem.* **1993**, *44*, 145.

[43] Bonnet, L. *J. Chem. Phys.* **2008**, *128*, 044109.

Chapter 7

Summary and Conclusions

Studies on ion-molecule or atom-molecular ion interactions comprising of rare gases and proton are one of the most interesting topic in chemical physics. In this thesis two cationic rare gas hydride species, $[\mathrm{HeHNe}]^+$ and $[\mathrm{NeHNe}]^+$ are investigated. For both the systems, global analytical ground state PESs are generated for the first time. Potential energy wells are found for both the systems for collinear and near-collinear geometries with He-H-Ne and Ne-H-Ne configurations. For each system, the global minimum of the well correspond to a collinear geometry. Bound states and eigen spectra are calculated for zero total angular momentum for the most stable structures. Reactive scattering dynamics are performed for first time for the proton transfer reactions, $\mathrm{He} + \mathrm{NeH}^+ \rightarrow \mathrm{HeH}^+ + \mathrm{Ne}$, $\mathrm{Ne} + \mathrm{HeH}^+ \rightarrow \mathrm{NeH}^+ + \mathrm{He}$ and $\mathrm{Ne} + \mathrm{NeH}^+ \rightarrow \mathrm{NeH}^+ + \mathrm{Ne}$ by using TDQM, TIQM and QCT methods on the newly generated analytical PESs. Effect of rotational and vibrational excitations of the reactants on these reactions are studied. Dense resonance structures of QM reaction probabilities are found for all the three reactions. For the $\mathrm{Ne}+\mathrm{NeH}^+$ reactive system, sharp resonances are found in the low energy region of the ICS curve for ground ro-vibrational state of the reactants. Rate constants calculated for $\mathrm{Ne} + \mathrm{HeH}^+ \rightarrow \mathrm{NeH}^+ + \mathrm{He}$ agree well with the available experimental result. State-to-state dynamics and different mechanisms associated with the $\mathrm{He}+\mathrm{NeH}^+$ and the reverse reactions are investigated for the ground ro-vibrational states of the reactants. Both the reactions favor forward scattering at low and high energies, and these processes are mainly direct in nature. However, indirect dynamics play some role at low collision energies for these reactions. For both the reactions, nearside as well as farside scattered products have been observed for the direct trajectories. The $\mathrm{Ne} + \mathrm{NeH}^+ \rightarrow \mathrm{NeH}^+ + \mathrm{Ne}$ reaction is strongly governed by complex-forming dynamics for low values of collision energies. Simple models like Langevin capture model describes the overall behavior of the processes like $\mathrm{Ne}+\mathrm{HeH}^+$ and $\mathrm{Ne}+\mathrm{NeH}^+$, well. In future, it will be interesting to study the effect of resonances on these reactions. At the end, it is expected that these theoretical studies will stimulate further researches on these systems.

Published Articles

1. Koner, D.; Vats, A.; Vashishta, M.; Panda, A. N. *ab initio* Electronic Structure Investigation of Protonated Mixed Rare Gas Dimers $[NeHHe]^+$, $[ArHHe]^+$ and $[ArHNe]^+$. Comput. Theor. Chem. **2012**, *1000*, 19-25.
2. Koner, D.; Panda, A. N. Quantum Dynamical Study of the He + NeH^+ Reaction on a New Analytical Potential Energy Surface. J. Phys. Chem. A **2013**, *117*, 13070-13078.
3. Koner, D.; Barrios, L.; González-Lezana, T.; Panda, A. N. Wave Packet and Statistical Quantum Calculations for the $He + NeH^+ \rightarrow HeH^+ + Ne$ Reaction on the Ground Electronic State. J. Chem. Phys. **2014**, *141*, 114302.
4. Koner, D.; Barrios, L.; González-Lezana, T.; Panda, A. N. Quantum, Statistical, and Quasiclassical Trajectory Studies For the $Ne + HeH^+ \rightarrow NeH^+ + He$ Reaction on the Ground Electronic State. J. Phys. Chem. A **2015**, *119*, 12052.
5. Koner, D.; Barrios, L.; González-Lezana, T.; Panda, A. N. Scattering Study of the $Ne + NeH^+ (v_0 = 0, j_0 = 0) \rightarrow NeH^+ + Ne$ Reaction on an *ab initio* Based Analytical Potential Energy Surface. J. Chem. Phys. **2016**, *144*, 034303.
6. Koner, D.; Barrios, L.; González-Lezana, T.; Panda, A. N. State-to-State Dynamics of the $Ne + HeH^+(v = 0, j = 0) \rightarrow NeH^+(v', j') + He$ Reaction. J. Phys. Chem. A **2016**, *doi:10.1021/acs.jpca.5b11477*.

Attended Conferences:

1. Poster presentation in International Symposium on Advances in Chemical Sciences 2012, IIT Guwahati
2. Poster presentation in Theoretical Chemistry Symposium 2012, IIT Guwahati
3. Poster presentation in Theoretical Chemistry Symposium 2014, NCL Pune
4. Oral presentation in Chem Convene 2015, IIT Guwahati

5. Poster presentation in Theoretical Chemistry Symposium 2016, University of Hyderabad